Physical origins of the properties of mesoscale convective systems and implications for high impact events

Sophie Abramian

▶ To cite this version:

Sophie Abramian. Physical origins of the properties of mesoscale convective systems and implications for high impact events. Climatology. Université Paris sciences et lettres, 2023. English. NNT : 2023UPSLE012 . tel-04809470

HAL Id: tel-04809470
https://theses.hal.science/tel-04809470v1

Submitted on 28 Nov 2024

THÈSE DE DOCTORAT
DE L'UNIVERSITÉ PSL

Préparée à Ecole Normale Supérieure

Physical origins of the properties of mesoscale convective systems and implications for high impact events

Soutenue par
Sophie Abramian
Le 05/12/2023

École doctorale nº129
Ecole Doctorale des Sciences de l'Environnement d'Ile de France

Spécialité
Sciences du climat, de l'atmosphère et des océans, terrestres et planétaires

Composition du jury :

S. Speich, Professeur Laboratoire de Météorologie Dynamique, Ecole Normale Supérieure de Paris, PSL	*Présidente*
J-P. Chaboureau, Physicien d'Observatoire Laboratoire d'Aérologie de l'Université de Toulouse	*Rapporteur*
P. Gentine, Professor Columbia University in the city of New-York	*Rapporteur*
S. Bony, DR CNRS Laboratoire de Météorologie Dynamique, Sorbonne Université	*Examinatrice*
R. Roca, DR CNRS Laboratoire d'études en Géophysique et océanographie spatiales	*Examinateur*
J. Haerter, Professor University of Potsdam and Niehls Bohr Institute	*Examinateur*
Caroline Muller, Assistant Professor Institute of Science and Technology Austria	*Directrice de thèse*
Camille Risi, CR CNRS Laboratoire de Météorologie Dynamique, Sorbonne Université	*Co-directrice de thèse*

Acknowledgement

Caroline, Camille, merci infiniment pour votre confiance, la liberté que vous m'avez donnée, et les directions, conseils et corrections si nombreux et si précieux qui font que je suis tellement fière du travail accompli! J'ai eu une chance incroyable d'être initiée et formée à la recherche par vous.

Je tiens à remercier sincèrement le jury, pour le temps que vous avez accordé à relire et examiner mon travail. En particulier, je remercie les rapporteurs, Jean-Pierre Chaboureau et Pierre Gentine, pour leurs commentaires et leurs questions, ainsi que les examinateurs, Sandrine Bony, Jan Haerter et Rémy Roca pour avoir évaluer mon travail, mais peut-être plus encore pour l'avoir motivé, encouragé et inspiré. Merci à Sabrina Speich d'avoir accepté d'être présidente du jury. Mes remerciements s'étendent également aux reviewers des articles présentés dans ce manuscrit, avec une pensée particulière pour Martin Singh.

Je remercie mes collègues, amis, et les scientifiques que j'ai pu rencontrer à Paris et aux quatre coins du monde, en commençant par Benjamin: quelle tristesse de quitter notre bureau, tes fulgurances scientifiques et ta force tranquille; j'ai hâte de les retrouver à notre prochaine grimpe ou autour d'un *vers* avec Pauline. Merci à Julie pour son énergie positive au quotidien! Merci Anna Lea (soon be reunited on the east coast!), Lucile, Aglaé, Pablo, Yann, Fabio, Alice, François, Alessandra et tout le département de géoscience; nos déjeuner et discussions sur la terrasse vont tellement me manquer! Un grand merci à mes collègues de Jussieu, Nicolas, Basile, Raphaela, Jean-Louis, Nicolas, Jessica, et de Toulouse, Thomas, Victorien ; j'ai hâte de vous retrouver lors de prochaines conférences. J'ai aussi eu la chance de rencontrer Yi-Ling, Lokahit, Andrea, Bidiyut, Sima, Andrea, Alex, Jiawei que je retrouvais avec tellement de joie lors de mes 'retraites au vert' en Autriche. Merci pour tout.

Je remercie bien-sûr mes grandes copines, Nina, Maïssane, Emilie, Manon, Camille pour leur présence, leur soutien et leurs rires lors de nos soirées parisiennes. Un grand merci à Claire, Antoine, Clément, Pierre, Anatole, Carla-Julie, Lucas, Mathilde, Philippe, Aurore, Simon (j'en oublie pleins!). Je vous adore! Je remercie aussi sincèrement la famille Bertin pour leur curiosité, leur soutien et leur énergie. Merci à Valentin pour nous avoir régalés!

Enfin un immense merci à mes parents pour leur confiance inébranlable et l'importance qu'ils ont accordée à la connaissance et aux études au sein de notre famille. Je remercie du fond du coeur ma grande soeur Anaïs, que j'aime et j'admire depuis toujours. Enfin, cette thèse n'aurait pas été possible sans toi Tristan, merci pour ton aide, ton oreille attentive, et l'intensité que tu mets dans chaque instant de ma vie.

Cette thèse a été financée par un contrat doctoral spécifique aux normaliens de l'Ecole normale supérieure de Paris-Saclay, et par le European Research Council (ERC) under the European Union's Horizon 2020 research and innovation program (Project CLUSTER, Grant Agreement No. 805041).

A tous les professeurs, gardiens du savoir,
à mes deux chats, et à mes deux grand-mères.

Résumé

Les orages de l'échelle de 100km, aussi appelés systèmes convectifs de méso-échelle (MCS), sont responsables de la plupart des évènements extremes dans les tropiques, comme les fronts de rafales puissants, les pluies torrentielles, ou encore les crues soudaines. Parmi eux, on trouve les cyclones tropicaux, dont les vents en rotation sont parmi les plus forts de notre planète. Il en existe d'autres types, comme les lignes de grains qui décrivent un alignement d'orages sur plusieurs centaines de kilomètres. Ces systèmes jouent un rôle fondamental dans le cycle de l'eau. Pourtant, leur organisation reste peu comprise et donc peu prise en compte dans les projections climatiques. Plus précisément, l'échelle caractéristique de la centaines de kilomètres des MCS est inférieure à la résolution spatiale des modèles climatiques globaux, qui traitent donc les systèmes convectifs profonds comme des phénomènes sous-maille. Leur dynamique est alors calculée à l'aide de paramétrisations, basées sur des modèles physiques simplifiés de processus non résolus. Les modèles climatiques actuels ne parviennent donc pas à anticiper la formation de ces phénomènes extrêmes et peinent à prédire leur évolution avec le réchauffement climatique. Cette barrière scientifique fait partie des grands défis énoncés par le programme mondial de recherche sur le climat: nuages, circulation et sensibilité climatique.

Mon travail de thèse cherche à clarifier les processus physiques qui sont à l'origine des systèmes convectifs de méso-échelle pour mieux comprendre et anticiper les extrêmes de pluies qui leur sont associés. Dans un premier temps, j'ai donc cherché à expliquer comment les lignes de grains s'organisent et pourquoi elles s'orientaient selon l'intensité du vent de cisaillement de basse altitude. Puis je me suis demandé si le degré d'organisation d'un MCS, et en particulier si sa capacité à s'étendre et devenir très grand, dépend uniquement des conditions initiales de son développement. Dans un second temps, pour évaluer l'impact de l'organisation de la convection sur les extrêmes de précipitation, j'ai regardé comment ces extrêmes changent selon l'orientation des lignes de grains, et par quelles contributions, dynamique, thermodynamique ou microphysique, l'organisation amplifiait les extrêmes. Enfin, pour évaluer la pertinence des mécanismes identifiés dans le cadre de changements climatiques, nous nous sommes intéressés à l'effet de l'organisation sur les distribution isotopiques de l'eau.

Pour étudier la formation des lignes de grains, nous utilisons un modèle de simulations numériques de haute résolution (10m à 1km) qui résout les équations dynamiques et thermodynamiques de l'air, couplées aux équations de microphysique des changements d'états de l'eau. Etant donné le grand coût de calcul, ces modèles sont lancés sur un domaine réduit et sur une période de 30 jours. Ces simulations idéalisés permettent d'étudier la formation des systèmes avec des paramètres contrôlés, pour mieux identifier les

mécanismes physiques mis en jeu.

Grâce à ces simulations, nous avons mis en évidence trois régimes de développement des lignes de grains en fonction de l'amplitude du vent: le régime sous-optimal, où les lignes se développent perpendiculairement au vent, le régime optimal transitoire, et enfin le régime super-optimal où les lignes de grains ont tendance à se tourner par rapport à la direction du vent. J'ai développé une méthode qui mesure automatiquement l'orientation des lignes de grains, notamment dans le régime super-optimal. Ces résultats ont permis d'élaborer un modèle théorique qui prédit leur orientation des lignes en fonction du vent imposé, qui prend en compte l'intensification des courants de densité, éléments clefs de leur formation. Cette étude a constitué la première partie de ma thèse et a été publiée dans le journal *Geophysical Research Letter*. J'ai aussi co-rédigée une approche plus grand public de ces résultats dans un article de vulgarisation, *Dynamique des nuages et des systèmes de tempêtes convectives* qui a fait la couverture du numéro de mai du célèbre journal *Physics Today* ; et sur lequel l'introduction est en partie basée.

Pour étendre nos résultats à des configurations plus réalistes, et en particulier prendre en compte la circulation générale des courants atmosphérique, nous nous appuyons sur une toute nouvelle générations de simulation globale haute résolution, les simulations DYAMOND (DYnamics of the Atmospheric general circulation Modeled On Non-hydrostatic Domains). Pour la première fois, ces modèles ont été lancés à l'échelle du globe, avec une résolution de 4km soit 100 fois plus fines que les modèles climatiques actuels. Dans ce contexte, je collabore avec une équipe du Laboratoire d'Etudes en Géophysique et Océanographie Spatiales de Toulouse pour étudier le cycle de vie de l'ensemble des MCS issus des simulations DYAMOND. Je développe des méthodes statistiques qui mêlent modèles physiques et intelligence artificielle pour comprendre quels facteurs internes (taux de croissance, forme, vitesse) ou externe (nombre de système voisins, température moyenne, vents de surface) au système contrôlent son aire maximale. Nous avons développé un modèle multi-linéaire interprétable qui permet de prédire avec 70% de confiance la taille maximale qu'atteindra un MCS. Ce travail a été présenté à la conférence *GASS*[1]-*CFMIP*[2] à Paris en juillet 2023 et a reçu le prix *Early Research Carreer* qui récompense les jeunes chercheurs dans les sciences atmosphériques.

La seconde partie de mon projet de thèse se concentre sur l'impact de l'organisation sur les extrêmes de précipitation. Nous nous sommes demandé comment l'orientation des lignes de grains influençent sur les extrêmes de précipitations. Toujours à l'aide de simulations, nous avons montré que les extrêmes de précipitations des lignes de grains sont plus élevés dans

---

[1] Global Atmospheric System Studies

[2] Cloud Feedback Model Intercomparison Project

le régime optimal et superoptimal. A l'aide d'un modèle théorique, nous avons identifié la contribution dynamique comme responsable des variations de précipitation d'un régime à l'autre, et cela s'explique non pas par une instabilité plus grande de l'atmosphère, mais par une initiation plus forte des cellules de convection au niveau de la couche limite. J'ai présenté cette étude à plusieurs conférences internationales, par exemple au WCO2[3] à Utrecht au Pays-Bas, à *AOFD* [4] à Breckenridge CO, au *GASS Meeting* à Monterey CA, ou encore à l'*EGU*[5] à Vienne en Autriche, et ces résultats font l'objet d'une publication acceptée au *Journal of Advances in Modeling the Earth System (JAMES)*.

Une implication supplémentaire, cette fois-ci imperceptible, se manifeste lors du développement et du cycle de vie des systèmes convectifs de méso-échelle. Ces phénomènes impliquent en effet une modification de la composition isotopique de l'eau au sein de leur environnement immédiat. L'objectif principal de cette dernière investigation est de mieux comprendre et décrire les variations de la distribution isotopique au sein de la structure méso-échelle des lignes de grains. Une attention particulière est portée aux signatures isotopiques de la vapeur d'eau dans la couche sous-nuageuse et aux précipitations. L'examen des régimes climatiques historiques offre à terme une direction précieuse pour évaluer la pertinence des mécanismes identifiés dans le contexte du changement climatique contemporain. Il convient de noter que ce chapitre se distingue des efforts de recherche précédents, car il résulte d'un projet collaboratif auquel j'ai participé mais dont je ne suis pas première auteure. Ce projet a abouti à la publication d'un article, paru dans le *Journal of Advances in Modeling Earth Systems en 2023.*

En conclusion, en essayant de comprendre l'organisation de la convection profonde et les phénomènes météorologiques extrêmes qui lui sont associés, mes recherches participent à réduire les biais récurrents des représentations conventionnelles du système atmosphérique, et répondent au besoin urgent d'anticiper les conséquences du changement climatique.

---

[3] Workshop on Cloud Organization

[4] Atmospheric and Oceanic Fluid Dynamics

[5] European Geosciences Union

Abstract

Storms on the scale of 100 km, also known as mesoscale convective systems (MCS), are responsible for most of the extreme events in the tropics, such as powerful gust fronts, torrential rains, and sudden floods. Among them are tropical cyclones, whose rotating winds are among the strongest on our planet. There are other types as well, like squall lines, which consist of an alignment of storms over several hundred kilometers. These systems play a fundamental role in the water cycle. However, their organization remains poorly understood and therefore is inadequately considered in climate estimates. Specifically, the characteristic scale of MCSs of hundreds of kilometers is smaller than the spatial resolution of global climate models, which treat deep convective systems as subgrid phenomena. Their dynamics are then calculated using parameterizations based on simplified physical models of unresolved processes. Current climate models thus struggle to predict the formation of these extreme phenomena and have difficulty projecting their behavior under climate warming. This scientific barrier is one of the major challenges outlined by the World Climate Research Program (WCRP): Clouds, Circulation, and Climate Sensitivity.

My doctoral research aims to clarify the physical processes underlying mesoscale convective systems in order to better understand and anticipate the associated rainfall extremes. Initially, I investigated how squall lines organize and why their orientation depends on the intensity of low-level wind shear. Then, I explored whether the degree of organization of an MCS, particularly its ability to expand and become very large, solely relies on the initial conditions of its development. Subsequently, to assess the impact of convection organization on precipitation extremes, I examined how these extremes changed based on the orientation of squall lines and the contributions from dynamic, thermodynamic, or microphysical aspects that amplify organization-induced extremes. Lastly, to evaluate the relevance of the identified mechanisms in the context of climate changes, we studied the effect of organization on isotopic distributions of water.

To study squall line formation, we utilize a high-resolution numerical simulation model (1km) that solves the dynamic and thermodynamic equations of the air, coupled with microphysical equations for changes in water states. Due to computational cost, these models are run on a reduced domain for a 30-day period. These idealized simulations enable us to study system formation with controlled parameters, better identifying the involved physical mechanisms.

Through these simulations, we unveiled three development regimes for squall lines based on wind amplitude: the suboptimal regime, where lines develop perpendicular to the wind; the transient optimal regime; and the superoptimal regime, where squall lines tend to rotate in relation to the wind direction.

I developed an automated method to measure the orientation of squall lines, particularly in the supercritical regime. These findings led to a theoretical model predicting line orientation based on imposed wind, incorporating the intensification of density currents, a key element in their formation. This study constituted the first part of my thesis and was published in the Geophysical Research Letters journal. I also co-authored an outreach article on these results in a piece titled ”Cloud Dynamics and Convective Strom systems” which was featured on the cover of the May issue of Physics Today; and on which the introduction is partly based.

To extend our results to more realistic configurations, especially considering the general circulation of atmospheric currents, we rely on a new generation of high-resolution global simulations called DYAMOND simulations. For the first time, these models were run on a global scale, with a resolution of 4km, approximately 25 times finer than current climate models. In this context, I collaborate with a team from the Laboratory of Studies in Geophysics and Space Oceanography in Toulouse to study the life cycle of all MCSs from DYAMOND simulations. I develop statistical methods that combine physical models and artificial intelligence to understand internal (growth rate, shape, speed) and external factors (number of neighboring systems, average temperature, surface winds) controlling the maximum area of systems. We developed an interpretable multilinear model that can predict with 70% confidence the maximum size an MCS will reach. These results are discussed in Chapter 3 and were presented at the GASS-CFMIP conference in Paris in July 2023 and received the Early Research Career Award, recognizing the work of young researchers in atmospheric sciences.

The second part of my thesis project focuses on the impact of organization on precipitation extremes (Chapter 4) and isotopes (Chapter 5). We first explored how the orientation of squall lines influences precipitation extremes. Through simulations, we demonstrated that precipitation extremes of squall lines are higher in the optimal and superoptimal regimes. Using a theoretical model, we identified dynamic contribution as responsible for precipitation variations from one regime to another, not due to greater atmospheric instability, but stronger initiation of convection cells in the boundary layer. I presented this study at several international conferences, and these findings are the subject of an accepted publication in the Journal of Advances in Modeling the Earth System (JAMES).

An additional, albeit imperceptible, consequence manifests during the development and lifecycle of mesoscale convective systems. This phenomenon entails a modification in the isotopic composition of water within the system’s immediate environment. The primary aim of this last investigation is to gain insight into the manner in which these variations progress within the mesoscale structure of squall lines. Particular attention is directed toward the isotopic signatures of water vapor in the sub-cloud layer and precipitation. Ultimately, the examination of historical climatic regimes provides a valuable avenue for assessing the applicability of identified mechanisms within the context of contemporary climate change. It is noteworthy to differentiate this chapter from preceding research efforts, as it is the result of a collaborative project in which I participated but did not directly produce the reported findings. The aforementioned project has yielded a published paper in the Journal of Advances in Modeling Earth Systems in 2023.

In conclusion, by seeking to understand the organization of deep convection and the extreme weather phenomena associated with it, my research contributes to reducing recurring biases in conventional representations of the atmospheric system, addressing the urgent need to anticipate the consequences of climate change.

Contents

Chapter 1

Introduction

Introduction

Résumé en français

L'objectif global de cette thèse est de clarifier l'origine physique de l'organisation des orages de grande échelle (chapitres 2 et 3) et d'évaluer son impact sur les précipitations extrêmes (chapitre 4) et la distribution des isotopes (chapitre 5). Dans cette introduction, nous présentons le contexte dans lequel nous avons soulevé ces questions scientifiques. Nous commençons par passer en revue la physique de la formation des nuages, ainsi que les rétroactions conduisant à l'organisation des orages et des multi-structures nuageuses. Nous discutons ensuite de son lien avec les précipitations extrêmes et de l'état de l'art pertinent. Les avancées dans les méthodes de simulations numériques et les outils théoriques pour décrire la convection profonde et les précipitations extrêmes associées sont présentées dans la section 1.3. Enfin, l'objectif général de ma recherche et la méthodologie utilisée pour sa réalisation sont exposés dans la dernière section.

Opening

The overall goal of this thesis is to clarify the physical origin of the organization of storms (Chapter 2 and 3) and to assess its impact on extreme precipitation (Chapter 4) and isotope distribution (Chapter 5). In this introduction, we provide some context relevant to those scientific questions. We start by reviewing some basics of cloud formation and physics, as well as the feedbacks leading to storms organization. We then discuss its link with extreme precipitation and the relevant state of the art. Advancements in simulating and studying deep convection and the associated precipitation extreme are presented in section 1.3. Subsequently, the overarching aim of the research and the methodology utilized for its realization are expounded upon in the last section.

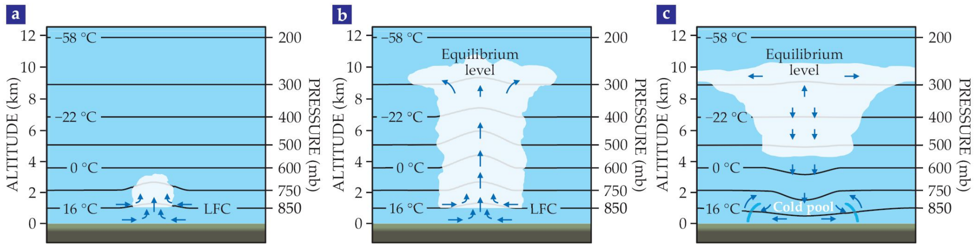

Figure 1.1: Convective-cloud life cycle. During a storm's developing stage (a), air starts rising, and when it reaches its level of free convection (LFC), it becomes buoyant. (b) It keeps rising until, at the cloud's mature stage, it reaches the equilibrium level, where its density matches that of the surrounding air. (c) The upper-level air then spreads horizontally, forming what's known as an anvil cloud. Liquid and ice droplets grow through microphysical processes and begin to fall toward the ground. In the dissipating stage, the partial evaporation of the precipitating condensates produces a mass of cooler air and generates a downdraft that spreads it horizontally at the surface. (Adapted from the COMET website at http://meted.ucar.edu of the University Corporation for Atmospheric Research, sponsored in part through cooperative agreement(s) with the National Oceanic and Atmospheric Administration, US Department of Commerce. ©1997–2023 UCAR.)

1.1 Uncovering the Dynamics of Deep Convection Organization

This section has been the subject of an outreach paper untitled The Cloud Dynamics of Convective Storms, C.Muller & S.Abramian, in Physics Today May 2023 (Front Cover). Its published version follows closely the content presented below.

1.1.1 Multiscale Insight into Deep Convection

The air's upward movement carries near-surface water vapor, whose large concentration at low altitudes decreases rapidly with height in the atmosphere. Through a process known as adiabatic expansion, the rising moist air cools as the pressure drops at higher altitude (figure 1.1.a). When the moist air is cold enough, its water vapor starts to form liquid or ice condensates, depending on temperature. The tiny, suspended condensates —typically a few tens of microns in diameter— form clouds, which unlike water vapor are visible to our eyes. At the mature stage of cloud formation, the rising air reaches its equilibrium level— the altitude where its density matches that of the environment—and the cloudy air is no longer buoyant (figure 1.1.b). For dense, deep clouds, the equilibrium level can be as high as the tropopause, an altitude of around 10–15 km.

Once the air stops rising, it spreads horizontally at the top of the cloud and forms what's called an anvil cloud, shown in figure 1c. The condensed droplets grow in the cloud through microphysical processes, and when large enough, they eventually start to precipitate and fall toward the ground. As they do so, they may partially evaporate, notably below the cloud base. The

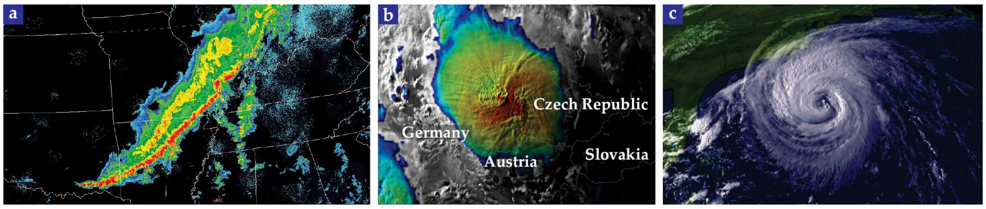

Figure 1.2: Mesoscale convective systems are storms in the atmosphere that can span hundreds of kilometers. Some examples include (a) squall lines, which are a type of elongated multicloud structure; (b) a circular multicloud structure; and (c) a tropical cyclone, composed of a rotating multicloud structure. (Panel a courtesy of Nolan Atkins; panel b © EUMETSAT 2011; panel c courtesy of the World Meteorological Organization.)

concomitant latent cooling leads to a cold air mass, known as a cold pool, that descends below the cloud and spreads horizontally at the surface. The downward motion counteracts the upward motion that started the convective storm, thereby ending the cloud life cycle. The whole process for a single cloud typically lasts from thirty minutes to few hours and spans a horizontal scale of roughly one to a few kilometers. Clouds can also form spectacular multicloud structures, several of which are shown in figure 1.2. At scales of hundreds of kilometers— the so- called mesoscale— organized convection can take the form of squall lines or mesoscale convective complexes. The most famous example is probably the tropical cyclone. At its center lies a relatively quiet eye, surrounded by a cloudy wall of rotating winds, which are among the strongest on the planet. Mesoscale organized systems like the ones shown in figure 1.2 lead to extreme weather and to changes in large- scale properties, notably cloud cover and water- vapor distribution. Although the physical processes that cause mesoscale organization are still poorly understood, the science is improving because of significant advances in the past decade. The breakthroughs were made possible by the increased capability of computer simulations and by many idealized and theoretical investigations. Notably, much progress has been made on a mode of convective organization called self-aggregation.

1.1.2 The Power of Internal Feedback: Self-Aggregation

Self-aggregation refers to the spectacular ability of deep clouds to spontaneously cluster in space, despite perfectly homogeneous boundary conditions in idealized numerical simulations (Bony *et al.* 2015) (see figure 1.3). The phenomenon occurs when sea surface temperature is constant, with neither large-scale forcing nor land–sea contrasts, and with reentrant boundary conditions —a cloud that exits the domain on one side reenters on the other side.

The clouds' spontaneous organization via internal feedbacks appears to be

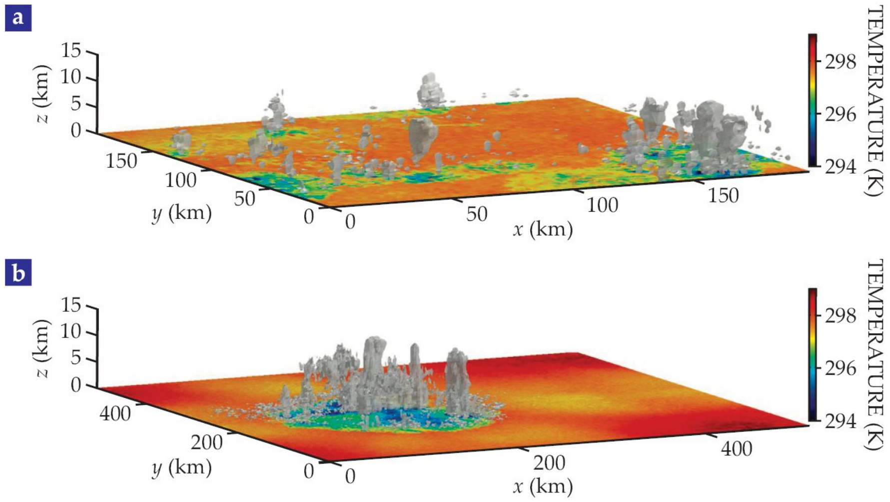

Figure 1.3: Idealized numerical simulations. In the absence of feedback mechanisms, (a) simulated clouds appear disorganized in space. (b) Under the influence of those mechanisms, however, clouds can self-aggregate into a coherent convective structure, and that behavior increases with domain size and temperature. Self-aggregation is associated with a large-scale drying of the atmosphere and enhanced large-scale outgoing radiative cooling to space. Based on observations of relative humidity, researchers have learned that the middle troposphere is consistent with modeled self-aggregation and is on average drier for an atmosphere in which the same amount of precipitation is concentrated into a small number of convective clusters. (Adapted from ref. 1.)

related to the interaction of clouds with their near environment. Researchers have put forward four feedback mechanisms to explain self-aggregation: radiative processes, entrainment at the edge of clouds, cold pools, and waves (Muller *et al.* 2022). All the aggregation feedbacks work in a similar fashion: They favor the formation of clouds in regions near clouds and disfavor formation in regions devoid of them. Both actions are positive feedbacks because they reinforce an existing cloud distribution. More clouds form where there are more clouds, and fewer form where there are fewer. That reinforcement leads to a spatial separation between cloudy, moist regions and noncloudy, dry ones. In radiative feedback, dry regions are associated with strong radiative cooling to space because of their relatively small amount of atmospheric water vapor. It is similar to a local greenhouse effect, in that water vapor acts as a greenhouse gas— less water vapor means fewer greenhouse gases and thus cooling. That cooling of the air triggers it to subside and flow in a diverging pattern near Earth's surface. Because most water vapor is located there, the relatively dry subsiding air from above replaces the relatively moist near- surface air, drying that part of the atmosphere further. The drier air is less buoyant and thus less receptive to convection and cloud formation (Bretherton *et al.* 2005; Muller and Bony 2015a). With entrainment feedback, as air rises and water vapor condenses to form a cloud, air viscosity causes the rising air to drag surrounding air with it. The edge of the cloud becomes highly turbulent and leads to the entrainment and the mixing of environmental air with the cloudy air. Mixing at the edge can significantly reduce cloud buoyancy if the entrained air is dry. Indeed, dry- air mixing will lead to the evaporation of some of the cloud droplets, and the concomitant latent cooling reduces the cloud buoyancy. Conversely, if the environmental air is moist, which would happen if a cloud formed near a recently formed one, the upward motion will not be arrested, and it'll form more easily. That possibility favors the clustering of clouds in the moistest region (Tompkins and Semie 2017). In cold-pool feedback, as cold pools spread at the surface below a precipitating cloud, they raise the surrounding warmer air at the edges. The mechanically induced upward motion encourages the formation of new clouds near the edge of cold pools. And by facilitating new clouds in the vicinity of existing ones, cold pools thus reinforce the clustering of clouds in space (Haerter 2019). In wave feedback, convection triggers internal gravity waves that propagate in stratified media (Mapes and Houze Jr 1993). Suppose that the atmosphere is a two- layer fluid: The denser, bottom layer of air ranges from the ground to the bases of the clouds at an altitude of about 1 km, and the lighter layer above spans from the clouds' bases to their tops at an altitude of about 10 km. In that simplified case, internal waves become interfacial waves that propagate between the two layers, similar to surface waves between air and water when a rock is thrown in a pond. Interfacial waves between the two layers are triggered by convection and propagate away from the clouds.

The waves can form standing wave packets that separate convectively active areas from inactive ones (Yang 2021). Because of the idealized settings in which self-aggregation is investigated, researchers are still debating its relevance to the real world. Ending that debate will require more observations, either from satellites or in situ measurements. With recent improvements to the fundamental understanding of the physical processes involved in self- aggregation, researchers should be positioned to identify each feedback in observations and determine to what extent each dominates in the real atmosphere.

1.1.3 Probing External Feedback: The case of Squall Line

Observation of Squall Lines

In addition to internal feedbacks, the interaction between clouds and the atmosphere's large-scale flow plays a significant role in organizing convection. One notable example of such interaction is observed in squall lines, which arise due to vertical wind shear—where surface winds differ in speed from those at higher altitudes. A pioneering study by Hamilton *et al.* 1945, titled 'Meteorology of Nigeria and Adjacent Territory,' investigated this form

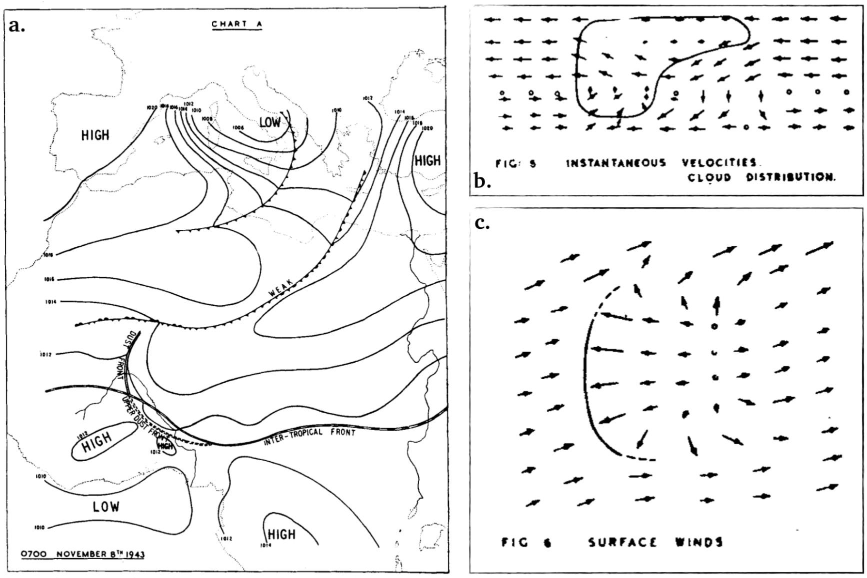

Figure 1.4: a. Map for the Hamilton and Archbol 1945 defining the region studied and showing the favored region for 'disturbance lines' to developp in West Africa. b. First sketch of the interaction between wind surface to produce squall and develop line-squall. c. Perturbation of surface flux by rain evaporation. Adapted from Hamilton *et al.* 1945

of convective organization by examining prevailing winds and weather patterns in West Africa. Using pilot balloon ascents, they detected rapid wind changes with altitude, indicating strong vertical wind shear. Additionally, they identified lines of disturbed weather along the coast, ranging from heavy cloud banks to belts of thunderstorms. These weather features exhibited a west-south-westerly direction with a speed of 25-30 m.p.h., accompanied by variable wind propagation during their lifespan. These disturbances, associated with heavy rain and intense updrafts in the cloud base, formed storm belts about 30 miles thick. The researchers coined the term "line-squall" for the most active disturbances, which eventually became the namesake for tropical squall lines. Hamilton and Archbol proposed that atmospheric instability underpinned the mechanism behind these lines. They also explored possible interactions with surface fluxes, as shown in Figure 1.4.a. Additionally, they described rain evaporation, hinting at the concept of cold pools, as depicted in Figure 1.4.b.c.

Several field experiments have yielded abundant data crucial for understanding tropical convective systems, including squall lines. For example, Betts *et al.* 1976; Betts 1976; Miller and Betts 1977 described mesoscale convective systems affecting Venezuela, undoubtedly squall lines. Zipser 1977 presented a case study of a Caribbean squall system, proposing a general airflow pattern that was well-supported. Key features included a gust front at the

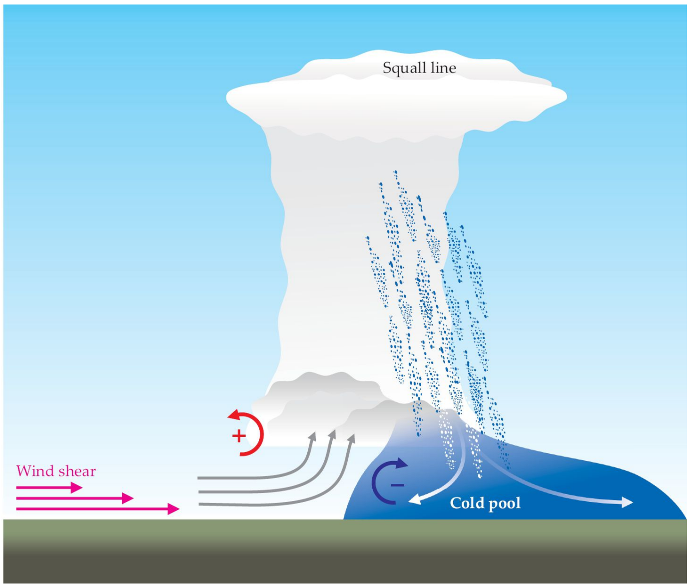

Figure 1.5: Several interactions lead to the formation of a squall line of clouds. Rain and its subsequent evaporation fuel the rise of a mass of cold air that spreads below a cloud. Incoming wind (gray arrows) blocks the spreading of the cold pool, which in turn acts as a ramp for raising moist warm air. The vertical variation of wind strength (pink arrows) induces a positive vorticity (red plus sign). That twisting motion interacts with the negative vorticity found in the cold pool (blue minus sign), which favors storm drafts and other upward motion that promotes the formation of squall lines in the atmosphere.

leading edge of advancing rain-cooled air near the surface, a line of convective cells ascending through the troposphere, producing sharp downdrafts, and a mesoscale downdraft likely caused by hydrometeor evaporation and melting underneath the anvil. In some cases, a rear inflow jet, resembling a jet-like downdraft, sloped downward in front of the squall line. A major field campaign, the Global Atmospheric Atlantic Tropical Experiment (Greenfield and Fein 1979), took place over the Atlantic Ocean from June to September 1974. Several of its investigations (Houze 1977; Tongjian and Houze 1987) focused on a tropical squall line, examining the physical processes involved, the factors influencing propagation speed, precipitation distribution between convective and stratiform regions, stratiform zone dynamics, and system evolution throughout its lifecycle. Squall lines also develop in mid-latitudes, with primary characteristics resembling those in the tropics (Bluestein and Jain 1985; Smull and Houze Jr 1985; Rutledge and Houze Jr 1987 for a review).

Theoretical Model

The theoretical explanation for the development of squall lines came from a foundational paper published 35 years ago, referred as Rotunno *et al.* 1988 (hereafter RKW; see also Garner and Thorpe 1992; Weisman and Rotunno 2004). It describes how wind shear can interact with the cold pool, which in this case plays a key role in maintaining the storm. The interaction is based on three main principles, shown schematically in figure 1.5. First, wind shear blocks the spread of the cold pool from where it originates. Second, the cold pool acts as a ramp that lifts the warm and moist air. Finally, wind shear and the cold pool together produce a vorticity dipole— the two counterrotating wind profiles, often indicated with a + sign and a – sign. The vorticity dipole supports upward motion between the wind profiles, which accelerate the upward motion and promote deep vertical convection. The edge of the cold pool then becomes an optimal spot for deep convective updrafts that lead to cloud formation, precipitation, and squall lines. In other words, the storm precipitation feeds the cold pool, which maintains the conditions that favor the storm updraft and subsequent precipitation. The series of interactions allows squall lines to last as long as 24 hours and to travel for thousands of kilometers. Intuitively, one would expect the coupling between the wind shear and the cold pool to depend on the shear intensity. When it's too weak, as illustrated in figure 1.6.a, there's no particular interaction and therefore no organization of the deep clouds. When the shear increases, however, a squall line tends to develop perpendicular to the imposed wind, as seen in figure 1.6.b, which corresponds to a horizontal wind variation of about 10 m/s over the 1 km layer closest to Earth's surface. Beyond wind speeds of 10 m/s, squall lines are oriented at an angle less than 90 degrees to the wind direction, as shown in figure 1.6.c.

The diverse patterns of squall lines are demonstrated here using cloud resolving models, which involve numerical simulations with explicit convection resolution. The correlation between these concepts and observations is discussed in section 5 of Rotunno *et al.* 1988. Although instances of optimal conditions are more likely to be observed, Dudhia *et al.* 1987 recounts a scenario where shear surpasses the influence of a cold pool. Describing the orientation of the squall line is challenging, as the theory at that time wasn't sufficiently developed to propose examining it. The occurrence of this oriented line phenomenon remains yet to be observed.

Wind shears with intensities up to the optimal value make squall lines more organized and, therefore, can drive their intensification. Recent climate-model simulations, for example, highlight that over the Sahel region in north-central Africa changing wind shear is the main reason for the enhancement of squall lines under warming conditions (Fitzpatrick *et al.* 2020). We note in passing how that case illustrates how wind shear adds a critical contribution to the intricate relationship between climate change and the degree of deep convection organization.

As a conclusion, the current literature in cloud physics doesn't know the

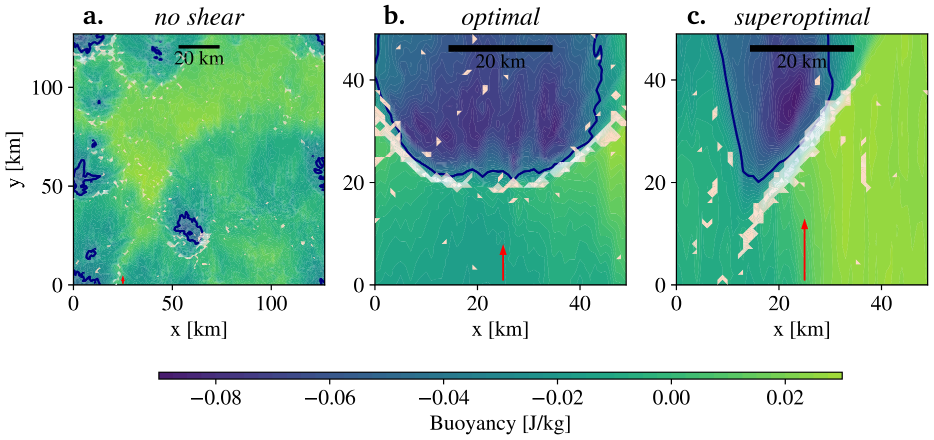

Figure 1.6: Wind shear influences the orientation of tropical squall lines. In each of the three simulation cases, the color denotes the buoyancy field, which is proportional to the atmosphere's anomalous temperature relative to the climatological average. The cloud locations are shown in white. (a) When no shear is imposed, no organization of a squall line is observed. (b) For a horizontal wind speed U = 10 m/s (red arrow), a squall line of clouds develops perpendicular to the wind direction (c) For U = 20 m/s, which corresponds to greater than the optimal shear, the squall line is oriented at an acute angle to the wind direction (Adapted from Abramian et al 2022)

extent to which internal feedbacks organize clouds in the real atmosphere compared with large-scale forcings, such as wind shear and land–ocean contrasts. The response of clouds to global warming is one of the largest uncertainties in current predictions of climate change from models (Schneider *et al.* 2021). Given the dependence of cloud cover on convective organization (Stein *et al.* 2017), how convection changes with climate change is of major importance. All the aforementioned idealized studies can help address the link between clouds and climate in observations and shed new light into the physical processes at stake in the atmosphere. That combination of idealized studies with analysis of real-world data will help researchers determine how cloud organization may change with global warming. Observing convective organization and the relevant physical processes is challenging. For instance, assessing the radiative feedback requires sensitive measurements of radiative cooling rates close to the surface, which are difficult to obtain from satellite measurements (Stevens *et al.* 2018). The recent international observational campaign EUREC4 provided invaluable in situ data of vertically resolved radiative cooling rates (Bony *et al.* 2017; Stevens *et al.* 2021). Those data helped researchers develop a theoretical basis for what dictates low-level cooling rates (Albright *et al.* 2021) notably their close relationship with water-vapor variations (Fildier *et al.* 2023). A global climatology of cold pools is also missing, as they are equally challenging to observe from satellites. Recent work using synthetic-aperture radar and machine learning to obtain images shows some promise (Brilouet *et al.* 2023). The European Space Agency's new Earth Explorer mission, Harmony (Harmony 2020), will provide finer resolution measurements of near-surface winds. Those observations will undoubtedly contribute to improved measurements and understanding of cold-pool properties. A recent study attributed the latest observed trend of precipitation extremes to changes in convective organization (Tan *et al.* 2015). Accurate predictions of the hydrological cycle, therefore, will require researchers to better understand convective organization and how it will change with warming. The next section focuses on the precise link between convective organization and extreme precipitation.

1.2 Extreme Rainfall's Relationship with Convection Organization

In the preceding section, we discussed the formation of thunderstorms and the processes involved – either internal self-aggregation or external wind shear effects for squall lines – which lead to the organization of deep clouds over hundreds of kilometers, resulting in the development of mesoscale convective systems. We also pointed out the inadequate representation of these systems in climate models like Global Circulation Models (GCMs), primarily due to their sub-grid scale nature and the reliance of parameterization models on incomplete theories. Notably, these systems are associated with strong meteorological events, including powerful gust fronts, heavy rainfall, and flash floods. Therefore, it is of paramount importance to gain a deeper insight into the connection and mechanisms underlying meteorological extremes, with a particular emphasis on extreme precipitation events driven by convective organization.

The aim of this section is to delve into the methodology used to establish a causal link between convective organization and extreme precipitation events. We will commence by defining the concept of extreme precipitation, followed by an exploration of methods to quantify convective organization. Finally, we will describe the protocols that have demonstrate their relationship, along with the underlying physical processes at play.

1.2.1 Defining Precipitation Extremes and Nature's Fury

Generalities on Precipitation

The Glossary of Meteorology defines precipitation as all hydrometeors formed in the atmosphere, encompassing liquid, solid, or mixed forms (e.g., resulting from incomplete melting, freezing, or accretion), large enough to fall due to gravity. Precipitation types include drizzle, rain, sleet, snow, ice pellets, graupel, and hail as shown in figure 1.7. Precipitation occurs when

Figure 1.7: Forms of frozen precipitation. Left to right : hail, graupel, sleet, snow. Credits to : NOAA National Severe Storms Laboratory

a portion of the atmosphere reaches saturation with water vapor (reaching 100% relative humidity), causing water to condense and fall. Fog and mist, in contrast, are colloids since water vapor does not condense sufficiently to precipitate. These processes are elucidated by cloud microphysics, which studies the population of hydrometeors in different categories and the processes converting them from one category to another. A cloud model's microphysics scheme may include equations governing the creation and destruction of cloud ice, cloud water, rain, and various types of precipitation ice (these are explained in more detail in the section relative to cloud resolving models and microphysic parametrization, see also Wallace and Hobbs 2006, chapter 6).

Precipitation measurement traditionally relies on rain gauges, the most widely used method providing direct and ground-based data at specific locations. This yields accurate and reliable information for local points, contributing to long-term climate studies and trend analysis. However, rain gauges have limited spatial coverage, hindering their ability to capture rainfall variability over vast regions and oceanic areas. Additionally, local obstructions like buildings and trees can lead to underestimation or overestimation of rainfall.

To address these limitations, satellite-based instruments, such as microwave radiometers and precipitation radars, come into play. These technologies estimate precipitation over extensive and remote areas, offering valuable global coverage and real-time monitoring. To enhance accuracy, satellite data is calibrated and validated using information from rain gauges. Prominent missions like the Tropical Rainfall Measuring Mission (TRMM) by NASA and JAXA paved the way for global precipitation measurement. Its successor, the Global Precipitation Measurement mission, delivers data products with spatial resolution of $10km \times 10km$ and temporal resolution of 30 minutes since 2015.

Precipitation is quantified in millimeters (mm) of height or depth. Alternatively, it can be expressed as a volumetric quantity, representing the amount of water per unit area, in liters per square meter (L/m^2). Since

$1L = 1dm^3 = 1mm \cdot m^2$, the area units ($m^2$) cancel out, simplifying to "mm." This volumetric representation also corresponds to an area density expressed in kilograms per square meter (kg/m^2), assuming 1 liter of water has a mass of 1 kilogram (water density), which is widely accepted for practical purposes. In meteorology, precipitation is measured over a specific accumulation period, often a day, resulting in a final unit of "mm/day."

Precipitation is not uniformly distributed across the globe partly due to variations in convection patterns. Climate classification is based on precipitation and temperatures, with the well-known Köppen classification (see Figure 1.8) dividing the Earth into five main climates: tropical (A), dry (B), mild temperate (C), cold temperate (D), and polar (E). Each climate is further subdivided into subclimates based on rainfall patterns. Within the tropical climate, there are distinctions such as equatorial climate, monsoon regime over the Indian Ocean, and tropical wet and dry climate.

On this map, the majority of precipitation occurs in the tropics, giving rise to the name "tropical rainbelt." The tropical rainbelt, also known as the Intertropical Convergence Zone (ITCZ), is a prominent band of intense rainfall and convective activity encircling the Earth near the Equator. It stands as one of the most significant features of the Earth's climate system. While the rainbelt shifts slightly north and south with the changing seasons, it generally remains within the tropical latitudes.

The formation of the tropical rainbelt is primarily influenced by the differential heating of the Earth's surface. Close to the Equator, incoming solar radiation is more direct and intense, leading to rapid surface and atmospheric warming. As warm, moist air rises from the heated surface, it cools and condenses, giving birth to clouds and heavy precipitation.

The convergence of trade winds from both hemispheres plays a pivotal role in creating a low-pressure area along the Equator. Within this convergence zone, trade winds meet and ascend, generating a persistent belt of rainfall and thunderstorms. The ITCZ can span several hundred kilometers wide and is known for its dynamic and occasionally unpredictable behavior, leading to the occurrence of extreme precipitation events.

Defining Extreme Precipitation

What constitutes a precipitation extreme? Ask a resident of Brest or Saint-Tropez and you'll likely get two different answers. The corollary in climate science is that extreme events are defined relative to the normal distribution of that event over time and space, as depicted in Figure 1.9. Precipitation extremes correspond to high percentile ranks of precipitation occurrence within a specific region and time period.

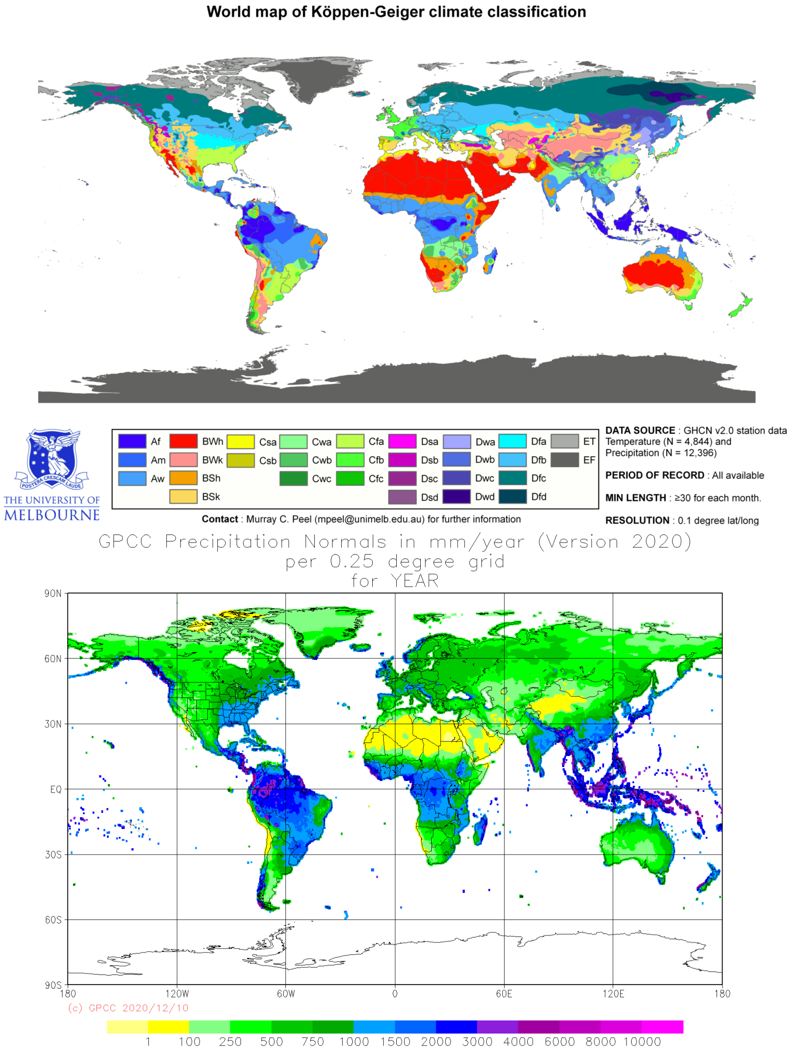

Figure 1.8: top. The Köppen-Geiger climate map by the University of East Anglia and the Deutscher Wetterdienst for the period 1951 to 2000. bottom. Total precipitation in mm/year wild world.

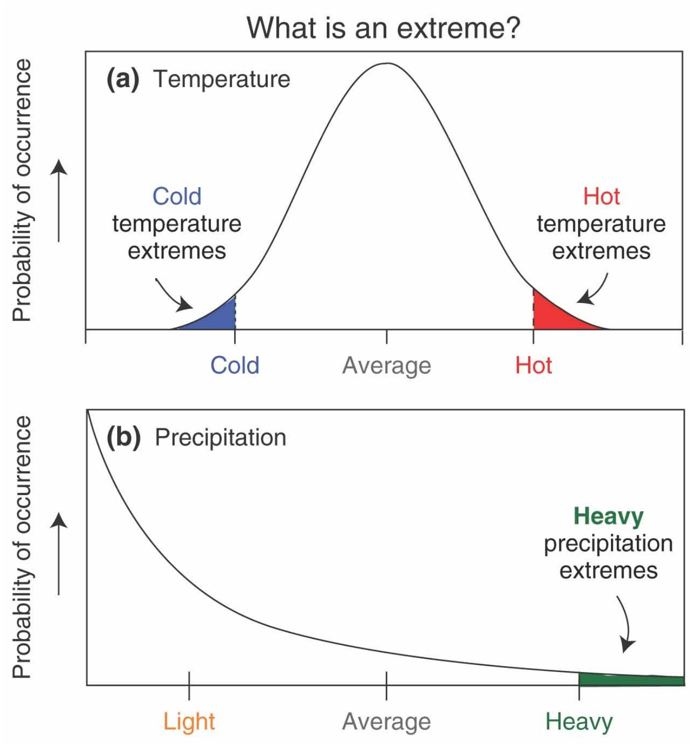

Figure 1.9: The probability distributions of daily temperature and precipitation. The higher the black line, the more often weather with those characteristics occurs. Extremes are denoted by the shaded areas. (Reprinted with permission from Ref 4. Copyright 2005 Intergovernmental Panel on Climate Change)

Extremes are related to high percentile; but which one ? from which distribution ? A recent study (Schär *et al.* 2016) shows that the use of precipitation percentiles in the literature exhibits a number of different methodologies. Three types of percentile indices were investigated :

1. All-day percentiles (e.g. Moberg *et al.* 2006; O'Gorman and Schneider 2009b; O'Gorman 2014; Ban *et al.* 2015): In this case the percentiles are expressed relative to all data, i.e. wet and dry days or hours.

2. Wet-day percentiles (e.g. Boroneant *et al.* 2006; Frei *et al.* 2006; Lenderink and Van Meijgaard 2008; Rajczak *et al.* 2013; Kendon *et al.* 2014). In this case precipitation percentiles are computed for the subset of days or hours with non-zero precipitation, i.e. with precipitation above daily or hourly thresholds of typically 1 mm/d or 0.1 mm/h, respectively. These thresholds have been motivated from observational constraints.

3. Frequency indices based on percentile thresholds (e.g. Karl and Knight 1998; Frei and Schär 2001; Durman *et al.* 2001; Klein Tank and Können 2003; Orlowsky and Seneviratne 2012; Sillmann *et al.* 2013; Llopart *et al.*

2014): In this case, percentile thresholds are derived for some reference period, and the subsequent analysis then targets the frequency with which these thresholds are exceeded. This procedure corresponds to the official recommendation of the World Climate Research Program (WCRP) and the World Meteorological Organization (Sevruk *et al.* 2009; Zhang *et al.* 2011). The methodology does not fully classify as a percentile methodology; it rather corresponds to a frequency methodology, but using a percentile-based definition of the thresholds.

Significant differences exist between different percentile methodologies, but the overall message of the scientific literature is quite clear and points towards an intensification of heavy events in many regions in response to greenhouse gas forcing along all these methodology.

Nature's Fury and need for a better understanding of extremes

From this statistical definition of precipitation extremes, at least two consequences arise. First, precipitation extremes are challenging to observe due to their rarity. Understanding these phenomena is thus limited, and anticipating them remains a real challenge. Second, inhabited areas exposed to such extremes are not designed to withstand these events, leading to human and material disasters. Tropical cyclones are rare events of extraordinary intensity. Cyclone Freddy (see Figure 1.10) was a long-lived, powerful, and deadly storm that traversed the southern Indian Ocean for over five weeks in February and March 2023. Freddy stands as the longest-lasting and highest-accumulated-cyclone-energy-producing tropical cyclone ever recorded worldwide. With maximum winds reaching 148 km/h and gusts up to 213 km/h, Freddy brought over 600mm of rainfall to certain areas, four times greater than the average monthly precipitation during the rainy season.

The consequences of such an event are dramatic and distressing: According to the latest data from the National Institute for Disaster Risk Management (INGD), Cyclone Freddy impacted a total of 253,466 people. In terms of damage, approximately 48,134 houses were partially or completely destroyed, with around 191,562 hectares of land damaged and an additional 38,000 hectares lost. Moreover, 52 health units and 1,561 classrooms were also damaged.

The example of Freddy seems to demonstrate that the organized and prolonged nature of convective events, ranging from aggregation to mesoscale convective systems, including organized mesoscale systems like squall lines or cyclones, favors the occurrence of extreme precipitation.

Efforts to quantify the link between organization and precipitation extremes, both in numerical simulations and observations, have intensified in recent years. It's important to note that the degree of organization has a more sig-

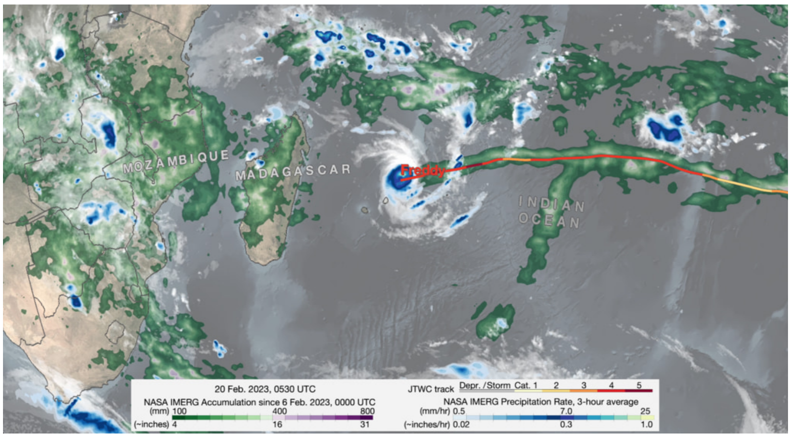

Figure 1.10: NASA Tracks Freddy, Longest-lived Tropical Cyclone on Record.

nificant impact on precipitation extremes than warming alone (Da Silva *et al.* 2021; Fildier *et al.* 2021; Muller 2013b). While warming can create conditions conducive to convective organization, this mechanism introduces significant uncertainty on the response in terms of extremes. However, the specific ways in which different organization modes influence precipitation distributions and shift extremes remain less understood. The following section will endeavor to describe the how convection organization is quantified and then how it is linked to precipitation extremes.

1.2.2 Measuring Convective Organization: the Key Metrics

Convective organization is a broad concept that encompasses various phenomena and can be more easily understood through its contrast with random (or popcorn) convection – where convective cells are randomly distributed in both space and time (Pendergrass 2020). Convective aggregation occurs when convective cells group or cluster together in space and are surrounded by relatively dry areas. Convective self-aggregation is a phenomenon that arises when the energy and momentum fluxes associated with convective cells and the dry regions they exist in cause these cells to move together. In addition to aggregation, convective organization can take the form of mesoscale convective systems (MCSs) (Nesbitt *et al.* 2006; Schumacher and Johnson 2005), tropical cyclones, and extra-tropical cyclones.

The question at hand is how to measure the degree of organization, or in other words, what metrics are used in the literature? Focusing on studies of convective organization in idealized settings, there seems to be three main metrics, with the first based on the spatial distribution of clusters and measuring its deviation from a random distribution. The second method examines the contrast between dry and moist areas by assessing the distribution of relative

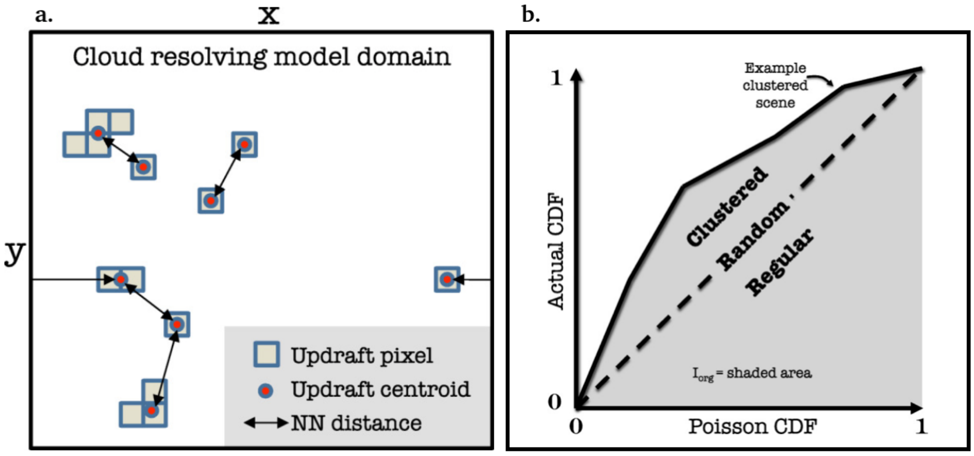

Figure 1.11: a. Schematic of NNCDF calculation. The domain is recursively traced to identify the geometric centroid of each updraft (red points) and the distance to its nearest neighbor is calculated (double headed arrows). The NNCDF is the normalized cumulative density function of these distances. b. Schematic of organizational index (Iorg) derivation from the model simulated NNCDF. The simulated normalized NNCDF (y axis) is plotted against the Poisson normalized NNCDF that would be obtained from a random distribution (x axis). Iorg is the integral under the curve. A perfectly random distribution of convection would lie on the diagonal dashed line and would have $Iorg = 0.5$. The graph shows a clustered example, for which $Iorg > 0.5$, while a regular distribution would lie below the diagonal as annotated. Note that for a given scene, the joint NNCDF can cross the diagonal, indicating both regular and clustered organization occurring at different spatial scales.

humidity. These two methods are primarily employed for self-aggregation. The final method, more suitable for mesoscale convective systems, seeks to quantify if the system's organization is optimal and enduring.

The first approach is rooted in the physical structure of aggregation and involves metrics like the Simple Convective Aggregation Index ($SCAI$) and the $Iorg$ index. $SCAI$ identifies convective regions based on pixels with brightness temperatures colder than 240 K and quantifies aggregation by counting the number of convective systems and measuring their distances. Similarly, the $Iorg$ index evaluates the organization of convection by comparing the distribution of distances between detected clusters to a random distribution of these distances (modeled by a Weibull distribution). The figure 1.11.a. ilustrates the clustering distribution and the distance between neighor (NN). The figure 1.11.b. shows the $Iorg$ as the distance between the two cumulative distribution and is interpreted as the area under the curve ($x = NNCDF_{random}, y = NNCDF$).

The second method of metrics focuses on the impact of aggregation. In highly aggregated states, intense convective cells are surrounded by vast areas of clear, dry atmosphere. Aggregation can be gauged using metrics like column-average relative humidity (CRH) or subsidence fraction (SF). For instance, the Average Relative Humidity index (ARH) is calculated as the mass-weighted average relative humidity from the surface to 200 hPa:

$$ARH = \frac{-\int_{p_s}^{p_t} RH\frac{dp}{g}}{-\int_{p_s}^{p_t} \frac{dp}{g}} \tag{1.1}$$

where RH is the relative humidity, p_s the surface pressure and p_t the pressure at the top of the troposphere and g the gravitational constant. There exists other index included fraction based on vertical velocity (also known as AF1). The more ARH, the more convective organization is found.

Furthermore, the concept of convective organization can also directly apply to pre-existing aggregated structures, such as mesoscale convective systems (MCSs). These MCSs can emerge from internal interactions (self-aggregation) or external influences (like wind shear), as discussed earlier. The literature concerning MCSs with $Iorg$ organization indices (or similar metrics) is somewhat limited. The level of organization within MCSs is evaluated through morphological standards and the evolution of the system over its lifecycle. Notably, this assessment highlights a class of systematically organized convective systems nested within mesoscale convective systems, which represent key system types as illustrated in 1.12, adapted from Schumacher and Rasmussen 2020. MCSs with greater longevity are regarded as more organized, as their endurance demonstrates enhanced persistence.

A noteworthy finding from recent investigations is that mesoscale convective systems (MCSs) frequently develop as interconnected clusters, interwoven with one another. While individual systems exhibit organization through factors like the upward movement of water vapor, stabilization of their environment, and propagation, the collective ensemble presents a sense of chaos. This observation further underscores the notion that the arrangement of convection varies with the scale of observation.

1.2.3 How and why Extremes increase with Organization?

Evidence of the influence of Organization on Extremes

The significance of mesoscale convective systems (MCSs) in contributing to annual rainfall is strongly demonstrated (Schumacher and Rasmussen 2020), as they account for more than half of the total rainfall in some regions, as depicted in Figure 1.13. The figure presents observations from the TRMM satellite between 1997 and 2004, highlighting the dominant role of MCSs in producing precipitation, particularly in the Sahel region, where they contribute to over 80% of the total rainfall. The critical question emerges:

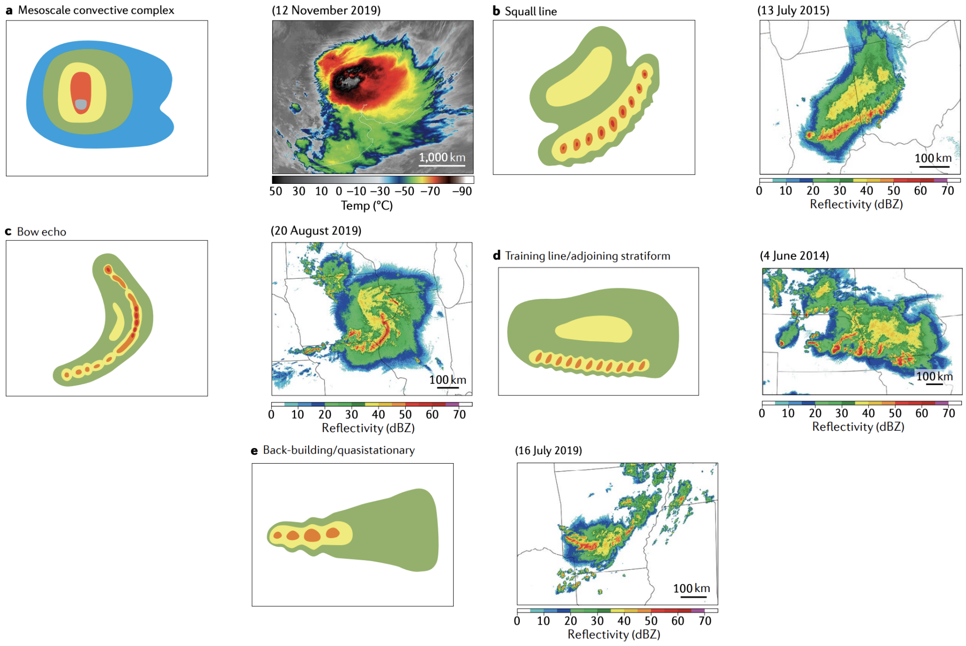

Figure 1.12: Key MCS types. Schematic illustration (left) and observed infrared or radar retrievals (right) of a mesoscale convective complex (panel a), squall line (panel b), bow echo (panel c), training line/adjoining stratiform mesoscale convective system (MCS; panel d) and back-building MCS (panel e). Radar data in panels b–e are from the Multi-Radar Multi-Sensor system183. MCSs can take on a wide variety of structures, with the examples shown here among the most highly organized. Schematics in panels d and e adapted from **schumacher2005formation** American Meteorological Society

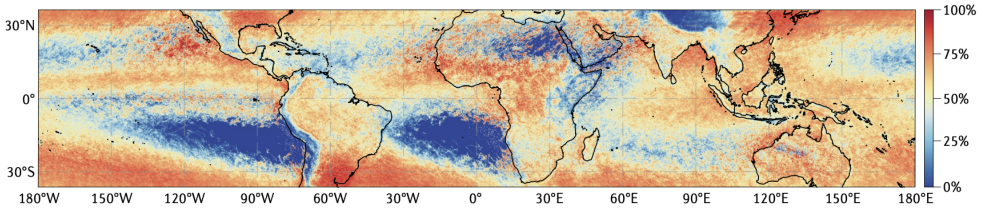

Figure 1.13: The contribution of MCSs to global rainfall. Fraction of annual rainfall produced by mesoscale convective systems (MCSs) based on observations from the Tropical Rainfall Measuring Mission (TRMM) satellite between December 1997 and September 2014. Figure from Schumacher and Rasmussen 2020, adapted from Nesbitt *et al.* 2006.

given the substantial contribution of MCSs to rainfall, do they also play a significant role in generating extreme precipitation events?

Semie and Bony 2020 investigates the relationship between mean precipitation, extreme precipitation, and the spatial organization of deep convection at the scale of $10^\circ \times 10^\circ$ domains in the tropics. It finds that domain-averaged precipitation primarily increases with the number of deep convective entities within the domain and is not significantly influenced by convective organization due to the presence of non-precipitating areas. However, mean local precipitation increases as the number of convective entities increases or convective organization decreases. On the other hand, the intensity of precipitation extremes intensifies as convective organization increases or the number of convective entities decreases. The study shows that extremes in domain-scale ($10^\circ \times 10^\circ$) precipitation depend closely on the total number of convective centroids within the domain and the total precipitating area, with little dependence on convective organization. In contrast, extremes in local precipitation mostly depend on the area of heavy precipitation, which is closely related to the degree of convective clustering.

These observations are consistent with modeling results (Bao *et al.* 2017; Pendergrass 2020; Pendergrass *et al.* 2016), which show that the spatial organization of deep convection is inversely related to the number of convective centroids. When convective organization increases, the area covered by deep convective clouds is reduced. The study also reveals that while domain-scale extreme precipitation is not strongly influenced by convective organization, the fractional area of heavy precipitation increases as convective organization strengthens. This means that areas of intense precipitation associated with spatially organized convection are not large enough to significantly impact domain-scale extreme precipitation. However, there is strong observational evidence for an enhancement of local precipitation with convective organization, consistent with previous modeling results. In other word, it is not the area of extreme precipitation that increases with aggregation, but rather its local intensity. For a given amount of precipitating condensates, what can enhance the intensity of precipitation results from microphysical processes. For example, if less rain is evaporating, precipitation rates would increase as a results. This is quantify by the precipitation efficiency, which measures the fraction of cloud droplets that effectively reaches the ground. Convective aggregation, by inducing a moister environment may enhance precipitation efficiency and leads to strong extremes.

An other aspect of the impact of convective organization is that it can duplicate the effect of warming. Muller 2013b investigates the response of precipitation extremes to warming in a cloud-resolving model, focusing on the role of convective organization induced by vertical wind shear. Several shear profiles are examined, including no shear, critical shear, and supercritical shear, as well as different domain sizes and resolutions. The study finds that the fractional rate of increase of precipitation extremes with warming is comparable to that of surface water vapor concentrations, which is significantly smaller than the increase in column water vapor. Despite varying convective organizations due to different shear profiles, the amplification of precipitation extremes without shear and with critical shear is similar, with a rate of increase slightly smaller than CC scaling. However, extremes are more sensitive to supercritical shear, yielding increases above CC scaling.

Explanation and physical processes involved

The explanation for the amplification of extremes with aggregation lies in several factors (Pendergrass 2020). When a cloud forms as part of a convective cluster, it tends to be surrounded by a moister environment compared to when it is isolated. This reduces the influence of dry air entrainment on convective updrafts, allowing them to become more intense. Additionally, precipitation in these convective clusters experiences less reevaporation, resulting in enhanced precipitation efficiency. Furthermore, the interaction between clouds within the aggregated cluster, specifically through collisions of cold pools associated with them, plays a significant role. Aggregation facilitates this interaction, leading to a memory effect where past precipitation and inter-cloud dynamics influence extreme precipitation events. To better simulate convective extremes and the diurnal cycle in global climate model projections, and in particular in general circulation model parametrization, it is essential to take into account the interaction between convective clouds, as highlighted by recent research (Moseley *et al.* 2016). This approach would enable more realistic representation of extreme precipitation events and their impacts in future climate scenarios, and this will be further investigated in chapter 4.

1.3 Advancements in Modeling Deep Convection and Extremes

1.3.1 Cloud Resolving Models as Numerical Laboratory

A Cloud Resolving Model (CRM) is a sophisticated numerical tool used in atmospheric sciences to explicitly simulate individual clouds by employing a fine grid resolution (Guichard and Couvreux 2017). The distinction between LES and CRM is primarily rooted in historical developments, wherein two explicit cloud models were created to study different types of clouds: shallow and short-lived cumulus clouds versus deep and long-lasting convective clouds. Although the early development of LES and CRM occurred concurrently, the two scientific communities initially had limited interactions (Wyngaard 2004).

Considered as numerical laboratories of the atmosphere, Cloud Resolving Models serve as powerful tools for exploring cloud phenomenology, conducting process studies, and gaining insights into transient motions associated with convective clouds. Due to the computational cost, these models are typically run over a limited domain, usually covering hundreds of kilometers in width. Some CRM simulations are idealized representations of the atmosphere, aiming to comprehend physical processes under well-controlled environmental conditions rather than reproducing realistic settings. These models can be used under the assumption of radiative convective equilibrium (RCE), a framework that describes the balance between atmospheric cooling through radiation and heating due to latent heat release and surface heat flux. RCE has long been utilized as a simple approach to investigate the behavior of moist convection (Held *et al.* 1993; Posselt *et al.* 2008; Robe and Emanuel 2001; Singh and O'Gorman 2013; Tompkins and Craig 1998).

There are many CRM models, by as IFS, NICAM, ARPEGE, ICON, FV3, GEOS5 UKMO, and SAM. In this context, we will focus on describing the equations of the System for Atmospheric Modeling (SAM, Khairoutdinov and Randall 2003) model, which is used in the subsequent chapters.

The fundamental principle behind numerical resolution in CRM involves using prognostic equations to predict the values of atmospheric variables for future time steps based on their current or previous values. To achieve this, a CRM needs to solve dynamical fields such as horizontal and vertical wind components (u, v, w), temperature variables (T, θ, θ_l), and water variables (q_v, q_c, q_t, etc.). These models rely on the conservation equations for mass and momentum.

To enhance computational efficiency and improve speed, certain assumptions can be applied. For instance, the SAM model employs anelastic equations of motion, assuming that pressure fluctuations rapidly balance out and are negligible compared to density or temperature fluctuations. In other words, the model filters out sound waves, enabling numerical stability and allowing longer time steps based on the elementary scale according to the Courant-Friedrichs-Lewy (CFL) condition.

Anelastic equations reads as follow

Continuity Equation

$$\bar{\rho}_r - \left(\frac{\partial u_j}{\partial x_j} + w\frac{\partial \bar{\rho}}{\partial z}\right) = 0 \tag{1.2}$$

Momentum Equation

$$\frac{\partial u_i}{\partial t} = \underbrace{\frac{1}{\bar{\rho}}\frac{\partial}{\partial x_j}(\bar{\rho} u_i u_j)}_{\text{Advective fluxes}} + \underbrace{\frac{1}{\bar{\rho}}\frac{\partial}{\partial x_j}(\tau_{ij})}_{\text{Turbulent fluxes}} - \underbrace{\frac{\partial}{\partial x_j}\frac{p'}{\bar{\rho}}}_{\text{Pressure gradient force}} \tag{1.3}$$

$$+ \underbrace{\delta_{i3}B}_{\text{Buoyancy}} + \underbrace{\varepsilon_{ij3} f(u_j - U_{gj})}_{\text{Coriolis}} + \underbrace{\left(\frac{\partial u_i}{\partial t}\right)_{l.s.}}_{\text{Large Scale forcing}} \tag{1.4}$$

Energy Equation

$$\frac{\partial h_L}{\partial t} = \underbrace{\frac{1}{\bar{\rho}}\frac{\partial}{\partial x_i}(\bar{\rho}u_i h_L + F_{h_L i})}_{\text{Advective fluxes (+subgrid.)}} \underbrace{-\frac{1}{\bar{\rho}}\frac{\partial}{\partial z}(L_c P_r + L_s P_s + L_s P_g)}_{\text{Heating from Precip.}} \tag{1.5}$$

$$+ \underbrace{(\frac{\partial h_L}{\partial t})_{rad}}_{\text{Heating from Rad.}} + \underbrace{(\frac{\partial h_L}{\partial t})_{l.s.}}_{\text{Large Scale advection}} \tag{1.6}$$

Total non-precipitating water equation

$$\frac{\partial q_T}{\partial t} = \underbrace{-\frac{1}{\bar{\rho}}\frac{\partial}{\partial x_i}(\bar{\rho}u_i q_T + F_{q_T i})}_{\text{Adv.}} + \underbrace{(\frac{\partial q_p}{\partial t})_{mic}}_{\text{Microphysical sources/sink}} + \underbrace{(\frac{\partial q_T}{\partial t})_{l.s.}}_{\text{Large Scale Advection}} \tag{1.7}$$

Total precipitating water equation

$$\frac{\partial q_p}{\partial t} = \underbrace{-\frac{1}{\bar{\rho}}\frac{\partial}{\partial x_i}(\bar{\rho}u_i q_p + F_{q_p i})}_{\text{Adv.}} + \underbrace{\frac{1}{\bar{\rho}}\frac{\partial}{\partial z}(P_r + P_s + P_g)}_{\text{Precipitation sources/sink}} + \underbrace{(\frac{\partial q_p}{\partial t})_{mic}}_{\text{Microphysical source/sink}} \tag{1.8}$$

Here, u_i ($i = 1, 2, 3$) are the resolved wind components along the Cartesian x, y, and vertical z directions, respectively; ρ is the air density; p is pressure; h_L is liquid/ ice water static energy [$= c_p T + gz - L_c(q_c + q_r) - Ls(q_i + q_s + q_g)$]; q_T is total non-precipitating water (water vapor + cloud water + cloud ice) mixing ratio ($= q_v + q_c + q_i = q_v + q_n$); q_p is total precipitating water (rain + snow + graupel) mixing ratio ($= q_r + q_s + q_g$); f is Coriolis parameter; U_g is prescribed geostrophic wind; B is buoyancy [$g(\rho'/\rho) = g(T'/T + 0.608q'_v - q_n - q_p - p'/p)$]; g is gravitational acceleration; c_p is specific heat at constant pressure; L_c and L_s are latent heat of evaporation and sublimation, respectively; τ_{ij} is subgrid-scale stress tensor; F_{h_L}, F_{q_T}, and F_{q_p} are subgrid-scale scalar fluxes; P_r , P_s , and P_g are rain, snow, and graupel precipitation fluxes, respectively; the subscript 'rad' denotes the tendency due to radiative heating; "mic" represents the tendency of precipitating water due to conversion of cloud water/ice and due to evaporation; 'l.s.' denotes the prescribed large-scale tendency; the overbar and prime represent the horizontal mean and perturbation from that mean, respectively.

In these equations, there are processes that operate on scales smaller than the model can resolve such as microphysics and turbulence, as well as exchanges of energy between the atmosphere and other sources called radiation. For the microphysics, a parametrization aims at separating hydrometeors into (i) cloud water suspended within the air mass and (ii) precipitating water falling with respect to the air mass. There are prognostic equation for each type. As shown in figure 1.14, there are many complex exchanges between different types of hydrometeors, such as condensation, auto-conversion, accretion, evaporation, melting, aggregation, or sedimentation. The microphysics approach used in SAM is a bulk model that assumes a particle size distribution for precipitating condensate, and a single moment scheme which calculate mixing ratios for different hydrometeors.

The turbulent processes, also too small to be resolved, which are represented by a scheme based on Khairoutdinov and Kogan 1999. The radiation scheme is adopted from National Center Atmospheric Research (NCAR) Community Climate Model (CCM3; Kiehl *et al.* 1998). Eventually, initial and boundary conditions are prescribed using academic vertical profiles or sounding data. Lateral boundray conditions are most of the time periodic, and the top boundary conditions are made with a wall above a sponge layer to absorb waves. Surface boundary conditions are prescribed or interactive with surface fluxes, surface temperature (soil moisture when the simulation is over land). All the simulations we perform neglect the Coriolis force, a reasonable approximation in the tropics.

Expanding Cloud Resolving Models to global scale

The representation of cloud processes in global atmospheric model's has been recognized for decades as the source of much of the uncertainty surrounding predictions of climate variability (Arakawa 1975; Bony *et al.* 2015; Houghton *et al.* 2001). The possibility of solving convection on a global scale appeared to be one of the solutions to this problem.

Around two decades ago, powerful Japanese supercomputer of its time (Matsuno 2016) was able to develop a global non-hydrostatic model using the Earth Simulator. This required a global grid and equation formulation capable of handling 5 km-scale motions. The result was the NICAM model, which simulated aqua-planets (Miura *et al.* 2005; Satoh *et al.* 2014), realistic configurations, and diverse inquiries, showcasing its ability to represent tropical convective storms within the broader atmospheric circulation. In the years following NICAM's introduction, several groups, originating using various modeling backgrounds, including ICON, Global SAM, and IFS, sought to simulate atmospheric circulation on non-hydrostatic domains, using increased computational capacity. These global cloud-resolving models (GCRMs) are poised to shape the future of weather and climate modeling, bypassing challenges posed by parameterizations (Randall *et al.* 2003; Stevens and Bony 2013) and shed a new light on long-standing questions, such as how tropical rainbands, or other patterns of weather, change with warming (Bony *et al.* 2015; Marotzke *et al.* 2017).

The first intercomparison of GCRMs, through a project called DYAMOND—the

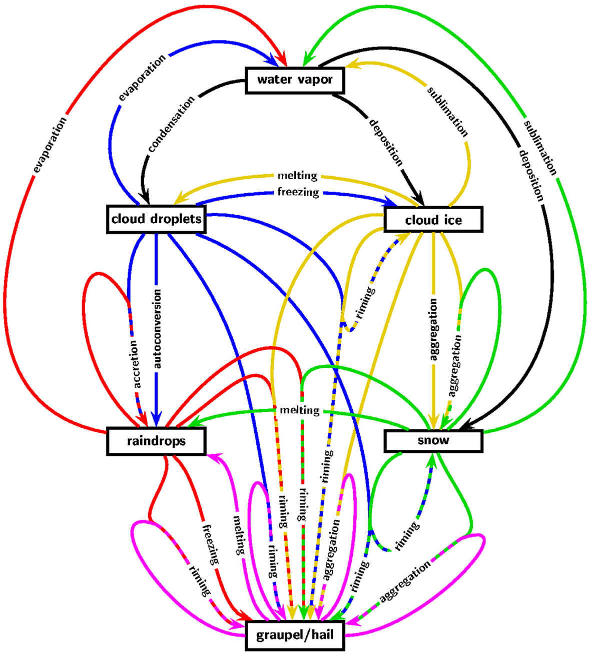

Figure 1.14: An example of schematic summarizing for a given one-moment microphysical parametrization, showing the selected water categories or species, with arrows indicating the different processes operating among these species. The colour of an arrow refers to the species that is transformed by a process (black: water vapour, blue: cloud droplets, red: raindrops, yellow: cloud ice, green: snow, pink: graupel/hail), and when two species are concerned, the arrow is two-coloured (© Copyright Axel Seifert, from Guichard and Couvreux 2017)

DYnamics of the Atmospheric general circulation On Non-hydrostatic Domains, aims at identifying apparent implementation bugs; focusing efforts on non-trivial problems, for instance the representation of turbulent mixing and cloud microphysical processes, or managing and efficiently analyzing output; and involving a larger community in the improvements of a new class of models. Improvements brought by DYAMOND project are continuing through a collaborative European project called NextGEMs. This project develops global storm-resolving models which represent more realistically, thanks to DYAMOND, the climate system for the next 30 years. This includes weather extremes and other components of the Earth system, such as carbon, aerosols and marine nutrients.

1.3.2 Artificial Intelligence for Climate Science

In recent decades, climate science has generated a wealth of data and has become a prime domain for big data and artificial intelligence (Reichstein *et al.* 2019). Data size now exceeds 100 petabytes, and is growing quasi-exponentially (tapering of the figure 1.15 to the right indicates decreasing

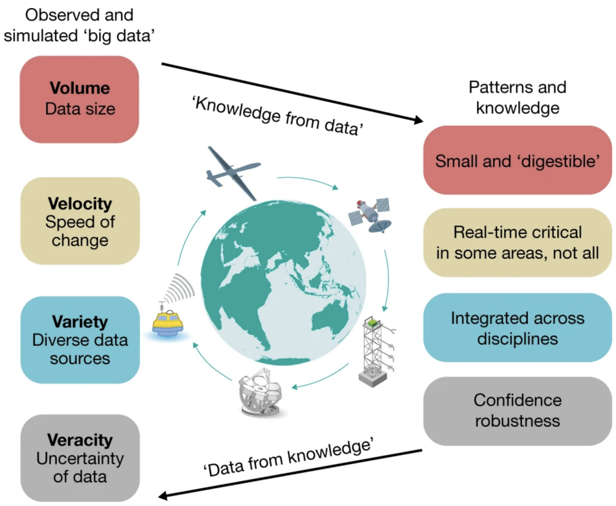

Figure 1.15: Data size now exceeds 100 petabytes, and is growing quasi-exponentially (tapering of the figure to the right indicates decreasing data size.) The speed of change exceeds 5 petabytes a year; data are taken at frequencies of up to 10 Hz or more; reprocessing and versioning are common challenges. Data sources can be one- to four-dimensional, spatially integrated, from the organ level (such as leaves) to the global level. Earth has diverse observational systems, from remote sensing to in situ observation. The uncertainty of data can stem from observational errors or conceptual inconsistencies. Figure credits to Reichstein *et al.* 2019

data size.) The speed of change exceeds 5 petabytes a year; data are taken at frequencies of up to 10 Hz or more; reprocessing and versioning are common challenges. Data sources can be one- to four-dimensional, spatially integrated, from the organ level (such as leaves) to the global level. Earth has diverse observational systems, from remote sensing to in situ observation.

Machine learning methods are "Universal Function Approximators": they can approximate any function as the number and width of layers go to infinity (Hornik *et al.* 1989). Specifically, the development of deep learning and deep neural networks, those with multiple hidden layers, has led to significant advancements in various fields such as object detection or game strategy learning (Dahl *et al.* 2011; Hinton *et al.* 2012; LeCun *et al.* 2015; Silver *et al.* 2016). These methods have been used to better predict certain atmospheric processes, such as rainfall prediction (Miao *et al.* 2015; Moazami *et al.* 2013), weather forecasting, soil moisture (Green *et al.* 2017; Kolassa *et al.* 2013; Kolassa *et al.* 2017), and surface turbulent flux retrievals (McColl *et al.* 2017). One of the advantages of Artificial Neural Networks (ANNs) is that once trained, they are computationally efficient, as most of the computational burden is dedicated to the training phase. Recently, deep learning models not only predict individual events but also begin to emulate global numerical weather prediction models (Bi *et al.* 2023, 2022; Keisler 2022; Pathak *et al.* 2022;

Zeng *et al.* 2023; Zhang *et al.* 2022). These models are competitive with the Integrated Forecast System (IFS) in forecasting upper-air variables against operational analysis and surface variables against observation. Once trained, a machine learning model runs 10^4 times faster than IFS and can be run from a personal laptop.

Where machine learning represents a major interest for climate science is not only in its ability to imitate or emulate the climate, but perhaps in its real ability to learn it and, even better, explain it. While atmospheric physics had not waited for the advent of machine learning to explain certain phenomena, it is clear that some equations remain too locked and computationally expensive to be solved, such as convective processes (Randall *et al.* 2003). Machine learning in this challenge has brought new conceptual tools to model the mesoscale in global models, particularly by bypassing the resolution of complex equations and focusing on variables of interest (Gentine *et al.* 2018). In this context, machine learning models have also helped understand the stochastic nature of precipitation extremes at the subgrid-scale cloud structure and organization level by predicting precipitation variability and stochasticity with a low-dimensional set of latent variables (Shamekh *et al.* 2023).

In this perspective, machine learning is used to find patterns in data, allowing us to gain physical insight. These patterns are often found in a reduced representation of the data (latent space), which can be done either using traditional methods such as Principal Component Analysis (PCA) or non linear reduced order algorithms, such as auto-encoder (Hinton and Salakhutdinov 2006; Tenenbaum *et al.* 2000). Recently, several studies have therefore been conducted to extract the embedding manifold of mesoscale shallow convective archetypes to quantify cloud organization, enabling the study of mechanisms behind transitions between regimes (in simulations and observations) by capturing the full continuum of organizational regimes (see for instance Denby 2023).

1.3.3 Beyond CC-Scaling : A recent theory for Extremes

In this paragraph, we will describe briefly the famous Clausis-Clapeyron Scaling for Extreme Precipitation, pointing out its advantages as well as its limits describing the effect of convective organization.

Clausius-Clapeyron Scaling

At first order, extreme precipitation should increase as the availability of moisture increases in a warmer climate. Given the small changes in model relative humidity (Soden and Held 2006), the atmospheric humidity is expected to increase according to the Clausius–Clapeyron (CC) equation

$$\frac{de_{v,s}}{dT} = \frac{L_v e_{v,s}}{R_v T^2} \tag{1.9}$$

where $e_{v,s}$ is the saturation vapor pressure, T the absolute temperature, L_v the latent heat of vaporization of water vapor and R_v the water vapor gas constant. For a reasonable ranges of temperatures, the latent heat L_v does not depend on T, which provides a simple solution for the saturation pressure

$$e_{v,s}(T) = e_{v,s}(T_0)\exp\left(\frac{L_v}{R_v}\left(\frac{1}{T_0} - \frac{1}{T}\right)\right) \tag{1.10}$$

In the case of a warming of few degrees, we can write $T = T_0 + \delta T$ with $\delta T << T_0$, yielding to

$$e_{v,s}(T) = e_{v,s}(T_0)\exp\left(\frac{L_v \delta T}{R_v T_0^2}\right) \tag{1.11}$$

Considering $T_0 = 273K$ the numerical application provides an increase in the availability of moisture in a warmer climate of 7%, and it can reaches $12\%K^{-1}$ depending on latitude (O'Gorman and Muller 2010). Clausius–Clapeyron (CC) scaling predicts an approximately exponential increase with temperature. An increase in atmospheric specific humidity has already been observed in recent years (Trenberth 2011). Over oceans, the increases are consistent with CC expectations with a constant relative humidity, while increases are somewhat lower over land especially where water availability is limited. It has been argued that the heaviest rainfall events occur when effectively all of the moisture in a volume of air is precipitated out (Allen and Ingram 2002; Pall *et al.* 2007; Trenberth 1999).

If the conditions under which the precipitation forms remain unchanged and only atmospheric water vapor increases, then precipitation extremes can be expected to scale with the increased available humidity in the atmosphere. There is now ample empirical evidence of significant departure of the CC-scaling in observations and simulations, as recently reviewed by Westra *et al.* 2014, this necessitates considering all contributions, including thermodynamic, dynamic, and microphysical factors, for the study of extremes, as described in the following.

Theoretical Scaling

A theoretical scaling for precipitation extremes has been introduced (Betts 1987; O'Gorman and Schneider 2009b) and refined to account for microphysics (Muller and O'Gorman 2011). The scaling can be derived from energetics (Muller and Takayabu 2020), and the final expression reads as

$$P_{extr.} \sim \varepsilon \int_0^H \rho w \frac{\partial q_{sat}}{\partial z} dz. \tag{1.12}$$

where $P_{extr.}$ is the precipitation extreme, ε the precipitation efficiency (fraction of condensation that makes it to the ground as surface precipitation), H the height of the atmosphere (we often consider only tropopause depending), ρ the density, w the vertical velocity and q_{sat} the saturation humidity. To say it simply, an extreme in precipitation can be seen as the consequence of a vertically perturbed saturated columns that will produce cloud condensate. The amount of suspended liquid or ice water droplets constitute the source of precipitation, and only a fraction ε of it would reaches the ground. It relates the changes of precipitation extremes to three contributions: a dynamic contribution related to vertical mass flux in extreme updrafts, a thermodynamic contribution related to water vapor (similar to the 'CC-scaling' mentioned above), and a microphysic contribution related to precipitation efficiency. The latter is typically less than one as some of the condensates are either advected away as clouds, or evaporate as they precipitate through unsaturated air below the cloud before reaching the surface. Each of these three contributions is subject to different theoretical constraints relative to the hypothesis evoked beyond.

1.4 General Objectives of my research

The overarching goal of this PhD thesis is to enhance the understanding and prediction of extreme rainfall events. In pursuit of this objective, we aimed to gain a deeper insight into convective organization and quantify its influence on rainfall extremes. This hypothesis was explored through two main aspects: the first sought to elucidate what are the physical origins of the formation and properties of mesoscale convective systems. The second aspect is dedicated to investigate their implications for precipitation extremes. More precisely, we address four fundamental questions related to the relationship between external feedback, convection organization and extreme precipitation events, aiming to understand the mechanisms that lead to the amplification of extremes, with a particular focus on squall lines in the tropics:

- Origins: Physical processes leading to the formation of squall lines and MCSs
    1. **Investigate Wind Shear Influence on Squall Line Orientation.** *Scientific Approach*: The research will involve conducting cloud resolving simulations in radiative convective equilibrium to explore the behavior of tropical squall lines under diverse shear regimes (defined in chapter 2), including sub-optimal and super-optimal shear conditions. Through rigorous quantitative analysis,

    the study aims to unravel the factors driving squall line orientation and intensity in response to varying magnitudes of wind shear. Special attention will be given to comprehensively understanding the role of cold pool spreading in maintaining equilibrium between wind shear and the orientation of squall lines.

  2. **Develop Predictive Models for Maximum Area of MCSs Based on Early Development Stages and Initial Environmental Conditions.**
     Scientific Approach: This research will adopt an innovative approach using the random forest technique to develop predictive models for estimating the maximum area of MCSs based on crucial early developmental stages and initial environmental conditions. High-resolution global simulations and the storm tracking algorithm, TOOCAN, will be utilized to capture critical parameters influencing the size of MCSs. The predictive models' performance will be rigorously evaluated using regression scores, leading to accurate and timely forecasts of MCS size, independent of their final lifespan.

- Implications: Impact of convective organization on precipitation extreme and water isotopes distribution

  1. **Explore the Implications of Wind Shear on Precipitation Extremes.**
     Scientific Approach: Leveraging a cloud resolving model, the thesis will simulate squall lines under optimal and superoptimal shear conditions to examine the associated precipitation extremes. A detailed investigation into the underlying mechanisms responsible for the amplification of precipitation extremes will be carried out, with a focus on understanding the influence of dynamic, thermodynamic and microphysic contributions. By integrating theoretical scaling and relevant scientific studies, the thesis aims to provide comprehensive insights into the factors contributing to the intensified rainfall patterns observed in squall lines.

  2. **Examine how convective processes influence the isotopic composition of water vapor and precipitation in organized convective systems** *Scientific Approach*: Employing cloud resolving model simulations in radiative-convective equilibrium and incorporating wind shear, this investigation seeks to unravel the intricate influence of convective processes on the isotopic composition of water vapor and precipitation within organized convective systems, such as squall lines. The simulations are analyzed to capture isotopic mesoscale variations, which are then compared with observed tropical squall lines. To interpret the isotopic variability, a robust

and simple water budget model for the sub-cloud layer is applied across different regions of the domain. The primary drivers of isotopic depletion, including rain evaporation and rain-vapor diffusive exchanges, are examined.

This PhD thesis aims to advance our understanding of convective organization and extreme weather phenomena in the tropics. The resulting findings and predictive models have the potential to contribute to improve scientific knowledge on convective processes and their role in shaping precipitation extremes, fostering a deeper understanding of the Earth's climate system.

Part I

Origins

Chapter 2

What is the Origin of Squall Line Orientation?

Résumé en français

Ce chapitre a fait l'objet d'un article publié, intitulé "Orientation des lignes de grains : Interaction entre cisaillement et convection", S. Abramian, C. Muller C. Risi, dans Geophysical Research Letters, 2022. Sa version diffère peu du contenu présenté ci-dessous.

Les lignes de grains sont connues pour être la conséquence d'une interaction entre un vent de cisaillement de basse altitude et les poches froides concomitantes aux courants descendants de la convection. Lorsque l'amplitude du cisaillement dépasse un seuil critique, les lignes de grains tendent à s'orienter. La littérature existante suggère que cette orientation réduit le cisaillement du vent entrant sur la ligne de grains, maintenant ainsi l'équilibre entre le cisaillement du vent et la propagation des poches d'air froid. Bien que cette théorie soit plutôt acceptée, très peu d'études quantitatives ont été menées, en particulier dans le régime superoptimal. Dans cette étude, nous testons cette hypothèse avec des lignes de grains tropicales obtenues en imposant un cisaillement vertical de vent dans des simulations haute résolution en conditions d'équilibre radiatif convectif. Dans le régime sous-optimal, les lignes de grains sont perpendiculaires au cisaillement. Dans le régime superoptimal, leur orientation maintient l'équilibre, ce qui confirme les théories existantes. Nous constatons également qu'à mesure que le cisaillement augmente, les poches froides deviennent plus intenses. Cependant, cette intensification a peu d'impact sur l'orientation des lignes de grains.

What is the Origin of Squall Line Orientation?

This chapter has been the subject of a published paper, untitled Shear-Convection Interaction and the Orientation of Squall Lines, S.Abramian, C.Muller & C.Risi, in Geophysical Research Letter, 2022. Its version follows closely from the content presented below.

Abstract

Squall lines are known to be the consequence of the interaction of low-level shear with cold pools associated with convective downdrafts. Also, as the magnitude of the shear increases beyond a critical shear, squall lines tend to orient themselves. The existing literature suggests that this orientation reduces incoming wind shear to the squall line, and maintains equilibrium between wind shear and cold pool spreading. Although this theory is widely accepted, very few quantitative studies have been conducted on superoptimal regime especially. Here, we test this hypothesis with tropical squall lines obtained by imposing a vertical wind shear in cloud resolving simulations in radiative convective equilibrium. In the sub-optimal regime, squall lines are perpendicular to the shear. In the super-optimal regime, their orientation maintain the equilibrium, supporting existing theories. We also find that as shear increases, cold pools become more intense. However, this intensification has little impact on squall line orientation.

Plain Language Summary

A squall line is a line of thunderstorms associated with heavy precipitation and only a well-informed meteorologist would notice that these convective bands are sometimes oriented with respect to the wind direction. Yet this is the case, and in this study we seek to understand what sets tropical squall lines orientation, and why. Using numerical simulations, we show quantitatively that the orientation of the squall lines restores the equilibrium between the wind and the cold pool spreading, providing for the first time a quantitative validation of existing theories.

2.1 Introduction

Squall lines are bands of thunderstorms of hundreds of kilometers, also called quasi-linear mesoscale convective systems. One key ingredient in the organization of squall lines is the presence of cold pools below precipitating clouds. These are areas of cold air with negative buoyancy anomaly, driven by the partial evaporation of rain and concomitant latent cooling, and observed to span 10–200 km in diameter (Romps and Jeevanjee 2016; Zuidema *et al.* 2017a). Cold pools spread radially at the surface as gravity currents, and can thus favor upward motion and the development of new deep convective cells at their edge as described in Tompkins 2001a and impact aggregation (Muller and Bony 2015b).

Based on observations (Bluestein and Jain 1985; Chalon *et al.* 1988; Chong *et al.* 1987; Houze 1977; Zipser 1977), a theory for squall lines was constructed by Rotunno *et al.* 1988 (hereafter RKW; see also Garner and Thorpe 1992; Weisman and Rotunno 2004), which is still the standard for their development today. RKW starts from the fact that in the absence of wind shear, deep convection developing at the edge of cold pools has a tilted updraft, and hence can not easily develop (see RKW notably their figure 18; figure 2.1adg).

One key parameter for the organization of deep convection into squall lines, is therefore the strength of cold pools and associated density currents, compared to the strength of the background wind shear. Depending on the shear amplitude, and assuming that the properties of the cold pools do not change with the shear, one can thus expect three regimes: the sub-critical regime, where density currents dominate, the critical regime where equilibrium is reached, and finally the super-critical regime where shear dominates. In the latter case, the squall lines tend to orient themselves at an angle to the shear (figure 2.1cfi). The literature suggests that the orientation of the line keeps the projected component of the shear close to the critical value, a hypothesis that we further investigate here.

Robe and Emanuel 2001 investigated the evolution of the squall line organization for a range of shears. In this numerical study and also in observational cases (Chong 2010; Coniglio *et al.* 2012; LeMone *et al.* 1998), RKW theory is widely accepted. However, the various models and observations are mainly confined to subcritical or critical speeds, and lack of quantitative and objective measure of angles. Indeed, it is difficult to assess quantitatively the organization of the lines, since they often form cloudy arcs, defining an orientation remains an obstacle. Another aspect that challenges the theory of RKW, suggested this time by Alfaro 2017, is that the strongest squall lines may produce the most intense cold pools and can thus shift the optimality regime and also modify the orientation of the lines.

The objective of our study is to clarify the physical processes responsible for the organization of deep clouds into squall lines in the tropics, and quantitatively test the RKW hypothesis up to the supercritical regime, in order to determine whether the cold pool and shear balance is sufficient to describe squall lines in cloud-resolving simulations. More precisely:

- How to measure the orientation of the squall lines?
- Does the orientation of the lines match the RKW hypothesis?
- Is it wrong to consider that the cold pools properties do not change with the shear?

The next section describes the cloud-resolving simulations, and the method to detect the angle of squall lines with respect to the background wind shear. Section 2.3 describes expectations from the RKW theory in more details, and investigates its valadity. Section 2.4 investigates the sensitivity of cold pools to shear strength, and its impact of squall line orientation. Concluding remarks are offered in section 2.5.

2.2 How to measure the orientation of the squall lines?

Before addressing the RKW theory in detail, the objective of this section is to describe the methodology that leads us to the estimate of the squall line angle with respect to the shear. Robe and Emanuel 2001 attempted such an angle detection, but using visual inspection. Here instead, we will derive a reproducible method based on image autocorrelation. We recall the set-up of the simulations (see Supplementary 1. for additional details) and then present our angle detection algorithm.

2.2.1 Model and Simulations

The simulations use the cloud-resolving model SAM (Khairoutdinov and Randall 2003). The resolution is 1 km in both horizontal directions, and gradually increasing in the vertical direction from 80 m near the surface to 400 m above 6 km. The 3D domain is doubly periodic in x and y with 128 km side, and the upper third of the domain (18 to 27 km) has a sponge layer to absorb gravity waves. We neglect the Earth rotation (a reasonable approximation in the tropics). All simulations are run to radiative-convective equilibrium (reached in about 30 days), after which we start our analysis, from day 30 to 35, with hourly outputs.

Following Muller 2013a, the convection is organized into squall lines by imposing a background vertical wind shear profile in the x-direction, with a background wind decreasing linearly from U_{sfc} at the surface to 0 m s^{-1} at $z = 1$ km. We perform nine simulations, with different shear strengths, i.e. with different surface wind U_{sfc} from 0 (no shear) to 20 m s^{-1}, with 2.5 m

s^{-1} increments. To avoid an impact of this imposed surface wind on surface fluxes, the domain-mean surface wind is removed before computing surface fluxes (see Supplementary Material for more details on the simulations).

Figure 2.1 shows three of our simulations. The 3D top graphs show buoyancy on the ground, and convective clouds in white. The 2D middle graphs show the same snapshots but from a top view and zoomed near the maximum precipitation. The bottom panels show a schematic of cold pool spreading (curve with triangles) and deep convection triggered at its edge, with increasing low level shear (U_{sfc} = 10 m s^{-1} middle panel, and 17.5 m s^{-1} right panels). With shear, convection triggering is favored in the downshear (decreasing x) direction, as described in more detail in section 3.

2.2.2 Automatic measurements of squall lines orientation

We define the angle a of the squall line orientation, as the angle between the squall line and the y direction. This definition allows to have a reference angle of 0 when the line is perpendicular to the background wind. To measure this angle a, we investigate the spatial autocorrelation of precipitable water (PW, which is the vertically integrated water vapor amount, shown figure 2.2 top panels). We choose this variable because PW has a long time persistence compared to other variables (for instance vertical velocity, or precipitation). Thus it has a longer memory of convective events and allows the mesoscale line organization to clearly appear.

Figure 2.2 provides a summary of the automatically estimated angle for each case (between 0 and $\pi/2$; see Supplementary Material for more details on the angle computation, notably Supplementary Figure S1 for time series of the squall line angle). Three PW snapshots are displayed on top, with the corresponding autocorrelation images below. Figure 2.2 highlights 1. the absence of a precise angle for the control case; 2. two regimes of the squall lines, the sub-critical one, where the lines are perpendicular to the wind (an angle close to 0) and the super-critical regime where the lines are oriented from 40 degrees to 45 degrees; 3. a critical case for U_{sfc} = 12.5 m s^{-1}, the last case before the orientation of the line.

We now compare these estimated angles to the theory of squall line orientation.

2.3 Does the orientation of the squall lines match the RKW hypothesis?

In this section, we use our simulations to understand the physical mechanisms behind the formation of tropical squall lines, and their orientation. The framework of RKW and Robe and Emanuel 2001 provides a theoretical

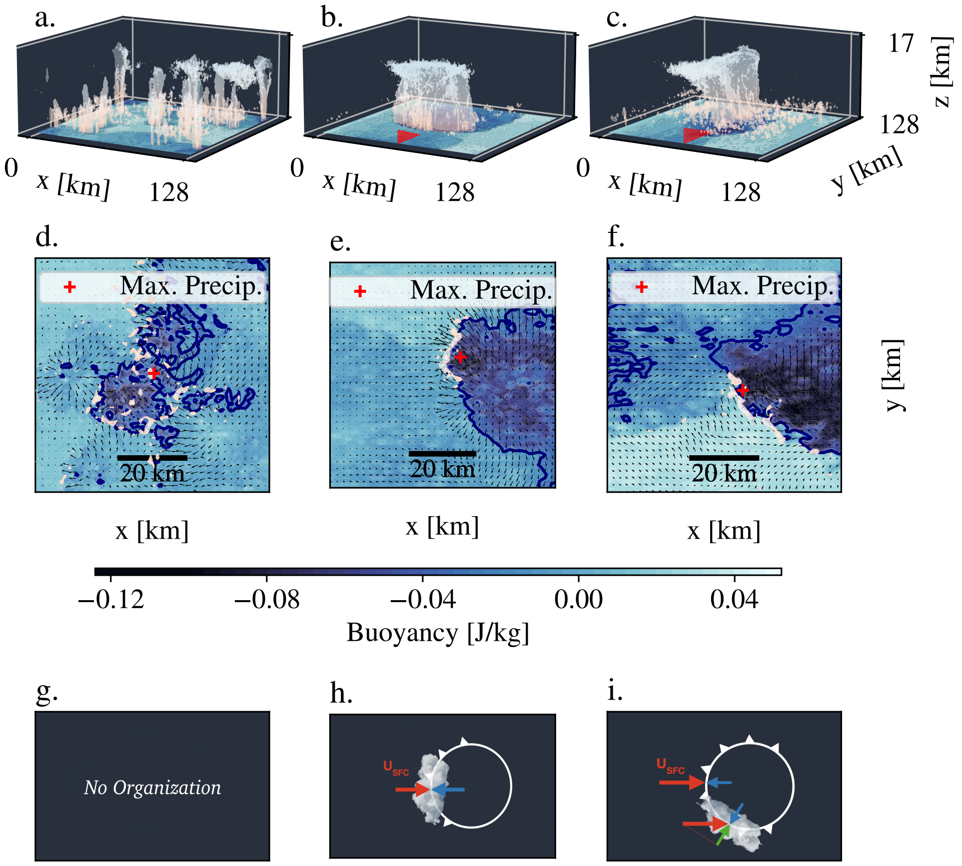

Figure 2.1: a. 3D overview of the control case $U_{sfc} = 2.5$ m s^{-1}, near critical case $U_{sfc} = 10$ m s^{-1} and supercritical case, $U_{sfc} = 17.5$ m s^{-1}. Buoyancy is displayed on the ground and the isosurface of cloud humidity equal to 0.02mm is in white. b. Top view of the three cases described above, zooming around the location of maximum precipitation (showing subregions with 70 km side). The colormap is the buoyancy, the quiver field represent the velocity field and the white area corresponds to the positive vertical velocity at 300m. c. Theoretical representation. For the control case, no organization is expected. In the critical case, the cold pool frontaly counterbalances the shear. In the supercritical case, the line tends to orient itself to conserve the projected wind (green).

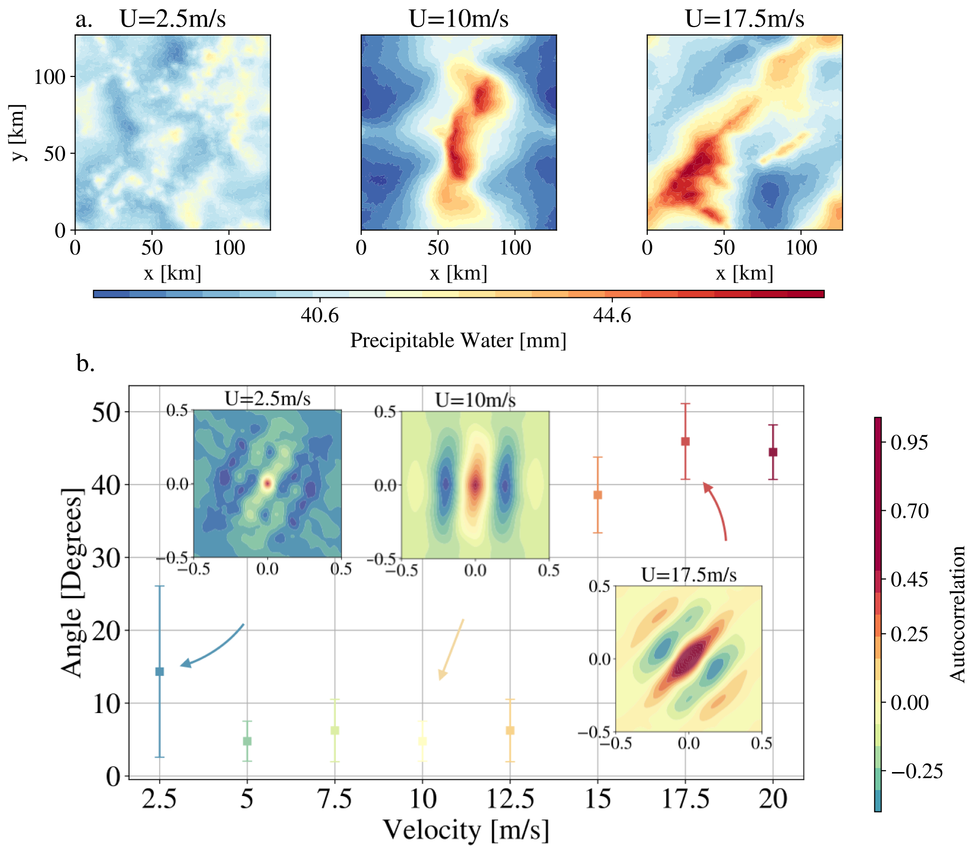

Figure 2.2: a. Snapshots (31st day) of the spatial distribution of Precipitable Water (PW) for different shear values. In the absence of shear, no squall lines are observed. For $U_{sfc} = 10$ m s^{-1}, arcs perpendicular to the wind, i.e. parallel to the y-axis, are formed. For $U_{sfc} = 17.5$ m s^{-1}, the squall line is oriented with respect to the y-axis. b. Results of the automatic method based on PW autocorrelation developed in this paper to detect the angle α between the squall line and the y-axis. The auto-correlations of PW corresponding to the three top snapshots are also displayed; they are normalized and the colorbar is saturated to highlight the correlation areas.

approach of this phenomenon, however the agreement of the orientation with this theory has never been clearly demonstrated. Using our angle measurement from section 2, we quantitatively test RKW theory.

2.3.1 RKW Theory and orientation of the squall lines

Figure 2.1a (control case) shows that without shear, convection develops randomly over the domain, similar to popcorn formation. In the presence of shear, for instance in the case U_{sfc} = 10 m s^{-1} (panels beh) we can see a deep convective line, with a length of 75 km, up to 10 km of altitude. The shear seems to constrain the convective cells at the edge of the cold pool. This is consistent with the aforementioned RKW theory of equilibrium between the incoming wind shear and that associated with spreading cold pools.

In the case U_{sfc} = 10 m s^{-1}, the line is perpendicular to the imposed wind, suggesting that it is a critical case (see also Figure 2.2). This means that the cold pool propagation is of the same order as the imposed background wind. In this case the location of the convective cell triggering, is on the extreme downshear front of the pool.

When the surface wind becomes stronger, we move into the super-critical regime. Considering the panel U_{sfc} = 17.5 m s^{-1}, we observe a deep convective line, oriented with respect to the imposed wind.

Consistent with RKW and Robe and Emanuel 2001, the convection still takes place at the edge of the cold pools, however, the optimal position is not at the downshear front anymore, because the wind is too strong compared to the cold pool propagation. The equilibrium position moves along the edge of the cold pools, such that cold pool velocity remains the same, but the wind projected radially becomes weaker (Figure 2.1i). In other words, the position of the equilibrium corresponds to the conservation of the projected wind near the cold pool propagation value; the critical one. Note that the equilibrium position is indifferently to the right (increasing y direction) or to the left (decreasing y direction) of the cold pool, which sometimes gives rise to a V-shaped pattern, with two lines, one to the left and one to the right of the cold pool.

In short, in the presence of shear, the triggering position of the convective cells is always at the downshear edge of the cold pool, and as the shear rate increases, so does the angle to the y-axis. This orientation is believed to keep the projection of the background wind perpendicular to the squall line direction, close to the propagation speed of cold pools. In the following, we propose to quantify this with the angle detection described in section 2.

2.3.2 Validation of RKW theory for squall lines orientation

Based on the angles estimated from the different simulations, several conclusions of RKW theory have already been validated : the existence of two regimes, subcritical and supercritical, and the emergence of a critical shear near 12.5 m s^{-1}. To quantitatively test the theory of squall line orientation, we plot the projection of the basal shear velocity perpendicular to the squall line $U_{sfc}\cos(\alpha)$ in figure 2.3 for the different simulation cases. The basal velocity is the average over the entire domain of the longitudinal component of the surface velocity. The angle that the wind speed makes with the direction perpendicular to the line corresponds to the angle determined by our method (figure 2.1 bottom right panel).

On Figure 2.3, we also show what is predicted by the theory (in red). For the sub-critical regime, we should have an increasing line with slope 1, which corresponds to a zero angle; the lines are perpendicular to the wind in order to maximize the incoming wind. This line reaches the critical case, for U_{sfc} = 12.5 m s^{-1}, and at this moment, the wind speed and the cold pool spreading speed are equal. We then enter the super-critical regime, and we expect saturation, i.e. the angle of the line maintains the cold pool/background wind equilibrium. In orange, we have plotted the results of our simulations. We observe a very good agreement in the sub-critical regime. In the supercritical regime, we also have a reasonable agreement with the theory, roughly within error bars. At this stage, we can conclude that the theory of the conservation of the shear projection on the direction perpendicular to the squall line allows to predict the orientation angle of the convective bands. We note in passing that the results are robust to reasonable changes in the relaxation timescale used to impose wind shear and to a prescribed large-scale upward vertical velocity, following Risi *et al.* 2021.

However, there is some discrepancy between the theory and our results in the supercritical regime, and we wanted to understand if this was really due to measurement uncertainty or if some other phenomenon was at stake. In particular, it was hypothesized that the potential change of cold pool properties with background shear could feed back on the squall line orientation (Alfaro 2017). Thus in the next section, we investigate in more detail the cold pools in our simulations.

2.4 Is it wrong to consider that the cold pools properties do not change with the shear ?

Cold pools have received increasing attention in observational studies (Feng *et al.* 2015; Touzé-Peiffer *et al.* 2021), and in climate modeling (Hourdin *et al.* 2020) due to their contribution to triggering new convection. In this section, we describe how cold pools properties evolve as the shear increases, and discuss its consequences on the cold pool-shear equilibrium that forms squall lines.

2.4.1 Cold pools intensification

To analyze the properties of cold pools, and how these may change with shear, we investigate buoyancy anomalies in the vicinity of maximum precipitation at each time step, and then average in time. These composites are shown in figure 2.4.a. for different shear cases.

With low shear (left), we observe a cold pool nearly symmetrical to the maximum precipitation and not very intense. In the case U_{sfc} = 10 m s^{-1}, we observe a dissymmetry of the pool, which reflects a resistance of the pool to the frontal wind. Finally, in the super critical case U_{sfc} = 17.5 m s^{-1}, we

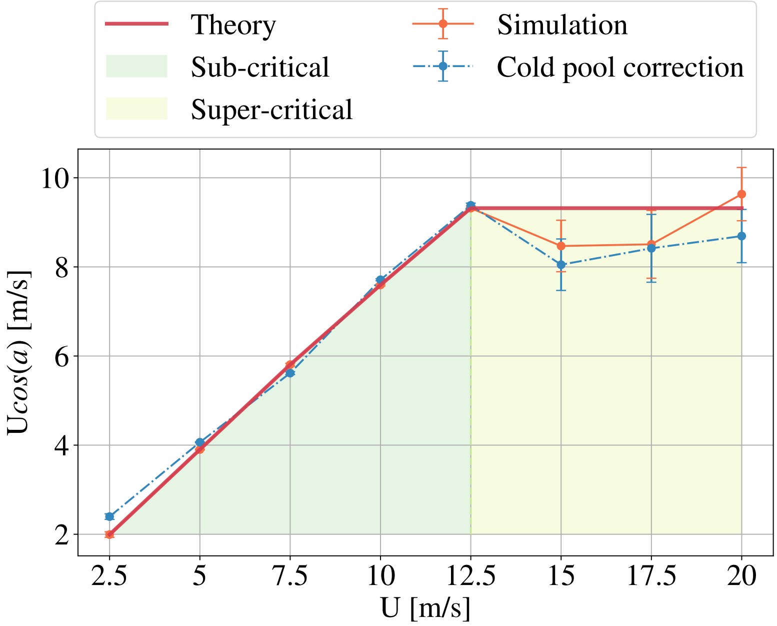

Figure 2.3: Evolution of the shear basal velocity projection perpendicular to the squall line, according to the 8 simulated cases. A very good agreement between the RKW theory and Robe and Emanuel 2001 (red) and our results (orange) is found. We observe a saturation level, separating the subcritical and supercritical shears. The critical state is found for $U_{sfc} = 12.5$ m s^{-1}. In our estimates of $U\cos(a)$, we used the actual simulated horizontal mean wind speed in the x direction at the first atmospheric level (which is slightly lower than the imposed target velocity towards which the horizontal mean surface wind is relaxed). The dashed blue line shows the same projection when the intensification of cold pools with shear is accounted for.

observe the same asymmetry, noting that the cold pool seems colder, and deeper.

To quantify this from our composite figures, we compute the cold pool potential energy in J kg^{-1} (following Meyer and Haerter 2020; Rotunno *et al.* 1988), defined as

$$E_p = \int_{cp} B(x,z)dxdz \tag{2.1}$$

where cp denotes the domain inside the cold pool, and $B(x,z)$ the composite value of buoyancy in (x,z) cross section around the location of maximum precipitation (see figure 2.4a.b.c.). We define the cold pool upper boundary as the $b = -0.02$ K buoyancy contour (following Tompkins 2001b), black contour figure 2.4 top panels), and integrate (2.1) from the surface to this upper boundary. Figure 2.4.b. shows the potential energy of the cold pools for each simulation, as a function of the distance to the maximum precipitation. At the precipitation maximum, a gradual increase in potential energy is observed as a function of the imposed shear. This figure shows an intensification of cold pools.

How to explain this intensification ? The intensification is due to the rain evaporation intensification with shear (see Supplementary Figure S3), which provokes both an increase in cold pool buoyancy anomaly and in the cold pool height. However, the latter is found to dominate (Supplementary Figure S2): the latent cooling is more intense and so downdrafts reach the isoline $b = -0.02K$ (cold pools upper boundary) higher in altitude. To determine why rain evaporation increases with shear, we show the evolution of relative humidity vertical profiles (estimated as averages within 10 km of the maximum precipitation location) for all shear cases (Figure 2.4). We observe that the top of the dry layer deepens monotonically with the shear (dashed line), and this trend is highly correlated with the rain evaporation (dotted line) and eventually the cold pool height (solid line). We found that 60% of the increase in rain evaporation between the highest shear case and the control one is due to a drier environment (see Supplementary S4). We hypothesize that it can be explained by the meso-scale circulation which affects the relative humidity profiles.

2.4.2 Impact on squall lines orientation

Does this intensification of cold pools impact the squall line orientation? The intensification of cold pools, insofar as they are associated with a higher propagation speed, could move the position of triggered convective cells downshear. More precisely, if we make the hypothesis of a total transfer of potential energy to horizontal kinetic energy of cold pool spreading, we can deduce a propagation speed of the pools, following Benjamin 1968; Meyer and Haerter 2020; Rotunno *et al.* 1988,

$$v_p = \sqrt{2E_p}. \tag{2.2}$$

Since the potential energy increases with the imposed shear (see figure 2.4), so does the velocity. We can take into account this increase of velocity in the equilibrium between cold pools and background shear, in order to bring a correction to the current theory. More precisely, we account for the cold pool velocity deviation from the critical case, i.e. the correction brought by the cold pools is $v'_p = v_p - v_p^{crit.}$. This lead to the following equilibrium,

$$U_{sfc}\cos(a) \sim U_{sfc}^{crit.} + v'_p \tag{2.3}$$

where $U_{sfc}^{crit.}$ corresponds to the critical case 12.5 m s^{-1}. Figure 2.3 shows in blue the correction brought by this calculation $U_{sfc}\cos(a) - v'_p$ (instead of

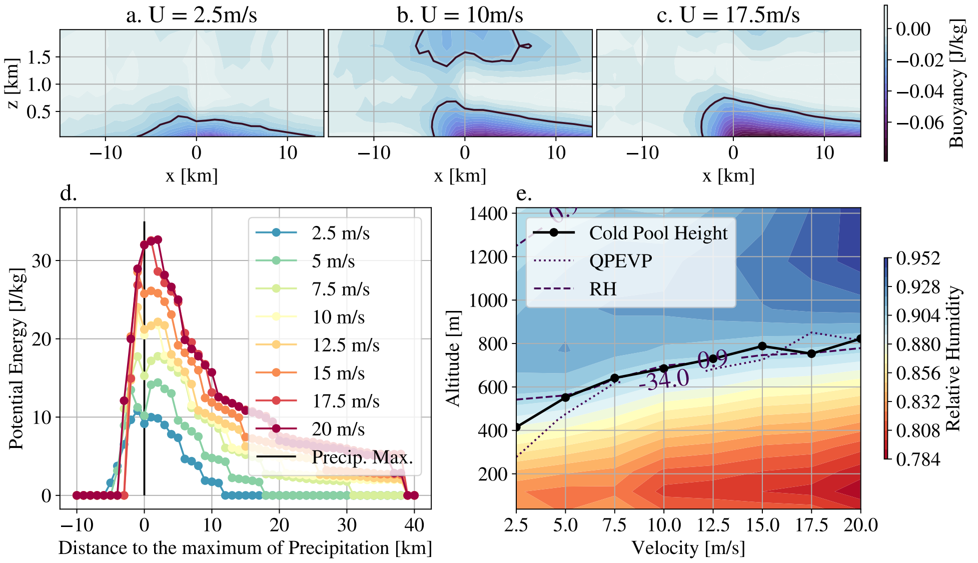

Figure 2.4: abc. Composite images of the buoyancy in (x, z) cross sections around the location of maximum precipitation (located at $x = 0$ in those composites). The compositing is performed at maximum precipitation, over 5 days of radiative-convective equilibrium with hourly outputs. In black, the boundary $b = -0.02$ K is drawn and delimits the cold pool. d. Potential energy of cold pools for each shear as a function of the distance to the maximum precipitation. The potential energy is computed at each x-location as the integral of the buoyancy up to the top of the composite cold pool. e. Cold pool height (estimated as the highest cold pool upper boundary on the composites) as a function of shear, as well as contours of relative humidity $RH = 0.9$ and rain evaporation $QPEVP = -34$ g kg^{-1} day^{-1} (estimated as averages within 10 km of the maximum precipitation location).

$U_{sfc} \cos(a)$). For the subcritical regime, we still have the same agreement. For the supercritical case, we observe that the correction brings the theoretical expectation in closer agreement with the CRM simulations. Since this correction is small, we conclude that the intensification of the cold pools is not a determining factor for the orientation of squall lines.

2.5 Conclusion

While the RKW angle theory was so far qualitatively supported, for the first time we support it with an objective and reproducible quantification of squall line orientation. Using autocorrelation image analysis of the integrated humidity profiles, we measure the orientation from CRM simulation of the squall lines and identify the subcritical and supercritical regimes, depending on the ratio between the basal shear velocity, and the spreading velocity of cold pools. The hypothesis of the conservation of the projected basal wind perpendicular to the squall line, that predicts the orientation of squall lines, is here validated.

We further investigate the properties of cold pools, and notably their evolution with shear. We measure an intensification and a deepening of the cold pools due to the drying of the lower atmosphere with increasing shear. However, the resulting intensification of the cold pools has a secondary impact on the orientation of the line.

Although these results are within an idealized framework, they draw our attention to the sensitivity of convective organization to wind shear. Squall lines are associated with extreme rainfall, and an interesting question could be the impact of squall line orientation on extreme precipitation rates. In the longer term, more work is desirable to extend these results beyond the CRM framework, for example by using satellite data (Fiolleau and Roca 2013; Roca and Fiolleau 2020). The deployment of satellite observations at fine-scale resolution (kilometers, for example within cold pools), such as those proposed in the ESA Harmony mission (the only Earth Explorer 10 candidate mission), would be essential to perfect our understanding of the processes (Harmony 2020).

2.6 Support Information

Contents of this file

1. **Model and simulations details.** In this section, we provide more detailed information on the cloud-resolving model used and the specific configurations of the simulations.
2. **Automatic detection of squall line angle: method description.** In this section, we describe in detail the method used in the paper to automatically detect the angle orientation of the squall line.
3. **Investigation of cold pool intensification with increasing background shear.** In this section, we analyze in more detail the changes of cold pool properties as the background wind is increased, and split this change into a change of cold pool depth and a change of cold pool averaged buoyancy anomaly.
4. **Investigation in cold pools, what are the origins of their intensification?** In this section, we describe the average relative humidity and rain evaporation profiles above cold pools. This can help understanding the link between the cold pool height and the rain evaporation altitude.

2.6.1 Model and simulations details

We simulate several cases of squall lines using the Cloud-Resolving Model (CRM) System for Atmospheric Modeling, or SAM (Khairoutdinov and Randall 2003). This model is based on a non-hydrostatic and anelastic formulation of atmospheric flows. It has the ability to cover a wide range of scales, from deep convective kilometric scale to mesoscale organization $\mathcal{O}$(100s km), and is thus adapted to the study of mesoscale systems such as squall lines. The prognostic thermodynamic variables of the model include total nonprecipitating water (vapor, cloud water, cloud ice) and total precipitating water (rain, snow, graupel). The mixing ratios of cloud water, cloud ice, rain, graupel, and snow is diagnosed from the prognostic variables using a temperature-dependent partition between liquid and ice phases. The frozen moist static energy, which is the sum of the liquid/ice water static energy and the total condensate amount times the latent heat of vaporization, is conserved during moist adiabatic processes in the model, including the freezing and melting of precipitation. The model is run to radiative-convective equilibrium, and once equilibrium is reached (in about 30 days) the organization of squall lines is analyzed, from day 30 to 35 with hourly outputs.

All simulations are three-dimensional on a square, doubly periodic horizontal domain, with horizontal resolution 1 km and domain size 128 km in x and y directions. The vertical grid has 64 levels (capped at 27 km with a rigid lid), with the first level at 37.5 m and grid spacing gradually increasing from 80 m near the surface to 400 m above 6 km, and a variable time step (10 s or less to satisfy the Courant–Friedrichs–Lewy condition). The surface fluxes are computed using Monin–Obukhov similarity. To reduce gravity wave reflection and buildup, a sponge layer with Newtonian damping is applied to all prognostic variables in the upper third of the model domain, from 18 to 27 km. We neglect the Earth rotation, a reasonable assumption in the deep tropics where the Coriolis parameter is small (set to zero in our simulations).

To organize the deep convection into squall lines, a linear shear in the x direction is imposed (following Muller 2013a). The imposed profile has a wind in the x-direction decreasing from U_{sfc} at the surface $z = 0$ km to $U_{1km} = 0$ m s^{-1} at $z = 1$ km. This background shear is imposed by relaxing the mean wind towards this profile with a relatively fast time scale of 2 hours. Nine simulations, with the surface wind U_{sfc} varied from 0 (no shear) to 20 m s^{-1}, with 2.5 m s^{-1} increments, are performed. To avoid an impact of this imposed surface wind on surface latent and sensible fluxes (which are proportional to surface wind magnitude), the domain-mean surface wind is removed before computing those surface fluxes.

2.6.2 Automatic detection of squall line angle

Figure 2 bottom panels in the paper shows the autocorrelation of the precipitable water at convective radiative equilibrium, for the sub-optimal U_{sfc} = 2.5 m s^{-1}, near-optimal U_{sfc} = 10 m s^{-1}, and super-optimal U_{sfc} = 17.5 m s^{-1} cases. In the sub-optimal case, we have the characteristic signal of a white noise, random, since we observe a peak in the center and a fast diffusion of the signal. In the optimal case, the orientation is along the y axis, consistent with the PW spatial distribution (top panels). In the super-critical case, a similar pattern is observed, with the two axes oriented at an angle. Thus the autocorrelation fields yield a centered representation of the convective organization. This next step will allow an automatic post-processing to measure the angle of the squall lines.

The angle a is defined as the angle between the squall line and the y-axis. To compute it, at each time step, we calculate the product between the spatial autocorrelation of PW (bottom contour plots of figure 2 in the main text) and a long (lengths 1 and 0.1 for major and minor axes) rotating 2D Gaussian oriented by a varying angle a. The selected angle a is the one that maximizes this product, i.e. that accounts for the best correlation.

By applying this method to all snaphots, we obtain a time distribution of the angle of the squall line with respect to the y-axis (between -$\pi/2$ and $\pi/2$). The mean of this distribution of angles in absolute value (between 0 and $\pi/2$) is our final angle, and its variance the incertitude (bottom curve in figure 2 of the main text).

Figure 2.5 shows the time evolution of the angle distribution for the three aforementioned cases. On the ordinate, we have the angle which varies from $-\pi/2$ to $\pi/2$, and on the abscissa, the time from the RCE equilibrium to the end of the simulation (5 days). Each pixel represents the probability density of an angle at a given time. In white, the evolution in time of the most probable angle is plotted. In the control case, we notice that the distributions are very wide, and decorrelated from one instant of time to another. In the sub-critical case, we have peaks around 0 during the whole evolution. In the super-critical case, we have three periods, first peaks of probability at -50, then a transition phase, and finally peaks in +50. This accounts for the indistinguishability between the 'right of the pool' and the 'left of the pool' for the projection of the angle, which sometimes gives rise to a broken line, similar to a V-shape.

From the time evolution of the angle distributions for each simulation, we can determine an averaged angle. We first reduced the angle to values between $[0, \pi/2]$ by taking its absolute value. Therefore, the final angle selected by our automatic method is the average over time of the absolute value of the most probable angle. We associate to each angle a measurement uncertainty, which corresponds to the variance of the distribution of the most probable angle (again in absolute value) in time. This method yields the angle estimate versus shear strength shown figure 2 bottom panel of the main paper. We note that this method has been tested on several data sets and compared to repeated and rigorous manual measurements, which attests to the reliability of this approach.

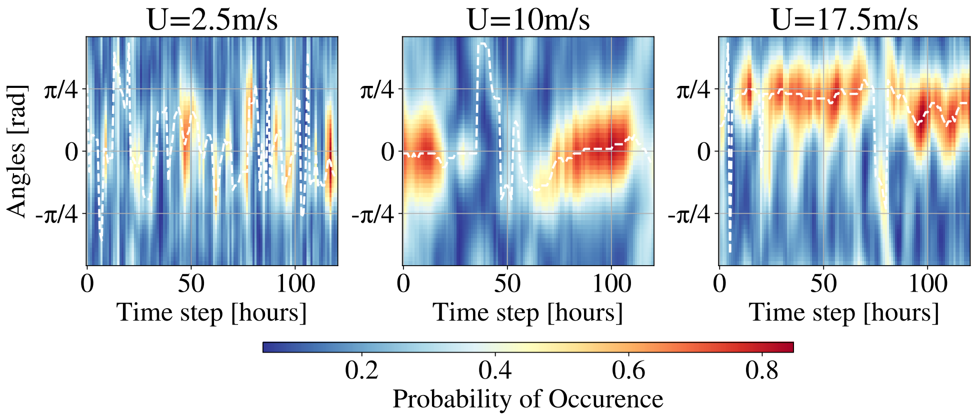

Figure 2.5: Time evolution of the distribution of angles of the squall lines with respect to the y-axis (perpendicular to the incoming wind) determined from the PW autocorrelation images.

2.6.3 Investigation of cold pool intensification with increasing background shear

Here we investigate whether the cold pool intensification with shear strength is due to the increase in depth, or to the increase in the buoyancy anomaly. We therefore calculate the contribution to changes in cold pool potential energy E_p from the height of the cold pool h and from the mean buoyancy anomaly in the cold pool E_p/h. To do this, we develop the energy as follows:

$$\frac{\Delta E_p}{E_p} = \frac{\Delta(E_p/h)}{(E_p/h)} + \frac{\Delta h}{h} + \mathcal{O}(\Delta^2) \tag{2.4}$$

where Δ is defined as

$$\Delta\varphi = \frac{\varphi_{ctrl} - \varphi}{\varphi_{ctrl}} \tag{2.5}$$

and Δ^2 denotes a second order error term (involving $\Delta(E_p/h) \times \Delta(h)$).

Figure 2.6 shows for each case this decomposition of the potential energy change. For example, for the case U_{sfc} = 20 m s^{-1}, we see that the potential energy has doubled compared to the control case; it has increased by 20% compared to the optimal case. This figure shows that the evolution of the potential energy is mainly due to the increase of the height, with a smaller (but not negligible) contribution from increased buoyancy anomaly. We interpret these changes as resulting from the drier conditions, yielding higher and larger rain evaporation with increasing shear, as further discussed in the main text.

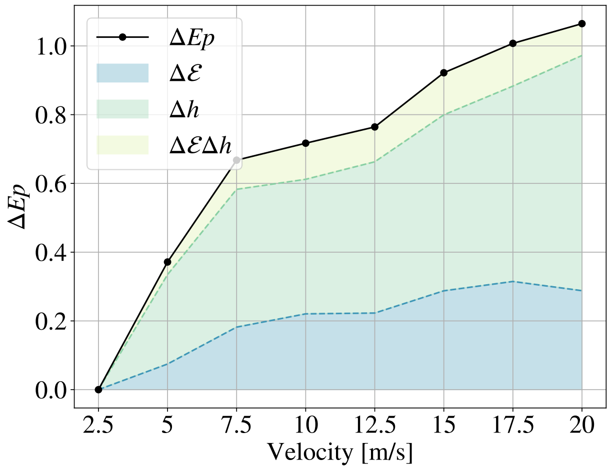

Figure 2.6: Evolution of the differential of the potential energy as a function of the shear strength. The differential is defined as $\Delta Ep = (Ep - Ep_{ctrl})/Ep_{ctrl}$. For each simulation, ΔEp is decomposed into a contribution from cold pool height h and cold pool strength $\mathcal{E} = E_p/h$ (and the second order error term). This figure shows that the intensification of the cold pools is mainly the consequence of deeper cold pools with increasing shear.

2.6.4 What are the origins of their intensification?

Investigation in rain evaporation profiles

The partial evaporation of rain, with its concomitant latent cooling is responsible for cold pool formation. We investigate rain evaporation profiles in the graph 2.7 where the vertical profiles of the relative humidity in dashed line, as well as the rain evaporation rate (QPEVP) in solid lines are displayed for each cases. The relative humidity field is calculated following Clausius-Clapeyron approximation. The rain evaporation rate is an output of the cloud resolving model SAM. We compute both these quantities in a composite way, i.e. we average in the vicinity of maximum precipitation at each time step. The vertical profiles are obtained by averaging in x and y near the maximum of precipitation (10km in x, 5km in y). In this graph, the thresholds QPEVP=34 g/kg/day and RH=0.9 are highlighted too.

We observe for highest shear case a maximum within the cold pool of $0.950 g/kg/day$ versus $0.830 g/kg/day$ for the control case. This intensification provokes both an increase in cold pool buoyancy anomaly and in the cold pool height. However, the latter is found to dominate (see Figure S2). The latent cooling is more intense and so downdrafts reach the isoline $b = -0.02K$ (cold pools upper boundary) higher in altitude.

In the graph 2.7 we can compare rain evaporation profiles and relative humidity, and observe that whereas rain evaporation increases with shear,

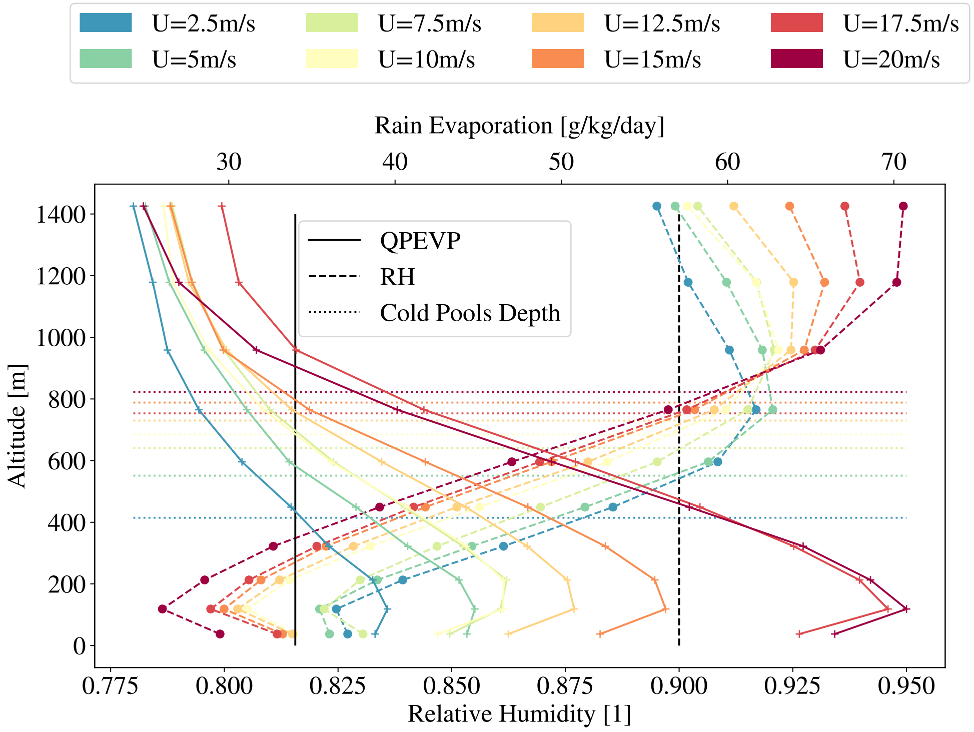

Figure 2.7: Vertical profiles of the relative humidity (dashed lines) and rain evaporation rate (solid lines). Cold pools depths are displayed in dotted lines. Each color represents a shear case. The threshold QPEVP=34g/kg/day and RH=0.9 are highlighted.

the relative humidity decreases. This supports a causal link between these two quantity. In fact, dry conditions favor evaporation; and in the next subsection we propose a proper scaling of the rain evaporation in order to explain its intensification with shear.

Scaling of rain evaporation

We use the scaling of rain evaporation as the product of the distance to saturation and the ventilation function (following the default microphysics of SAM Khairoutdinov and Randall 2003).

$$QPEVP = \frac{\partial q_m}{\partial t}_{evap} = f(v_T)(1 - RH) \tag{2.6}$$

where: QPEVP is the rain evaporation, the rate of evaporation of precipitating water of type m (q_m); t is the time, $f(v_T)$ is the so called ventilation function which increases with v_T the terminal velocity, and RH is the relative humidity (RH).

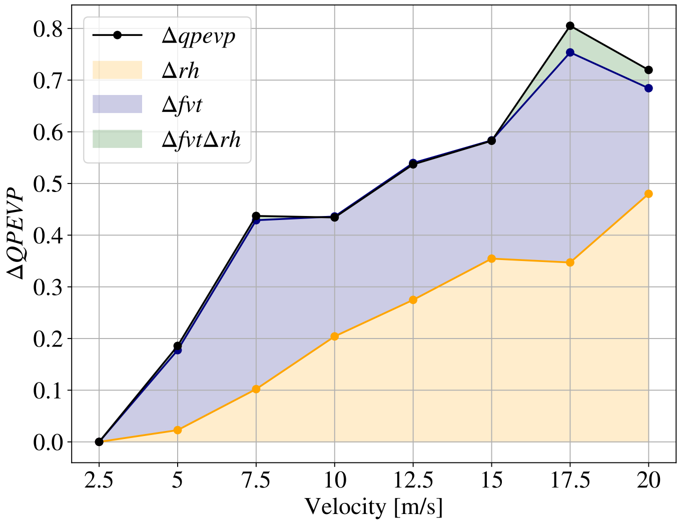

Figure 2.8: Evolution of the differential of the rain evaporation (QPEVP) as a function of the shear strength. The differential is defined as $\Delta A = (A - A_{ctrl}/A_{ctrl})$. For each simulation $\Delta QPEVP$ is decomposed into a contribution from the distance to saturation $(1 - RH)$ shortened to Δrh, and ventilation function $\Delta f(v_T)$, (and second order terms). This figure shows that intensification of rain evaporation is mainly due to the drying up with increasing shear.

We thus compute the evolution of the differential of the rain evaporation as a function of the shear strength. The differential is defined as $\Delta QPEVP = (QPEVP - QPEVP_{ctrl})/QPEVP_{ctrl}$. For each simulation,$\Delta QPEVP$ is decomposed into a contribution from relative humidity and ventilation function factor (and the second order error term), see Fig.2.8. In this picture, we observe that the rain evaporation increases by 60% between the control case and the higher shear case. 40% of this increase is due to the drying of the air in this layer, and 20% corresponds to the ventilation function. This figure shows that the variation of rain evaporation is mainly the consequence of relative humidity decrease with shear.

The reasons why shear impacts relative humidity and the ventilation function deserves more investigation. We hypothesize that the relative humidity increase is due to changes in the meso-scale circulation which affects the relative humidity profiles. For the increase of ventilation factor, according to Khairoutdinov and Randall 2003, Appendix, Equation (A24),we can relate it to the precipitating water (of type rain, snow or graupel). In our case, the temperatures are warm enough at those heights for rain to dominate. Thus, $f(v_T)$ can be written as

$$f(v_T) \sim A_{em} q_r^{1/2} + B_{em} q_r^{5+bm/8}, \tag{2.7}$$

where q_r is the precipitating rain mixing ratio. We observe that q_r increases

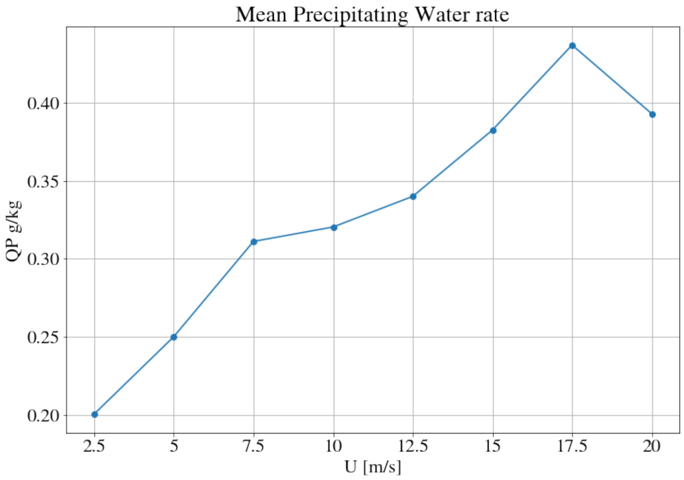

Figure 2.9: Evolution of the mean precipitating rain (QP) above cold pool as the shear increases. We observe that the stronger the shear, the more intense mean precipitating rain is. As there is more rain, provided the environment is dryer enough, rain evaporation is more intense and cold pool as well.

with the shear (see Figure S5), consistent with the increase of $f(v_t)$. The reason why the precipitating water increase with shear remains unclear and further work is needed.

Chapter 3

What does the initial growth of MCSs say about their life cycle?

Résumé en français

Ce chapitre fait l'objet d'un article en préparation, intitulé "Un modèle prédictif pour le cycle de vie des MCSs, S. Abramian, C. Muller, C. Risi, R. Roca & *T. Fiolleau. Sa version suit de près le contenu présenté ci-dessous.*

Les systèmes convectifs de méso-échelle qui deviennent très grands ou qui ont une durée de vie prolongée peuvent contribuer de manière disproportionnée aux précipitations extrêmes. En effet, la littérature suggère que lorsque la convection devient plus agrégée, les précipitations associées sont de plus en plus intenses. Mieux comprendre les facteurs qui déterminent si un système deviendra très grand pourrait donc améliorer notre compréhension des phénomènes météorologiques extrêmes. L'émergence récente de simulations à l'échelle globale haute résolution issues du projet DYAMOND (Stevens *et al.* 2019), associée à un algorithme de suivi des tempêtes appelé TOOCAN (Fiolleau and Roca 2013), offre une nouvelle opportunité pour étudier le lien entre le cycle de vie des MCS et les précipitations extrêmes dans les tropiques. Dans cette étude, nous utilisons des algorithmes d'apprentissage automatique pour prédire la surface maximale des MCS en fonction de leur premier stade de développement et des conditions environnementales initiales. Les résultats révèlent que l'évolution initiale du système anticipe sa surface maximale. De manière remarquable, en observant l'évolution du taux de croissance au cours des deux premières heures du développement du système, nous pouvons prédire sa surface maximale avec un score de régression (R-2) de 0,8, indépendamment de sa durée de vie finale. En incorporant des caractéristiques supplémentaires liées à la forme, aux champs physiques, à la trajectoire et à l'influence des systèmes environnants, un score de 0,87 est atteint. Le délai de prédiction réduit à seulement une heure fournit un score de régression de 0,7. Des attributs physiques notables, tels que la présence de glace dans l'environnement du système, la proximité des systèmes environnants, l'intensité de la vitesse verticale à 500 hPa et la distance de migration, ont été identifiés comme des facteurs significatifs pour améliorer la précision de ces prédictions. Un modèle multi-linéaire est développé pour estimer le rôle de l'environnement dans la croissance du système.

What does the initial growth of MCSs say about their life cycle?

This chapter is the subject of paper in preparation, untitled A Predictive Model for MCS life cycle, S.Abramian, C.Muller, C.Risi, R. Roca & T. Fiolleau, exp. 2024. Its version follows closely the content presented below.

Abstract

Mesoscale Convective Systems that become very large or have long lifespans can contribute disproportionately to extreme rainfall. When convection becomes more aggregated, we observe increasingly intense rainfall. Gaining a better understanding of the factors that determine whether a system will become very large could improve our understanding of extreme weather phenomena. The recent emergence of high-resolution global simulations from the DYAMOND project (Stevens *et al.* 2019), coupled with a storm tracking algorithm called TOOCAN (Fiolleau and Roca 2013), has provided a groundbreaking opportunity to study the link between MCSs life cycle and extreme precipitation in the tropics. In this study we use machine learning algorithms to predict the maximum area of MCSs based on their early development stages and initial environmental conditions. The results reveal that the initial evolution of the system anticipates its maximum area. Remarkably, by observing the growth rate of area evolution within the first two hours of the system's development, we can predict its maximum area with a regression score (R-squared) of 0.8, regardless of its final lifespan. By incorporating additional features related to the shape, physical fields, trajectory, and influence of surrounding systems, a score at 0.87 is reached. The prediction timeframe reduced to just one hour, provides a regression score of 0.7. Noteworthy physical attributes, such as the presence of ice in the system's environment, proximity to surrounding systems, intensity of vertical velocity at 700hPa, and the migration distance, have been identified as significant factors in improving the accuracy of these predictions. A linear model is derived to estimate the role of the environment in the growth of the system.

Plain Language Summary

In this study, we investigated mesoscale thunderstorm systems known as MCSs and their connection to extreme rainfall. By using advanced simulations and a storm tracking algorithm called TOOCAN, we examined MCSs in the tropics. Using a machine learning technique called random forest, we

predicted the maximum size that the MCS raches during its life cycle based on its early development and environmental conditions. Interestingly, we found that observing the growth rate within the first two hours allowed us to predict the maximum size with good accuracy (R-squared of 0.8). By adding more features, the maximum size is predicted with a score of 0.87. Reducing the prediction time to just one hour leads to a R-squared of 0.7, providing valuable insights into extreme precipitation.

3.1 Introduction

Mesoscale convective systems (MCSs) exert a profound influence on tropical rainfall patterns, contributing to over 50% of precipitation and playing a pivotal role in extreme precipitation events. The disproportionate impact of MCSs that attain remarkable size (more than 120km in one direction) or exhibit lifespans equal to more than a day on extreme rainfall (Roca and Fiolleau 2020) underscores the need to unravel the factors governing their development (Schiro *et al.* 2020). As convection becomes more concentrated within these systems, the intensity of rainfall significantly escalates, making it crucial to gain a better understanding of their growth dynamics and predictability.

Historically, limited access to observations of dynamical fields from satellites and in-situ measurements has posed challenges in comprehensively addressing the intricacies of MCSs. Additionally, numerical simulations such as Radiative-Convective Equilibrium (RCE) have struggled to accurately replicate the realistic conditions necessary for modeling MCS development. However, recent advances have opened new avenues for studying MCSs in unprecedented detail. High-resolution global simulations, like DYAMOND (Stevens *et al.* 2019), combined with sophisticated storm tracking methods such as TOOCAN (Fiolleau and Roca 2013), now provide over 70,000 tropical (30S to 30N, see figure 3.1) MCSs in August 2016 as an extensive dataset to explore.

In this study, we employ machine learning algorithms, namely random forest, multilinear regression, and multi-layer perceptron, to predict the maximum area that a MCS reaches during its life cycle based on its early development stages and initial environmental conditions in high-resolution global simulations. Our primary objective is to address the fundamental question of whether the fate of MCSs -i.e. its maximal area - is predetermined or if rare events during their mature development phase drive their exceptional size of more than 120km in one direction. Moreover, we aim to evaluate the model's performance -i.e. random forest, multilinear regression and multi layer perceptron - across a wide range of areas and investigate whether the behavior of large MCSs aligns with that of smaller ones.

An intriguing observation motivating our approach is that MCSs, regardless of their size, lifespan, or location (ocean or continent), follow a consistent life cycle pattern: linear growth leading up to their maximum area, followed by a nearly symmetrical linear decline (the area of the MCS in the storm tracking algorithm represents the area of the cloud shield identified with an OLR threshold, see methods for details). This simple life cycle can be effectively captured by a model with three key parameters: maximum area (A_{max}), lifespan (D), and duration of the growth phase (t_{max}) as described in the figure 3.3. Notably, approximately 60% of cases exhibit a symmetrical life cycle, where t_{max} is equal to half of the lifespan.

Furthermore, we delve into the underlying physical mechanisms governing the growth rate of convective systems, drawing insights from a recent study (Elsaesser *et al.* 2022) proposing a growth rate model based on mass balance equations:

$$\frac{dA}{dt} = A_{c,src} - \frac{1}{\rho}\frac{dM_c}{dz} - \frac{1}{\rho}\frac{dM_s}{dz} - \frac{A}{\tau} \tag{3.1}$$

where A represents the cloud shield area, A_c is the convective area, and the subscript "src" denotes the temporal generation of new convective area. Additionally, M_c and M_s correspond to the convective and stratiform mass flux, respectively. Parameters ρ and τ stand for the atmospheric density and cloud shield area decay timescale. A high growth rate may arise from a strong convective source, elevated mass flux, rapid transition from convective to stratiform regions, or gradual transformation of cloud water to precipitation. Understanding these mechanisms will shed light on whether a high growth rate indicates a robust and enduring MCS or merely a transient phenomenon. Moreover, we investigate the influence of environmental factors on MCS development. Parameters such as the system's shape, propagation speed, distance traveled, and the presence of neighboring systems are examined to determine their impact on MCS growth and trajectory.

In summary, large-scale MCSs significantly influence extreme precipitation events, making their accurate prediction a critical endeavor. The simple life cycle characterized by three shared parameters (A_{max}, D, and t_{max}) suggests that early development stages and initial environmental conditions may determine the MCS's maximum area, primarily driven by its growth rate. This study aims to test this hypothesis and specifically address the following three questions:

- Can the maximum area of MCS be predicted based on its early growth rate? If so, at what specific stage in its development?
- Does the prediction accuracy and timing improve with the incorporation of additional features describing the system and its environment?

- Which features, those associated with the MCS itself or its surrounding environment, have a stronger impact on the prediction?

To address these questions, machine learning algorithms are employed to establish a connection between the onset of MCS (Mesoscale Convective System) and its maximum area. The subsequent section outlines the mesoscale convective systems under study, introduces the machine learning pipelines implemented, and elaborates on the two experiments intended to predict the maximum size of these systems: the first relying solely on the growth rate of the area, and the second incorporating additional features (which will be described). Section 3 presents the outcomes, assesses model predictions, and provides a physical interpretation. Finally, in Section 4, a discussion is presented, followed by the conclusion in Section 5.

3.2 Methodology: How to capture the first hours of MCSs development and link it to their size?

3.2.1 Global CRM coupled with storm Tracking algorithm

Current satellite data does not provide sufficient information on the vertical structure of dynamic fields, therefore, we have turned to simulation data for our study. To investigate the life cycle of mesoscale convective systems (MCSs), we rely on the latest generation of high-resolution global simulations known as DYAMOND (Stevens *et al.* 2019). This project represents the first intercomparison of global storm-resolving models, with nine models submitting simulation output for a 40-day period (1 August–10 September 2016). Eight of these models employed a tiling of the sphere with a resolution uniformly less than 5 km. By resolving the transient dynamics of convective storms in the tropics, global storm-resolving models eliminate the need to parameterize tropical deep convection, leading to a more robust representation of the climate system and a more natural connection to high-resolution data from satellite-borne sensors. For our study, we use the System for Atmospheric Model (SAM, Khairoutdinov and Randall 2003), an anelastic model of fluid dynamics with parametrized microphysics.

Most DYAMOND models, including SAM, accurately capture essential MCS characteristics such as lifetime, cloud shield area, and volume of rainfall (Feng *et al.* 2023). Simulated MCS movement speeds over the ocean generally agree with observations, but over land, some models produce faster speeds, possibly indicating stronger cold pool intensities that promote MCS movements. To detect, track, and measure the evolution of MCSs, we utilize the TOOCAN storm tracking algorithm. This algorithm works with a volume of infrared images to identify and track MCSs in a single 3D (spatial+time) segmentation step, employing a Lagrangian approach to study convective systems. Deep convective regions are identified using a cold OLR threshold

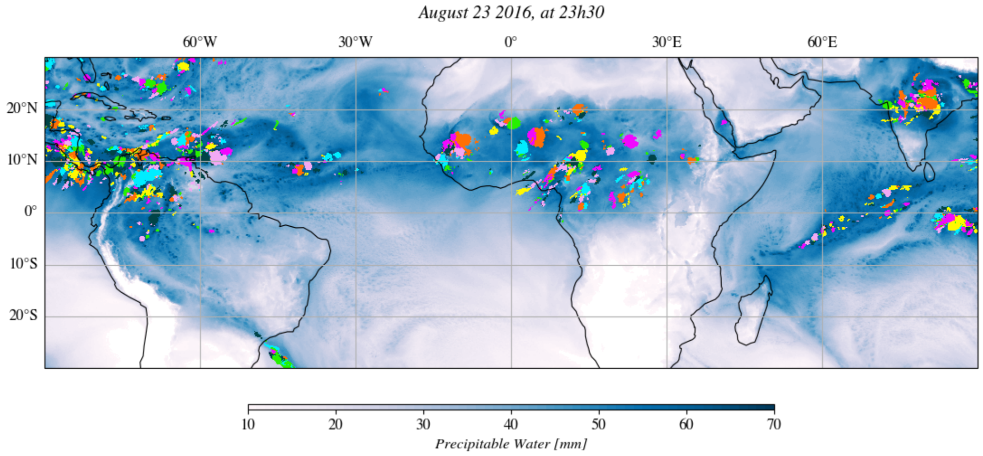

Figure 3.1: Snapshot from DYAMOND-SAM winter simulations during August 23 2016 at 23h30 of the Precipitable Water with on top the Mesoscale Convective Systems tracked by TOOCAN focusing only on the tropics.

of 172 W/m^2. The initial dataset comprises more than 70,000 simulated systems during August 2016. In the following paragraphs, we describe the pre-processing steps applied to the data.

3.2.2 Pre-processing of data

From the systems tracked by TOOCAN, we will focus solely on tropical MCSs, restricting our analysis to within +-30 degrees of latitude. Our particular interest lies in relatively long-lasting and large-scale systems, defined as those with a minimum lifespan of 5 hours and a maximum extent of at least 40 km. From the initial 70,000 systems, we then focus on 55,000 MCSs. During the observation of system life cycles, we notice that some take considerable time to dissipate, as shown in figure 3.2.a., and although they last for more than 5 hours, their effective duration is shorter. In a smaller proportion of cases, a system may also experience a delayed growth phase. In both instances, we choose to concentrate on the *active* life cycle of the systems, namely those with significant growth and decay rates of area, only at the boundary of the life cycle. To determine these thresholds, we aim to strike a balance between maximizing the correlation between maximum area and lifespan while minimizing the number of systems removed (often active cycles fall below the 5-hour minimum lifespan threshold).

Figure 3.2.a. depicts the evolution of the first criterion (correlation between area and lifespan) and the second criterion (number of systems removed) based on different thresholds applied to the growth and decay rates. An optimal compromise is found at 1000km^2/h. It is worth noting that the growth rate of area threshold remains fixed and independent of the maximum

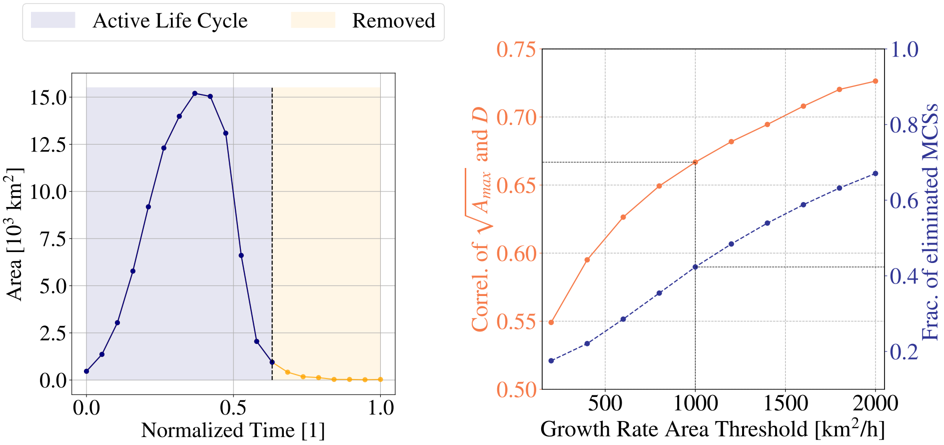

Figure 3.2: a. Example of a system evolution truncation of the life cycle to consider only the active life cycle. b. Determination of threshold in area growth rate as a trade off between a maximize correlation of duration and the square root of maximal area and minimize the number of systems removed. Empirically, the threshold is found at 1000km^2/h.

area of the systems, ensuring there are no a priori biases or information embedded in this threshold.

Finally, size, lifespan, and growth time distributions are displayed in Figure 3.4, alongside the correlation between lifespan and maximum area 3.4. This dataset of over 35,000 systems, coupled with high-resolution physical fields, represents an unprecedented opportunity for the application of machine learning. In the next section, we will describe the protocols utilizing machine learning algorithms to address the overarching question of this study: What determines, during the early stages of growth, whether a system will become larger than 120km for instance, and why?

3.2.3 Implementation of Machine Learning Pipelines: models, input, output and error quantification

Handling all this data is challenging, especially considering that the dynamic and thermodynamic fields are accessible for all systems. The machine learning approach can be seen as an initial step towards developing a physical model. Learning occurs when a program solves tasks without being explicitly programmed for them. In the case of supervised learning, as is the focus here, programs primarily create a model that minimizes the average statistical error with respect to the target task.

Our method aims to first understand statistically what leads to significant extensions of the systems and then to comprehend the physical interpretation of this learning. The protocol involves training a learning model on a subset

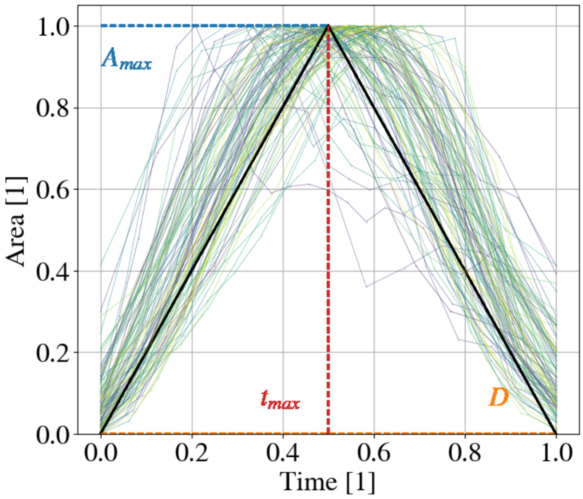

Figure 3.3: Superimposed evolution of the life cycle of tracked Mesoscale Convective Systems (arbitrarily chosen) - i.e. the normalized area evolution as a function of the normalized time for 100 systems. The solid black line represent the simple model described in Roca *et al.* 2017 which captures the life cycle with 3 parameters, the maximal area, the duration and the time of maximal area which is most of the time equal to half of the duration.

of MCSs (the train and validation datasets represent 85% of all systems) to predict the maximum area of an MCS based on its early growth information. Subsequently, we assess its performance on new systems, separately in a test set (the remaining 15% of MCSs). In the following, we define the model we will use and precisely specify the input characteristics of the model. We compare three methods: a multilinear model, a neural network, and a random forest.

Machine Leaning models

The multilinear model optimizes the weights of a linear form that maps the input vector of system characteristics to the target maximum size. Here, we employ a Lasso model, which includes weight regularization, requiring the model to minimize the prediction error and also minimize the L1 norm of the linear form. For the neural network, the principle is the same, except there are non-linear activation thresholds in the layers. Lastly, the random forest consists of a collection of decision trees. Each decision tree describes a set of possible outcomes (also known as leaves), each representing the consequence of a logical decision made at each tree node. The decision is determined by a threshold applied to an input variable. The order of variables and the threshold are optimized in the training process to minimize the prediction error. The iteration involves promoting variables with a high Gini impurity score, which represents a variable's ability to be correlated with the output compared to a random variable. The random forest aggregates predictions

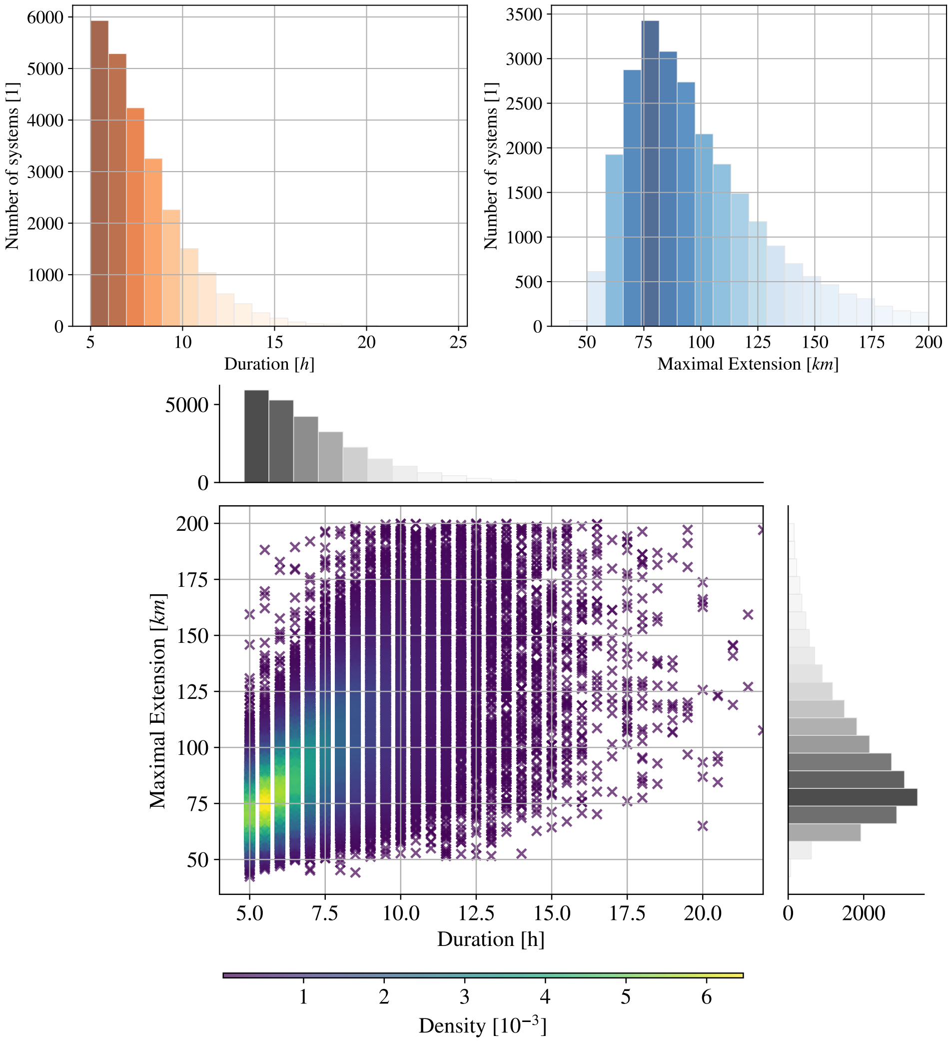

Figure 3.4: a. Distribution Mesoscale Convective Systems duration and b. maximal extension (square root of maximal area). c. Joint distribution of the duration and the maximal extension for all considered systems. The color indicate the density of points. Through post-processing of data, see figure 3.2, correlation between maximal extension and duration is equal to 0.67 consistent with observations of mesoscale convective systems.

from the collection of trees, allowing for a more robust prediction. The advantage is that the average Gini score for each variable can be known, facilitating result interpretation. All our analysis uses the Sklearn Python Package (Pedregosa *et al.* 2011).

Output variable and error quantification

We trained three machine learning models to predict the square root of maximum area of an MCS (we made the arbitrary choice to work with square root of area instead of area, although similar results are obtained with area prediction, not shown), based on the evolution of the early stage of the system, observed at intervals ranging from 30 minutes up to 5 hours (the minimum duration of all systems). To assess the performance of each model, we used the Pearson correlation coefficient, denoted as r, which is defined as:

$$r = \frac{cov(y_{pred}, y_{target})}{\sigma(y_{pred})\sigma(y_{target})} \tag{3.2}$$

where y_{pred} represents the set of model-predicted square root of maximum areas, y_{target} is the true target square root of maximum areas, cov denotes covariance, and σ denotes variance. This score measures how well the model's predictions align with the target values, accounting for any recurrent biases. It is important to note that a high correlation does not necessarily mean the model is accurate, as systematic overestimation or underestimation could still lead to a high correlation.

To evaluate if the model achieves its intended goal, we consider a second criterion, the Root Mean Squared Error (*rmse*), defined as:

$$rmse = \sqrt{E[(y_{pred} - y_{target})^2]} \tag{3.3}$$

where E represents the first moment operator, and y_{pred} and y_{target} are defined as above. The mean squared error is the criterion minimized during model training, meaning that the correlation coefficient still incorporates this information, but does not include it explicitly.

Input variables

Regarding the input data, as described in the introduction, we designed two experiments. In the first experiment, we input only the evolution of the growth rate of the area to predict the maximum size. More precisely, for each MCS we compute the following array

$$\left\{ \frac{dA}{dt}(t = t_0 + \Delta t), \frac{dA}{dt}(t = t_0 + 2\Delta t), .., \frac{dA}{dt}(t = t_0 + n\Delta t) \right\}, \tag{3.4}$$

where A is the area of the cloud shield, t_0 is the birth time of the system, Δt is equal to 30min, n is an integer less or equal to 10 (which correspond to 5h of development), and dA/dt is estimated by finite difference between the timestep and the previous one. We conduct 10 cases, by varying the observed period of evolution of the system from 30min to 5h. We note in passing that in the theoretical model described in figure 3.3 the growth rate is constant in the increasing phase, but in the data there are some small variations in area growth rate which we retain. This protocol serves as our baseline and will investigate if the growth rate already incorporates environmental parameters.

In the second step, we will integrate new features into the model, following a feature engineering approach. The features fall into four categories: cloud shape, surrounding physical fields in the near environment, system migration, and the influence of neighboring MCSs. Concerning the physical fields, we considered only the available 2D fields from the simulation, selecting 12 variables of interest: long-wave net top of atmosphere, precipitable water, relative humidity at 700hPa and 500hPa, surface temperature at 2m, ice water path, meridional and zonal wind velocities at 10m, vertical wind velocity at 850hPa, 700hPa, and 500hPa, and the land mask. Figure 3.5 show example of physical fields for a given MCS at 1h of development. For each variable, we calculated the mean and standard deviation over a 5-degree by 5-degree window centered around the system's barycenter. Additionally, we computed the mean and standard deviation just inside the system (by applying the mask) and only outside the system (by multiplying with the complement of the mask). The aim was to distinguish the contributions from the system and its environment.

For the interaction with neighboring MCSs, we defined both an average influence factor and a maximum influence factor. To compute these, we again used a 5-degree by 5-degree window centered around the system. We weighted the influence of each neighboring system (see figure 3.5.b.) by its distance to the center (using $exp(-(d/d_0)^2)$, where d is the distance to the center, and $d_0 = 50km$), and then averaged them to obtain the average influence factor. For the maximum influence factor, we took the maximum value instead of the average.

These features can be calculated at each time step of the system's evolution, and we concatenate them into a single vector to provide as input to the model. To give the same weight to all input features, all the input variables are standardized by removing the mean and scaling to unit variance. We trained the three models (random forest, lasso, and neural network) by adding these features. Similar to the first experiment, we varied the time window of observation.

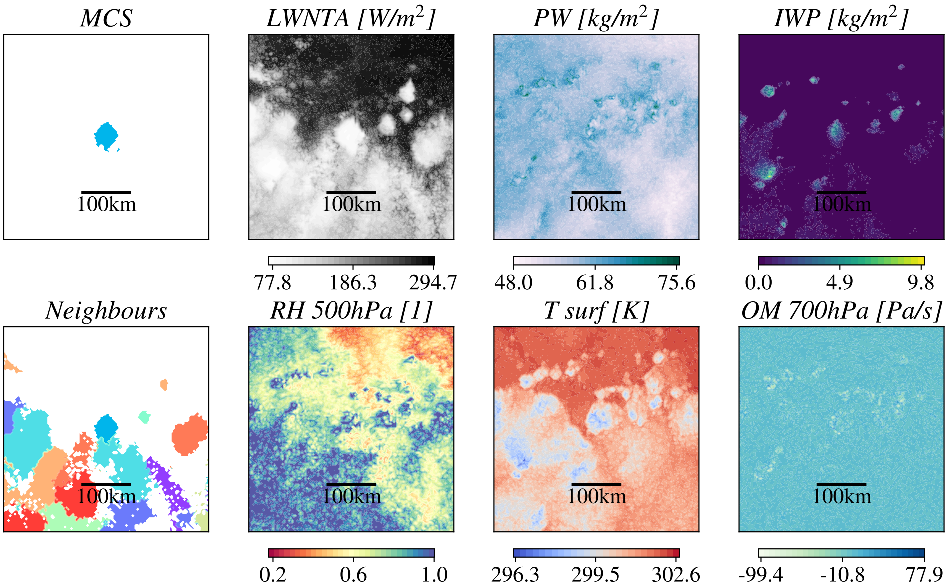

Figure 3.5: Example of considered physical fields for a given MCS at 1h of development : a. the system alone. b. its neighbors. c. long wave top of atmosphere. d. precipitable water. e. ice water path. f. relative humidity at 500hPa. g. surface temperature. g. vertical velocity at 700hPa.

3.3 Results: What controls the mature size of MCSs and why ?

By applying the previously described methodology, this section endeavors to address the three questions stated in the introduction. These questions are as follows: whether the evolution of the area growth rate allows for predicting the maximum area of an MCS, and if so, from when the prediction becomes reliable; how the evolution of other physical factors that characterize the system and its environment influences this prediction; and finally, what are the relevant variables that enable drawing conclusions about the future of the systems. These questions are tackled in sequence, each within a distinct subsection.

3.3.1 Prediction of maximal area with growth rate only

Focusing solely on the evolution of the growth rate of the area, we begin by examining the impact of the observation duration of the system on the final prediction of its maximum area. The figure 3.6.a. shows the evolution of the mean squared error and the R-Squared indice for each trained model (random forest, linear regression, and neural network) based on the observation period of the growth rate, ranging from 30 minutes up to 5 hours. Firstly, we can see that increasing the observation period improves the model performance, such that after 5 hours, they can predict the final area of the system with an average accuracy of 10 to 5 kilometers. However, since the systems on average last 7.5 hours and reach their maximum area around 3 hours, beyond this time point, the task becomes too easy, and the models detect it effortlessly. We note in passing that models easily incorporate this information and succeed in resolving it. Secondly, at the 1.5-hour mark, all three models predict the maximum system size with a score of approximately 0.7 and an average error of 20 kilometers. This experiment demonstrates a strong correlation between the evolution of the growth rate and the maximum area of the system.

Finally, it is observed that the three models exhibit similar performance within the first three hours. In the following of the paper we will only focus on random forest and multi-linear model that are both easier to interpret. The figure 3.6.a displays the error evaluation criteria across the entire dataset, we now further examine the prediction of these two models on a system-by-system basis.

On Figure 3.9 we can see four one-to-one diagrams of prediction and ground truth for the multi-linear model (top) and for the random forest model (bottom) for an observation period equal to 1h (left column) and 1.5h (on the right column). With only one hour, the linear model adopts the strategy to only predict the mean of small systems (the most representative) while the random-forest picks a value in a range around the mean. They both fail in providing a good prediction. However, with 30min more of data, we observed that both model improve their prediction for systems smaller than 100km : the scatter is sharper and follows the $y = x$ function. Multi linear model tends to overestimate system sizes with a systematic biais of 10-15km for these kind of systems (smaller than 100km). Random forest prediction for 1.5h of observation shows lower performance in the small system but is more able to predict large system evolution.

The figure 3.8a.c. displays the mean (dashed line) and deviation (error bar) of the mean-square error as a function of the maximal extension of MCSs. The multi-linear model (lasso, on the top) and the random forest (bottom) with the prediction based only the area growth rate (first column). The black line is the mean square error value for a constant prediction equal to the mean of the dataset, and it has the typical shape of a 'v'. For 30min (blue curve), we see that the prediction for both models follow closely the 'v-shape', assessing that models has a low degree of elaboration for the prediction. At 1h (turquoise curve) the error is lower but is still large (40%) for small (below 60km) and very large (beyond 160km). At 1h30 (orange curve), the error of the model is under the 'v-shaped' curve showing and is flattened. The error is reduced by 15% for very small systems (smaller than 60km) and reduced by 5% for systems as large as 140km. For 2h (red curve), the scatter is flattened near below 20%, supporting that the model has learned how

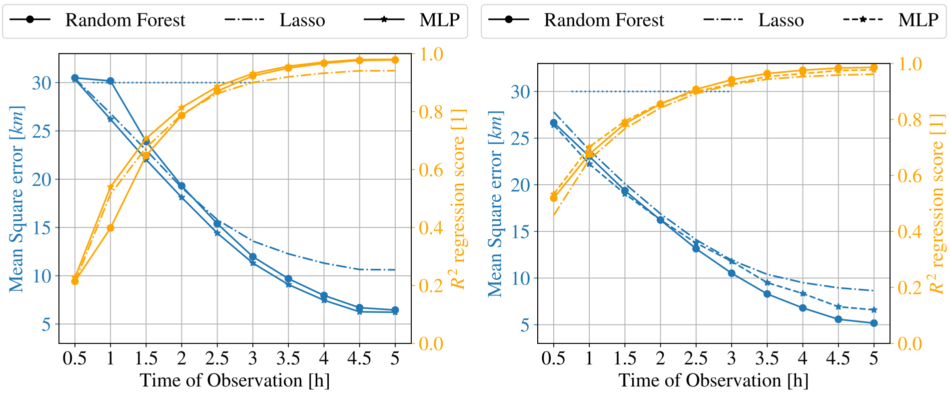

Figure 3.6: a. Evolution of R-Squared criteria in orange and Mean Square Error in blue for three machine learning models - Random Forest in solid dotted, Linear Regularized Regression in dashed and Multi Layer Perceptron in solid star trained on the evolution of the growth rate during a considered observed period. b. Same with additional features added, which include system shape, physical field mean and standard deviation, trajectory and neighbor influence.

to predict the maximal extension. We observe that the mean square error is increasing for larger systems, as well as the standard deviation, and this might be due to the nudging of statistically more likely system.

These results indicate that the explosiveness of the system partly determines its maximum size, which aligns with previous findings (Coniglio *et al.* 2010; Fritsch and Forbes 2001; McAnelly and Cotton 1986). This raises questions about whether the theoretical model is the primary factor for prediction or whether the score of 0.7 can be improved by adding features. We also can wonder which systems are sensitive to the input of new features and we also explore whether it is possible to predict the maximum system size from as early as one hour. To address these questions, we will examine the results of the second experiment in the next subsection.

3.3.2 Improving prediction with features engineering

In this part, we investigate the input value of providing additional features relative to the system and its environment during its early stage of development (described in section 3.2.3). The first results of this second experiment are shown in Figure 3.9. As before, The figure 3.6.b. shows the evolution of the mean squared error and the R-Squared indice for each trained model (random forest, linear regression, and neural network) based on the observation period of the growth rate and additional features, ranging from 30 minutes up to 5 hours. On this figure, we observe an increasing performance, as the observation period increases. Compared to the previous experiment, we found lower quantitative error from the initial 30 minutes, and after one hour, we achieve a Pearson-R coefficient of over 0.7. With 1.5 hours of observation,

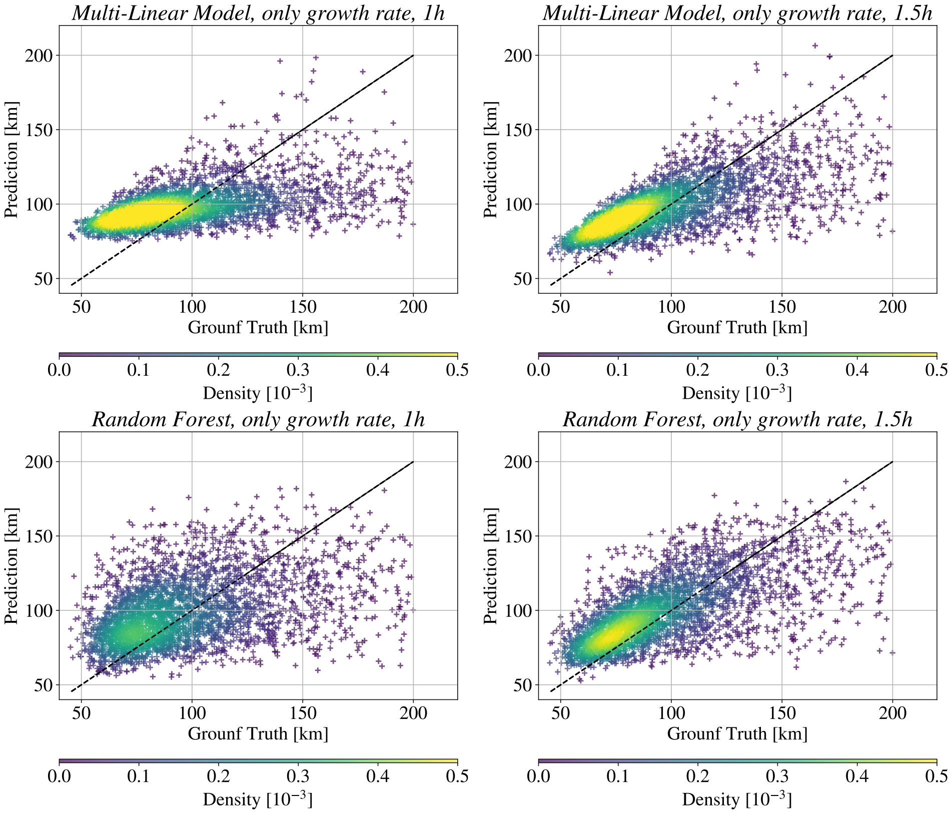

Figure 3.7: One-to-one diagrams for the prediction and the target for the multi-linear model (top) and random forest (bottom). On the right, the results are displayed for models trained over 1h with only the area growth rate evolution. On the left, the results are displayed for 1.5h of observation.

we reach a score of 0.8 and an average error of less than 20km. Here again, the three models exhibit similar performance within the first three hours. and we focus on the multilinear one and the random forest.

To gain further insight, we can specifically examine the prediction at 1 hour from the multilinear (top) and random forest (bottom) models with the added features (Figure 3.9.b.e.) compared to the prediction at 1 hour with only the growth rate (3.9.a.d.). We also display the one-to-one diagram with all features included and an observed period equal to 1.5h. We can see that adding the features has led to an improvement in prediction for both small systems (smaller than 100km) and larger systems (larger than 120km), whether it is for the lasso model or the random forest.

We can quantify these observation by looking at figure 3.8.c.d., which compare the evolution of the mean square error as a function of the maximal size of MCS for the lasso model (top) and random forest (bottom). On the right, we can see the experiment with all features, as a function of the time observation

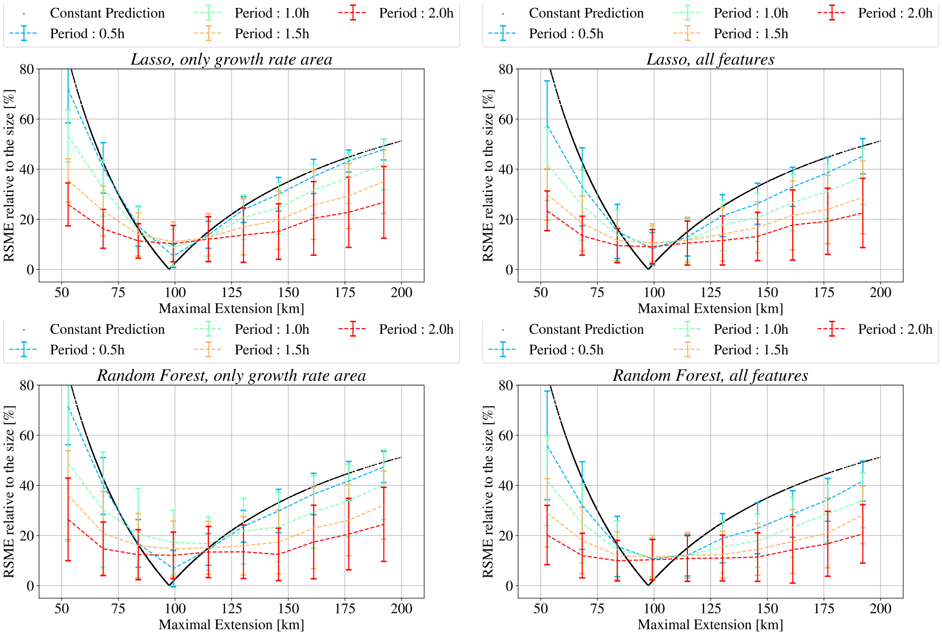

Figure 3.8: Mean (dashed line) and standard deviation (error bars) of the mean squared error from the multi-linear model (lasso, top panels) and random forest model (bottom panels) prediction as a function of the effective maximum size of MCSs (x axis). Blue curve corresponds to 30min of observation and the red one is after 2h of observation. The black line represents the mean squared error for a model that predicts constantly the mean of the set. On the left, only growth rate of area is considered to predict the final size whereas on the right models use additional features, including shape, physical fields, migration distance and neighboring systems influence

(colors curves). From the minimal time of observation, 30min (blue curve), the signal is better than a constant prediction, which means that it is less random. Overall, the models with all features included seem to get 30min in advance of the baseline with only the growth rate of area. We see that the random forest and the multilinear model show equivalent results.

At this stage, we can be confident that the future behavior of the MCS is well captured in the first hour of its development, and it is possible to predict its maximum extent with an average error of 20%. If the uncertainty on the prediction is larger for larger system, the performance of the model is not likely to depend on the size of MCSs. While we intuit that the growth rate plays a role in this prediction, we wonder about the other variables at play. Are the environment or the characteristics of the system itself more influential in this prediction?

3.3.3 Feature importance and dimensionality reduction

Focusing solely on the 1-hour prediction, we now seek to identify the features that contribute to predicting the maximum area. It is interesting to determine

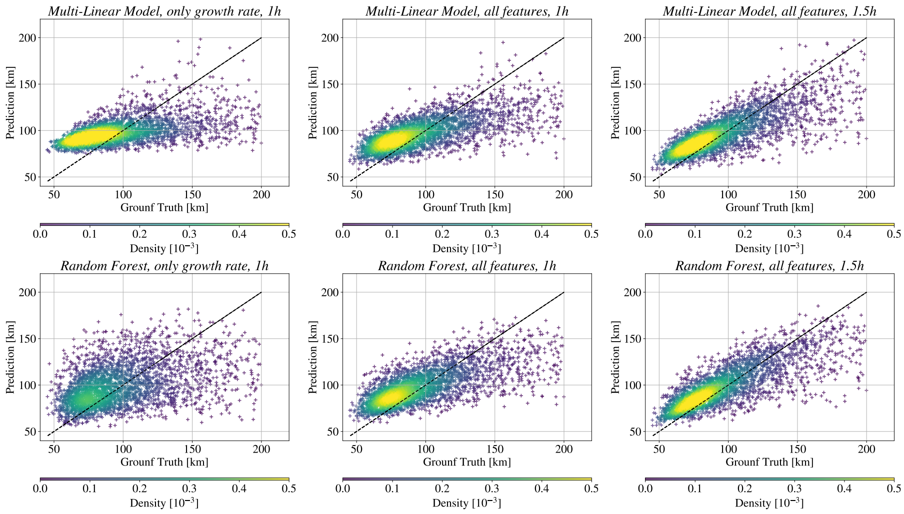

Figure 3.9: One-to-one diagrams for the prediction and the target for the multi-linear model (top) and random forest (bottom). Right: the results are displayed for models trained over 1h with only the growth rate evolution. Middle: added features, including shape, physical fields, migration distance and neighboring systems influence, are considered by the models improving the prediction and the observed period is 1h also. Left: all features included with an observed period of 1.5h.

if the linear and random forest models rely on the same variables or not. To find out, we can determine the important features for each model. For the linear model, we have the list of coefficients assigned to each variable. For the random forest, we can retrieve the average Gini index scores over all decision trees for each variable. Figure 3.10 shows the top 14 important variables for the linear model.

Although they do not appear in exactly the same order, we find the same variables for both models, which leads us to focus only on the multi-linear model (both models exhibit equivalent performance but this one is explicit). Among these variables, we find the growth rate, the standard deviation of the ice water path (IWP), the mean and standard deviation of the long-wave emitted solely by the system, the average and maximum interaction with neighboring MCSs, the vertical velocity at 700hPa, eccentricity, migration distance, and land mask variance. Beyond these variables, others do not significantly contribute to the prediction. These 14 variables form a representational basis for predicting the maximum area. They are not independent, and the correlation matrix is shown in Figure 3.11. For example, there is a high correlation between the mean and standard deviation of the IWP, as well as an expected link between IWP and the brightness temperature (LW).

Within these variables, we can identify three distinct categories. The first encompasses the leading-order variables, which include the growth rate of the area and the system's diameter. Using these two variables and following

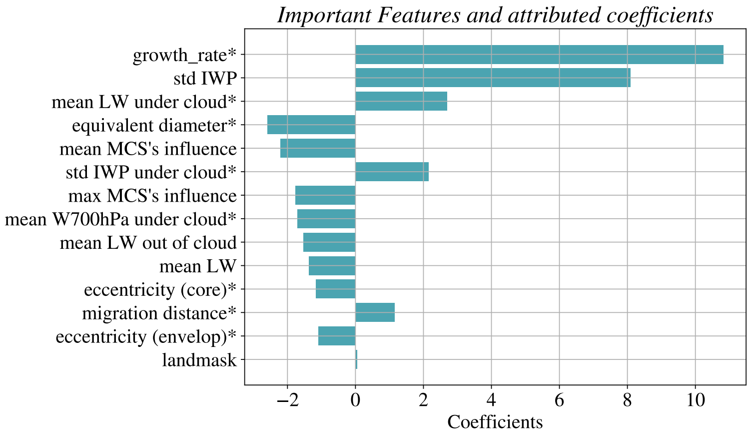

Figure 3.10: Coefficient optimized for the multi-linear model to solve the supervised task of predicting the maximal extension based on the first 1h evolution MCS's growth rate and development features. The coefficient are sorted with their absolute value. There are 14 features displayed, other features are considered negligeable (coefficient are below 0.01). These coefficients are applied to normalized input. Stars shows features associated with the system itself in opposition to its environment.

the simplified theoretical model, the model can estimate the maximum area of the system. The second category consists of variables that account for the strength of convection. For instance, the variance of the ice water path and the brightness temperature both indicate that the convective event has reached a critical altitude where condensates crystallize. This signifies a strong event that has significantly injected ice into the upper troposphere. This category helps anticipate the future size of the system, as strong convective events are more likely to persist over time and expand significantly, exceeding 140km. Conversely, if a system exhibits weak convective strength, it is unlikely to do so. The third and final category pertains to conditions conducive to aggregation, which is quantified by the influence of surrounding systems.

The capability of a statistical model to effectively predict the dimensions of Mesoscale Convective Systems (MCSs) suggests the preordained nature of MCS life cycles. On one hand, when all three categories exhibit significant strength, it implies that the system is likely to ultimately attain a substantial size. On the other hand, the relative importance of each category becomes less evident when only one of them is enhanced. In the subsequent portion of this study, we therefore delve into the influence of both the system's surrounding environment and the system itself on the likelihood of its enlargement. To achieve this, we integrate the elements pertaining to the system's intrinsic characteristics with those associated with its external milieu. While a clear demarcation between the system and its environment may not be readily discernible due to their interactive nature, where the system's manifestation

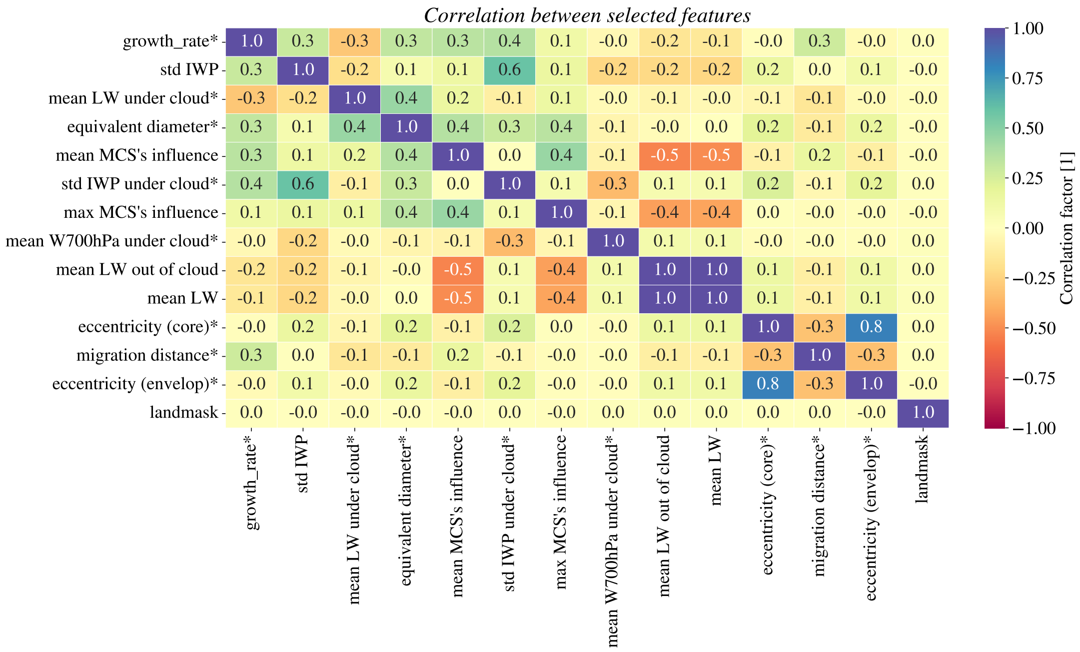

	growth_rate*	std IWP	mean LW under cloud*	equivalent diameter*	mean MCS's influence	std IWP under cloud*	max MCS's influence	mean W700hPa under cloud*	mean LW out of cloud	mean LW	eccentricity (core)*	migration distance*	eccentricity (envelop)*	landmask
growth_rate*	1.0	0.3	-0.3	0.3	0.3	0.4	0.1	-0.0	-0.2	-0.1	-0.0	0.3	-0.0	0.0
std IWP	0.3	1.0	-0.2	0.1	0.1	0.6	0.1	-0.2	-0.2	-0.2	0.2	0.0	0.1	-0.0
mean LW under cloud*	-0.3	-0.2	1.0	0.4	0.2	-0.1	0.1	-0.0	-0.1	-0.0	-0.1	-0.1	-0.0	-0.0
equivalent diameter*	0.3	0.1	0.4	1.0	0.4	0.3	0.4	-0.1	-0.0	0.0	0.2	-0.1	0.2	-0.0
mean MCS's influence	0.3	0.1	0.2	0.4	1.0	0.0	0.4	-0.1	-0.5	-0.5	-0.1	0.2	-0.1	-0.0
std IWP under cloud*	0.4	0.6	-0.1	0.3	0.0	1.0	0.1	-0.3	0.1	0.1	0.2	-0.1	0.2	0.0
max MCS's influence	0.1	0.1	0.1	0.4	0.4	0.1	1.0	-0.1	-0.4	-0.4	0.0	-0.0	-0.0	-0.0
mean W700hPa under cloud*	-0.0	-0.2	-0.0	-0.1	-0.1	-0.3	-0.1	1.0	0.1	0.1	-0.0	-0.0	-0.0	0.0
mean LW out of cloud	-0.2	-0.2	-0.1	-0.0	-0.5	0.1	-0.4	0.1	1.0	1.0	0.1	-0.1	0.1	0.0
mean LW	-0.1	-0.2	-0.0	0.0	-0.5	0.1	-0.4	0.1	1.0	1.0	0.1	-0.1	0.1	0.0
eccentricity (core)*	-0.0	0.2	-0.1	0.2	-0.1	0.2	0.0	-0.0	0.1	0.1	1.0	-0.3	0.8	0.0
migration distance*	0.3	0.0	-0.1	-0.1	0.2	-0.1	-0.0	-0.0	-0.1	-0.1	-0.3	1.0	-0.3	0.0
eccentricity (envelop)*	-0.0	0.1	-0.0	0.2	-0.1	0.2	-0.0	-0.0	0.1	0.1	0.8	-0.3	1.0	-0.0
landmask	0.0	-0.0	-0.0	-0.0	-0.0	0.0	-0.0	0.0	0.0	0.0	0.0	0.0	-0.0	1.0

Figure 3.11: Correlation matrix between the 14 selected features from the value of their coefficient. It shows that features are not independant and there might be redundant information. Stars shows features associated with the system itself in opposition to its environment.

is an outcome of environmental processes that reciprocally impact it, we define certain attributes such as shape indices, trajectory data, and statistical metrics just beneath the cloud as being indicative of the system, while other variables are indicative of the environment. Consequently, in Figure 3.12, we have projected the MCSs onto a two-dimensional graph, where the x-axis encapsulates the system's internal conditions, while the y-axis represents the external environmental conditions. To be more precise, we can express this as follows:

$$\mathcal{A}_{max} = \ell(f_1, f_2, ...f_n) \sim \ell(f_1, f_2, ...f_{15}) \sim c_1 f_1 + c_2 f_2 + ... + c_{15} f_{15} \tag{3.5}$$

where ℓ is the linear form trained on all features, f_i are the features in order of importance, and c_i are the associated coefficients. We can then separate the features into those related to the system and those related to the environment:

$$\mathcal{A}max = \sum_{i \in sys*} c_i f i + \sum_{j \in env} c_j f_j \tag{3.6}$$

We can calculate these two terms for all MCSs and observe how the maximum area of the system varies in this phase diagram. This result is shown in Figure

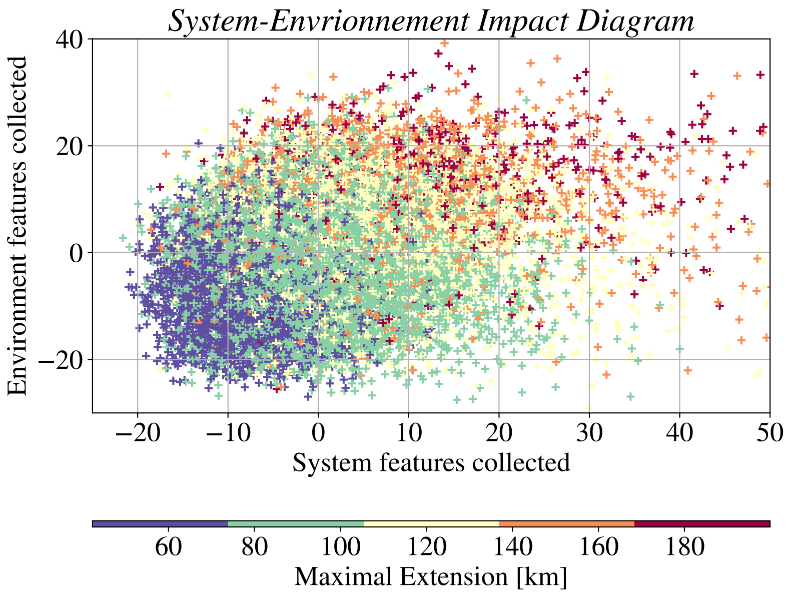

Figure 3.12: This figure represents the dependance of the final maximal extension of a given MCS with respect to the initial components from its own characteristics (example : eccentricity, migration distance) and the ones from its initial environment (example : std IWP, mean vertical velocity). It shows that the multi-linear regression is sensitive to both the environment and the system to predict the maximal extension.

3.12. The color of the markers represents the maximum area of the system. We observe that the maximum area increases linearly with the increase in both axes. For very low values of x, we see that the system will be small regardless of the value of y. Beyond this, both the environment and the system jointly contribute to the prediction.

3.4 Discussion

This study is unique in its combination of several novel tools, including high-resolution global simulations, a Lagrangian approach to mesoscale convective systems, and machine learning methods. Consequently, there have been few similar studies conducted in the literature, raising the question of whether the results described below are satisfactory or if better or worse outcomes could have been expected.

Previously, the hypothesis that the growth rate is strongly correlated with the mature state of the system has been documented in the literature without proposing a quantifiable score or relationship Coniglio *et al.* 2010; Fritsch and Forbes 2001; McAnelly and Cotton 1986. The use of machine learning models, with no a priori assumptions about the existing relationship between growth rate and maximal extension, appears to support this hypothesis. However, even with the addition of numerous variables, the predictive score reaches a plateau of 0.7, indicating that not all factors contributing to the relationship have been captured.

While the initial conditions of the system seem to play a significant role, contrasting them with the system's boundary conditions, i.e., an unexpected event occurring during the growth phase unrelated to the initial state, could provide valuable insights. Efforts were made to correlate the prediction error with variables such as distance traveled, presence of a coastline, or final system lifespan, but these attempts yielded no conclusive signals. Further investigation into this matter would be beneficial.

One interesting finding is that features based on both the MCS and its environment contribute to the prediction, showing that a given environment does not necessarily constrain the size of a system. This observation is particularly intriguing when considering systems developing within a cohort of mesoscale convective systems, where CAPE (Convective Available Potential Energy) appears to be consumed. Understanding the organization between mesoscale convective systems and the processes that allow a system to thrive among many others warrants further in-depth research.

Finally, the true contribution of employing machine learning models to address this problem raises questions. First and foremost, these models demonstrate a significant data exploration capability. Unlike correlation matrices and multivariate correlations, which are often challenging to interpret, machine learning models can uncover patterns that may not be apparent otherwise. Notably, the use of interpretable models has validated hypotheses previously formulated in the literature. The model comparison methodology employed has led to the construction of a multi-linear model; however, understanding the complex relationship between early development moments and maximal extension remains a challenge.

3.5 Conclusion

In our study, we investigated the relationship between mesoscale convective systems (MCSs) the factors in their early stage of development and their maximal size. We utilized high-resolution global simulations (SAM) from the DYAMOND project, coupled with the storm tracking algorithm TOOCAN. To predict the maximum area of MCSs, we compared three different machine learning models based on early development stages and initial environmental conditions of our systems. Interestingly, we found that the initial growth rate of the system strongly anticipated its eventual maximum area. By observing the growth rate within the first two hours of development, we achieved a regression score of 0.8, regardless of the system's final lifespan, but with only 1h the score is near 0.5. By incorporating additional features related to the shape, physical fields, trajectory, and influence of surrounding systems, we reduced the prediction timeframe to just one hour, achieving a regression score of 0.7. Several noteworthy factors emerged as significant contributors to prediction accuracy, including the presence of ice in the system's environment, proximity to surrounding systems, intensity of vertical velocity at 500hPa, and migration distance. Our study stands out due to the combination of novel tools, such as high-resolution global simulations, a Lagrangian approach, and machine learning methods, which are not commonly found in existing literature on this topic. While the hypothesis linking growth rate and system maturity has been suggested before, our study provides quantifiable evidence to support it. However, we acknowledge that the predictive score plateauing at 0.7 suggests that not all contributing factors have been fully captured yet. Throughout our investigation, we recognized the importance of considering both initial and boundary conditions to gain a comprehensive understanding of MCS behavior. Although we attempted to correlate prediction errors with various variables, we did not find conclusive signals, which highlights the need for further research in this area.

Part II

Implications

Chapter 4

What is the impact of Shear on Extremes Precipitation in Tropical Squall Lines?

Résumé en français

Comment l'intensité du cisaillement de vent de basse altitude influence les extrêmes de précipitation dans les lignes de grains tropicales ?

Ce chapitre a fait l'objet d'un article publié intitulé "Précipitations extrêmes dans les lignes de grains tropicales" rédigé par S. Abramian, C. Muller et C. Risi dans le Journal of Advances in Modeling Earth Systems en 2023. Son contenu reprend l'essentiel des résultats présentés ci-dessous.

Les lignes de grains sont fortement influencées par l'interaction entre le vent de cisaillement à basse altitude et les poches froides qui se forment à leur base. Au-delà d'une amplitude de cisaillement optimale, les lignes de grains ont tendance à s'orienter d'un certain angle par rapport à la direction du vent. Alors que les mécanismes sous-jacents à l'orientation des lignes de grains semblent être de mieux en mieux compris, des incertitudes persistent quant aux conséquences de cette orientation, notamment son impact sur les extrêmes de précipitation. En effet, une récente étude (Roca and Fiolleau 2020) montre que les systèmes convectifs de méso-échelle de durée prolongée, y compris les lignes de grains, jouent un rôle disproportionné dans les extrêmes de précipitations au sein des régions tropicales. En utilisant un modèle de résolution des nuages, nous avons simulé des lignes de grains dans des conditions d'équilibre radiatif convectif, couvrant des régimes dominés par le cisaillement (super optimal), équilibrés (optimal) et dominés par l'écoulement sortant (suboptimal). Nos résultats montrent que les extrêmes de précipitations dans les lignes de grains sont 40% plus intenses dans le cas d'un cisaillement optimal et demeurent supérieurs de 30% en régime superoptimal par rapport à un cas désorganisé. À l'aide d'un modèle théorique des extrêmes de précipitations (Muller and Takayabu 2020), nous montrons que les taux de condensation contrôlent l'amplification des événements de précipitations extrêmes dans les lignes de grains tropicales, principalement en raison de leur variation dans le flux vertical de masse (composante dynamique). La réduction de la dilution par entraînement explique la moitié de cette variation, en accord avec Mulholland *et al.* 2021. L'autre moitié est expliquée par l'augmentation de l'intensité de la vitesse à la base des nuages dans les lignes de grains optimales et superoptimales.

What is the impact of Shear on Extremes Precipitation in Tropical Squall Lines?

This chapter has been the subject of a published paper, untitled Extreme Precipitation in Tropical Squall Lines, S.Abramian, C.Muller & C.Risi, in Journal of Advances in Modeling Earth Systems, 2023. Its version follows closely from the content presented below.

Abstract

Squall lines are substantially influenced by the interaction of low-level shear with cold pools associated with convective downdrafts. Beyond an optimal shear amplitude, squall lines tend to orient themselves at an angle with respect to the low-level shear. While the mechanisms behind squall line orientation seem to be increasingly well understood, uncertainties remain on the implications of this orientation. Roca and Fiolleau 2020 show that long lived mesoscale convective systems, including squall lines, are disproportionately involved in rainfall extremes in the tropics. This article investigates the influence of the interaction between low-level shear and squall line outflow on squall line generated precipitation extrema in the tropics. Using a cloud resolving model, simulated squall lines in radiative convective equilibrium amid a shear-dominated regime (super optimal), a balanced regime (optimal), and an outflow dominated regime (suboptimal). Our results show that precipitation extremes in squall lines are 40% more intense in the case of optimal shear and remain 30% superior in the superoptimal regime relative to a disorganized case. With a theoretical scaling of precipitation extremes (Muller and Takayabu 2020), we show that the condensation rates control the amplification of precipitation extremes in tropical squall lines, mainly due to its change in vertical mass flux (dynamic component). The reduction of dilution by entrainment explains half of this change, consistent with Mulholland *et al.* 2021. The other half is explained by increased cloud-base velocity intensity in optimal and superoptimal squall lines.

Plain Language Summary

Squall lines are bands of clouds and thunderstorms spanning hundreds of kilometers, also called quasi-linear mesoscale convective systems. These systems are associated with extreme weather conditions, including extreme rainfall rates. To better understand and therefore predict this high impact phenomenon, this study investigates the physical processes leading to enhanced precipitation rates when clouds are organized into squall lines, using

idealized high-resolution simulations. Interestingly, the dynamics of squall lines, notably their wind structures, are found to play a key role in setting the intensity of extreme rainfall rates.

4.1 Introduction

In the tropics, the organization of deep convection at mesoscales (i.e. hundreds of kilometers) is ubiquitous, and these mesoscale convective systems (MCSs) plays a major role in producing heavy precipitation (Mathon *et al.* 2002; Nesbitt *et al.* 2006; Semie and Bony 2020). In particular, long-lived mesoscale convective systems, such as squall lines, contribute disproportionally to extreme tropical precipitation (Roca and Fiolleau 2020). Understanding the physical mechanisms behind the formation of these systems, as well as those that lead to rainfall extremes, is an important step toward improving prediction models for extreme events.

The key ingredient in squall line formation is the presence of cold pools under precipitating clouds. These are areas of cold air with a negative buoyancy anomaly, driven by partial evaporation of rain and concomitant latent cooling, and have been described to extend from 10 to 200 km in diameter (Romps and Jeevanjee 2016; Zuidema *et al.* 2017a). Cold pools propagate at the surface as gravity currents, and thus can promote upward motion and the development of new deep convective cells at their edge, as described in Tompkins 2001a, and can impact convective aggregation (Jensen *et al.* 2022; Muller and Bony 2015b).

Most of the time, squall lines arise when cold pools interact with a background vertical wind shear. Using idealized cloud-resolving simulations, Robe and Emanuel 2001 show that depending on the intensity of the imposed shear, squall lines tend to orient themselves with respect to the direction of the wind shear. For weak to medium intensity of shear, squall lines are perpendicular to the wind shear direction. For larger shear, squall lines are oriented at an angle with respect to the shear. The orientation aims at restoring a vorticity balance between the environmental shear and the cold pool propagation, as predicted by Bryan and Rotunno 2014; Robe and Emanuel 2001; Rotunno *et al.* 1988, and verified in Abramian *et al.* 2022. The existence of an optimal balance between shear and cold pools thus makes it possible to define three regimes of squall line development: the suboptimal regime, where the environmental shear is weaker than the shear induced by cold pool spreading; the optimal regime, where equilibrium between environmental shear and cold pools is reached; and the superoptimal regime, where the shear wins, and where the squall lines orient themselves at an angle to the shear, so that the shear projected perpendicular to the squall line is at equilibrium with cold pools (see figure 4.1 adapted from Abramian *et al.* 2022). A recent study (Mulholland *et al.* 2021) has also shown that entrainment is reduced in the optimal shear regime, leading to more buoyant and intense updrafts. However, the implication of these regimes for extreme precipitation rates remains poorly documented. A natural question that we address here is then: Are precipitation extemes intensified in suboptimal, optimal or superoptimal squall lines, and if so, why?

More precisely, to answer these questions, a theoretical scaling for precipitation extremes is used, first introduced in Betts 1987 and O'Gorman and Schneider 2009a, and refined to link it to microphysics in Muller *et al.* 2011; Muller and Takayabu 2020. We draw the attention of the reader on that we focus on small-scale local extreme precipitation that depends on local processes, rather than mean precipitation which generally depends on larger scale and energy budgets (O'Gorman and Muller 2010). We expect organization to impact both short-time hourly and long-time daily precipitation extremes (Bao and Sherwood 2019; Da Silva *et al.* 2021), but these can come from different physical processes. This study focuses on hourly precipitation. The aforementioned scaling allows one to decompose changes in precipitation extremes into three contributions: a thermodynamic contribution related to water vapor, a dynamic contribution related to vertical mass flux in updrafts, and a microphysical contribution related to precipitation efficiency.

With warming, idealized simulations often predict an increase of precipitation extremes following the thermodynamic component in disorganized convection (Muller *et al.* 2011; Muller and Takayabu 2020; Romps 2011). But the thermodynamic contribution is not always the dominant term when ice and mixed-phase processes are important (Singh and O'Gorman 2014) or when comparing disorganized and organized convection at a given temperature. Recent works (Bao and Sherwood 2019; Da Silva *et al.* 2021) show that the microphysical contribution may contribute significantly to the increase of extreme precipitation rates in self-aggregated convection relative to non-aggregated convection (Muller *et al.* 2022). The objective here is to apply this methodology on a set of simulations of squall lines in a cloud-resolving model, and attempt to answer three questions:

- How do the precipitation extremes evolve with the suboptimal, optimal and superoptimal organization of squall lines? Notably, in the superoptimal regime, how does the orientation of squall lines impact extreme rainfall rates?
- Which contribution mainly explains the response of extreme rainfall rates to squall line organization? Is it the thermodynamic, the dynamic, or the microphysical contribution?
- What physical mechanisms control the behavior of these contributions?

The next section (§4.2) describes the cloud-resolving model and introduce the theoretical scaling. Extreme precipitation rates, as well as the thermodynamic, dynamic and microphysical contributions, in the suboptimal, optimal and superoptimal squall lines are analyzed in §4.3. We then provide a physical interpretation for all these contribution changes with increasing shear in §4.4. Conclusions, as well as key implications of our results, are discussed in §4.5.

4.2 Methodology

In this section, we describe the model and simulations (§ 4.2.1), introduce the theoretical scaling used to analyze contributions to precipitation extremes (§ 4.2.2), and describe in detail how extremes and contributions are computed from the simulations outputs (§ 4.2.3).

4.2.1 Model and Simulations

The simulations use the Cloud-Resolving Model (CRM) SAM (Khairoutdinov and Randall 2003). The setup is the same as Abramian *et al.* 2022, namely the resolution is 1 km in both horizontal directions[1], and gradually increases in the vertical direction from 80 m near the surface to 400 m above 6 km. The 3D domain is doubly periodic in x and y with 128 km side, and the upper third of the domain (18–27 km) has a sponge layer to absorb gravity waves. Therefore, only the troposphere is simulated in our experiments. We neglect the Earth rotation (a reasonable approximation for mesoscales in the tropics), and there is no diurnal cycle; we use an imposed radiative profile constant in space and time, obtained as the mean equilibrium profile of a shear-free simulation (which used the radiation code from the National Center for Atmospheric Research (NCAR) Community Atmosphere Model (CAM)). The sea surface temperature is fixed and equal to a value of 300 K. The advection scheme used is MPDATA (following Abramian *et al.* 2022). All simulations are run to radiative-convective equilibrium (reached in about 30 days), after which we start our analysis, from day 30 to day 35, with hourly outputs (all variables used in this paper are hourly mean outputs).

Following Abramian *et al.* 2022; Muller 2013a, the convection is organized into squall lines by imposing a background vertical wind shear profile in the x-direction, with a background wind decreasing linearly from U_{sfc} at the surface to 0 m/s at $z = 1$ km. It is imposed by relaxing the domain-mean wind to the target profile with a time scale of two hours. We perform nine simulations, with different shear strengths, that is, with different surface

---

[1] Although 1 km may not be sufficient to resolve details of cold pools, it is sufficient to capture the interaction of cold pools with shear, and the generation of squall lines Abramian *et al.* 2022; Muller 2013a. A recent study **weisman2022simulations** shows that 1 km resolution well captures reflectivity characteristics and the smaller leading-line mesoscale vortices compared to 3 km.

wind U_{sfc} from 0 (no shear) to 20 m/s, with 2.5 m/s increments. The range of shear strength allows three regimes of development for squall lines (again following Abramian *et al.* 2022; Muller 2013a) and is supported by the estimation of the optimal shear in Rotunno *et al.* 1988 (see Section 4. Eq. 9).The case without shear $U_{sfc} = 0$ m/s is very similar to $U_{sfc} = 2.5$ m/s, so we do not discuss it further and define 2.5 m/s as our control case. To avoid an impact of this imposed surface wind on surface fluxes, the domain-mean surface wind is removed before computing surface fluxes (see Supplementary § S1 for more details on the simulations and settings).

Figure 4.1 shows three of our simulations ($U_{sfc} = 2.5$ m/s, $U_{sfc} = 10$ m/s and $U_{sfc} = 20$ m/s). On the top, we can see 3D graphs representing buoyancy fields on the ground and clouds in white. On the bottom, the 2D graphs also display the buoyancy fields, with the vertical velocity at 500 hPa exceeding 2 m/s in white. In $U_{sfc} = 2.5$ m/s, no organization is observed; as mentioned above, this constitutes our control case. For U=10 m/s we observe strong squall lines, with a typical horizontal scale of 100 km. Consistent with Abramian *et al.* 2022, the squall lines are typically perpendicular to the wind direction for $U_{sfc} = 10$ m/s (angle $a = 0$ with respect to the y-axis), while squall lines are oriented at an angle $a > 0$ for $U_{sfc} = 20$ m/s. This angle preserves the normal shear (orange arrow figure 4.1.f) near optimal value, i.e. such that $U_{sfc} \cos(a) = U_{sfc,opt}$.

4.2.2 Theoretical scaling for Precipitation

As mentioned in the introduction, our study of extreme precipitation in squall lines is based on a theoretical scaling that allows to decompose extreme precipitation into three contributions: a thermodynamic contribution related to water vapor, a dynamic contribution related to the vertical mass flux in extreme updrafts and a microphysical contribution related to the precipitation efficiency. The latter is defined as the fraction of condensation in a convective updraft that finally reaches the surface as precipitation. It is generally less than one because some of the condensates are either advected away as clouds, or evaporate as they fall into the unsaturated air below the cloud before reaching the surface. Each of these three contributions is subject to different theoretical constraints, and may respond differently to to the imposed shear cases of squall lines. An overview of the origin of this theoretical scale is provided in Muller and Takayabu 2020. Although it was first derived using an energy budget, this scaling can be interpreted in terms of the water budget. This allows, under certain approximations (notably the weak horizontal temperature gradient), to relate the precipitation to the condensation rate, with a precipitation efficiency factor, which as mentioned above represents the fraction of condensates that reach the ground as surface precipitation. This scaling can be written as follows

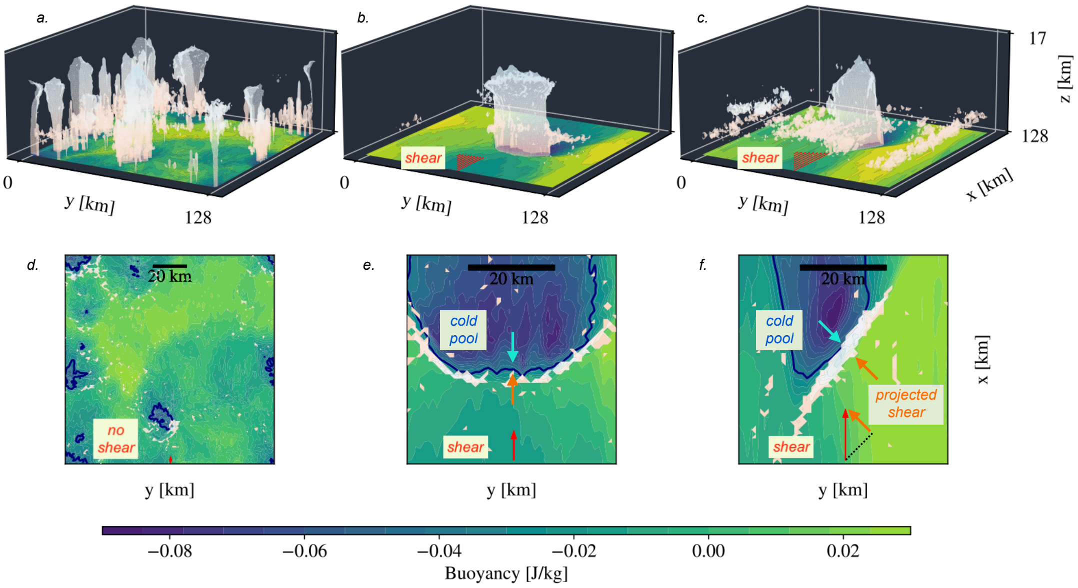

Figure 4.1: Top. 3D graphs for three simulation cases (U_{sfc}=2.5 m/s, U_{sfc}=10 m/s and U_{sfc}=20 m/s), the buoyancy field is displayed on the ground (integrated to the first atmospheric level) and clouds are in white. The imposed wind is represented by red arrows. As the vertical shear of this horizontal wind increases, the simulations move from a disorganized case to an optimal and then superoptimal squall line. Bottom. Buoyancy field surrounded by high value of mid-tropospheric vertical velocity in white, zoomed near a convective zone to highlight the interaction between wind shear and cold pool spreading at the edge of cold pools in the optimal and superoptimal regimes.

$$P \sim \varepsilon C \sim \varepsilon \int_0^{H_t} \rho w \frac{-\partial q_{sat}}{\partial z} dz \tag{4.1}$$

where P is the precipitation, C is the condensation rate, ε the precipitation efficiency, H_t the top of the troposphere (because the vertical domains only extends up to 18 km), ρ the density, w the vertical velocity, q_{sat} the saturated specific humidity and z the altitude. Following Da Silva *et al.* 2021, the precipitation efficiency is estimated as a residual, and is thus computed as the quotient of the condensation rates over the precipitation rates. More generally, the detailed computation of each term in the simulations will be described in the next section § 4.2.3. But before, we describe how this theoretical scaling is used to compare precipitation extremes between different simulations with different shears.

Indeed, in our study, we are more specifically addressing the variations of precipitation extremes P in squall lines compared to an unorganized case $\overline{P}$ ($U_{sfc} = 2.5$ m/s). We therefore apply the scaling to the relative change in precipitation

$$\frac{\Delta P}{\overline{P}} = \frac{P - \overline{P}}{\overline{P}},$$

and similarly, $\frac{\Delta \varepsilon}{\overline{\varepsilon}}$ and $\frac{\Delta C}{\overline{C}}$ denote relative changes with respect to the unorganized case $U_{sfc} = 2.5$ m/s. Similarly to a logarithmic derivative leads to :

$$\frac{\Delta P}{\overline{P}} = \frac{\Delta \varepsilon}{\overline{\varepsilon}} + \frac{\Delta C}{\overline{C}} + \frac{\Delta \varepsilon}{\overline{\varepsilon}} \frac{\Delta C}{\overline{C}}. \tag{4.2}$$

Neglecting the second order terms, which are much smaller, finally gives

$$\frac{\Delta P}{\overline{P}} \sim \frac{\Delta \varepsilon}{\overline{\varepsilon}} + \frac{\Delta C}{\overline{C}}. \tag{4.3}$$

At this stage, the condensation rate can be split into two contributions. Indeed, a variation of the condensation rate can be explained either by a stronger vertical advection leading to more condensation for a given saturation profile, this is the dynamic contribution; or by saturation decreasing faster also producing more condensation for a given advection. This further decomposition can be written as

$$\frac{\Delta C}{\overline{C}} \sim \underbrace{\frac{1}{\overline{C}} \int_0^{H_t} \Delta \rho w \frac{-\partial \overline{q_{sat}}}{\partial z} dz}_{dynamic} + \underbrace{\frac{1}{\overline{C}} \int_0^{H_t} \overline{\rho w} \Delta \frac{-\partial q_{sat}}{\partial z} dz}_{thermodynamic} \tag{4.4}$$

where overbars denote values of the unorganized case and Δ is the difference compared to the control case. We check that second order terms can be neglected here, which is consistent numerically.

Finally,

$$\frac{\Delta P}{\overline{P}} \sim \frac{\Delta \varepsilon}{\overline{\varepsilon}} + \underbrace{\frac{1}{\overline{C}} \int_0^{H_t} \Delta \rho w \frac{-\partial \overline{q_{sat}}}{\partial z} dz}_{\frac{\Delta dyn}{\overline{C}}} + \underbrace{\frac{1}{\overline{C}} \int_0^{H_t} \overline{\rho w} \Delta \frac{-\partial q_{sat}}{\partial z} dz}_{\frac{\Delta therm}{\overline{C}}}. \tag{4.5}$$

Hereafter, the relative dynamic and thermodynamic contributions will be respectively called $\frac{\Delta dyn}{\overline{C}}$ and $\frac{\Delta therm}{\overline{C}}$.

4.2.3 Evaluation of extremes of precipitation, condensation and other contributions in simulations

In our study, we define extreme precipitation as the tails of the distribution of hourly mean precipitation (including zeros). More precisely we investigate the response of high precipitation percentiles to the increasing shear. We investigate various percentiles around the 99.9^{th} precipitation percentile (extreme of hourly precipitation occuring 0.1% of the time), and whether this extreme rain rate increases with the squall line organization, and if so why.

One difficulty in evaluating the various terms of equation 4.5 is that different extremes occur at different times and locations during the cloud life cycle. Indeed, one expects maximum condensation early in the life cycle of a cloud, and maximum precipitation at the end of the life cycle, as condensation leads to precipitation. To avoid this problem, we follow Da Silva *et al.* 2021; Singh and O'Gorman 2014 and compute the terms not at a given point in space and time, but at a fixed percentile rank. In other words, we compute precipitation extremes at a given precipitation percentile, and condensation extremes at a given condensation percentile, without regard to space and time. The precipitation efficiency is deduced from these two extremes and is thus interpreted as an effective efficiency defined as the fraction of extreme condensation that become extreme precipitation on the ground,

$$(\frac{\Delta P}{\overline{P}})^{99.9} \sim (\frac{\Delta \varepsilon}{\overline{\varepsilon}})^{99.9} + (\frac{\Delta C}{\overline{C}})^{99.9}. \tag{4.6}$$

The underlying assumption is that an extreme in condensation leads to an extreme in precipitation of similar percentile rank, which is equivalent to an ergodicity hypothesis. To motivate this hypothesis, figure 4.2 shows the precipitable water field of the simulation case $U_{sfc} = 10$ m/s for three successive time steps. We observe a squall line developing perpendicular to the wind. The red crosses represent the condensation extremes, i.e. the points for which condensation is greater than 99.9^{th} percentile, and the green crosses represent the precipitation extremes. We notice 1) the extremes of precipitation and condensation do not coincide in space at each time step, and 2) the extremes of condensation anticipate the extremes of rainfall, and thus account for the same convective event. This figure shows that if we consider the locations of condensation and precipitation extremes, everything happens as if we were following a cell through its life cycle. The theoretical scaling therefore remains consistent at each percentile rank. A more detailed statistical analysis (Supplementary § S2 and figure S1) confirms that for high percentiles, precipitation and condensation are strongly correlated in space and time.

Extremes of condensation are decomposed according to equation 4.33 into a dynamic and a thermodynamic contribution, both evaluated at extremes of

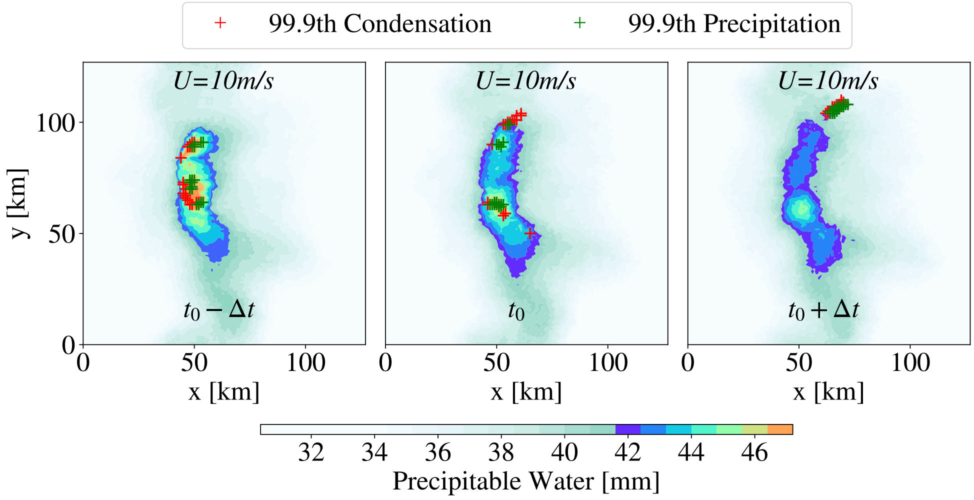

Figure 4.2: Precipitable Water field of an optimal squall line ($U_{sfc} = 10$ m/s) displayed for three consecutive time steps (hourly). The red crosses are the extremes of condensation extremes (taken at 99.9$^{\text{th}}$) and green ones are the precipitation extremes (at 99.9$^{\text{th}}$ too). This figure underlines 1) extremes of condensation and precipitation are shifted in time and space; 2) condensation extremes anticipate precipitation extremes.

condensation following Da Silva *et al.* 2021; in other words, the vertical mass flux and saturation specific humidity profiles are computed at condensation extremes. Similarly the precipitation efficiency will be decomposed into a term involving the conversion of non precipitating cloud condensate into precipitating condensate and a term involving the fraction of the precipitating condensate that arrives at the surface as precipitation (α and β respectively in equation 4.9, the physical interpretation of these terms will be discussed in more detail in section 4.4.2) following Lutsko and Cronin 2018. This computation involves the microphysical flux Q_p of non precipitating condensates into precipitating ones (unit of kg m^{-2} s^{-1}). This variable is directly output from the model at the same frequency as precipitation and other variables (hourly mean outputs). Each term is evaluated at its own extreme i.e. P, C and Q_p are evaluated at the 99.9$^{\text{th}}$ percentile of P, C and Q_p respectively. Here again we use the hypothesis that consequential events in the life cycle of a convective cell are linked together in their own extreme rank of percentile (an extreme of condensation C leads to an extreme of precipitating condensate production Q_p, which itself leads to an extreme of surface precipitation P).

4.3 Results: how do precipitation extremes evolve with the shear in tropical squall lines? Which contributions of the scaling explain this change?

4.3.1 Evolution of precipitation extremes

Figure 4.3 shows results from our different simulations with increasing wind shear. As noted in the introduction and in 4.2.1, the orientation of the squall lines aims at restoring the balance between cold pool and the imposed shear perpendicular to the squall lines (see figure 4.1). Consistently, we recover the three regimes of Abramian *et al.* 2022

In the suboptimal regime (green), the vorticity of the imposed shear is weaker than that of cold pools. The squall line is perpendicular to the imposed shear (angle $a = 0$ between the squall line and the y axis), which optimizes the projected shear. The projected shear thus increases linearly until the optimal case. In the optimal regime (blue, around $U_{sfc,opt} \approx 11$ m/s in our simulations; we note in passing that the projected shear is slightly weaker than the target shear to which we relax the mean wind profile. Indeed, the domain-mean wind is slightly weaker than the imposed target wind profile due to drag and subgrid-scale momentum flux, which oppose the relaxation towards the target profile), the incoming shear balances cold pools. In the superoptimal regime (yellow), the shear is higher than the optimal value, and the lines orient themselves at an angle $a > 0$ in order to reduce the projected incoming shear $U_{sfc}\cos(a)$. This angle conserves the projected shear near optimal value, so that the projected shear remains approximately constant above $U_{sfc}\cos(a) = U_{sfc,opt}$.

If we superimpose the extreme precipitation - 99.9th percentile of precipitation - for each case, we obtain the green curve. In the disorganised case, $U_{sfc} = 2.5$ m/s, the extreme is 450 mm/day and increases almost linearly as the shear increases, reaching 650 mm/day in the optimal regime. In the superoptimal regime, the rainfall extreme is observed to be constant around 575 mm/day, slightly below the rate at optimal shear.

Panel b. shows the change of precipitation extremes relative to the control case for different percentiles (indicated by the colorbar) as a function of the shear. Quantitatively, there is an increase in extreme precipitation of about $30 - 40\%$ in the optimal regime relative to the control case, and it declines in the superoptimal regime but is maintained around $20 - 30\%$, again relative to the control case. The signal is robust to the chosen definition of extreme; from now on, we will only show results at the 99.9th percentile.

The focus of the present study shall be to understand what controls this evolution of precipitation extremes with squall lines organization, and what physical mechanisms are involved.

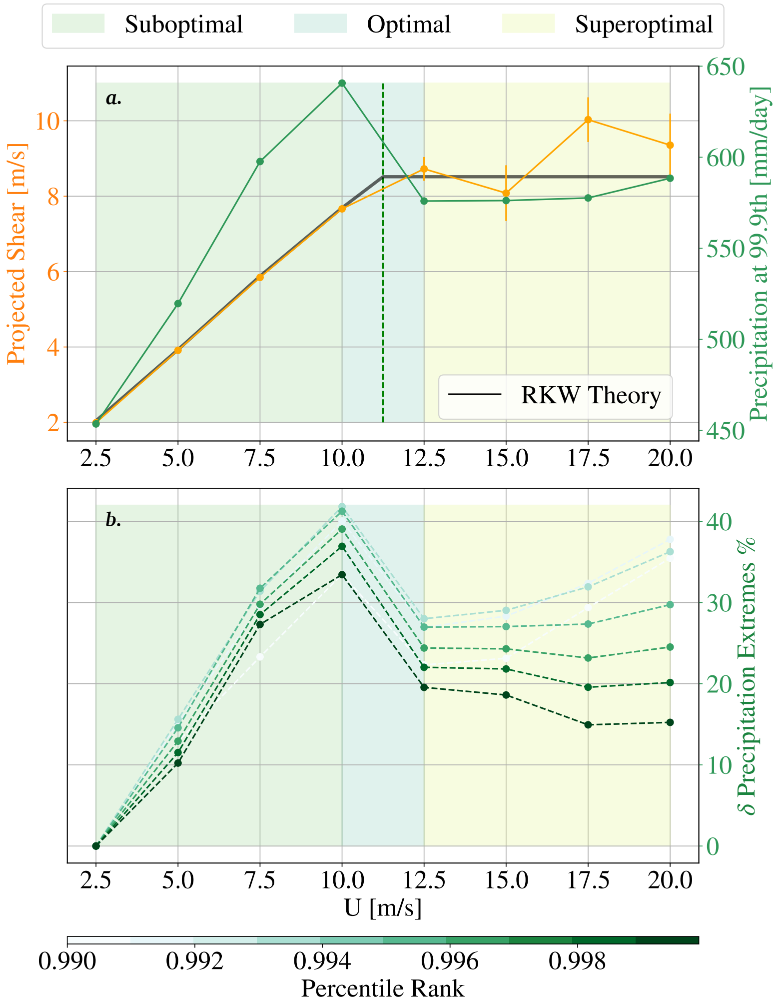

Figure 4.3: a. Superposition of the incoming wind shear on squall lines for all simulation cases (orange, near-surface wind projected in the direction perpendicular to the squall line) and the respective extreme precipitation rate taken at 99.9$^{\text{th}}$ percentile (green). The black line represents the theoretical value of the projected wind (described in Rotunno *et al.* 1988) and we observe a very good agreement with the measured one, consistent with Abramian *et al.* 2022. In dashed green the optimal case is highlighted, around 11 m/s, and allows to identify the three regimes of development : sub-optimal (light green), the optimal (light blue) and the superoptimal (light yellow). This figure demonstrates the sensitivity of extreme precipitation to the regime of squall lines. b. Changes in precipitation per percentile rank, from 99$^{\text{th}}$ to 99.99$^{\text{th}}$. Values of extremes are calculated relative to the control case ($U_{sfc} = 2.5$ m/s). Extremes increase by 30% to 40% in the optimal case, and remain 20% to 30% higher in the superoptimal case. The trend of extremes with squall lines regime is robust to the percentile.

4.3.2 Results of the scaling

Figure 4.4 shows the various contributions from the scaling (equations 4.33 and 4.5) in each simulation. We have displayed the value of the extremes (99.9%) of precipitation for each simulation in green, the extremes of condensation in red and the efficiency of precipitation in blue. The thermodynamic and dynamic contributions are shown in light and dark orange respectively (both taken at extreme condensation columns as described in § 4.2.3).

This decomposition indicates for instance that for the case $U_{sfc} = 10$ m/s, the increase in precipitation extremes of 40% is due to an increase in condensation of 60% and a decrease in precipitation efficiency of about 15% (the residual difference is due to higher order terms neglected in equation 4.2). Overall, in all the simulations, the variations in the condensation rate explain the variations in precipitation. Focusing on the two contributions, dynamic and thermodynamic, we notice, still for the case $U_{sfc} = 10$ m/s, that when condensation increases by 60%, this is due to an increase of 50% in dynamics, and 10% in thermodynamics. More generally, in all the simulations, the dominant contribution to changes in extreme precipitation is the dynamic contribution. In the next section § 4.4, we investigate the physical processes at play.

4.4 What physical mechanisms control the behavior of these contributions?

4.4.1 Dynamics driven by cloud-base updraft velocity

Figure 4.5.a. shows the mass flux profiles at condensation extremes. In this figure, we note that as the shear increases, the profile changes from a parabolic shape, for $U_{sfc} = 2.5$ m/s, to a so-called "bottom heavy" profile. Quantitatively, the value of w in the low troposphere, for instance at 2 km, increases until the 10 m/s case, and then decreases. This trend is maintained throughout the lower layer, and in particular at the top of the boundary layer (around 1km).

In order to further investigate vertical velocities, we look at the change of atmospheric instability as measured by CAPE. Figure 4.5.b shows the temperature profiles of a parcel in an adiabatic lift (solid lines), as well as the temperature of the environment (dashed line) on a SkewT diagram. These profiles are calculated at the extremes of the pointwise, vertically-integrated CAPE, because we assume that extremes of condensation rates follow extremes of CAPE (see Supplementary § S3 for details of the CAPE computation). In this diagram, the CAPE is read as the area between the parcel and the environmental profile, since we neglect virtual effect.

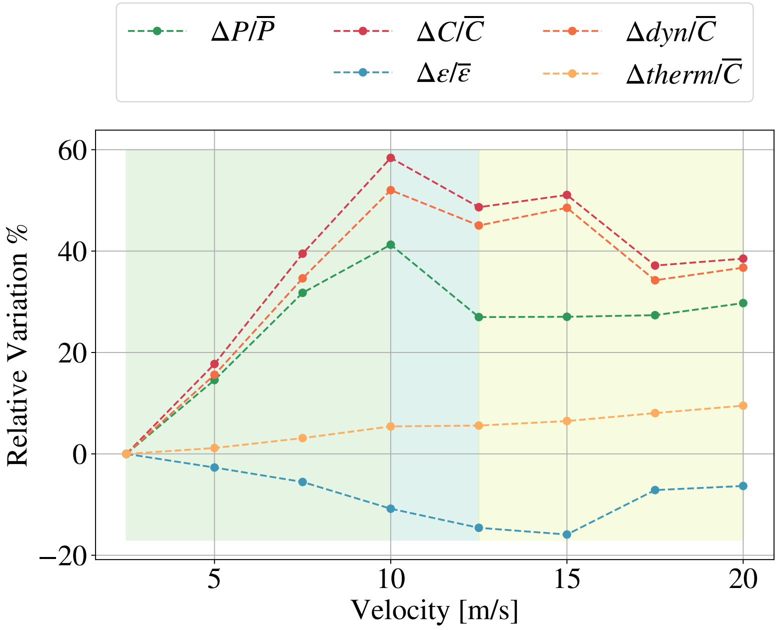

Figure 4.4: Relative sensitivity to shear of precipitation extremes ($\frac{\Delta P}{P}$) and its decomposition into dynamic ($\frac{\Delta dyn}{\overline{C}}$), thermodynamic ($\frac{\Delta thermo}{\overline{C}}$) and microphysical ($\frac{\Delta\varepsilon}{\overline{\varepsilon}}$) components using the scaling for all simulations (see equation 4.5). The 99.9$^{\text{th}}$ percentile of precipitation is in dashed green, the 99.9$^{\text{th}}$ percentile of condensation rate is in dashed red, itself decomposed into the dynamic (orange) and thermodynamic (yellow) contributions; the microphysics contribution is in dashed blue. The values of extremes are displayed relative to the control case ($U_{sfc} = 2.5$ m/s). For example, in the optimal case, $U_{sfc} = 10$ m/s, the increase of 40% of precipitation is due to an increase in 60% in condensation, of which 55% of dynamics and 5% of thermodynamics, and by a decrease of 15% in microphysics. Over all cases, the change in precipitation are due first to dynamics, then to microphysics and eventually to thermodynamics.

CAPE seems to be insensitive to shear, since both the domain and parcel warm at a similar rate as the shear is increased, keeping the CAPE constant between cases (see figure 4.5.b.). We note in passing that organization is accompagnied by warming, consistent with Bretherton *et al.* 2005; Muller and Held 2012. This suggests that the increased dynamic contribution with shear is not related to atmospheric instability as measured by CAPE (acceleration of the parcel as it moves upward). However, what can indeed play a non negligible role is the fraction of conversion of CAPE into kinetic energy, which can vary with imposed shear, and depends on entrainment processes. This quantity can be estimated as a residual of the acceleration of an undiluted parcel ascent and the vertical velocity profiles from our simulation outputs (captured by the conversion factor λ in equation 4.7 below). Qualitatively, we expect the conversion fraction to increase with organization, since the entrained air in organized convection is moister and has a lower dilution effect, as has been described in the literature (Becker *et al.* 2018; Feng *et al.* 2015; Mulholland *et al.* 2021). On the basis of these studies, entrainment is expected to play a dominant role in modifying the conversion rate, but other processes may also contribute, such as condensate loading. Further work is needed to fully assess these effects.

We argue that the change in the dynamics are not only due to the change in CAPE conversion, but may also be related to the cloud-base velocity (initial velocity of the upward moving parcel at the top of the boundary layer). Intuitively, this is also consistent with the bottom heavy profiles of mass flux in figure 4.5. We further investigate this assumption with a conservation of energy, written as

$$w^2(z) = w_{cb}^2 + 2\lambda(z)CAPE(z) \tag{4.7}$$

where $w(z)$ denotes the vertical velocity at altitude z, w_{cb} is the cloud-base ($\sim$ 1 km) updraft velocity, CAPE(z) the convective available potential energy between the first level of the atmosphere and the level z and $\lambda(z)$ the conversion fraction, computed as a residual. (This budget implicitly neglects the contributions to vertical velocity from viscosity and from pressure perturbations.) This equation can be interpreted as the decomposition into a cloud-base initial updraft velocity, and a term that reflects the acceleration above cloud-base due to the instability of the atmosphere. Taking differential with respect to the control case yields

$$\Delta w = \underbrace{\frac{\overline{w_{cb}}\Delta w_{cb}}{\overline{w}}}_{\Delta cb/\overline{w}} + \underbrace{\frac{\overline{\lambda}\Delta CAPE}{\overline{w}}}_{\Delta pe/\overline{w}} + \underbrace{\frac{\overline{CAPE}\Delta\lambda}{\overline{w}}}_{\Delta ent/\overline{w}}, \tag{4.8}$$

where Δ refers to a difference to the control case (2.5m/s), overlined quantities are taken at the control case, w, λ are defined above, and cb, pe, ent correspond to cloud-base, potential energy and entrainment respectively. We calculate this decomposition to quantify the role of cloud-base updraft vertical velocity, CAPE and dilution in changing the dynamics (using equation 4.8 in the integral of the dynamical term in equation 4.5). The cloud-base updraft velocity w_{cb} is computed as the vertical velocity at 1 km at locations of extreme condensation (figure 4.5.a.). Its increase, as well as the other terms in equation 4.8, are quantified in figure 4.6.

The evolution of the dynamic contribution is in dashed dark orange (repeated from figure 4.4 to ease comparison), and the three dynamic sub-contributions, the convective cloud-base updraft velocity, the atmospheric instability and the conversion fraction, are represented respectively in solid orange, brown and yellow. This figure shows the dominant roles of the cloud-base velocity that initiates convective updraft and the conversion fraction in the dynamic variation with shear. As mentioned above, we expect the conversion fraction to follow the degree of organization of squall lines, and consistently it increases in the suboptimal and optimal regime, and then reaches a plateau.

What is more unexpected is that the cloud-base velocity is also found to saturate in the superoptimal regime (figure 4.6). The cloud-base updraft velocity may then only depend on the balance of the projected horizontal shear and the cold pool spreading. This is apparently what suggests the figure 4.12. The panels on the left show the surface winds at extreme condensation rate, where we see that the horizontal wind is perturbed as it crosses the cold pool, and in the superoptimal case, we observe that the excess momentum in the incoming shear is removed in the direction tangential to the squall line. In both cases, we find that the circulation is more complex than the simple picture of the cold pool spreading at equilibrium with the incoming shear; indeed, part of the horizontal wind is found to make it through the cold pool, and only the converging fraction into the black rectangle is expected to contribute to the vertical cloud base initial velocity. When we look at anomaly of horizontal wind instead, shown in the right panels, we find the expected low-level convergence. In these cross sections, horizontal wind anomalies are displayed on top of the buoyancy field, both composited at extreme condensation rate. The cloud-base updraft velocity results from the convergence in the horizontal plane below 1 km and probably encapsulates the effects of the pressure perturbation that deflects the incoming horizontal flow into the vertical direction.

To quantify this further, we compute a mass balance at the edge of the cold pool, in the reference frame of the squall line (black rectangles figure 4.12). The reference frame is aligned with the squall line and since the lines are oriented at an angle a as the shear increases, the frame of reference is also rotated. We consider a volume centered at maximum condensation, with angle $a = 0$ to the y-axis in the suboptimal and optimal squall lines, and angle $a > 0$ increasing in the superoptimal squall lines consistent with its orientation (i.e. such that $U_{sfc} \cos(a) = U_{sfc,opt}$, see figure 4.1). The rectangular volume has length $L = 6$ km parallel to the squall line, width $l = 1.5$ km across the line, and height $H = 1$ km.

Mass balance decomposition in the rectangle of figure 4.12 is displayed in figure 4.14.a. In blue, the incoming and outgoing horizontal winds perpendicular to the squall line are displayed ($< u_{in} >$ and $< u_{out} >$, where $< . >$ denotes averaging over the rectangle sides). We observe that as the shear increases, the net incoming wind $\Delta u =< u_{in} - u_{out} >$ increases, until the optimal shear is reached, and then the difference remains constant. In green, the increase of the tangential components ($< v_{in} >$ and $< v_{out} >$) in the superoptimal regime is clear. This supports that the exceeding momentum in the incoming shear in the superoptimal squall lines is removed in the direction tangential to the squall line. However the net incoming ($\Delta v =< v_{in} - v_{out} >$) slightly increases until the optimal shear is reached, and then remains approximately constant in the superoptimal regime. As a consequence, the convergence $\Delta u + \Delta v$ increases until the optimal case, and then saturates (dashed red), consistent with the mean velocity at the top of the volume at 1 km $< w_{1km} >$ (solid red) as expected from mass balance (the small difference is due to interpolation approximation near the rectangle). We notice that the value of the vertical velocity is almost 10 times smaller than the horizontal velocities, and this is explained by the mean flow passing through the cold pool. Investigating what controls the mean flow intensity and how it is related to the imposed wind shear would provide a theoretical scaling for the mean cloud-base velocity. We can hypothesize a dependence to the projected shear, but more work is needed to answer this question.

The figure 4.14.b. compares the evolution of the difference with the control case of the cloud-base updraft velocity (w_{cb} from equation 4.7), and the mean cloud-base velocity at the top of the rectangular volume (same as in 4.14.a). Both evolutions are similar, except that the mean velocity is lower, due to the effect of averaging. This suggests that the cloud-base updraft velocity variation results from those of the convergence in the horizontal plane, itself controlled by the orientation of the squall line, which removes exceeding momentum of the incoming shear into the tangential direction.

Thus, to leading order, precipitation extremes follow the dynamical contribution, itself dictated by the change of conversion fraction and the cloud-base updraft velocity at the top of the boundary layer, which follow the degree of organization, and consequently the regime of development of squall lines. The change of conversion of CAPE with organization is consistent with the literature (Becker *et al.* 2018; Feng *et al.* 2015; Mulholland *et al.* 2021), and is in our opinion an interesting impact of organization which would deserve further investigation. The change in initial cloud-base velocity of updrafts is also an important aspect in our squall lines. We explain this phenomenon with the increased winds perpendicular to the squall line in the suboptimal and optimal regimes. The saturation in the superoptimal regime is due to the squall line orientation, which maintains the projected wind perpendicular to the squall line close to its optimal value. The rest of the paper is now devoted to the other, smaller thermodynamic and microphysical contributions.

4.4.2 Microphysical component driven by conversion rate

The change of precipitation efficiency reaches about -15% in the optimal and -5% in the superoptimal simulations (Figure 4.4). In order to further investigate this change in precipitation efficiency, we follow Lutsko and Cronin 2018 and split the precipitation efficiency ε into two terms. The first

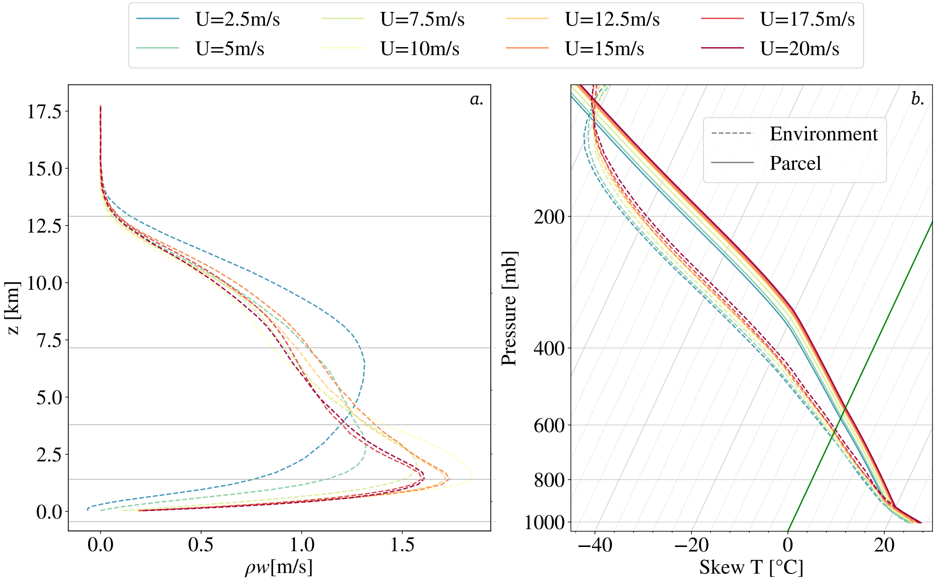

Figure 4.5: a. Mass flux profiles (ρw) for all cases, computed for high condensate columns (beyond 99.9$^{\mathrm{th}}$). The control case ($U_{sfc} = 2.5$ m/s), in blue, is a near parabolic profil, and as the shear increases we observe profiles becoming more "bottom heavy", consistant with Abbott *et al.* 2020. The mass flux at the boundary layer increase until the optimal regime and slowly decrease in the superoptimal regime. b. Environment temperature profile, averaged near an extreme of CAPE (beyond 99.9$^{\mathrm{th}}$) in dashed lines, and adiabatic parcel ascent in solid lines are displayed in Skew-T diagrams. The CAPE for each case is read as the area between two profiles of same color. This graph highlights the low sensitivity of the CAPE to shear changes accross simulation experiments.

term α is the rate of conversion from cloud to precipitating condensates Q_p (in kg m^{-2} s^{-1}), normalized by the rate of conversion from water vapor to cloud condensate C. It captures how efficiently cloud condensates are converted into precipitating condensates. Therefore, α is called conversion efficiency (Lutsko and Cronin 2018). The second term, $(1 - \beta)$, referred to as sedimentation efficiency (Lutsko and Cronin 2018), represents the fraction of source of precipitating condensate (Q_p) from microphysics which reaches the ground as surface precipitation (P). This fraction is typically less than unity because a fraction β of rain evaporates as precipitating condensates fall through subsaturated air. The microphysical variable Q_p is diagnosed directly from the model, and those two terms are computed using the following:

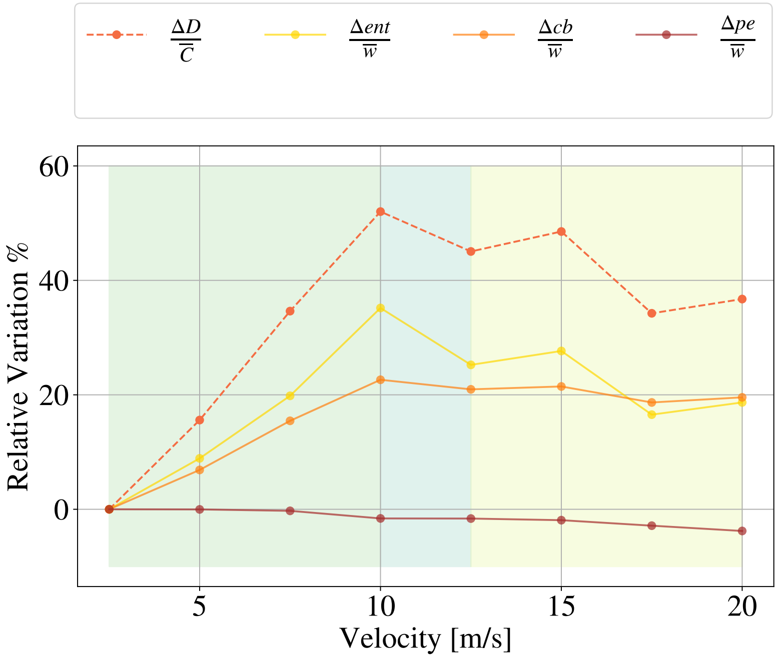

Figure 4.6: Decomposition of the dynamic contribution (dashed dark orange $\Delta D/\overline{C}$) into a cloud-base velocity term (solid orange $\Delta cb/\overline{C}$), an atmospheric instability term (solid brown $\Delta pe/\overline{C}$) and the conversion rate (solid yellow, $\Delta ent/\overline{C}$) for all simulation cases. The cloud-base velocity and the conversion term dominate the change in dynamic contribution.

$$\varepsilon \sim \frac{P}{C} \sim \underbrace{\frac{Q_p}{C}}_{\alpha} \times \underbrace{\frac{P}{Q_p}}_{1-\beta} . \tag{4.9}$$

Figure 4.9 represents the relative variations of the precipitation efficiency, the conversion and the sedimentation in the different simulations. We observe that changes in precipitation efficiency are mainly driven by changes in conversion. Further investigation (see Supplementary § S4; figures S2 and S3), decomposing α into contributions from accretion and auto-conversion, shows that the decrease of conversion is mainly due to a decrease of accretion. Intuitively, this suggests that the stronger updraft causes more cloud condensate due to not enough time for the auto-conversion process in the optimal and super-optimal balance experiments.

4.4.3 Thermodynamical component driven by change in surface humidity

The objective of this sub-section is to understand the origin of the small increase of the thermodynamic contribution, which increases by 10% in

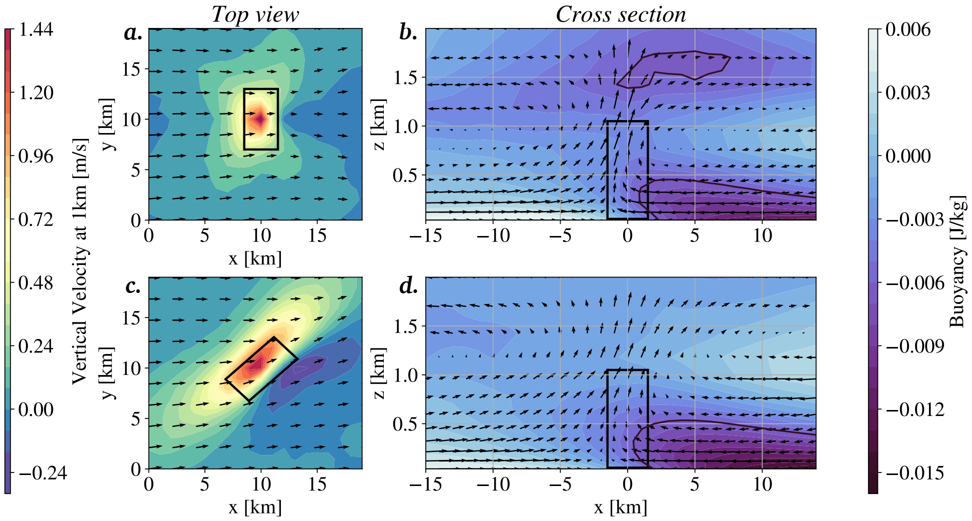

Figure 4.7: Vertical velocity maps at 1km height and buoyancy cross section fields for two cases, 12.5 m/s and 20 m/s are displayed. These fields are composited near the extreme of condensation (99.9^{th}). Horizontal velocity anomaly, at 1km too, are displayed in quiver in the top view. We observe stronger updraft in organized cases (12.5 m/s and 20 m/s), with a subsidence zone. This figure also highlights the orientation of the line in the superoptimal regime. For the cross section, the quiver represent the incoming flow both from the shear and the cold pool. We compute the mass balance in a volume represented by the black rectangle, in order to deduce the strength of the convective cloud-base updraft velocity at 1km.

the $U = 20$ m/s case compared to the control case. The thermodynamic contribution is written

$$\frac{1}{\overline{\overline{C}}}\int_0^{H_t} \overline{\rho w}\Delta\left(\frac{-\partial q_{sat}}{\partial z}\right) dz. \tag{4.10}$$

We can approximate this contribution as

$$\frac{1}{\overline{\overline{C}}}\int \overline{\rho w}\Delta\left(\frac{-\partial q_{sat}}{\partial z}\right) dz \sim \frac{1}{\overline{\overline{C}}}\overline{\rho w}_{500hPa}\Delta\int \frac{-\partial q_{sat}}{\partial z} dz = \frac{1}{\overline{\overline{C}}}\overline{\rho w}_{500hPa}\Delta(q_{sat}^{sfc}). \tag{4.11}$$

This equation yields an approximate relationship between the thermodynamic component and surface saturation humidity. As the temperature increases when a stronger shear wind is imposed (figure 4.5b), this leads to an increase in the saturation humidity at the surface. This increase can therefore explain the changes in thermodynamic contribution. We have plotted in figure 4.10 the variation of the saturation humidity at the surface (solid red line), as well as over the whole height of the boundary layer (solid orange)

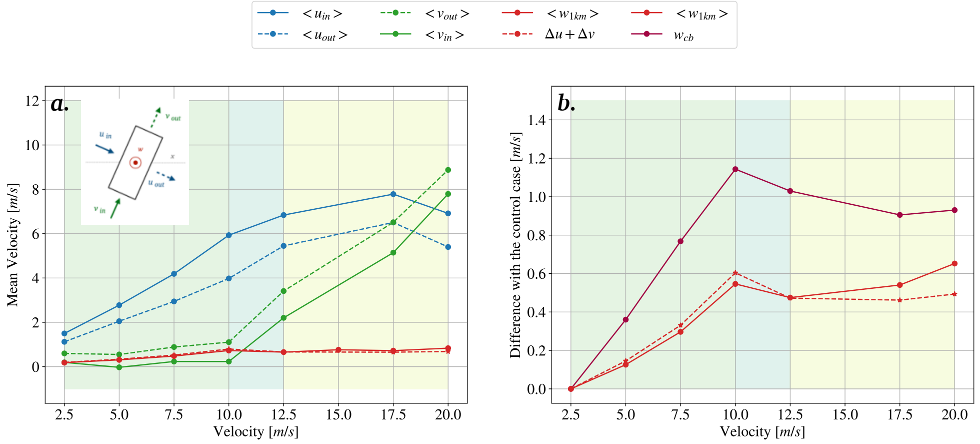

Figure 4.8: a. The inflow (solid line) and outflow (dashed) in the perpendicular (blue) and parallel (green) direction of the squall line, as well as the outflow at the top of the volume (red) are shown for each experiments (the inset shows the rectangle repeated from figure 4.12 with notations). We observe the saturation of the perpendicular component from the optimal case, as well as the increase of the tangential component, which supports our initial hypothesis. b. Relative evolution of the the mean cloud base velocity (red) compared to the one of the cloud base updraft velocity at extremes of condensation (purple). The variations of these two quantities are coherent and support our approach of modeling the cloud base velocity at extremes of condensation with the mean value of vertical velocity obtained from a mass balance. (The case $U = 15$ m/s has a changing propagation from increasing y to decreasing y which distorts the composites and has thus been removed in parallel and perpendicular estimates).

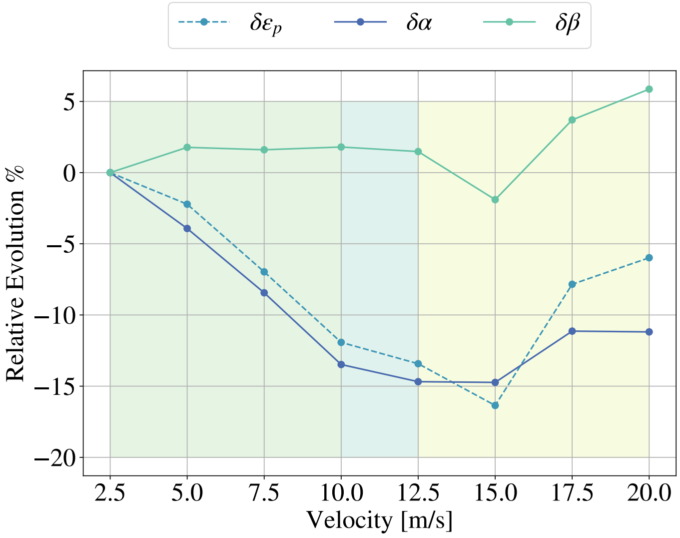

Figure 4.9: Decomposition of the precipitation efficiency (dashed blue) into a sedimentation term (green) and a conversion (blue) for all cases. The decrease in microphysics contribution is mainly explained by the decrease in conversion.

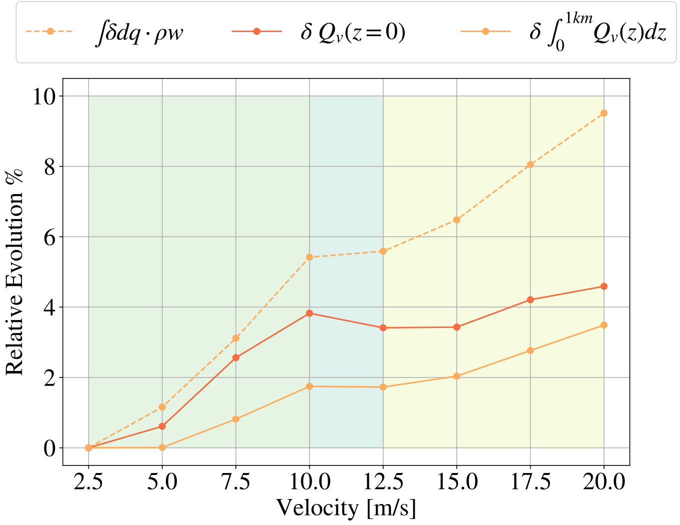

Figure 4.10: Comparison between the thermodynamic contribution (dashed yellow) and a simplified scaling, taking into account the change of humidity at saturation at the surface (solid orange), and the change integrated in the boundary layer (solid yellow). This figure shows that out of 10% of thermodynamic increase, almost half is due to near surface changes.

to compare them to the total thermodynamic contribution (dashed orange). This figure shows that out of 10% of thermodynamic increase, almost half is due to surface changes. As noted above, equation 4.11 is an approximate relation between the thermodynamic component and near-surface saturation humidity. So quantitatively, we do not expect a perfect agreement, but qualitatively, the thermodynamic contribution increase is consistent with the humidity increase.

4.5 Conclusion

Squall lines, and more generally organized convection, are associated with extreme weather conditions, notably extreme rainfall rates. Here, we investigate in idealized cloud-resolving simulations, the physical origin of the amplification of precipitation extremes in squall lines. We also clarify how this amplification varies in the suboptimal, optimal and superoptimal squall line regimes. These regimes are obtained in the simulations by increasing low-level shear following Abramian *et al.* 2022. We find that precipitation extremes are sensitive to the squall line regime and most notably to their orientation with respect to the shear. We observe a gradual increase of precipitation extremes in the suboptimal regime, up to a $30-40\%$ increase in the optimal regime. This increase saturates at $20-30\%$ in the superoptimal regime.

To understand these changes, we use a theoretical scaling, described in Muller and Takayabu 2020, which estimates the precipitation as the amount of water that condenses through vertical advection in updrafts, multiplied by a precipitation efficiency. This efficiency takes into account the part of the water that remains in the clouds, and the droplets that re-evaporate into the subsaturated air. The particularity of our method is to consider this scaling statistically true at each percentile rank rather than at a specific point in space (following Da Silva *et al.* 2021), to account for the cloud life cycle (an extreme of condensation in the early stage of a cloud leads to an extreme in precipitation at a later stage). Using this method, we are able to identify that the increase in precipitation extremes is due to an increase in condensation rates with imposed shear. More precisely, we show that the dynamic component is mainly responsible for the condensation increase. The microphysical contribution plays a secondary, but not negligible, damping role. The thermodynamic contribution is the weakest.

We also focus on the physical mechanisms at the origin of these variations. For the dynamical contribution, we show that it is the effect of dilution by entrainment and the cloud-base updraft velocity of the convective cells between cases that are most important. The former is consistent with reduced effective entrainment with organization, as updrafts in organized convection are surrounded by moister air. The latter is explained by the fact that the orientation, by re-establishing the equilibrium between cold pools and incoming shear, acts to maintain constant the cloud-base velocity that initiates convective updrafts. This is what differentiates the suboptimal regime where precipitation extremes increase with shear, from the optimal and superoptimal regimes preventing further increase of extremes in superoptimal squall lines. For the microphysical component, conversion rates are lower in the optimal regime presumably because the conversion of non-precipitating hydrometeors to rain is slower than the condensation of water vapor into non-precipitating hydrometeors. Finally, the thermodynamic component seems to increase with near-surface humidity which is sensitive to the increase in temperature with shear.

These results should draw our attention to the consequences of the organization of convection, and in particular its sensitivity to temperature increase. The 40% increase in optimal squall lines are larger than the thermodynamic increase in extremes associated with a 3 K warming expected from the Clausius-Clapeyron equation (7%/K increase). These results highlight the need to understand changes in the organization of convection, especially in the context of global warming. Changes in organization have a potentially more severe effect on rainfall extremes than warming. Over Sahel, where observations indicate the leading role of large mesoscale convective systems in explaining the trends in extreme precipitation, recent convection-permitting climate model simulations highlight tropospheric wind shear changes as the primary reason for intensifying squall lines under warming conditions (Fitzpatrick *et al.* 2020). Extending our idealized simulation results to more realistic data would be desirable, to better understand changing organization and implications for precipitation extremes. The global cloud-resolving simulations of the Dyamond/Next-GEMS project (Stevens *et al.* 2019) could be useful tools to address this important scientific question. Observations of surface properties at fine-scale resolution (kilometers, notably within cold pools), such as those proposed in the ESA Harmony mission (Earth Explorer 10 mission), will be crucial to perfect our understanding of the interaction between cold pools, shear and precipitation extremes (Harmony 2020).

4.6 Support Information

Contents of this file

1. **Model and simulations details.** In this section, we provide more information on the cloud-resolving model used and the specific configurations of the simulations.
2. **Joint Distribution of Precipitation and Condensation Rate** A probabilistic measure of the correlation between precipitation and condensation extreme is provided.
3. **Computation of Convective Available Potential Energy** The code of the CAPE and its consistency with SAM microphysic is detailed.
4. **Mass Flux Calculation** The calculation of the mean cloud base vertical updraft velocity is derived in this section.
5. **Microphysics Investigations** Vertical Profiles of Precipitating and Non Precipitating Water are provided to better undertand the behaviour of conversion rate.
6. **Additional Supporting Information (Files uploaded separately)** Dataset and Python package are released here.
7. **Supporting first-order approximation for precipitation and condensation decomposition** Evolution of second order terms from decomposition of theoretical scaling for precipitation and condensation rate for all experiments.

4.6.1 Model and simulations details

We simulate several cases of squall lines using the Cloud-Resolving Model (CRM) System for Atmospheric Modeling, or SAM (Khairoutdinov and Randall 2003). This model is based on a non-hydrostatic and anelastic formulation of atmospheric flows. It has the ability to cover a wide range of scales, from deep convective kilometric scale to mesoscale organization $\mathcal{O}$(100s km), and is thus adapted to the study of mesoscale systems such as squall lines. The prognostic thermodynamic variables of the model include total nonprecipitating water (vapor, cloud water, cloud ice) and total precipitating water (rain, snow, graupel). The mixing ratios of cloud water, cloud ice, rain, graupel, and snow is diagnosed from the prognostic variables using a temperature-dependent partition between liquid and ice phases. The frozen moist static energy, which is the sum of the liquid/ice water static energy and the total condensate amount times the latent heat of vaporization, is conserved during moist adiabatic processes in the model, including the freezing and melting of precipitation. The model is run to radiative-convective equilibrium, and once equilibrium is reached (in about 30 days) the organization of squall lines is analyzed, from day 30 to 35 with hourly outputs.

All simulations are three-dimensional on a square, doubly periodic horizontal domain, with horizontal resolution 1 km and domain size 128 km in x and y directions. The vertical grid has 64 levels (capped at 27 km with a rigid lid), with the first level at 37.5 m and grid spacing gradually increasing from 80 m near the surface to 400 m above 6 km, and a variable time step (10 s or less to satisfy the Courant–Friedrichs–Lewy condition). The surface fluxes are computed using Monin–Obukhov similarity. To reduce gravity wave reflection and buildup, a sponge layer with Newtonian damping is applied to all prognostic variables in the upper third of the model domain, from 18 to 27 km. We neglect the Earth rotation, a reasonable assumption in the deep tropics where the Coriolis parameter is small (set to zero in our simulations).

To organize the deep convection into squall lines, a linear shear in the x direction is imposed (following Muller 2013a). The imposed profile has a wind in the x-direction decreasing from U_{sfc} at the surface $z = 0$ km to $U_{1km} = 0$ m s^{-1} at $z = 1$ km. This background shear is imposed by relaxing the mean wind towards this profile with a relatively fast time scale of 2 hours. Nine simulations, with the surface wind U_{sfc} varied from 0 (no shear) to 20 m s^{-1}, with 2.5 m s^{-1} increments, are performed. To avoid an impact of this imposed surface wind on surface latent and sensible fluxes (which are proportional to surface wind magnitude), the domain-mean surface wind is removed before computing those surface fluxes.

4.6.2 Joint Contribution of P and C

In this paper, we assume that the scaling of precipitation extreme is consistent with an ergodic hypothesis, and this allows us to shift from a time and space to a statistical calculation. In this part, we provide motivation for this assumption, and we demonstrate its relevance. The aim of the following is to measure the correlation in time and space of an extreme of precipitation and an extreme of condensation rate. We define the quantity $F(q, q')$ as the probability that an extreme q of precipitation is *near* an extreme q' in condensation rate. By near, we consider a distance of $R \sim 1km$ in space and an interval $T \sim 5h$. This probability can be written as

$$F(q,q') = \sum_{\Delta t<T} \sum_{\Delta r<R} \sum_{\Delta\theta<\Theta} \Pi(P(r,\theta,t) \geq P^q \bigcap C(r+\Delta r, \theta+\Delta\theta, t+\Delta t) \geq C^{q'}), \tag{4.12}$$

where Π is a probalilty function, P is the precipitation, P^q is the value of P at the q^{th} percentile rank, $\bigcap$ is the logical *and* function, C is the condensation rate and $C^{q'}$ is the value of the q'^{th} percentile rank. Following Fildier *et al.* 2018, this quantity needs to be normalized by an independent joint distribution, in order to measure if the precipitation and the condensation are at least more correlated than two independent variables. We define $\overline{F}(q,q')$ the probability of an extreme q of a random variable X is near an extreme q' in an other random variable Y, where (X,Y) are independent with each other. It can be written as

$$\begin{aligned}
\overline{F}(q,q') &= \sum_{\Delta t<T} \sum_{\Delta r<R} \sum_{\Delta\theta<\Theta} \Pi(X(r,\theta,t) \geq X^q \bigcap Y(r+\Delta r, t+\Delta t) \geq Y^{q'}) && (4.13)\\
&= \sum_{\Delta t<T} \sum_{\Delta r<R} \sum_{\Delta\theta<\Theta} \Pi(X(r,\theta,t) \geq X^q) \times \Pi(Y(r+\Delta r, \theta+\Delta\theta, t+\Delta t) \geq Y^{q'}) && (4.14)\\
&= 2\pi RTqq'. && (4.15)
\end{aligned}$$

Eventually, we can define κ the ratio of the measured correlation between P and C, and the theroretical correlation of two independent variables,

$$\begin{aligned}
\kappa(q,q') &= \frac{F(q,q')}{\overline{F}(q,q')} && (4.16)\\
&= \sum_{\Delta t<T} \sum_{\Delta r<R} \sum_{\Delta\theta<\Theta} \frac{\Pi(P(r,\theta,t) \geq P^q \bigcap C(r+\Delta r, \theta+\Delta\theta, t+\Delta t) \geq C^{q'})}{2\pi RTqq'}. && (4.17)
\end{aligned}$$

We compute $\kappa(q,q')$ for the case $U_{sfc} = 10m/s$ and it is displayed in figure 4.11. A pixel of this figure represents the co-located dependency of the condensation rate and the precipitation rate at a given percentile. For instance, the colocation of a precipitation of 99.9th and a condensation rate of 99.9th is 200 times more likely as if these two variables were independent. It shows that for percentile rank greater than $99.9th$ precipitation and condensation rate are strongly correlated in space and time. For percentile rank greater than 99.99th κ is not define since it tends to a ratio $0/0$.

4.6.3 Computation of Convective Available Potential Energy

In this section, we describe more in details the computation of the convective available potential energy used in the study. The particularity of this computation is the consistency with the microphysic scheme in the Cloud Resolving Model SAM, and also the use of in-built python optimisation function that provides a 3D resolution of the adiabatic temperature field. The time dependence loop is optimized using parallelization of CPU.

The code is in two main parts, with first the computation the dry adiabatic ascent and second the moist adiabatic ascents. For the first part, we have to calculate the level of free convection for each point of the domain. The problem is formulated as an optimization formulae

$$(T(z), p(z), z) \text{ such as } r_{sat}(T(z), p(z), z) - r_0 = 0 \tag{4.18}$$

where r_{sat} is the saturation mixing ratio, T denotes the temperature field, p the pressure, z the altitudes and r_0 the humidity at the ground. Using the package *scipy* from Python, and importing the module *optimize* we solve this first equation with a Newton method. T, p have been interpolated in order to obtain the closest value for the z and further for dry static energy.

We note in passing that the calculation of the saturation mixing ratio follows the microphysic scheme of SAM, and takes into account the quantity of ice contained in the parcel. More precisely, it writes

$$r_{sat}(T(z), p(z)) = \omega_m q^w_{sat}(T(z), p(z)) + (1 - \omega_m) q^i_{sat}(T(z), p(z)) \tag{4.19}$$

where ω_m is the partition function among the hydrometeors and only depends on temperature, q^w_{sat} is the saturated humidity for water and q^i_{sat} is for ice.

Once we solve (1) and obtain a the level of lifted condensation z_{LCL}, we deduce the parcel temperature profile

$$T_{parc}(z) = T(0) - \frac{g}{c_p} z \text{ for } z \leq z_{LCL}. \tag{4.20}$$

From the level z_{LCL} the parcel starts a moist adiabatic ascent that conserves the moist static energy written as

$$MSE(T, p, z) = T(z) + \frac{g}{c_p} z + (L_{cond} w_n + L_{sub}(1 - w_n))(r_{sat}(z) - r_0), \tag{4.21}$$

where L_{cond} and L_{sub} are the latent heat of condensation and sublimation. The temperature profile for a parcel with a moist adiabatic ascent is such that the MSE is conserved from the level of lifted convection (z_{LCL}) to the tropopause. This can also be written as an optimization problem

$$T_{parc}(z) \text{ such that } MSE(T_{parc}(z), p(z), z) - MSE_{LCL} = 0. \tag{4.22}$$

Here again, using a $3D$ solver we compute the moist adiabatic parcel ascent.

4.6.4 Mass Flux Calculation

We propose to do the mass balance at the level of a volume taken at the edge of the pool which contains the updraft (see figure 4.13 for the description of the framework and quantities). In theory, we can consider the velocity profiles

$$\vec{u}_{forcing}(z) = u_{sfc}(1 - \frac{z}{H})\vec{e_x} \tag{4.23}$$

$$\vec{u}_{cp}(z) = -u_{sfc}\cos(\alpha)(1 - \frac{z}{H})^2\vec{e_r}, \tag{4.24}$$

$$\vec{e_x} \cdot \vec{e_r} \mid_{trig} = -\cos(\alpha) \tag{4.25}$$

where $u_{forcing}$ is the imposed linear wind shear, H is equal to 1km, u_{cp} is the cold pool spreading velocity profiles, $\vec{e_r}$ is the radial unitary vector regarded to the cold pool. The quadratic spreading velocity of the cold pool is inspired by the analysis of cold pools in our simulations, empirically determined to spread out following a quadratic shape. The angle α, also called the orientation of the squall line, is defined as the scalar product of the unitary radial vector of the cold pool with the unitary vector in the direction of the imposed wind shear. We have the mass balance written in the integral form,

$$\int\int_{S_z} \vec{U} d\vec{S}_z + \int\int_{S_{//}} \vec{U} d\vec{S}_{//} + \int\int_{S_\perp} \vec{U} d\vec{S}_\perp = 0, \tag{4.26}$$

where $\vec{U}$ is the 3-dimensionnal velocity field, $d\vec{S}_z$ is the surface vector equal to $(0, 0, 1)$ (top of the volume), $d\vec{S}_{//}$ is equal to $(\cos(\alpha), \sin(\alpha), 0)$ (long side of the volume), and $d\vec{S}_\perp$ is equal to $(-\sin(\alpha), \cos(\alpha), 0)$ (wide side of the volume). By replacing $\vec{U}$ by its value at the edge of the box, and performing the scalar product, it leads to

$$< w(H) > \cdot S_z = L \int_0^H u_{sfc}\cos(\alpha)(1 - \frac{z}{H})\{(1 - \frac{z}{H}) - 1\}dz \tag{4.27}$$

Finally, this results in

$$< w(1km) >\sim u_{sfc}\cos(\alpha)\frac{H}{6l}. \tag{4.28}$$

We can numerically calculate the mass balance around a volume as described above. The figure 4.12 shows the vertical velocity map centered on the 99.9th percentile of condensation is shown for 3 simulation cases (U=2.5m/s, 10m/s and 20m/s), as well as the horizontal vector field (U,V) at 1km, around the 99.9th percentile of condensation. For each case, the condensation maximum shows an updraft, we observe a subsidence zone behind which stands the cold pool. We also observe the orientation of the squall line in the U=20m/s case.

In Figure 4.14.a. the inflow (solid line) and outflow (dashed) in the parallel (blue) and perpendicular (green) direction of the squall line, as well as the outflow at the top of the volume (red) are shown for each cases. We observe the saturation of the perpendicular component from the critical case, as well as the increase of the tangential component, which supports our initial hypothesis. In solid red, the mean cloud base evolution is displayed. The second panel Figure 4.14.b. shows the relative evolution of the the mean cloud base velocity, and it is compared to the one of the cloud base updraft velocity at extremes of condensation. The variations of these two quantities are coherent and support that we model the cloud base velocity at extremes of condensation with the mean value of a mass balance.

4.6.5 Microphysics Investigations

Following Lin *et al.* 1983, the 1-moment microphysics scheme that we use in Khairoutdinov and Randall 2003 calculates the conversion as the sum of the cloud droplets that are entrained by precipitating condensate (autoconversion), and the precipitative condensate produced by super-cold droplets (under 0°), also known as Bergeron effect (accretion). The models used to calculate these contribution are, on the one hand for accretion

$$\frac{\partial q_p}{\partial t}_{acc} \sim q_n q_p^{a_p}, \tag{4.29}$$

where q_p is the precipitating condensate amount, t the time, *acc* stands for accretion, q_n is the non precipitative condensate and a_p depends slightly on the precipitation type (rain, graupel or snow in SAM) but is typically close to 1. And on the other hand for auto-conversion,

$$\frac{\partial q_p}{\partial t}_{auto} \sim (q_n - q_{n0})^+, \tag{4.30}$$

where q_{n0} is a constant threshold different for cloud liquid and cloud ice, and where $^+$ is the positive part function.

Decomposition of α into contributions from both processes (accretion and auto-conversion) is displayed in figure 4.15.b.. We see that the decrease of the conversion is mainly due to the decrease of accretion term.

The Figure 4.16 shows vertical profiles of precipitating water (Q_p) and non precipitating water (Q_n) conditionned at respective extremes. We can see that precipitating water increase for all altitudes between the control case and the critical case, but the non-precipitating water remains the same between these two case. The accretion increases a bit but not as much as the condensation rate, and this is explained by the failure of producing non precipitating droplet as fast as precipitating ones.

4.6.6 Supporting first-order approximation for precipitation and condensation decomposition

The theoretical scaling for precipitation writes as follow,

$$P \sim \varepsilon C \sim \varepsilon \int_0^{H_t} \rho w \frac{-\partial q_{sat}}{\partial z} dz \tag{4.31}$$

considering the relative changes with respect to the unorganized case, it leads to

$$\frac{\Delta P}{\overline{P}} = \frac{\Delta \varepsilon}{\overline{\varepsilon}} + \frac{\Delta C}{\overline{C}} + \underbrace{\frac{\Delta \varepsilon}{\overline{\varepsilon}} \frac{\Delta C}{\overline{C}}}_{\text{2nd order}} . \tag{4.32}$$

where second order terms are neglected. When we further decompose the condensation rate, we also neglect the second order terms,

$$\frac{\Delta C}{\overline{C}} \sim \frac{1}{\overline{C}} \int_0^{H_t} \Delta \rho w \frac{-\partial \overline{q_{sat}}}{\partial z} dz + \frac{1}{\overline{C}} \int_0^{H_t} \overline{\rho w} \Delta \frac{-\partial q_{sat}}{\partial z} dz + \underbrace{\frac{1}{\overline{C}} \int_0^{H_t} \Delta \rho w \Delta \frac{-\partial q_{sat}}{\partial z} dz}_{2nd\ order} . \tag{4.33}$$

In this section, we support why this approximation is fair enough. We display in figure 4.17 the evolution of second order terms from equation 4.32 and 4.33 for all experiment. In this figure, we see that first-order approximation for precipitation has an error of less than 10%, and first-order decomposition of condensation rate less than 2%.

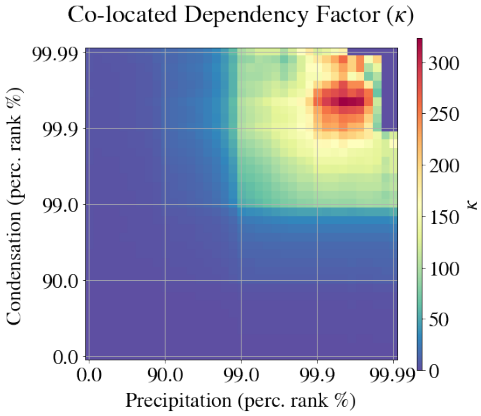

Figure 4.11: A pixel of this figure represents the co-located dependency of the condensation rate and the precipitation rate at a given percentile. For instance, the colocation of a precipitation of 99.9th and a condensation rate of 99.9th is 200 times more likely as if these two variables were independent. It shows that for percentile rank greater than $99.9th$ precipitation and condensation rate are strongly correlated in space and time. For percentile rank greater than 99.99th κ id not define since it tends to a ratio $0/0$.

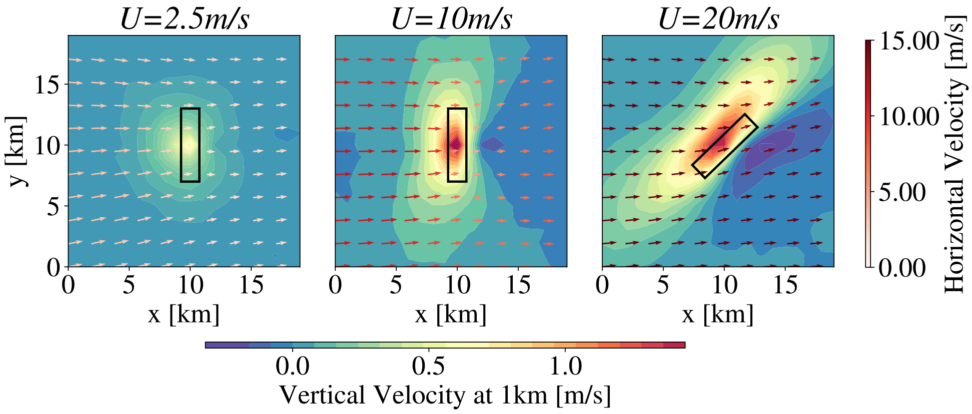

Figure 4.12: Vertical velocity maps at 1km height for three cases, 2.5m/s, 10m/s and 20m/s are displayed. These fields are composited near the extrme of condensation (99.9th). Horizontal velocity, at 1km too, are displayed in quiver. We observe stronger updraft in organized cases (10m/s and 20m/s), with a subsidence zone. This figure also highlight the orientation of the line in the super-critical regime. We compute the mass balance in a volume represented by the black rectangle, in order to deduce the strength of the convective triggering at 1km.

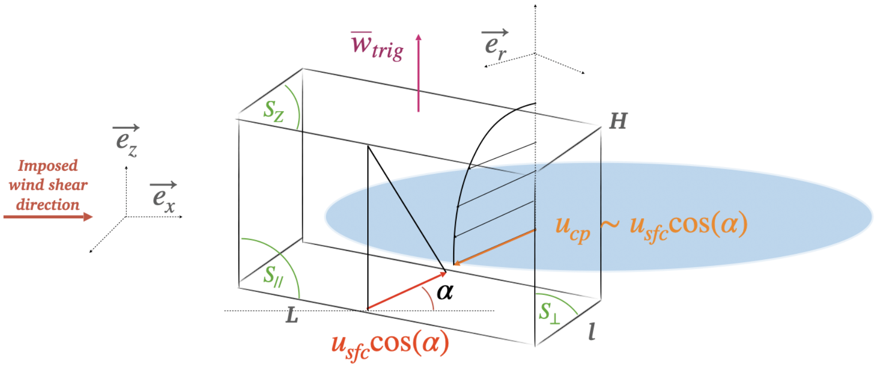

Figure 4.13: Definition of direction and quantities used for the mass balance computation. We perform a mass balance in a parallepipedic volume at the edge of the cold pool (in blue) where the convective cell is triggering. The box is H=1km height, l=3km wide and L=6km long. The abolute referential (e_x, e_y, e_z) is represented on the left. The impose wind shear is in the $\vec{e_x}$ direction. Depending on the intensity of the wind shear, the triggered cell occurs at a certain angle α regarding to the imposed wind direction. The balance between wind shear and cold pool spreding is restablish by this orientation, such that $u_{cp} \sim u_{sfc}\cos(\alpha)$. The radial direction of the cold pool is supported by $\vec{e_r}$.

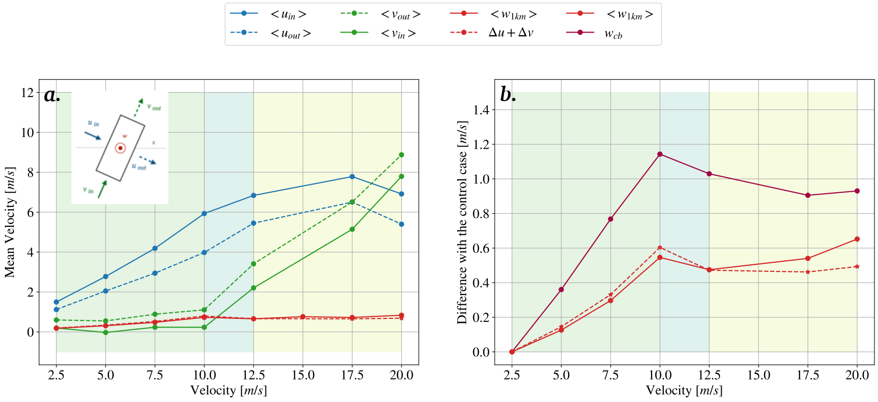

Figure 4.14: a. the inflow (solid line) and outflow (dashed) in the perpendicular (blue) and parallel (green) direction of the squall line, as well as the outflow at the top of the volume (red) are shown for each cases. We observe the saturation of the perpendicular component from the critical case, as well as the increase of the tangential component, which supports our initial hypothesis. b. Relative evolution of the the mean cloud base velocity (red) compared to the one of the cloud base updraft velocity at extremes of condensation (purple). The variations of these two quantities are coherent and support that we model the cloud base velocity at extremes of condensation with the mean value of a mass balance. (The case $U = 15$m/s has a changing propagation from increasing y to decreasing y which distorts the composites and has thus been removed in parallel and perpendicular estimates).

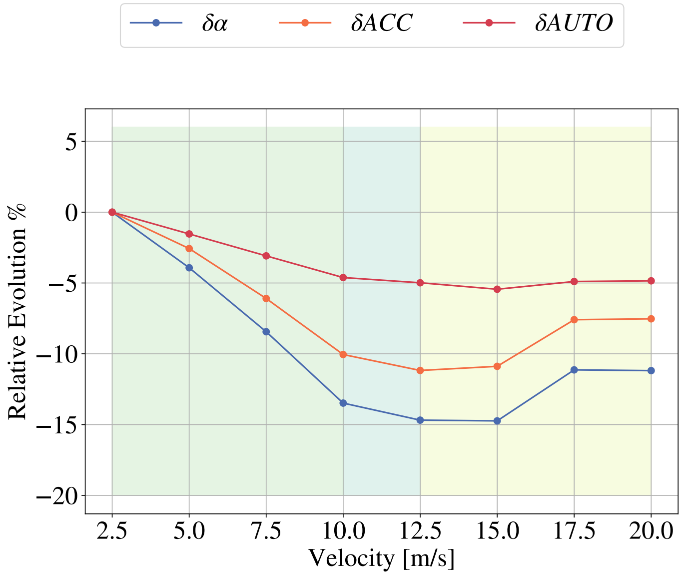

Figure 4.15: Decomposition of the conversion term α into two contribution : the accretion term (orange) and the auto-conversion term (blue). This figure shows that change in accretion rate is responsible for change in conversion α.

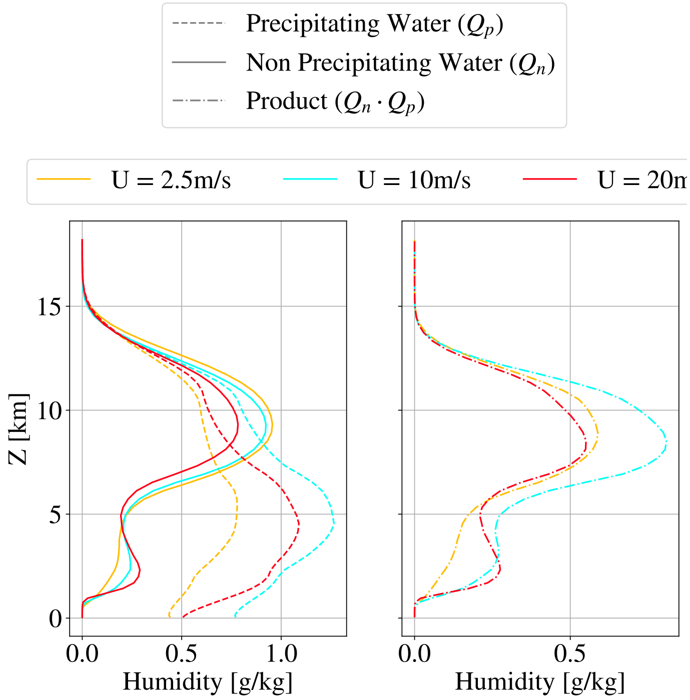

Figure 4.16: This figure shows on the first panel vertical profiles of precipitating water (q_p) in dashed line and non precipitating water (q_n) in solid one, conditionned at precipitation efficiency extremes. The second panel shows the product of these two variables, that is the accretion term. We can see that precipitating water increase for all altitudes between the control case and the critical case, but the non-precipitating water remains the same between these two case. The accretion increases a bit but not as much as the condensation rate, and this is explained by the fail of producing non precipitating droplet as fast as precipitating ones. Humidity here denotes condensate mixing.

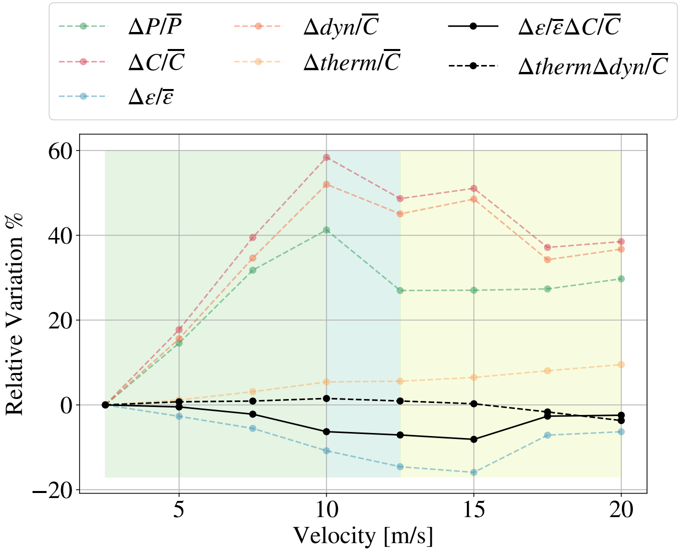

Figure 4.17: Relative sensitivity to shear of precipitation extreme and its decomposition into dynamic, thermodynamic and microphysic components using the scalling, as well as sensitivity of second order terms evolution (see equation 4.33). First-order approximation for precipitation has an error of less than 10%, and first-order decomposition of condensation rate less than 2%. This figure supports that we neglect second-order terms.

Chapter 5

How do Squall Lines influence Isotopic Composition in the Tropics?

Résumé en français

Dans la première partie de ce manuscrit, nous présentons des preuves démontrant que les mécanismes régissant la formation des lignes de grains sont significativement influencés par l'interaction entre la cisaillement des vents en basse altitude et les poches d'air froid. Pour évaluer l'applicabilité de ces mécanismes identifiés dans le contexte du changement climatique contemporain, l'examen des régimes climatiques historiques offre une opportunité précieuse. Cette approche nous permet d'étudier les principales transitions climatiques et de collecter des données couvrant des époques temporelles prolongées, englobant les systèmes convectifs de méso-échelle et les événements météorologiques extrêmes associés. Par conséquent, le domaine émergent de la paléo-tempétologie basée sur les isotopes a suscité une attention considérable, car il offre le potentiel de faciliter la reconstitution des fréquences historiques des cyclones et des lignes de grains. Pour y parvenir, il est impératif d'acquérir une compréhension plus complète de l'impact des systèmes convectifs de méso-échelle sur la composition isotopique de la vapeur d'eau et des précipitations en dessous de la couche nuageuse. Tel est l'objectif de ce chapitre, qui examine en détail la signature isotopique et les processus pertinents dans les lignes de grains tropicales.

Il est important de distinguer ce chapitre des travaux de recherche précédents, car il résulte d'un projet collaboratif auquel j'ai participé, mais dont je n'ai pas directement produit les résultats rapportés. Le projet mentionné a donné lieu à un article publié intitulé "Quels sont les facteurs de contrôle des variations à méso-échelle de la composition isotopique de l'eau au sein des cyclones tropicaux et des lignes de grains ? Simulations de modèles à résolution nuageuse en équilibre radiatif-convectif", rédigé par Camille Risi, Caroline Muller, Françoise Vimeux, Peter Blossey, Grégoire Védeau, Clarisse Dufaux et Sophie Abramian, publié dans le Journal of Advances in Modeling Earth Systems en 2023. Il est essentiel de reconnaître que la portée de ce chapitre diffère substantiellement du contenu présenté dans l'article, notre principal objectif ici étant dirigé vers les lignes de grains, compte tenu de ma participation principale à la configuration des simulations de modèles pour ce système convectif spécifique.

Les isotopes de l'eau sont des traceurs des processus de convection et sont souvent utilisés comme indicateurs pour les précipitations passées. Ces applications exigent une meilleure compréhension de l'impact des processus de convection sur la composition isotopique de la vapeur d'eau et des précipitations. Une manière d'améliorer cette compréhension est d'analyser les variations isotopiques au sein de systèmes de convection organisée tels que les cyclones tropicaux ou les lignes de grains. L'objectif de cette étude est de comprendre comment évoluent ces variations au sein de la structure meso-échelle des systèmes, en portant une attention particulière aux signaux isotopiques de la vapeur d'eau dans la couche sous-nuageuse, et ceux des précipitations. Ces signaux sont cruciaux dans la reconstruction de climats passés car ils peuvent être présents dans les observations et dans les indicateurs paléoclimatiques. Dans cette perspective, nous avons effectué des simulations à l'aide d'un modèle qui résout les equations de la convection en équilibre radiatif-convectif auquel nous avons ajouté un cisaillement de vent, nous permettant ainsi de simuler des lignes de grains. Les simulations reproduisent les aspects robustes des variations isotopiques de méso-échelle observées dans les lignes de grains. Nous interprétons ces variations à travers six contributions principales dérivées d'un modèle de bilan de l'eau simple pour la couche sous-nuageuse de différentes parties du domaine. Nous constatons que l'évaporation de la pluie et les échanges diffusifs entre la pluie et la vapeur d'eau sont les principaux moteurs de l'appauvrissement isotopique au sein des lignes de grains. Cette étude contribue à notre compréhension de la variabilité isotopique à méso-échelle et fournit des arguments physiques soutenant l'interprétation des archives isotopiques paléoclimatiques dans les régions tropicales en termes d'activité cyclonique passée.

How do Squall Lines influence Isotopic Composition in the Tropics?

In the first part of this manuscript, we present evidence demonstrating that the mechanisms governing the formation of squall lines is significantly influenced by the interplay of low-level wind shear and cold pools. To assess the applicability of these identified mechanisms within the context of contemporary climate change, the examination of historical climatic regimes provides a valuable avenue. This approach allows us to investigate major climatic transitions and to collect data spanning extended temporal epochs, encompassing MCSs and associated extreme meteorological events. Consequently, the emerging field of isotope-based paleo-tempestology has attracted considerable attention, as it holds the potential to facilitate the reconstruction of historical frequencies of cyclones and squall lines. To achieve this, it is imperative to acquire a more comprehensive understanding of the impact of MCSs on the isotopic composition of sub-cloud layer water vapor and precipitation. This is the goal of this chapter, which investigates in detail the isotopic signature and relevant processes in tropical squall lines.

It is noteworthy to differentiate this chapter from preceding research efforts, as it is the result of a collaborative project in which I participated but did not directly produce the reported findings. The aforementioned project has yielded a published paper titled "What Controls the Mesoscale Variations in Water Isotopic Composition Within Tropical Cyclones and Squall Lines? Cloud Resolving Model Simulations in Radiative-Convective Equilibrium," authored by Camille Risi, Caroline Muller, Françoise Vimeux, Peter Blossey, Grégoire Védeau, Clarisse Dufaux, and Sophie Abramian, published in the Journal of Advances in Modeling Earth Systems in 2023. It is essential to acknowledge that the scope of this chapter substantially differs from the content presented in the paper, with our primary focus here directed toward squall lines, given my principal involvement in configuring the model simulations for this specific convective system.

Abstract

Water isotopes are tracers of convective processes and are often used as proxies for past precipitation. These applications require a better understanding of the impact of convective processes on the isotopic composition of water vapor and precipitation. One way to advance this understanding is to analyze the isotopic mesoscale variations during organized convective systems such as tropical cyclones or squall lines. The goal of this study is to understand these isotopic mesoscale variations with particular attention to isotopic signals in near-surface vapor and precipitation that may be present in observations and in paleoclimate proxies. With this aim, we run cloud resolving model simulations in radiative-convective equilibrium in which wind shear is added, allowing us to simulate squall lines. The simulations capture the robust aspects of mesoscale isotopic variations in observed squall lines. We interpret these variations through six main contributions derived from a simple water budget model for the sub-cloud layer of different parts of the domain. We find that rain evaporation and rain-vapor diffusive exchanges are the main drivers of isotopic depletion within squall lines. This study contributes to our understanding of mesoscale isotopic variability and provides physical arguments supporting the interpretation of paleoclimate isotopic archives in tropical regions in terms of past cyclonic activity.

Plain Language Summary

Naturally available, stable water molecules can be light (one oxygen atom and two hydrogen atoms) or heavy (one hydrogen atom is replaced by a deuterium atom). These different molecules are called water isotopes. In large, long-lived, severe storms such as tropical cyclones or squall lines (thunderstorms that organize into lines), the rain is observed to be more depleted in heavy isotopes. Several studies have exploited this property to reconstruct the past variations in the frequency of occurrence of tropical cyclones or severe thunderstorms based on isotope variations observed in speleothems. The aim of this study is to understand what controls the depletion in heavy isotopes of the rain in squall lines. With this aim, for the first time we use high-resolution simulations (2–4 km in horizontal) to simulate the internal dynamics of squall lines and their isotope composition. We design a simple model to interpret the results. We show that the rain evaporation and rain-vapor exchanges deplete the water vapor, and the subsequent rainfall, in heavy isotopes.

5.1 Introduction

Two isotopes are atoms that have the same number of protons and electrons but a different number of neutrons. As a result, they react chemically in the same way but have a different atomic mass. For example, the hydrogen atom can exist in the form of ^{1}H (no neutrons), ^{2}H (also known as deuterium D, with one neutron), or ^{3}H (also known as tritium T, with two neutrons). The oxygen atom can exist in the form of ^{16}O, ^{17}O, or ^{18}O. Water is primarily composed of molecules of $H_2^{16}O$, but it also contains a few heavier molecules of $H_2^{17}O$ (0.004%), $H_2^{18}O$ (0.2005%), HDO (0.0155%), and HTO (currently in very small quantities). These different molecules are called isotopologues or, colloquially, ”water isotopes.”

The relative proportion of these different molecules is called the isotopic composition and is quantified by the notation $\delta\cdot$:

$$\delta\cdot = (\frac{R_{sample}}{R_{SMOW}} - 1) \cdot 1000 \tag{5.1}$$

where R_{sample} is the ratio of heavy molecules to the total number of molecules in the sample, and R_{SMOW} is the same ratio in an international reference corresponding to an average surface ocean water: Standard Mean Ocean Water (SMOW). $\delta\cdot$ is expressed in per mil (‰). Thus, $\delta^{17}O$, $\delta^{18}O$, and δD are defined to quantify the abundance of $H^{17}2O$, $H^{18}2O$, and HDO, respectively. To first order, δD variations are 8 times those in $\delta^{18}O$ (Craig, 1961), so we will focus on δD here. However, slight deviations in the $\delta D - \delta^{18}O$ relationship can be quantified by the second-order parameter d-excess: $d = \delta D - 8 \times \delta^{18}O$. It reflects kinetic effects associated with diffusivity differences between the different water isotopologues.

The isotopic composition of water vapor evolves during the water cycle as phase changes occur, giving rise to isotopic fractionation. Convection, being associated with numerous phase changes such as condensation in updrafts, re-evaporation during detraining into the environment, and droplet re-evaporation in undersaturated conditions, exerts a significant influence on the isotopic composition of water. This influence becomes more pronounced when convection is organized. Understanding how organized convective systems influence the isotopic composition of precipitation or near-surface water vapor can thus be valuable for comprehending how convective organization is documented in paleoclimate records. Notably, the isotopic composition of precipitation, as recorded in paleoclimate archives, has significantly contributed to our understanding of past hydrological changes in tropical regions (Cruz *et al.* 2009; Wang *et al.* 2001). This chapter's objective is to enhance our comprehension of how convective organization impact water's isotopic composition.

In tropical regions, the organization of convection can take the form of mesoscale convective systems, which are responsible for over half of total precipitation (Houze 2004; Nesbitt *et al.* 2006). These systems are associated with processes that lead to a depletion of heavy isotopes in water vapor. Notably, observational investigations have underscored the role of rain evaporation (Worden *et al.* 2007), diffusive liquid-vapor exchanges (Lawrence *et al.* 2004), mesoscale downdrafts (Kurita 2013; Risi *et al.* 2010), and microphysical processes within stratiform regions of convective systems (Aggarwal *et al.* 2016). Modeling studies employing high-resolution simulations have corroborated the pivotal role of rain evaporation and diffusive liquid-vapor exchange (Torri 2022, 2021), as well as microphysical processes within stratiform regions of convective systems, particularly the melting of depleted snow followed by evaporation (Risi *et al.* 2021).

Especially, more organized convective systems such as squall lines (Maupin *et al.* 2021; Risi *et al.* 2008; Tremoy *et al.* 2014) or tropical cyclones (Chakraborty *et al.* 2016; Jackisch *et al.* 2022) have been observed to be linked with water vapor and precipitation that are more depleted in heavy isotopes compared to unorganized systems. Specifically, the reduced heavy isotope content in the rain from tropical cyclones leaves a distinct signature in surface waters (Welsh and Sánchez-Murillo 2020) and can significantly impact long-term averages of precipitation or surface water isotopic composition (Baldini *et al.* 2016; Lawrence *et al.* 1998). This suggests that the annual or multi-annual mean isotopic composition of precipitation recorded in speleothems can be utilized to reconstruct past cyclonic activity (Chen *et al.* 2021; Frappier *et al.* 2007), although this can be a challenging endeavor (Jackisch *et al.* 2022). In recent years, several studies have interpreted speleothems in terms of cyclonic frequency (Baldini *et al.* 2016; Medina-Elizalde and Rohling 2012; Nott *et al.* 2007). Additionally, the observed depletion in Texan speleothems has been attributed to heightened activity of large, long-lived, organized convective systems (Maupin *et al.* 2021). Beyond paleoclimate applications, comprehending how convective processes influence water's isotopic composition is also pertinent for assessing the utility of water isotopic measurements in quantifying convective processes and improving their representation in models (Bony *et al.* 2008; Diekmann *et al.* 2021; Field *et al.* 2014; Ramos *et al.* 2022.

What remains poorly documented is that the relationship between water's isotopic composition and precipitation rate can exhibit temporal and spatial variability. This dependence may hinge on factors such as the proportion of stratiform versus convective rain (Aggarwal *et al.* 2016), convective organization (Chakraborty *et al.* 2016; Lawrence *et al.* 2004), or the shape of vertical velocity profiles (Lacour *et al.* 2017; Moore *et al.* 2014; Torri *et al.* 2017). For a more robust and quantitative interpretation of water isotopic records in terms of past hydrological variations or cyclonic activity, a deeper understanding of how these factors influence the isotopic composition of water vapor and precipitation is needed. More precisely, quantifying the variation of the isotopic composition in the different parts of organized systems and identifying the relative importance of processes at play would help improve our current representation of MCSs signature in paleoclimate records.

This study's objective is to investigate the processes governing the evolution of near-surface water vapor (δD_v) and precipitation (δD_p) isotopic composition within squall lines. Specifically, we aim to address three key questions:

- How does the water isotopic composition vary within the mesoscale structure of simulated tropical squall lines?

- Is this variation consistent with observed tropical squall lines?
- What are the underlying physical processes driving these variations?

To date, these questions have often been tackled using observational studies or simple box models (Bhattacharya *et al.* 2022; Fudeyasu *et al.* 2008; Gedzelman *et al.* 2003; Lawrence *et al.* 2002; Tremoy *et al.* 2014; Xu *et al.* 2019). For the first time, this study employs three-dimensional high-resolution simulations, explicitly representing convective motions, to simulate the isotopic composition of water vapor and precipitation within squall lines. The next section is dedicated to the description of the simulations, the definition of the subdomains of interests in squall lines. In the following section, results and answers to the aforementionned questions are proposed, and we end with a last section of conclusion.

5.2 Method: how to model water isotopic distribution within the mesoscale structure of squall lines?

5.2.1 Cloud Resolving Model and simulation set-up

We used the same Cloud Resolving Model (CRM) as that used in the previous chapters namely the System for Atmospheric Modeling (SAM) non-hydrostatic model (Khairoutdinov and Randall 2003), except that now it is enabled with water isotopes (Blossey *et al.* 2010). This model solves anelastic conservation equations for momentum, mass, energy, and water, which is present in the model under six phases: water vapor, cloud liquid, cloud ice, precipitating liquid, precipitating snow, and precipitating graupel. We used the bulk, mixed-phase microphysical parameterization from Thompson *et al.* 2008 in which water isotopes were implemented (Moore *et al.* 2016).

Simulations are three-dimensional, with a doubly periodic domain. They are run in radiative-convective equilibrium over an ocean surface. The sea surface temperature (SST) was set at 30°C. We did not prescribe any diurnal cycle. Organized convection is typically observed in regions of large-scale ascent (Jakob *et al.* 2019; Tan *et al.* 2013). Therefore, we impose a large-scale vertical ascent with a cubic shape, reaching -40 hPa/d at 5 km and 0 hPa/d at the surface and above 100 hPa (Risi *et al.* 2020). Simulations were also run without vertical ascent, and gave similar results except that the convective systems were smaller and with a less well-defined internal structure. We thus focus on the simulations with large-scale ascent in the following. The simulations were run for 50 days. The last 10 days of simulation are analyzed with one three-dimensional output file every day. In radiative-convective equilibrium, all snapshots exhibit similar behavior.

We used a domain of 256 × 256 km with a horizontal resolution of 2 km and 96 vertical levels. Squall lines spontaneously develop in radiative-convective equilibrium simulations when horizontal wind shear is added (Abramian *et al.* 2022; Robe and Emanuel 2001). We added a horizontally uniform wind in the x direction that reaches 10 m/s at the surface and linearly decreases to 0 m/s at 1 km. According to Rotunno *et al.* 1988, the shear with our settings leads to the formation of a strong and long-lived squall line, perpendicular to the background wind. The uniform surface wind is subtracted when calculating surface fluxes, to avoid this simulation from having significantly higher surface fluxes. The radiative fluxes are imposed, because interactive radiation leads to some radiative feedbacks that disfavors the organization into squall lines. The convection quickly organizes into a line, after about 1 day of simulation.

5.2.2 Definition of mesoscale subdomains

In order to investigate the isotopic composition within the mesoscale structure of our simulated squall lines, we divide the grid points into four sub-domains: convective, stratiform, trailing, and environment, as detailed in the paper. Given the continuous transition in our simulations, we define the convective and stratiform sub-domains based on a precipitation threshold.

Specifically, the convective region (blue rectangle Figure 5.1) corresponds to precipitation above a threshold, adjusted to coincide with the transition from condensation through the entire troposphere to condensation above the melting level and rain evaporation below (Figure 5.1c), consistent with the transition from the convective to the stratiform region (Chong and Hauser 1990; Gamache and Houze Jr 1983). The stratiform region (pink rectangle Figure 5.1) corresponds to precipitation below a threshold, which was adjusted to coincide with the maximum extension of the anvil clouds, consistent with the typical structure of a squall line (Houze 1977). The horizontal winds near the surface spread the cold pool rearward beyond the precipitating region. We also define a sub-domain called ″trailing″ (yellow rectangle Figure 5.1) with temperature colder than a threshold ($T(x) \leq T(x_{gust}) - 1$, where T is the near-surface temperature in K and the gust is located at the front of the squall line, see Risi *et al.* 2023 for details). All grid points that are not categorized as ″convective,″ ″stratiform″ or ″trailing″ are called ″environment″ (white in Figure 5.1).

In the following, we aim at understanding how the isotopic composition of water vapor and precipitation vary in each of these subdomains in squall line simulations.

5.3 Results: what controls the mesoscale variations in water isotopic composition within squall lines?

5.3.1 How does the water isotopic composition vary within the mesoscale structure of simulated tropical squall lines?

Before we discuss the evolution of the isotopic composition of water vapor within subdomains in simulated tropical squall lines, we start by documenting the evolution of surface variables of the squall line shown in Figure 5.2. As shown in Figure 5.2a, the precipitation rate is maximum just after the gust front (dashed red line), consistent with observations (Chong 2010). The precipitation maximum is located where the along-x near-surface surface wind becomes null (Figure 5.2c), favoring the maintenance of strong updrafts (Rotunno *et al.* 1988). Elsewhere, the surface wind blows rearward. Near the gust front, the temperature drops and the relative humidity rises (Figure 5.2b). The recovery to their environment value is slow due to the rearward advection. Our simulated squall line shows only one precipitation peak. This is at odds with observations that often show two peaks, one for the convective region and one for the stratiform region, separated by a transition region (Biggerstaff and Houze 1991; Chong 2010). In our simulation, the convective region transitions continuously to the stratiform region. Increasing the horizontal resolution to 1 km did not help to simulate a transition region.

We plot composites of meteorological and isotopic variables as a function of the along-x distance to the gust front (Figures 5.1). In spite of this shortcoming, the convective and stratiform regions of the squall line can be identified from water vapor tendencies (Figure 5.1c). The convective region can be identified by its intense condensation throughout the entire troposphere (Figure 5.1c, around 50–60 km). The stratiform region can be identified by the condensation restricted to the upper troposphere (the anvil) and evaporation below (mesoscale downdraft) (Figure 5.1c, around 60–80 km). This pattern of condensation and evaporation is consistent with what we know from the squall line water budgets (Chong and Hauser 1990; Gamache and Houze Jr 1983).

Simulated squall lines show a progressive depletion of the vapor in the convective region, maximum depletion at the end of the convective region, and a long recovery in the stratiform and trailing regions (Figure 5.2e). The δD_v reaches its environment value about 100 km after the convective peak.The δD_p varies in concert with δD_v (Figure 5.2d). In the convective and stratiform regions, δD_p is lower than in equilibrium with the vapor (green in Figure 5.2e), consistent with a quick fall and little evaporative enrichment. The weak precipitation that falls upwind of the convective region, where the air is dry, has a δD_p higher than that in equilibrium with vapor, indicating evaporative enrichment during rain evaporation. The d-excess in the vapor is

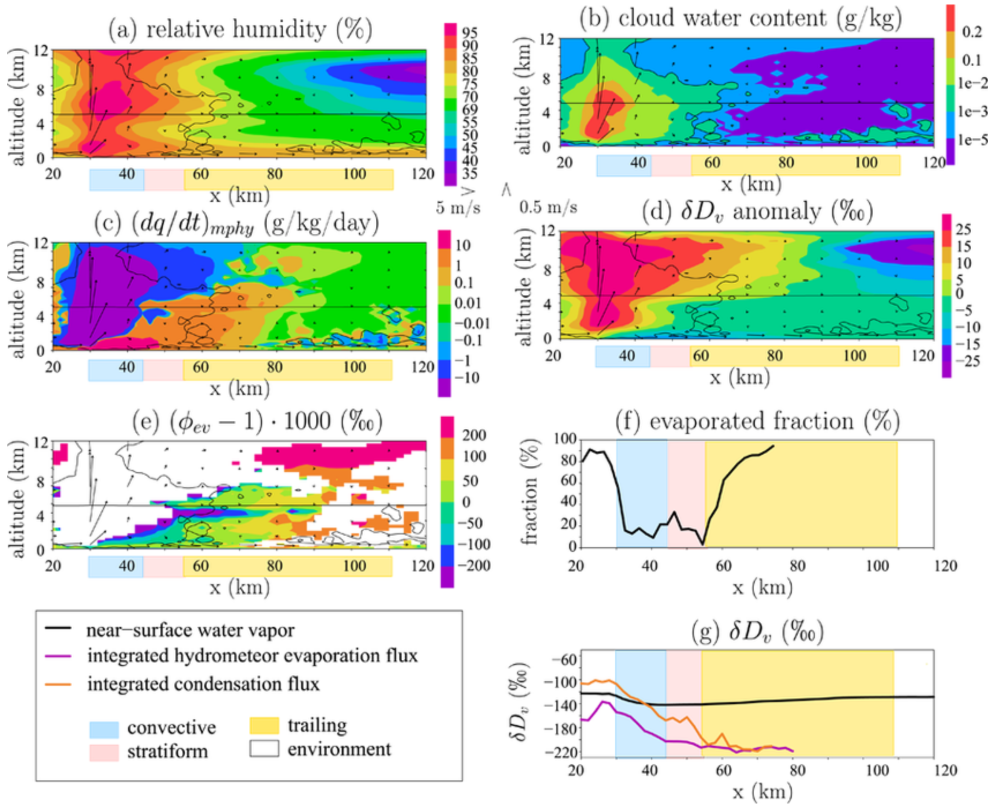

Figure 5.1: Variables as a function of altitude and of the distance along x-axis: (a) Relative humidity; (b) cloud water content (cloud condensate and cloud ice); (c) specific humidity tendency due to phase changes (negative and positive values represent condensation/deposition and evaporation/sublimation respectively); (d) water vapor δD anomaly relative to the domain-mean δD_v at each level; (e) $(\varphi_{ev} - 1) \times 1000$, where $\varphi_{ev} = R_{ev}/R_v$ is the relative enrichment of the isotopic ratio of the hydrometeor evaporation/sublimation relative to the water vapor isotopic ratio. φ_{ev} is shown only when significant hydrometeor evaporation/sublimation occurs; (f) fraction of the vertically integrated condensation flux that evaporates before reaching the ground; (g) δD in the near-surface vapor (black), in the vertically integrated condensation flux (orange) and in the vertically integrated evaporation flux (purple). The vertically integrated condensation and evaporation fluxes are calculated as the volumetric-mass weighted integrals of the specific humidity tendency due to phase changes (c) where the tendency is respectively negative and positive. In (a-e), the vectors show the radial and vertical components of the wind, with the vertical wind multiplied by 20 for better readability. The nearly horizontal black line shows the 0C isotherm. The black contours highlights the 10^{-3} g/kg contour for cloud water content. The blue, pink, and yellow boxes indicate the convective, stratiform, and trailing regions.

higher in the convective and stratiform regions, and to a lesser extent in the trailing region, than in the environment (Figure 5.2f). The low d-excess in the precipitation reflect the effect of evaporative enrichment, especially before the gust front and in the trailing region.

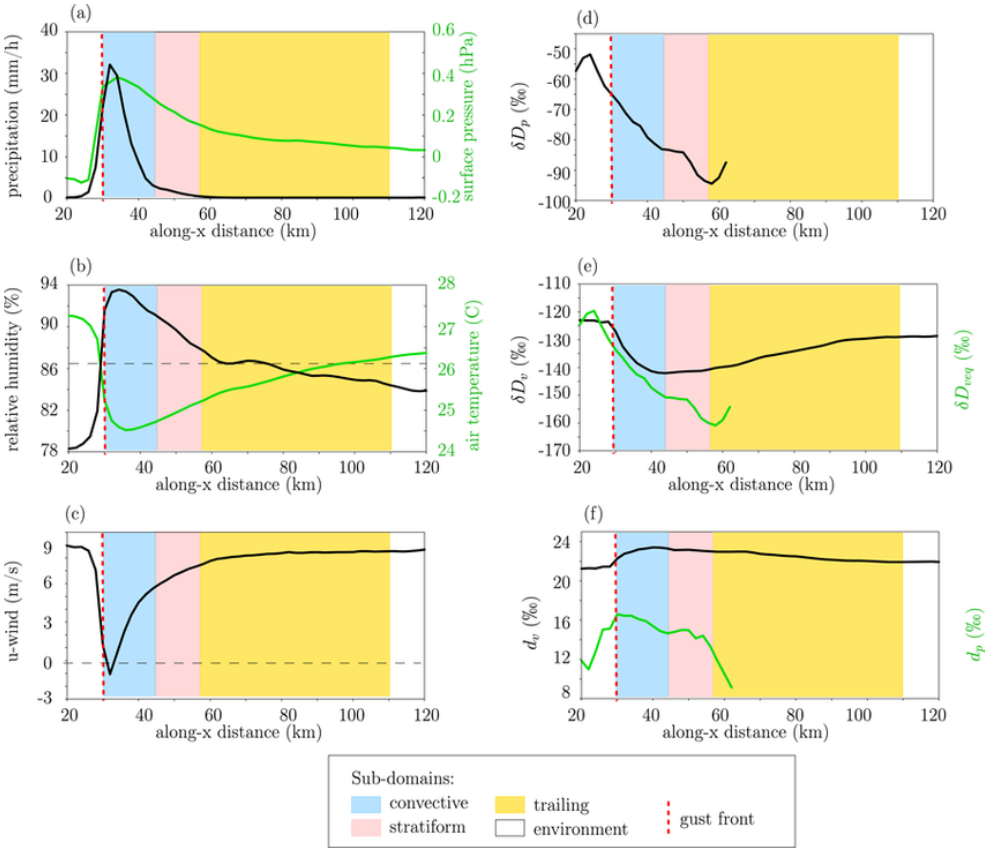

Figure 5.2: Evolution of surface variables as a function of distance along the x-axis: precipitation rate (a, black), surface pressure (a, green), near-surface air temperature (b, black), near-surface relative humidity (b, green), tangential (c, black) and radial (c, green) wind, surface precipitation δD_p (d), near-surface water vapor δD_v (e, black), water vapor $\delta D_{v,eq}$ that would be in equilibrium with the precipitation (e, green), near-surface water vapor d-excess d_v (f, black) and precipitation d-excess d_p (f, green). The colored rectangles indicate the convective (blue), stratiform (pink), and trailing (yellow) sub-domains defined in Section 5.2.2. The location of the gust front is indicated by the vertical red dashed line.

5.3.2 Is it consistent with observed squall lines?

Investigation of the vapor isotopes of the squall lines in the Sahel showed that the isotopic evolution can be diverse, but some robust features emerge (Tremoy *et al.* 2014):

- Isotopic observations during squall lines often show a ″W″ shape with minimum δD_p in the convective and stratiform regions and a local maximum in the transition region (Risi *et al.* 2010). Our simulation is consistent with this observation, except that since our simulation does not exhibit any transition region, it shows a ″V″ shape instead of a ″W″ shape.
- In 80% of 74 observed squall lines (Tremoy *et al.* 2014), there is a depletion in the convective region compared to the environment before the squall line. This is consistent with our simulation.
- More than half of the observed squall lines show additional depletion in the stratiform region (Tremoy *et al.* 2014). This is also consistent with our simulation.
- For squall lines showing an isotopic depletion in the convective or stratiform region, the recovery from this depletion takes several hours after the end of the rain (Tremoy *et al.* 2014). Considering a propagation speed of about 20 m/s, this is consistent with the recovery distance of about 100 km in our simulation.
- In 78% of observed squall lines, the ″W″ shape often observed in the precipitation is not observed in the vapor (Tremoy *et al.* 2014). Our simulations are thus consistent with this majority of squall lines

Our simulated isotopic evolution during the squall line thus captures the features that are most commonly observed in squall lines. Some squall lines may feature different variations, and even enrichment in the convective and stratiform regions (Tremoy *et al.* 2014). To check whether our simulations could capture such a diversity of isotopic variations, we performed many sensitivity tests, including simulations without large-scale ascent, with large-scale ascent peaking in the upper troposphere to favor stratiform development (Su *et al.* 2000), increased horizontal resolution, interactive radiation, reduced sublimation or reduced rain evaporation to favor the maintenance of the stratiform region (Bryan and Morrison 2012; Yang and Houze Jr 1995), bowling alley domain, or prescribed horizontal wind in the upper troposphere to favor the development of the stratiform region (Caniaux *et al.* 1994). Depending on the simulations, the stratiform region is more or less extended and the squall lines are more or less organized, but the meteorological and isotopic evolution is always similar. We thus keep in mind that our simulations match the majority of squall lines, but not all of them.

5.3.3 What are the physical processes at play?

At this point, our simulations succeed in reproducing a realistic variation of water vapor and precipitation isotopic composition variations. This allows us to go a step further and investigate the physical mechanisms that explain the progressive depletion of the vapor in the convective region, maximum depletion at the end of the convective region, and a long recovery in the stratiform and trailing regions. In the paper, using a simple model for the subcloud layer (not included here, since this chapter focuses on my own contributions to this work which are the numerical results), rain evaporation and diffusive exchanges are found to be the dominant contribution in depleting the water vapor under the convective and stratiform regions of the squall line. This depletion is due to the higher condensation altitude, the lower evaporated fraction of the rain and the moister air in which the evaporation occurs (not shown).

To confirm the effect of rain evaporation and rain-vapor diffusive exchanges in our simulations, additional runs in which these effects are de-activated were performed, as in Field *et al.* 2010; Risi *et al.* 2021. The fractionation coefficients were set to unity during all post-condensational processes. This impacts the simulation of isotopic variables, but not the simulation of meteorological variables. In squall line simulations, δD_v would be higher without fractionation during rain evaporation than with fractionation (solid lines in Figures 5.3), and the rain would be more depleted than if in equilibrium with the vapor (dashed lines in Figure 5.3). The δD_p would be minimum under the stratiform region in the squall line simulation, reflecting the higher condensation altitude in these regions. With fractionation during rain evaporation, the rain-vapor diffusive exchanges make the vapor more isotopically enriched and the rain more isotopically depleted, thus bringing the rain and the vapor close to isotopic equilibrium (black lines in Figure 5.3). This explains why δD_v and δD_p vary in concert. The δD_v is most negative where the condensation forms high in altitude and where the rain rate is strong enough to isotopically impact the water vapor. This explains why the δD_v is most negative near the transition between the convective and stratiform region for the squall line (black solid lines in Figures 9a and 9b). Without fractionation during rain evaporation, the mesoscale δD_v variations would be strongly reduced (Figure 5.3d). Peak-to-peak variations are respectively 18‰ and 8‰ in the squall line case. This confirms the key role of rain evaporation and rain-vapor diffusive exchanges to deplete the low-level water vapor at the mesoscale scale.

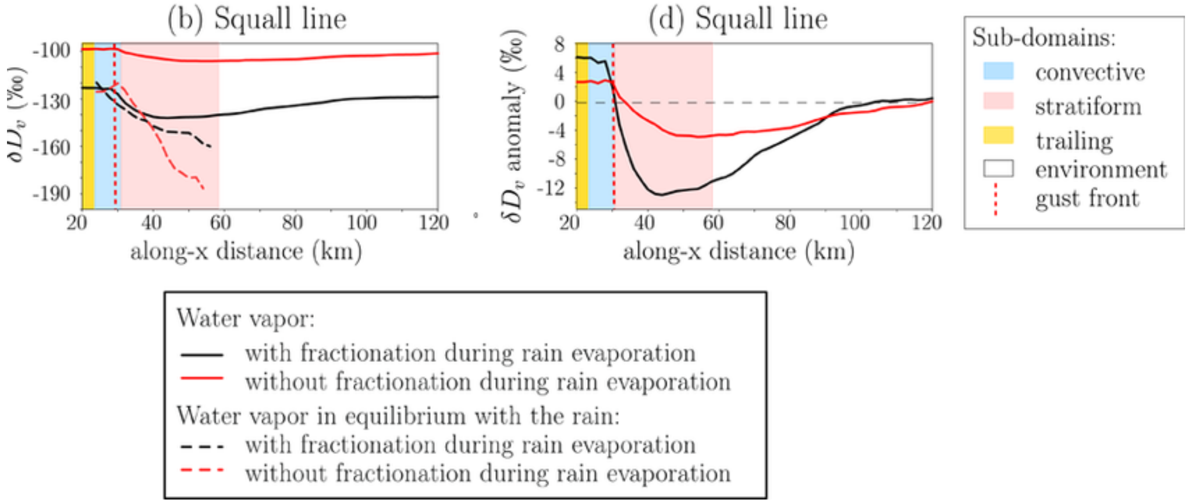

Figure 5.3: Results of the simulations with de-activated fractionation during rain evaporation. (b) Evolution of near-surface δD_v (solid) and of the water vapor δD in equilibrium with the near-surface precipitation (dashed) as a function of x for squall lines. in simulations where rain evaporation and rain-vapor diffusive exchanges are activated (black) and de-activated (red). Evolution of the near surface δD_v anomaly relative to the environment as a function of x for squall lines (d). This figure is adapted from panels b and d of figure 9 in Risi *et al.* 2023.

5.4 Conclusion

Using CRM simulations of squall lines, we investigate how convective processes impact the isotopic composition of water vapor and precipitation at the mesoscale. We show that the main factors depleting heavy isotopes of the water vapor at the mesoscale is rain evaporation, especially in the mesoscale downdraft of the stratiform region in squall lines (purple in Figure 5.4). These mechanisms are overall consistent with those suggested in previous studies (Tremoy *et al.* 2014). This study contributes to our understanding of mesoscale isotopic variability. It provides physical arguments for the more depleted rain observed in squall lines relative to the rain in small-scale convection. Therefore, this study supports the interpretation of paleoclimate isotopic archives in tropical regions in terms of past frequency of large, long-lived, organized convective systems such as squall lines (Maupin *et al.* 2021). However, when considering paleoclimate records at the annual scale or larger, the isotopic composition reflects an average over many convective systems of different organization types. In our simulations, this is equivalent to the domain-mean δD in simulations of squall lines relative to the domain-mean δD in simulations of isolated cumulonimbi, rather than the δD in squall lines relative to their environment in a given simulation. This paper focuses on mesoscale isotopic variations and does not discusses domain-mean values, because the realism of simulated mesoscale variations could be more easily

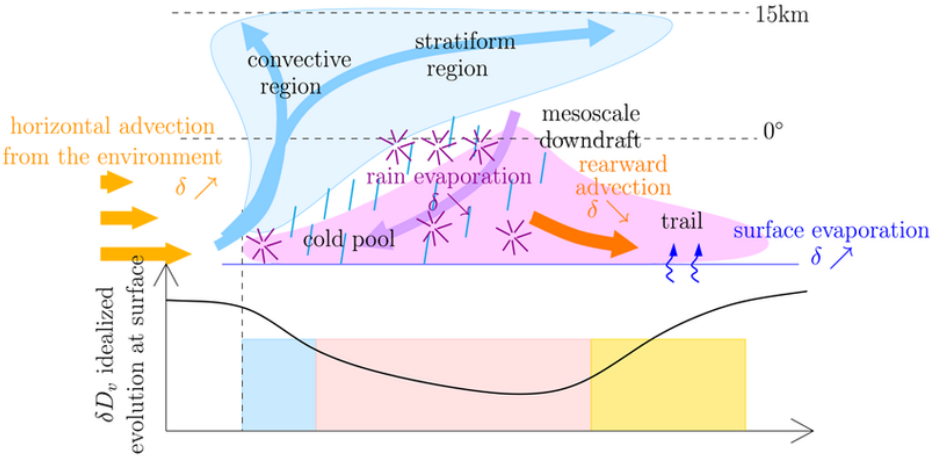

Figure 5.4: A schematic of the processes controlling the water vapor composition inside squall lines. The key driver is rain evaporation, indicated by purple stars. Rain evaporation depletes water vapor in the convective and stratiform regions of squall lines. Horizontal advection then reshapes this pattern. Dark orange arrows indicate horizontal advection from depleted regions to less depleted regions, contributing to the spread of the depleted anomalies rearward in squall lines. Light orange arrows indicate horizontal advection from less depleted regions to more isotope depleted regions, partially compensating the depletion in most depleted regions.

assessed than the realism of domain-mean values.

In parallel, the interplay between large-scale circulation and convective organization deserves to be better documented in observations. To rigorously assess the role of convective organization, we would need to compare isotopic observations for different kinds of convective organization but for the same precipitation rate and large-scale context, as is now done for humidity (Tobin *et al.* 2012). This will allow us to rigorously assess the realism of the domain-mean isotopic composition in our simulations and will be the subject of a future study. Finally, many other processes need to be investigated before drawing any paleoclimate conclusions from this study, including large-scale horizontal advection (Chen *et al.* 2021), land-atmosphere interactions along the air mass trajectories, infiltration processes. Our study is a first step toward a more comprehensive understanding of water isotopic variations.

Chapter 6

Conclusion and Perspectives

Conclusion and Perspectives

6.1 Conclusion

The overarching goal of this thesis was to enhance the understanding of mesoscale convective organization as well as the prediction of extreme rainfall events. These two topics are interrelated as organized convection is strongly associated with extreme weather. This work has eventually participated in clarifying how and why physical processes leading to the formation of MCSs are precisely those which favor precipitation extremes.

The first part of this thesis focused on clarifying the interactions between mesoscale convective systems and their environment. To that end, we started with an idealized approach (Chapter 2), investigating in detail a specific environmental factor, namely wind shear, and its impact on squall lines in radiative-convective equilibrium simulations. Using a cloud-resolving model (CRM), we conducted multiple simulations of squall lines while progressively increasing the wind shear. Our study concluded that **as wind shear increases beyond optimal, squall lines maintain their optimal degree of organization by orienting themselves**, confirming hypotheses previously formulated by RKW Rotunno *et al.* 1988 and later by Robe and Emmanuel Robe and Emanuel 2001. Our study introduces a quantitative and replicable method for determining the orientation of squall lines. Through autocorrelation image analysis of integrated humidity profiles derived from cloud-resolving simulations, we determined the orientation of squall lines across suboptimal, optimal, and superoptimal regimes. Our findings supported the hypothesis that line orientation maintains an equilibrium between the projected basal wind and the spread of cold pools. Furthermore, we explored the characteristics of cold pools and their evolution under the influence of wind shear. Our observations revealed that increased shear-induced drying in the lower atmosphere led to more intensified and deeper cold pools. However, the influence of intensified cold pools on squall line orientation remained secondary.

We then extended our detailed idealized study, with a comprehensive analysis of a large number of MCSs in realistic simulations (Chapter 3). We examined tropical mesoscale convective systems (MCSs) and the role of their initial environmental conditions in their potential to grow to a significant size (more than 140 km in characteristic size). To achieve this, we utilized high-resolution global simulations from the SAM-DYAMOND project coupled with the MCS tracking algorithm TOOCAN. Using machine learning tools, we demonstrated that **the initial, namely the first hour, environmental and internal properties of Mesoscale Convective Systems largely deter-**

mine their maximum size. The growth rate observed within the first two hours of MCS development emerged as a strong predictive factor, yielding a regression score of 0.8, irrespective of the system's eventual lifespan. By incorporating additional features related to shape, physical fields, trajectory, and the influence of neighboring systems, we refined our prediction interval to just one hour, achieving a regression score of 0.7. Throughout our comprehensive study, we gained a deeper appreciation for the importance of both the initial developmental stage and the surrounding conditions. Interestingly, the presence of neighboring systems seemed to impact the ultimate fate of MCSs, for reasons which are hypothesized in the relevant chapter (Chapter 3). Despite earnest efforts to establish connections between prediction errors and various factors, identifying robust links proved challenging, highlighting the need for ongoing research.

These systems are associated with extreme weather conditions, including extreme rainfall rates. Recent observations show that most of the regional increase of tropical precipitation is associated with changes in the frequency of organized convection Tan *et al.* 2015. A natural question then, is whether the processes which modulate the degree of convective organization, investigated in the first part of this thesis, also impact the occurrence of extreme rainfall, and if so why.

The second part of this thesis investigated how convective organization influenced precipitation extremes and whether the processes driving system formation specifically favored extreme events. Once again, we started in idealized settings, exploring the factors contributing to amplified extreme rainfall rates in squall lines using idealized cloud-resolving simulations (Chapter 4). We examined how precipitation extremes varied across different regimes of squall lines—suboptimal, optimal, and superoptimal—induced by controlling low-level wind shear levels. Our findings demonstrated that the intensity of precipitation extremes is influenced by the type of squall line regime. **We observed a gradual increase in precipitation extremes in the suboptimal regime, up to a $30-40\%$ increase in the optimal regime, followed by a plateau at a $20-30\%$ increase in the superoptimal regime**. To understand these patterns, we applied a theoretical scaling approach based on vertical advection, condensation and precipitation efficiency. To bypass the limitation associated with the time delay between condensation and precipitation in the cloud life cycle, we applied this scaling statistically across percentile ranks (i.e. a high percentile of condensation was assumed to lead to a high percentile of precipitation). We determined that the enhancement of precipitation extremes primarily arose from increased condensation rates driven by dynamics, for which the dilution effects of entrainment and the cloud-base updraft velocity played a major role. Microphysical and thermodynamic contributions played a secondary role.

The final chapter of this thesis, which is based on collaborative work, focused on the long-term impacts that squall lines can leave, especially their influence on the isotopic composition of water. Isotopic paleotempestology, a method involving the identification and dating of ancient weather events, could enable the reconstruction of past squall line frequencies; which brings new opportunity to investigate the interplay between these systems, their environment and the climate. To achieve this, it is imperative to acquire a more comprehensive understanding of the signature of these systems on the isotopic composition of sub-cloud layer water vapor and also the underlying processes at play. Using idealized simulation in a cloud resolving model, **this study shows that simulated squall lines show a progressive depletion of the vapor in the convective region, maximum depletion at the end of the convective region, and a long recovery in the stratiform and trailing regions**. In both the convective and stratiform parts of the squall line, the depletion relative to the environment is mainly due to the rain evaporation and rain-vapor diffusive exchanges in the subcloud layer.

Collectively, these studies provided a multifaceted exploration of convective systems, shedding light on mechanisms at the origin of squall line orientation as well as the link between early-stage development and mature stage. What we discovered is the profound relationship between processes leading to the system's shape and those enhancing extreme precipitation, especially in the case of squall lines and shear-convection interaction. In fact, interaction of wind shear and cold pool spreading not only enhance convective organization but also mainly contribute to enhance extreme precipitation. While each chapter focused on a distinct aspect, all the chapters together converged to emphasize the intricate relationship between the system and its environment. This work attempted to provide certain answers, but it also undoubtedly generated new questions spanning the short and longer terms, as described next.

6.2 Perspectives

6.2.1 Short Term

Can our findings be extrapolated to datasets with higher realism? The findings presented in this study were based on cloud-resolving models, applied within the context of either radiative convective equilibrium or global-scale simulations. This approach has represented a significant advancement in the comprehension of intricate processes encompassing the genesis and orientation of tropical squall lines, along with the enhancement of precipitation events. Moreover, this has facilitated the elucidation of interrelationships existing between internal attributes and external factors associated with MCSs as they transition into their mature phases. Building upon these findings, a natural question that I plan to address, is whether these results hold in more realistic simulations and in observations.

Can we observe the different developmental regimes of squall lines in high-resolution global simulations? If so, is the RKW theory validated in this context? Are the characteristics of the cold pools similar to those observed in RCE?

Investigative Hypothesis: As studied in idealized RCE configuration, observed super-optimal squall lines should be oriented at an angle that restores the equilibrium between wind shear and cold pool spreading. Is this verified in realistic high-resolution global simulations?

To observe squall lines in Global Cloud-Resolving Models (GCRMs), a preliminary approach could focus on West Africa where squall lines are frequent. However, several studies have indicated that squall lines in this region are consistently in suboptimal or optimal configurations and do not orient themselves. There are other areas where the orientation of squall lines is visible and can even be parallel to the wind shear (Grant *et al.* 2020). In highly humid zones, cold pools tend to be weaker due to reduced rain evaporation (Liu and Moncrieff 2017). The primary objective of this project would thus be to detect all tropical squall lines in order to identify cases exhibiting superoptimal regime characteristics. We would use the MCS tracking algorithm TOOCAN on DYAMOND-SAM simulations, focusing on those MCSs that exhibit squall line attributes.

This project has already started, since we collaborated with undergraduate (L3) and graduate (M2) interns to develop a characterization method for squall lines in GCRMs. Previous attempts to classify MCSs and detect squall lines has been conducted, by using initially the Jirak classification which only depends on morphological criteria (Jirak *et al.* 2003). They defined mesoscale convective complexes (MCCs), persistent elongated convective systems (PECSs), meso-β circular convective systems (MβCCSs), and meso-β elongated convective systems (MβECSs), in which squall lines are included. However, considering only shape indices could not differentiate squall line from convective lines, which are similar but lack the shear/cold pool equilibrium, often being stationary without rear flow.

The second approach involved characterizing squall lines based on the dynamic pattern of the cold pools. This was motivated by a recent study which differentiated spiraling bands from squall lines based on these criteria (Yu *et al.* 2018). An unexpected obstacle was that squall lines were mistaken with the ITCZ's edge itself. In fact, the ITCZ, when it is thin enough, shows similar dynamical characteristics with squall lines (Beucler *et al.* 2020; Windmiller and Stevens 2023), with a strong interaction between wind and cold pools at it edge (see figure 6.1).

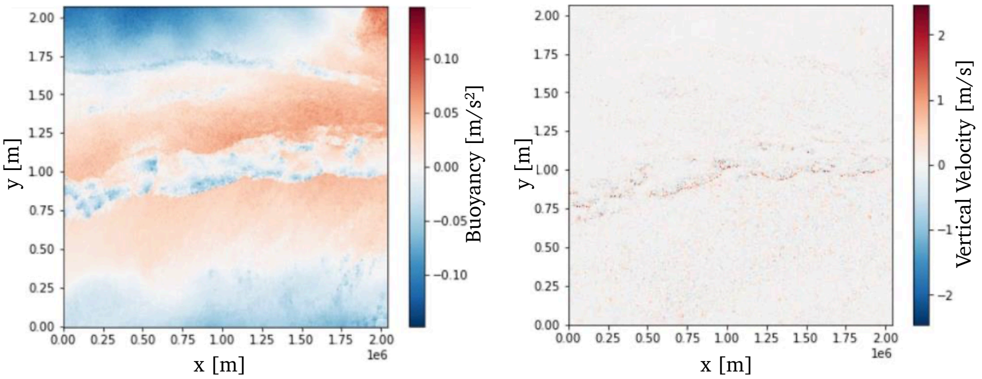

Figure 6.1: Buoyancy field (left) and vertical velocity (right) near the edge of ITCZ in DYAMOND-SAM winter. The ITCZ is similar to a line of MCSs and has been detected in this figure using morphological criteria.

The quest of squall lines is a demanding path, and might get insight from new tools from artificial intelligence. Using unsupervised machine learning models, similar to Denby 2020, on dynamically based selected squall lines, systems can be clustered in a reduced order space. During the collaboration with interns, dataloaders and systems filtering have been implemented to pursue this objective.

Detecting squall lines in GCRMs is an intriguing challenge as it raises questions about system characterization. The explorations described, stemming from co-supervised internships with Camille Risi, instill confidence in achieving this goal. Subsequently, the aim is to measure squall line orientation and compare it to the theoretical RKW model using the methodology outlined in Chapter 2.

Special attention will be given to cold pools and their properties in terms of temperature anomalies and depth. A recent study has investigated cold pools in global high resolution simulations (Garg *et al.* 2022) from DYAMOND-ICON. The method used here is a threshold in virtual temperature. Physically based definition of cold pool methods (Rochetin *et al.* 2021; Zuidema *et al.* 2017b) can be used in these GCRMs to improve the description and understanding of involved processes. Once this methodology validated in GCRMs, a similar analysis could be conducted in satellite observations in the long run.

In high-resolution global simulations, what are the rates of precipitation extremes? Does the developmental regime of squall lines influence precipitation extremes? Which contributions, dynamic, thermodynamic, or microphysical, dominate across the different regimes?

Investigative Hypothesis: Building upon our results in idealized CRM simulations, precipitation extremes are expected to follow the developmental regimes of squall lines. Specifically, they should increase in the sub-optimal regime, peak in the optimal regime, then slightly decrease and remain constant in the super-optimal regime. Continuing from our previous conclusions, the dynamic contribution should dominate precipitation scaling, especially with the initiation speed at the edges of cold pools. However, large-scale circulation might play a role in cell initiation, potentially amplifying or inhibiting this effect.

To test this hypothesis, we can use the method of squall line detection in GCRM described in the previous paragraph. For each squall lines, we can compute the extreme of precipitation within its life cycle, the highest percentiles of condensation rates, as well as the dynamic and thermodynamic contributions. Although not all dynamical variables may be easily obtained from observations, a similar investigation of precipitation extremes in squall lines could be conducted in observations in the long run.

Can the prediction of maximum MCS area from the first hour of development be applied to nowcasting methods?

Investigative Hypothesis: Our method can be applied to observational data and should yield similar results, provided that spatial resolution and important features are available.

The use of GCRMs in Chapter 3 was motivated by the availability of dynamic fields, which are more difficult to access with satelite data. The final results of our study in chapter 3 shows that a good approximation of the maximal extension of MCSs can be reached only with the growth rate of area. Moreover, features from the systems and the environment can be added to improve the prediction and this does not entirely rely on dynamic variables. This is why the method can be transposed to observationnal data, such as satellite observation. Databases (Fiolleau *et al.* 2020) include 5-year period of observational data for each region of interest (Eastern-Pacific, America, Africa, India, Western-Pacific). A notable difference between observation and simulation is the stratiform zone which is often underestimated in simulations (Feng *et al.* 2023), leading to bias in area prediction. Our object-oriented approach could shed new light into the origin of this bias. If the results prove satisfactory, it would be valuable to test them in real-time, a possibility enabled by the TOOCAN tracking algorithm. Preliminary discussion with researchers from Meteo-France and NOAA have been started to question whether these methods are suitable for nowcasting predictions.

What is the archetype of unpredictable MCS?

Investigative Hypothesis: What our study has revealed is that predicting the maximum area based on scalar data of the system and its environment at a 1-hour interval plateaued at a regression score of 0.7. A preliminary endeavor was made to correlate the model's error with other data, such as the final lifespan, the presence of a coastline, or propagation velocity, but without success. One missing piece of data could be the spatial structure of the system and the presence of a pattern, whether in humidity or temperature, that could serve as a signature for conditions conducive to system expansion.

The objective of this project would be to identify systems for which the model exhibits significant errors based on the findings from Chapter 3 and to describe their characteristics and those of their environment in a two-dimensional manner. In other words, it would involve creating a profile of these systems. This follows the approach of Roca *et al.* 2017 unifying MCSs life cycle but this time applied to the subset of MCSs whose expansion is not well predicted by mean fields.

Subsequently, a machine learning model trained directly on images of fields, rather than simply on scalar features, could be developed to predict the area and components of the systems' life cycle (Reichstein *et al.* 2019; Schiro *et al.* 2020). Convolutional neural network models have the capability to extract patterns and pattern co-localizations by applying successive filters that are optimized during training. These methods show promise for such applications (Shamekh *et al.* 2023).

6.2.2 Long Term

My post-doctoral and longer term research will subsequently enable me to address a more fundamental question : *What explains the variability of Mesoscale Convective Systems within a given environment?* It is a continuation of the previous section 6.2.1, but investigating in more detail the physical processes behind this variability.

The environment of a mesoscale convective system (MCS) is generally defined as combination of large-scale factors that surround it. Among these factors are the dynamic and thermodynamic fields, geographical and topographical features, the influence of equatorial waves, the mesoscale circulation (shallow or deep), and the presence of other nearby cloud systems. The boundary between the system and its environment is not well-defined, for at least two reasons. The first reason is the existence of a smooth transition between the system and its environment, particularly due to cloud-edge entrainment and detrainment. The second reason is that the system affects the environment through feedback mechanisms; in other words, the definition of the environment changes over the life cycle of the system. Furthermore, the existing literature does not specify whether external factors like equatorial waves or self-aggregation feedbacks should be regarded as inherent environmental features or as factors influencing the environment.

Despite those challenges, previous studies show that ”the environment” plays a significant role in the expansion rate of MCSs (Elsaesser *et al.* 2022; Machado *et al.* 2004; Yuan and Houze 2010), but internal variability persists even when observing MCSs for a given environment. In Chapter 3, a multilinear model was developed to explain the variability of MCS areas based on environmental features and system-specific features, see figure 3.12. This study shows that for a given environment, there is a certain variability in the area of the system. Building upon this observation, the objective of this project is to quantify this variability and comprehend the underlying physical processes. Ultimately, this question could help introduce a new definition of environnement based on its impact on MCSs.

To address this question, we will investigate three main avenues: the influence of self-aggregation feedbacks, the role of synoptic forcings, and the population dynamics of MCSs, as discussed in more detail below. All these processes can influence the expansion of the systems. The goal of this project is not to predict the size of the systems anymore but to understand what explains the variability of systems area in an environment under the influence of the aforementioned phenomena.

The role of self-aggregation feedbacks

The variability in the size of systems within a specific environmental context can be attributed to the presence of self-aggregation feedback mechanisms. These mechanisms are well-established (Muller *et al.* 2022) and encompass phenomena such as intensified radiative cooling in arid regions, coupled with shallow divergent atmospheric circulations, turbulent entrainment of ambient air, the formation of cold pools in the boundary layer driven by evaporation, and the emission of boundary layer waves. Nonetheless, uncertainties persist regarding the occurrence of self-aggregation in observation as discussed in Holloway *et al.* 2017; Muller *et al.* 2022. The utilization of Global Cloud-Resolving Models in investigating aggregation feedbacks offers a novel perspective on these intricate processes.

In the realm of numerical modeling, previous research has explored the impact of radiative feedback on convective organization and, more specifically, on cyclone characteristics. For instance, Muller and Romps 2018 conducted investigations aimed at elucidating whether self-aggregation feedbacks can expedite tropical cyclone genesis. Their findings underscored the significance of longwave radiative cooling at lower atmospheric levels outside the cyclone, along with the associated low-level circulation, as crucial factors influencing cyclone genesis and intensification. Observations also show a link between the degree of organization and drying of the environment (Tobin *et al.* 2012).

Current understanding is that we postulate that environments exhibiting aggregation feedback mechanisms are predisposed to yielding a less diverse range of sizes among MCSs, with more intense systems (Da Silva *et al.* 2021). The novelty of our research lies in its dual approach: firstly, in examining the relationship between aggregation and MCSs within Global Cloud-Resolving Models (GCRMs), and secondly, in establishing a connection between aggregation indices and the distribution of MCS sizes.

The role of synoptic forcing

A second factor that appears to be instrumental in shaping an environment's capacity to generate a diverse array of systems pertains to the broader-scale impacts arising from synoptic forcing, including factors like the presence of wind shear or interactions with equatorial waves.

Many studies show the impact of larger-scale synoptic features on MCSs. The Madden-Julian Oscillation (MJO), widely acknowledged as the prevailing mode of tropical intraseasonal variability (e.g., Kiladis *et al.* 2009; Zhang and Delworth 2006), encompasses convective organization spanning a spectrum of scales, ranging from the local cumulus level to the planetary scale. This includes the formation of cloud clusters and superclusters on intermediary scales (Nakazawa 1988) and exerts its influence across a comprehensive spectrum of meteorological and climatic phenomena (Lau and Waliser 2011). The El Niño-Southern Oscillation (ENSO) is also known to influence MCSs properties (Sullivan *et al.* 2019). The established correlation between convective system aggregation and equatorial waves has been extensively investigated in prior research. For example, in a previous study, Sakaeda and Torri 2022 elucidated the interplay between aggregation phenomena and the MJO, demonstrating that the frequency of system occurrences tended to rise with positive moisture anomalies induced by the MJO.

Recent findings by Cheng *et al.* 2023, utilizing satellite data, have brought to light the modulation of MCS properties by convectively coupled equatorial waves (CCEWs). Their observations indicate that MCSs manifest heightened precipitation intensities, produce greater cumulative rainfall over their lifecycle, and undergo size expansion during instances of alignment with the active phases of CCEWs. Future research could involve the application of this investigative methodology (collocating variables that capture wave amplitude with the Lagrangian tracks of MCSs) in GCRMs to investigate the influence of equatorial waves within specific environmental contexts. By clarifying the impact of anomalies associated with waves (including moisture, wind shear and large-scale vertical velocity) on MCS growth, this work could also help shed light into the impact of ENSO and the MJO on MCSs.

The role of population dynamics of MCSs

The third avenue for elucidating the variability in the size of systems within a given environment lies in comprehending the population dynamics of mesoscale convective systems, and the influence of neighboring systems. Pioneering studies in this domain, such as Mapes 1993, demonstrated that gravity waves generated by the formation of convective clouds induce a circulation pattern at low levels within a mesoscale vicinity surrounding the system. Consequently, conditions near an existing MCS, albeit beyond the MCS outflow region, become more conducive to the initiation of additional convection.

Furthermore, research by Feng *et al.* 2015 (and also Haerter 2019; Sakaeda and Torri 2023; Schlemmer and Hohenegger 2014) underscores the interaction between convective clouds through the dynamics of their cold pools and their interaction with moisture (notably over land Chaboureau *et al.* 2004). For example, utilizing data from the AMIE/DYNAMO field campaign, they illustrated that intersecting cold pools engender larger clouds with reduced spacing between them.

Lastly, another mechanism likely capable of influencing the variability in system size is convective inertia, often referred to as ”convective memory,” as highlighted by Colin and Sherwood 2021. Their study demonstrates that a predator-prey model incorporating memory effects can replicate certain characteristic convective phenomena, where small-scale atmospheric structures exhibit a persistent appetite for large-scale convective potential.

The objective of this project is to investigate the amplitude of all these feedbacks in GCRMs comparing systems that have neighboring convective systems to those which evolve alone. At larger scale, the morphology and climatological variability of MCSs lay the groundwork for determining the radiative effect of MCSs on the tropical circulation Yuan and Houze 2010.

List of Figures

Bibliography

[1] T. H. Abbott, T. W. Cronin, and T. Beucler, “Convective dynamics and the response of precipitation extremes to warming in radiative–convective equilibrium,” *Journal of the Atmospheric Sciences*, vol. 77, no. 5, pp. 1637–1660, 2020.

[2] S. Abramian, C. Muller, and C. Risi, “Shear-convection interactions and orientation of tropical squall lines,” *Geophysical Research Letters*, vol. 49, no. 1, e2021GL095184, 2022.

[3] P. K. Aggarwal *et al.*, “Proportions of convective and stratiform precipitation revealed in water isotope ratios,” *Nature Geoscience*, vol. 9, no. 8, pp. 624–629, 2016.

[4] A. L. Albright, B. Fildier, L. Touzé-Peiffer, R. Pincus, J. Vial, and C. Muller, “Atmospheric radiative profiles during eurec4a,” 2021.

[5] D. A. Alfaro, “Low-tropospheric shear in the structure of squall lines: Impacts on latent heating under layer-lifting ascent,” *J. Atmos. Sci.*, vol. 74, no. 1, pp. 229–248, 2017.

[6] M. R. Allen and W. J. Ingram, “Constraints on future changes in climate and the hydrologic cycle,” *Nature*, vol. 419, no. 6903, pp. 224–232, 2002.

[7] A Arakawa, “Modelling clouds and cloud processes for use in climate models,” *WMO The Phys. Basis of Climate and Climate Modelling p 183-197(SEE N 76-19675 10-47)*, 1975.

[8] L. M. Baldini *et al.*, “Persistent northward north atlantic tropical cyclone track migration over the past five centuries,” *Scientific reports*, vol. 6, no. 1, p. 37 522, 2016.

[9] N. Ban, J. Schmidli, and C. Schär, “Heavy precipitation in a changing climate: Does short-term summer precipitation increase faster?” *Geophysical Research Letters*, vol. 42, no. 4, pp. 1165–1172, 2015.

[10] J. Bao and S. C. Sherwood, "The role of convective self-aggregation in extreme instantaneous versus daily precipitation," *J. Adv. Model. Earth Syst.*, vol. 11, no. 1, pp. 19–33, 2019.

[11] J. Bao, S. C. Sherwood, M. Colin, and V. Dixit, "The robust relationship between extreme precipitation and convective organization in idealized numerical modeling simulations," *J. Adv. Model. Earth Syst.*, vol. 9, no. 6, pp. 2291–2303, 2017.

[12] T. Becker, C. S. Bretherton, C. Hohenegger, and B. Stevens, "Estimating bulk entrainment with unaggregated and aggregated convection," *Geophysical Research Letters*, vol. 45, no. 1, pp. 455–462, 2018. DOI: `https://doi.org/10.1002/2017GL076640`. [Online]. Available: `https://agupubs.onlinelibrary.wiley.com/doi/abs/10.1002/2017GL076640`.

[13] T. B. Benjamin, "Gravity currents and related phenomena," *Journal of Fluid Mechanics*, vol. 31, no. 2, pp. 209–248, 1968.

[14] A. Betts, R. Grover, and M. Moncrieff, "Structure and motion of tropical squall-lines over venezuela," *Quarterly Journal of the Royal Meteorological Society*, vol. 102, no. 432, pp. 395–404, 1976.

[15] A. K. Betts, "The thermodynamic transformation of the tropical subcloud layer by precipitation and downdrafts," *Journal of atmospheric sciences*, vol. 33, no. 6, pp. 1008–1020, 1976.

[16] A. K. Betts, "Thermodynamic constraint on the cloud liquid water feedback in climate models," *Journal of Geophysical Research: Atmospheres*, vol. 92, no. D7, pp. 8483–8485, 1987.

[17] T. Beucler, D. Leutwyler, and J. M. Windmiller, "Quantifying convective aggregation using the tropical moist margin's length," *Journal of Advances in Modeling Earth Systems*, vol. 12, no. 10, e2020MS002092, 2020.

[18] S. K. Bhattacharya, A. Sarkar, and M.-C. Liang, "Vapor isotope probing of typhoons invading the taiwan region in 2016," *Journal of Geophysical Research: Atmospheres*, vol. 127, no. 21, e2022JD036578, 2022.

[19] K. Bi, L. Xie, H. Zhang, X. Chen, X. Gu, and Q. Tian, "Accurate medium-range global weather forecasting with 3d neural networks," *Nature*, pp. 1–6, 2023.

[20] K. Bi, L. Xie, H. Zhang, X. Chen, X. Gu, and Q. Tian, "Pangu-weather: A 3d high-resolution model for fast and accurate global weather forecast," *arXiv preprint arXiv:2211.02556*, 2022.

[21] M. I. Biggerstaff and R. Houze, "Kinematic and precipitation structure of the 10–11 june 1985 squall line," *Monthly weather review*, vol. 119, no. 12, pp. 3034–3065, 1991.

[22] P. N. Blossey, Z. Kuang, and D. M. Romps, "Isotopic composition of water in the tropical tropopause layer in cloud-resolving simulations of an idealized tropical circulation," *Journal of Geophysical Research: Atmospheres*, vol. 115, no. D24, 2010.

[23] H. B. Bluestein and M. H. Jain, "Formation of mesoscale lines of pirecipitation: Severe squall lines in oklahoma during the spring," *J. Atmos. Sci.*, vol. 42, no. 16, pp. 1711–1732, 1985.

[24] S. Bony, C. Risi, and F. Vimeux, "Influence of convective processes on the isotopic composition (δ18o and δd) of precipitation and water vapor in the tropics: 1. radiative-convective equilibrium and tropical ocean–global atmosphere–coupled ocean-atmosphere response experiment (toga-coare) simulations," *Journal of Geophysical Research: Atmospheres*, vol. 113, no. D19, 2008.

[25] S. Bony *et al.*, "Clouds, circulation and climate sensitivity," *Nature Geoscience*, vol. 8, no. 4, pp. 261–268, 2015.

[26] S. Bony *et al.*, "Eurec 4 a: A field campaign to elucidate the couplings between clouds, convection and circulation," *Surveys in Geophysics*, vol. 38, pp. 1529–1568, 2017.

[27] C Boroneant, G Plaut, F Giorgi, and X Bi, "Extreme precipitation over the maritime alps and associated weather regimes simulated by a regional climate model: Present-day and future climate scenarios," *Theoretical and Applied Climatology*, vol. 86, pp. 81–99, 2006.

[28] C. S. Bretherton, P. N. Blossey, and M. Khairoutdinov, "An energy-balance analysis of deep convective self-aggregation above uniform SST," *J. Atmos. Sci.*, vol. 62, no. 12, pp. 4273–4292, 2005.

[29] P.-E. Brilouet *et al.*, "Trade wind boundary layer turbulence and shallow precipitating convection: New insights combining sar images, satellite brightness temperature, and airborne in situ measurements," *Geophysical Research Letters*, vol. 50, no. 2, e2022GL102180, 2023.

[30] G. H. Bryan and H. Morrison, "Sensitivity of a simulated squall line to horizontal resolution and parameterization of microphysics," *Monthly Weather Review*, vol. 140, no. 1, pp. 202–225, 2012.

[31] G. H. Bryan and R. Rotunno, "The optimal state for gravity currents in shear," *Journal of the Atmospheric Sciences*, vol. 71, no. 1, pp. 448–468, 2014.

[32] G Caniaux, J. Redelsperger, and J. P. Lafore, "A numerical study of the stratiform region of a fast-moving squall line. part i: General description and water and heat budgets," *Journal of the atmospheric sciences*, vol. 51, no. 14, pp. 2046–2074, 1994.

[33] J.-P. Chaboureau, F Guichard, J.-L. Redelsperger, and J.-P. Lafore, "The role of stability and moisture in the diurnal cycle of convection over land," *Quarterly Journal of the Royal Meteorological Society: A journal of the atmospheric sciences, applied meteorology and physical oceanography*, vol. 130, no. 604, pp. 3105–3117, 2004.

[34] S Chakraborty, N. Sinha, R Chattopadhyay, S Sengupta, P. Mohan, and A Datye, "Atmospheric controls on the precipitation isotopes over the andaman islands, bay of bengal," *Scientific reports*, vol. 6, no. 1, p. 19 555, 2016.

[35] J. Chalon, G Jaubert, J. Lafore, and F Roux, "The west african squall line observed on 23 june 1981 during copt 81: Mesoscale structure and transports," *Journal of Atmospheric Sciences*, vol. 45, no. 19, pp. 2744–2763, 1988.

[36] F. Chen *et al.*, "Typhoon control of precipitation dual isotopes in southern china and its palaeoenvironmental implications," *Journal of Geophysical Research: Atmospheres*, vol. 126, no. 14, e2020JD034336, 2021.

[37] Y.-M. Cheng, J. Dias, G. Kiladis, Z. Feng, and L. R. Leung, "Mesoscale convective systems modulated by convectively coupled equatorial waves," *Geophysical Research Letters*, vol. 50, no. 10, e2023GL103335, 2023.

[38] M. Chong, "The 11 august 2006 squall-line system as observed from mit doppler radar during the amma sop," *Quarterly Journal of the Royal Meteorological Society*, vol. 136, no. S1, pp. 209–226, 2010.

[39] M. Chong, P. Amayenc, G. Scialom, and J. Testud, "A tropical squall line observed during the copt 81 experiment in west africa. part 1: Kinematic structure inferred from dual-doppler radar data," *Monthly Weather Review*, vol. 115, no. 3, pp. 670–694, 1987.

[40] M. Chong and D. Hauser, "A tropical squall line observed during the copt 81 experiment in west africa. part iii: Heat and moisture budgets," *Monthly weather review*, vol. 118, no. 8, pp. 1696–1706, 1990.

[41] M. Colin and S. C. Sherwood, "Atmospheric convection as an unstable predator–prey process with memory," *Journal of the Atmospheric Sciences*, vol. 78, no. 11, pp. 3781–3797, 2021.

[42] M. C. Coniglio, S. F. Corfidi, and J. S. Kain, "Views on applying rkw theory: An illustration using the 8 may 2009 derecho-producing convective system," *Monthly Weather Review*, vol. 140, no. 3, pp. 1023–1043, 2012.

[43] M. C. Coniglio, J. Y. Hwang, and D. J. Stensrud, "Environmental factors in the upscale growth and longevity of mcss derived from rapid update cycle analyses," *Monthly weather review*, vol. 138, no. 9, pp. 3514–3539, 2010.

[44] F. W. Cruz *et al.*, "Orbitally driven east–west antiphasing of south american precipitation," *Nature Geoscience*, vol. 2, no. 3, pp. 210–214, 2009.

[45] N. A. Da Silva, C. Muller, S. Shamekh, and B. Fildier, "Significant amplification of instantaneous extreme precipitation with convective self-aggregation," *J. Adv. Model. Earth Syst.*, vol. 13, no. 11, e2021MS002607, 2021.

[46] G. E. Dahl, D. Yu, L. Deng, and A. Acero, "Context-dependent pre-trained deep neural networks for large-vocabulary speech recognition," *IEEE Transactions on audio, speech, and language processing*, vol. 20, no. 1, pp. 30–42, 2011.

[47] L Denby, "Discovering the importance of mesoscale cloud organization through unsupervised classification," *Geophysical Research Letters*, vol. 47, no. 1, e2019GL085190, 2020.

[48] L. Denby, "Charting the realms of mesoscale cloud organisation using unsupervised learning," *arXiv preprint arXiv:2309.08567*, 2023.

[49] C. J. Diekmann *et al.*, "A lagrangian perspective on stable water isotopes during the west african monsoon," *Journal of Geophysical Research: Atmospheres*, vol. 126, no. 19, e2021JD034895, 2021.

[50] J Dudhia, M. Moncrieff, and D. So, "The two-dimensional dynamics of west african squall lines," *Quarterly Journal of the Royal Meteorological Society*, vol. 113, no. 475, pp. 121–146, 1987.

[51] C. Durman, J. M. Gregory, D. C. Hassell, R. Jones, and J. Murphy, "A comparison of extreme european daily precipitation simulated by a global and a regional climate model for present and future climates," *Quarterly Journal of the Royal Meteorological Society*, vol. 127, no. 573, pp. 1005–1015, 2001.

[52] G. S. Elsaesser, R. Roca, T. Fiolleau, A. D. Del Genio, and J. Wu, "A simple model for tropical convective cloud shield area growth and decay rates informed by geostationary ir, gpm, and aqua/airs satellite data," *Journal of Geophysical Research: Atmospheres*, vol. 127, no. 10, e2021JD035599, 2022.

[53] Z. Feng, S. Hagos, A. K. Rowe, C. D. Burleyson, M. N. Martini, and S. P. de Szoeke, "Mechanisms of convective cloud organization by cold pools over tropical warm ocean during the amie/dynamo field campaign," *Journal of Advances in Modeling Earth Systems*, vol. 7, no. 2, pp. 357–381, 2015.

[54] Z. Feng, L. R. Leung, J. Hardin, C. R. Terai, F. Song, and P. Caldwell, “Mesoscale convective systems in dyamond global convection-permitting simulations,” *Geophysical Research Letters*, vol. 50, no. 4, e2022GL102603, 2023.

[55] R. D. Field, D. B. Jones, and D. P. Brown, “Effects of postcondensation exchange on the isotopic composition of water in the atmosphere,” *Journal of Geophysical Research: Atmospheres*, vol. 115, no. D24, 2010.

[56] R. D. Field, D. Kim, A. N. LeGrande, J. Worden, M. Kelley, and G. A. Schmidt, “Evaluating climate model performance in the tropics with retrievals of water isotopic composition from aura tes,” *Geophysical Research Letters*, vol. 41, no. 16, pp. 6030–6036, 2014.

[57] B. Fildier, W. D. Collins, and C. Muller, “Distortions of the rain distribution with warming, with and without self-aggregation,” *Journal of Advances in Modeling Earth Systems*, vol. 13, no. 2, e2020MS002256, 2021.

[58] B. Fildier, C. Muller, R. Pincus, and S. Fueglistaler, “How moisture shapes low-level radiative cooling in subsidence regimes,” *AGU Advances*, vol. 4, no. 3, e2023AV000880, 2023.

[59] B. Fildier, H Parishani, and W. Collins, “Prognostic power of extreme rainfall scaling formulas across space and time scales,” *Journal of Advances in Modeling Earth Systems*, vol. 10, no. 12, pp. 3252–3267, 2018.

[60] T. Fiolleau and R. Roca, “An algorithm for the detection and tracking of tropical mesoscale convective systems using infrared images from geostationary satellite,” *IEEE transactions on Geoscience and Remote Sensing*, vol. 51, no. 7, pp. 4302–4315, 2013.

[61] T. Fiolleau, R. Roca, S. Cloché, D. Bouniol, and P. Raberanto, “Homogenization of geostationary infrared imager channels for cold cloud studies using megha-tropiques/scarab,” *IEEE Transactions on Geoscience and Remote Sensing*, vol. 58, no. 9, pp. 6609–6622, 2020.

[62] R. G. Fitzpatrick *et al.*, “What drives the intensification of mesoscale convective systems over the west african sahel under climate change?” *Journal of Climate*, vol. 33, no. 8, pp. 3151–3172, 2020.

[63] A. B. Frappier, D. Sahagian, S. J. Carpenter, L. A. González, and B. R. Frappier, “Stalagmite stable isotope record of recent tropical cyclone events,” *Geology*, vol. 35, no. 2, pp. 111–114, 2007.

[64] C. Frei and C. Schär, “Detection probability of trends in rare events: Theory and application to heavy precipitation in the alpine region,” *Journal of Climate*, vol. 14, no. 7, pp. 1568–1584, 2001.

[65] C. Frei, R. Schöll, S. Fukutome, J. Schmidli, and P. L. Vidale, "Future change of precipitation extremes in europe: Intercomparison of scenarios from regional climate models," *Journal of Geophysical Research: Atmospheres*, vol. 111, no. D6, 2006.

[66] J. Fritsch and G. Forbes, "Mesoscale convective systems," in *Severe convective storms*, Springer, 2001, pp. 323–357.

[67] H Fudeyasu *et al.*, "Isotope ratios of precipitation and water vapor observed in typhoon shanshan," *Journal of Geophysical Research: Atmospheres*, vol. 113, no. D12, 2008.

[68] J. F. Gamache and R. A. Houze Jr, "Water budget of a mesoscale convective system in the tropics," *Journal of Atmospheric Sciences*, vol. 40, no. 7, pp. 1835–1850, 1983.

[69] P. Garg, S. W. Nesbitt, T. J. Lang, and G. Priftis, "Tropical oceanic mesoscale cold pools in a high-resolution global cloud-resolving model from dyamond initiative," *Authorea Preprints*, 2022.

[70] S. T. Garner and A. J. Thorpe, "The development of organized convection in a simplified squall-line model," *Quart. J. Roy. Meteor. Soc.*, vol. 118, no. 503, pp. 101–124, 1992.

[71] S. Gedzelman *et al.*, "Probing hurricanes with stable isotopes of rain and water vapor," *Monthly Weather Review*, vol. 131, no. 6, pp. 1112–1127, 2003.

[72] P. Gentine, M. Pritchard, S. Rasp, G. Reinaudi, and G. Yacalis, "Could machine learning break the convection parameterization deadlock?" *Geophysical Research Letters*, vol. 45, no. 11, pp. 5742–5751, 2018.

[73] L. D. Grant, M. W. Moncrieff, T. P. Lane, and S. C. van den Heever, "Shear-parallel tropical convective systems: Importance of cold pools and wind shear," *Geophysical Research Letters*, vol. 47, no. 12, e2020GL087720, 2020.

[74] J. K. Green *et al.*, "Regionally strong feedbacks between the atmosphere and terrestrial biosphere," *Nature geoscience*, vol. 10, no. 6, pp. 410–414, 2017.

[75] R. S. Greenfield and J. S. Fein, "The global atmospheric research programs's atlantic tropical experiment," *Reviews of Geophysics*, vol. 17, no. 7, pp. 1762–1772, 1979.

[76] F. Guichard and F. Couvreux, "A short review of numerical cloud-resolving models," *Tellus A: Dynamic Meteorology and Oceanography*, vol. 69, no. 1, p. 1 373 578, 2017.

[77] J. O. Haerter, "Convective self-aggregation as a cold pool-driven critical phenomenon," *Geophysical Research Letters*, vol. 46, no. 7, pp. 4017–4028, 2019.

[78] R. Hamilton, J. Archbold, and C. Douglas, “Meteorology of nigeria and adjacent territory,” *Quarterly Journal of the Royal Meteorological Society*, vol. 71, no. 309-310, pp. 231–264, 1945.

[79] Harmony. “Harmony Mission Description.” (2020), [Online]. Available: `https://esamultimedia.esa.int/docs/EarthObservation/EE10_Harmony_Report-for-Assessment-v1.0_13Nov2020.pdf`.

[80] I. M. Held, R. S. Hemler, and V. Ramaswamy, “Radiative-convective equilibrium with explicit two-dimensional moist convection,” *J. Atmos. Sci.*, vol. 50, no. 23, pp. 3909–3909, 1993.

[81] G. Hinton *et al.*, “Deep neural networks for acoustic modeling in speech recognition: The shared views of four research groups,” *IEEE Signal processing magazine*, vol. 29, no. 6, pp. 82–97, 2012.

[82] G. E. Hinton and R. R. Salakhutdinov, “Reducing the dimensionality of data with neural networks,” *science*, vol. 313, no. 5786, pp. 504–507, 2006.

[83] C. Holloway *et al.*, “Observing convective aggregation,” *Surv. Geophys.*, vol. 38, 2017.

[84] K. Hornik, M. Stinchcombe, and H. White, “Multilayer feedforward networks are universal approximators,” *Neural networks*, vol. 2, no. 5, pp. 359–366, 1989.

[85] J. T. Houghton *et al.*, *Climate chage 2001*. 2001.

[86] F. Hourdin *et al.*, “Lmdz6a: The atmospheric component of the ipsl climate model with improved and better tuned physics,” *Journal of Advances in Modeling Earth Systems*, vol. 12, no. 7, e2019MS001892, 2020.

[87] R. A. Houze Jr., “Mesoscale convective systems,” *Rev. Geophys.*, vol. 42, no. 4, RG4003, 2004.

[88] R. A. Houze, “Structure and dynamics of a tropical squall–line system,” *Monthly Weather Review*, vol. 105, no. 12, pp. 1540–1567, 1977.

[89] D. Jackisch *et al.*, “Precipitation stable isotopic signatures of tropical cyclones in metropolitan manila, philippines, show significant negative isotopic excursions,” *Natural Hazards and Earth System Sciences*, vol. 22, no. 1, pp. 213–226, 2022.

[90] C Jakob, M. Singh, and L. Jungandreas, “Radiative convective equilibrium and organized convection: An observational perspective,” *Journal of Geophysical Research: Atmospheres*, vol. 124, no. 10, pp. 5418–5430, 2019.

[91] G. G. Jensen, R. Fiévet, and J. O. Haerter, “The diurnal path to persistent convective self-aggregation,” *J. Adv. Model. Earth Syst.*, e2021MS002923, 2022.

[92] I. L. Jirak, W. R. Cotton, and R. L. McAnelly, "Satellite and radar survey of mesoscale convective system development," *Monthly weather review*, vol. 131, no. 10, pp. 2428–2449, 2003.

[93] T. R. Karl and R. W. Knight, "Secular trends of precipitation amount, frequency, and intensity in the united states," *Bulletin of the American Meteorological society*, vol. 79, no. 2, pp. 231–242, 1998.

[94] R. Keisler, "Forecasting global weather with graph neural networks," *arXiv preprint arXiv:2202.07575*, 2022.

[95] E. J. Kendon, N. M. Roberts, H. J. Fowler, M. J. Roberts, S. C. Chan, and C. A. Senior, "Heavier summer downpours with climate change revealed by weather forecast resolution model," *Nature Climate Change*, vol. 4, no. 7, pp. 570–576, 2014.

[96] M. F. Khairoutdinov and Y. L. Kogan, "A large eddy simulation model with explicit microphysics: Validation against aircraft observations of a stratocumulus-topped boundary layer," *J. Atmos. Sci.*, vol. 56, no. 13, pp. 2115–2131, 1999.

[97] M. F. Khairoutdinov and D. A. Randall, "Cloud resolving modeling of the arm summer 1997 iop: Model formulation, results, uncertainties, and sensitivities," *J. Atmos. Sci.*, vol. 60, no. 4, pp. 607–625, 2003.

[98] J. T. Kiehl, J. J. Hack, G. B. Bonan, B. A. Boville, D. L. Williamson, and P. J. Rasch, "The National Center for Atmospheric Research Community Climate Model: CCM3," *J. Climate*, vol. 11, no. 6, pp. 1131–1149, 1998.

[99] G. N. Kiladis, M. C. Wheeler, P. T. Haertel, K. H. Straub, and P. E. Roundy, "Convectively coupled equatorial waves," *Rev. Geophys.*, vol. 47, no. 2, 2009.

[100] A. Klein Tank and G. Können, "Trends in indices of daily temperature and precipitation extremes in europe, 1946–99," *Journal of climate*, vol. 16, no. 22, pp. 3665–3680, 2003.

[101] J Kolassa, F. Aires, J. Polcher, C. Prigent, C. Jimenez, and J.-M. Pereira, "Soil moisture retrieval from multi-instrument observations: Information content analysis and retrieval methodology," *Journal of Geophysical Research: Atmospheres*, vol. 118, no. 10, pp. 4847–4859, 2013.

[102] J. Kolassa, R. Reichle, and C. S. Draper, "Merging active and passive microwave observations in soil moisture data assimilation," *Remote sensing of environment*, vol. 191, pp. 117–130, 2017.

[103] N. Kurita, "Water isotopic variability in response to mesoscale convective system over the tropical ocean," *Journal of Geophysical Research: Atmospheres*, vol. 118, no. 18, pp. 10–376, 2013.

[104] J. Lacour, C Risi, J Worden, C Clerbaux, and P. Coheur, “Isotopic signature of convection’s depth in water vapor as seen from iasi and tes d observations,” *Earth and Planetary Science Letters*, vol. 7, no. 15, pp. 9645–9663, 2017.

[105] W. K.-M. Lau and D. E. Waliser, *Intraseasonal variability in the atmosphere-ocean climate system*. Springer Science & Business Media, 2011.

[106] J. R. Lawrence, S. D. Gedzelman, J. Gamache, and M. Black, “Stable isotope ratios: Hurricane olivia,” *Journal of Atmospheric Chemistry*, vol. 41, pp. 67–82, 2002.

[107] J. R. Lawrence, S. D. Gedzelman, X. Zhang, and R. Arnold, “Stable isotope ratios of rain and vapor in 1995 hurricanes,” *Journal of Geophysical Research: Atmospheres*, vol. 103, no. D10, pp. 11 381–11 400, 1998.

[108] J. R. Lawrence *et al.*, “Stable isotopic composition of water vapor in the tropics,” *Journal of Geophysical Research: Atmospheres*, vol. 109, no. D6, 2004.

[109] Y. LeCun, Y. Bengio, and G. Hinton, “Deep learning,” *nature*, vol. 521, no. 7553, pp. 436–444, 2015.

[110] M. A. LeMone, E. J. Zipser, and S. B. Trier, “The role of environmental shear and thermodynamic conditions in determining the structure and evolution of mesoscale convective systems during toga coare,” *Journal of the Atmospheric Sciences*, vol. 55, no. 23, pp. 3493–3518, 1998.

[111] G. Lenderink and E. Van Meijgaard, “Increase in hourly precipitation extremes beyond expectations from temperature changes,” *Nature Geoscience*, vol. 1, no. 8, pp. 511–514, 2008.

[112] Y.-L. Lin, R. D. Farley, and H. D. Orville, “Bulk parameterization of the snow field in a cloud model,” *Journal of Applied Meteorology and climatology*, vol. 22, no. 6, pp. 1065–1092, 1983.

[113] C. Liu and M. W. Moncrieff, “Shear-parallel mesoscale convective systems in a moist low-inhibition mei-yu front environment,” *Journal of the Atmospheric Sciences*, vol. 74, no. 12, pp. 4213–4228, 2017.

[114] M. Llopart, E. Coppola, F. Giorgi, R. P. Da Rocha, and S. V. Cuadra, “Climate change impact on precipitation for the amazon and la plata basins,” *Climatic Change*, vol. 125, pp. 111–125, 2014.

[115] N. J. Lutsko and T. W. Cronin, “Increase in precipitation efficiency with surface warming in radiative-convective equilibrium,” *J. Adv. Model. Earth Syst.*, vol. 10, no. 11, pp. 2992–3010, 2018.

[116] L. Machado, H Laurent, N Dessay, and I Miranda, “Seasonal and diurnal variability of convection over the amazonia: A comparison of different vegetation types and large scale forcing,” *Theoretical and applied climatology*, vol. 78, pp. 61–77, 2004.

[117] B. E. Mapes, "Gregarious tropical convection," *J. Atmos. Sci.*, vol. 50, no. 13, pp. 2026–2037, 1993.

[118] B. E. Mapes and R. A. Houze Jr, "Cloud clusters and superclusters over the oceanic warm pool," *Monthly Weather Review*, vol. 121, no. 5, pp. 1398–1416, 1993.

[119] J. Marotzke *et al.*, "Climate research must sharpen its view," *Nature Climate Change*, vol. 7, no. 2, pp. 89–91, 2017.

[120] V. Mathon, H. Laurent, and T. Lebel, "Mesoscale convective system rainfall in the sahel," *Journal of applied meteorology*, vol. 41, no. 11, pp. 1081–1092, 2002.

[121] T. Matsuno, "Prologue: Tropical meteorology 1960–2010—personal recollections," *Meteorological Monographs*, vol. 56, pp. vii–xv, 2016.

[122] C. R. Maupin *et al.*, "Abrupt southern great plains thunderstorm shifts linked to glacial climate variability," *Nature Geoscience*, vol. 14, no. 6, pp. 396–401, 2021.

[123] R. L. McAnelly and W. R. Cotton, "Meso-β-scale characteristics of an episode of meso-α-scale convective complexes," *Monthly weather review*, vol. 114, no. 9, pp. 1740–1770, 1986.

[124] K. A. McColl, S. H. Alemohammad, R. Akbar, A. G. Konings, S. Yueh, and D. Entekhabi, "The global distribution and dynamics of surface soil moisture," *Nature Geoscience*, vol. 10, no. 2, pp. 100–104, 2017.

[125] M. Medina-Elizalde and E. J. Rohling, "Collapse of classic maya civilization related to modest reduction in precipitation," *Science*, vol. 335, no. 6071, pp. 956–959, 2012.

[126] B. Meyer and J. O. Haerter, "Mechanical forcing of convection by cold pools: Collisions and energy scaling," *Journal of Advances in Modeling Earth Systems*, vol. 12, no. 11, e2020MS002281, 2020.

[127] Y. Miao, M. Gowayyed, and F. Metze, "Eesen: End-to-end speech recognition using deep rnn models and wfst-based decoding," in *2015 IEEE workshop on automatic speech recognition and understanding (ASRU)*, IEEE, 2015, pp. 167–174.

[128] M. Miller and A. Betts, "Traveling convective storms over venezuela," *Monthly Weather Review*, vol. 105, no. 7, pp. 833–848, 1977.

[129] H. Miura, H. Tomita, T. Nasuno, S.-i. Iga, M. Satoh, and T. Matsuno, "A climate sensitivity test using a global cloud resolving model under an aqua planet condition," *Geophysical research letters*, vol. 32, no. 19, 2005.

[130] S. Moazami, S. Golian, M. R. Kavianpour, and Y. Hong, “Comparison of persiann and v7 trmm multi-satellite precipitation analysis (tmpa) products with rain gauge data over iran,” *International journal of remote sensing*, vol. 34, no. 22, pp. 8156–8171, 2013.

[131] A. Moberg *et al.*, “Indices for daily temperature and precipitation extremes in europe analyzed for the period 1901–2000,” *Journal of Geophysical Research: Atmospheres*, vol. 111, no. D22, 2006.

[132] M Moore, P. Blossey, A Muhlbauer, and Z. Kuang, “Microphysical controls on the isotopic composition of wintertime orographic precipitation,” *Journal of Geophysical Research: Atmospheres*, vol. 121, no. 12, pp. 7235–7253, 2016.

[133] M. Moore, Z. Kuang, and P. Blossey, “A moisture budget perspective of the amount effect,” *Geophysical Research Letters*, vol. 41, no. 4, pp. 1329–1335, 2014.

[134] C. Moseley, C. Hohenegger, P. Berg, and J. O. Haerter, “Intensification of convective extremes driven by cloud–cloud interaction,” *Nature Geoscience*, vol. 9, no. 10, pp. 748–752, 2016.

[135] J. P. Mulholland, J. M. Peters, and H. Morrison, “How does vertical wind shear influence entrainment in squall lines?” *Journal of the Atmospheric Sciences*, vol. 78, no. 6, pp. 1931–1946, 2021.

[136] C. J. Muller, “Impact of convective organization on the response of tropical precipitation extremes to warming,” *J. Climate*, vol. 26, pp. 5028–5043, 2013.

[137] C. J. Muller and I. M. Held, “Detailed investigation of the self-aggregation of convection in cloud-resolving simulations,” *J. Atmos. Sci.*, vol. 69, pp. 2551–2565, 2012.

[138] C. J. Muller and P. A. O’Gorman, “An energetic perspective on the regional response of precipitation to climate change,” *Nature Climate Change*, vol. 1, no. 5, pp. 266–271, 2011.

[139] C. J. Muller, P. A. O’Gorman, and L. E. Back, “Intensification of precipitation extremes with warming in a cloud-resolving model,” *J. Climate*, vol. 24, no. 11, pp. 2784–2800, 2011.

[140] C. J. Muller and D. M. Romps, “Acceleration of tropical cyclogenesis by self-aggregation feedbacks,” *Proc. Natl. Acad. Sci. (USA)*, p. 201 719 967, 2018.

[141] C. Muller, “Impact of convective organization on the response of tropical precipitation extremes to warming,” *Journal of climate*, vol. 26, no. 14, pp. 5028–5043, 2013.

[142] C. Muller and S. Bony, “What favors convective aggregation and why?” *Geophysical Research Letters*, vol. 42, no. 13, pp. 5626–5634, 2015.

[143] C. Muller and Y. Takayabu, "Response of precipitation extremes to warming: What have we learned from theory and idealized cloud-resolving simulations, and what remains to be learned?" *Environ. Res. Lett.*, vol. 15, no. 3, p. 035 001, 2020.

[144] C. Muller *et al.*, "Spontaneous aggregation of convective storms," *Annu. Rev. Fluid Mech.*, vol. 54, pp. 133–157, 2022.

[145] C. Muller and S. Bony, "What favors convective aggregation and why?" *Geophys. Res. Lett.*, vol. 42, 2015.

[146] T. Nakazawa, "Tropical super clusters within intraseasonal variations over the western pacific," *Journal of the Meteorological Society of Japan. Ser. II*, vol. 66, no. 6, pp. 823–839, 1988.

[147] S. W. Nesbitt, R. Cifelli, and S. A. Rutledge, "Storm morphology and rainfall characteristics of trmm precipitation features," *Monthly Weather Review*, vol. 134, no. 10, pp. 2702–2721, 2006.

[148] J. Nott, J. Haig, H. Neil, and D. Gillieson, "Greater frequency variability of landfalling tropical cyclones at centennial compared to seasonal and decadal scales," *Earth and Planetary Science Letters*, vol. 255, no. 3-4, pp. 367–372, 2007.

[149] P. A. O'Gorman and T. Schneider, "Scaling of precipitation extremes over a wide range of climates simulated with an idealized GCM," *J. Climate*, vol. 22, pp. 5676–5685, 2009.

[150] P. A. O'Gorman and T. Schneider, "The physical basis for increases in precipitation extremes in simulations of 21st-century climate change," *Proceedings of the National Academy of Sciences*, vol. 106, no. 35, pp. 14 773–14 777, 2009.

[151] B. Orlowsky and S. I. Seneviratne, "Global changes in extreme events: Regional and seasonal dimension," *Climatic Change*, vol. 110, pp. 669–696, 2012.

[152] P. O'Gorman and C. J. Muller, "How closely do changes in surface and column water vapor follow clausius–clapeyron scaling in climate change simulations?" *Environmental Research Letters*, vol. 5, no. 2, p. 025 207, 2010.

[153] P. A. O'Gorman, "Contrasting responses of mean and extreme snowfall to climate change," *Nature*, vol. 512, no. 7515, pp. 416–418, 2014.

[154] P. Pall, M. Allen, and D. A. Stone, "Testing the clausius–clapeyron constraint on changes in extreme precipitation under co 2 warming," *Climate Dynamics*, vol. 28, pp. 351–363, 2007.

[155] J. Pathak *et al.*, "Fourcastnet: A global data-driven high-resolution weather model using adaptive fourier neural operators," *arXiv preprint arXiv:2202.11214*, 2022.

[156] F. Pedregosa *et al.*, "Scikit-learn: Machine learning in Python," *Journal of Machine Learning Research*, vol. 12, pp. 2825–2830, 2011.

[157] A. G. Pendergrass, "Changing degree of convective organization as a mechanism for dynamic changes in extreme precipitation," *Current climate change reports*, vol. 6, pp. 47–54, 2020.

[158] A. G. Pendergrass, K. A. Reed, and B. Medeiros, "The link between extreme precipitation and convective organization in a warming climate: Global radiative-convective equilibrium simulations," *Geophysical Research Letters*, vol. 43, no. 21, pp. 11–445, 2016.

[159] D. Posselt, S. Van Den Heever, and G. Stephens, "Trimodal cloudiness and tropical stable layers in simulations of radiative convective equilibrium," *Geophysical Research Letters*, vol. 35, no. 8, 2008.

[160] J Rajczak, P Pall, and C Schär, "Projections of extreme precipitation events in regional climate simulations for europe and the alpine region," *Journal of Geophysical Research: Atmospheres*, vol. 118, no. 9, pp. 3610–3626, 2013.

[161] R. Ramos *et al.*, "Constraining clouds and convective parameterizations in a climate model using paleoclimate data," *Journal of Advances in Modeling Earth Systems*, vol. 14, no. 8, e2021MS002893, 2022.

[162] D. Randall, M. Khairoutdinov, A. Arakawa, and W. Grabowski, "Breaking the cloud parameterization deadlock," *Bulletin of the American Meteorological Society*, vol. 84, no. 11, pp. 1547–1564, 2003.

[163] M. Reichstein *et al.*, "Deep learning and process understanding for data-driven earth system science," *Nature*, vol. 566, no. 7743, pp. 195–204, 2019.

[164] C. Risi, S. Bony, and F. Vimeux, "Influence of convective processes on the isotopic composition (δ18o and δd) of precipitation and water vapor in the tropics: 2. physical interpretation of the amount effect," *J. Geophys. Res.*, vol. 113, no. D19, 2008.

[165] C. Risi, S. Bony, F. Vimeux, M. Chong, and L. Descroix, "Evolution of the stable water isotopic composition of the rain sampled along sahelian squall lines," *Quarterly Journal of the Royal Meteorological Society*, vol. 136, no. S1, pp. 227–242, 2010.

[166] C. Risi, C. Muller, and P. Blossey, "Rain evaporation, snow melt, and entrainment at the heart of water vapor isotopic variations in the tropical troposphere, according to large-eddy simulations and a two-column model," *Journal of Advances in Modeling Earth Systems*, vol. 13, no. 4, e2020MS002381, 2021.

[167] C. Risi, C. Muller, and P. Blossey, “What controls the water vapor isotopic composition near the surface of tropical oceans? results from an analytical model constrained by large-eddy simulations,” *J. Adv. Model. Earth Syst.*, vol. 12, no. 8, e2020MS002106, 2020.

[168] C. Risi *et al.*, “What controls the mesoscale variations in water isotopic composition within tropical cyclones and squall lines? cloud resolving model simulations in radiative-convective equilibrium,” *Journal of Advances in Modeling Earth Systems*, vol. 15, no. 4, e2022MS003331, 2023.

[169] F. R. Robe and K. A. Emanuel, “The effect of vertical wind shear on radiative-convective equilibrium states,” *J. Atmos. Sci.*, vol. 58, no. 11, pp. 1427–1445, 2001.

[170] R Roca, T Fiolleau, and D Bouniol, “A simple model of the life cycle of mesoscale convective systems cloud shield in the tropics,” *Journal of Climate*, vol. 30, no. 11, pp. 4283–4298, 2017.

[171] R. Roca and T. Fiolleau, “Extreme precipitation in the tropics is closely associated with long-lived convective systems,” *Communications Earth & Environment*, vol. 1, no. 1, pp. 1–6, 2020.

[172] N. Rochetin, C. Hohenegger, L. Touzé-Peiffer, and N. Villefranque, “A physically based definition of convectively generated density currents: Detection and characterization in convection-permitting simulations,” *Journal of Advances in Modeling Earth Systems*, vol. 13, no. 7, e2020MS002402, 2021.

[173] D. M. Romps, “Response of tropical precipitation to global warming,” *J. Atmos. Sci.*, vol. 68, no. 1, pp. 123–138, 2011.

[174] D. M. Romps and N. Jeevanjee, “On the sizes and lifetimes of cold pools,” *Quarterly Journal of the Royal Meteorological Society*, vol. 142, no. 696, pp. 1517–1527, 2016.

[175] R. Rotunno, J. B. Klemp, and M. L. Weisman, “A theory for strong, long-lived squall lines,” *J. Atmos. Sci.*, vol. 45, no. 3, pp. 463–4, 1988.

[176] S. A. Rutledge and R. A. Houze Jr, “A diagnostic modelling study of the trailing stratiform region of a midlatitude squall line,” *Journal of Atmospheric Sciences*, vol. 44, no. 18, pp. 2640–2656, 1987.

[177] N. Sakaeda and G. Torri, “The behaviors of intraseasonal cloud organization during dynamo/amie,” *Journal of Geophysical Research: Atmospheres*, vol. 127, no. 7, e2021JD035749, 2022.

[178] N. Sakaeda and G. Torri, “The observed effects of cold pools on convection triggering and organization during dynamo/amie,” *Journal of Geophysical Research: Atmospheres*, e2023JD038635, 2023.

[179] M. Satoh *et al.*, "The non-hydrostatic icosahedral atmospheric model: Description and development," *Progress in Earth and Planetary Science*, vol. 1, no. 1, pp. 1–32, 2014.

[180] C. Schär *et al.*, "Percentile indices for assessing changes in heavy precipitation events," *Climatic Change*, vol. 137, no. 1-2, pp. 201–216, 2016.

[181] K. A. Schiro *et al.*, "Environmental controls on tropical mesoscale convective system precipitation intensity," *Journal of the Atmospheric Sciences*, vol. 77, no. 12, pp. 4233–4249, 2020.

[182] L. Schlemmer and C. Hohenegger, "The formation of wider and deeper clouds as a result of cold-pool dynamics," *Journal of the Atmospheric Sciences*, vol. 71, no. 8, pp. 2842–2858, 2014.

[183] T. Schneider, N. Jeevanjee, and R. Socolow, "Accelerating progress in climate science," *Physics Today*, vol. 74, no. 6, pp. 44–51, 2021.

[184] R. S. Schumacher and R. H. Johnson, "Organization and environmental properties of extreme-rain-producing mesoscale convective systems," *Monthly weather review*, vol. 133, no. 4, pp. 961–976, 2005.

[185] R. S. Schumacher and K. L. Rasmussen, "The formation, character and changing nature of mesoscale convective systems," *Nature Reviews Earth & Environment*, vol. 1, no. 6, pp. 300–314, 2020.

[186] A. G. Semie and S. Bony, "Relationship between precipitation extremes and convective organization inferred from satellite observations," *Geophysical Research Letters*, vol. 47, no. 9, e2019GL086927, 2020.

[187] B Sevruk, M Ondrás, and B Chvíla, "The wmo precipitation measurement intercomparisons," *Atmospheric Research*, vol. 92, no. 3, pp. 376–380, 2009.

[188] S. Shamekh, K. D. Lamb, Y. Huang, and P. Gentine, "Implicit learning of convective organization explains precipitation stochasticity," *Proceedings of the National Academy of Sciences*, vol. 120, no. 20, e2216158120, 2023.

[189] J Sillmann, V. Kharin, X Zhang, F. Zwiers, and D Bronaugh, "Climate extremes indices in the cmip5 multimodel ensemble: Part 1. model evaluation in the present climate," *Journal of geophysical research: atmospheres*, vol. 118, no. 4, pp. 1716–1733, 2013.

[190] D. Silver *et al.*, "Mastering the game of go with deep neural networks and tree search," *nature*, vol. 529, no. 7587, pp. 484–489, 2016.

[191] M. S. Singh and P. A. O'Gorman, "Influence of entrainment on the thermal stratification in simulations of radiative-convective equilibrium," *Geophys. Res. Lett.*, vol. 40, no. 16, pp. 4398–4403, 2013.

[192] M. S. Singh and P. A. O'Gorman, "Influence of microphysics on the scaling of precipitation extremes with temperature," *Geophys. Res. Lett.*, vol. 41, no. 16, pp. 6037–6044, 2014.

[193] B. F. Smull and R. A. Houze Jr, "A midlatitude squall line with a trailing region of stratiform rain: Radar and satellite observations," *Monthly weather review*, vol. 113, no. 1, pp. 117–133, 1985.

[194] B. J. Soden and I. M. Held, "An assessment of climate feedbacks in coupled ocean-atmosphere models," *J. Climate*, vol. 19, no. 14, pp. 3354–3360, 2006.

[195] T. H. Stein, C. E. Holloway, I. Tobin, and S. Bony, "Observed relationships between cloud vertical structure and convective aggregation over tropical ocean," *Journal of Climate*, vol. 30, no. 6, pp. 2187–2207, 2017.

[196] B. Stevens and S. Bony, "What are climate models missing?" *science*, vol. 340, no. 6136, pp. 1053–1054, 2013.

[197] B. Stevens, H. Brogniez, C. Kiemle, J.-L. Lacour, C. Crevoisier, and J. Kiliani, "Structure and dynamical influence of water vapor in the lower tropical troposphere," *Shallow clouds, water vapor, circulation, and climate sensitivity*, pp. 199–225, 2018.

[198] B. Stevens *et al.*, "DYAMOND: The DYnamics of the atmospheric general circulation modeled on non-hydrostatic domains," *Prog. Earth Planet. Sc.*, vol. 6, no. 1, p. 61, 2019.

[199] B. Stevens *et al.*, "Eurec 4 a," *Earth System Science Data Discussions*, vol. 2021, pp. 1–78, 2021.

[200] H. Su, C. S. Bretherton, and S. S. Chen, "Self-aggregation and large-scale control of tropical deep convection: A modeling study," *J. Atmos. Sci.*, vol. 57, no. 11, pp. 1797–1816, 2000.

[201] S. C. Sullivan, K. A. Schiro, C. Stubenrauch, and P. Gentine, "The response of tropical organized convection to el niño warming," *Journal of Geophysical Research: Atmospheres*, vol. 124, no. 15, pp. 8481–8500, 2019.

[202] J. Tan, C. Jakob, W. B. Rossow, and G. Tselioudis, "Increases in tropical rainfall driven by changes in frequency of organized deep convection," *Nature*, vol. 519, no. 7544, p. 451, 2015.

[203] J. Tan, C. Jakob, and T. P. Lane, "On the identification of the large-scale properties of tropical convection using cloud regimes," *Journal of Climate*, vol. 26, no. 17, pp. 6618–6632, 2013.

[204] J. B. Tenenbaum, V. d. Silva, and J. C. Langford, "A global geometric framework for nonlinear dimensionality reduction," *science*, vol. 290, no. 5500, pp. 2319–2323, 2000.

[205] G. Thompson, P. R. Field, R. M. Rasmussen, and W. D. Hall, “Explicit forecasts of winter precipitation using an improved bulk microphysics scheme. part ii: Implementation of a new snow parameterization,” *Monthly weather review*, vol. 136, no. 12, pp. 5095–5115, 2008.

[206] I. Tobin, S. Bony, and R. Roca, “Observational evidence for relationships between the degree of aggregation of deep convection, water vapor, surface fluxes, and radiation,” *J. Climate*, vol. 25, pp. 6885–6904, 2012.

[207] A. M. Tompkins, “Organization of Tropical Convection in Low Vertical Wind Shears: The Role of Cold Pools,” *J. Atmos. Sci.*, vol. 58, 1650ï¿½1672, 2001.

[208] A. M. Tompkins, “Organization of tropical convection in low vertical wind shears: The role of water vapor,” *J. Atmos. Sci.*, 2001.

[209] A. M. Tompkins and G. C. Craig, “Time-scales of adjustment to radiative-convective equilibrium in the tropical atmosphere,” *Quarterly Journal of the Royal Meteorological Society*, vol. 124, no. 552, pp. 2693–2713, 1998.

[210] A. M. Tompkins and A. G. Semie, “Organization of tropical convection in low vertical wind shears: Role of updraft entrainment,” *J. Adv. Model. Earth Syst.*, vol. 9, no. 2, pp. 1046–1068, 2017.

[211] W. Tongjian and R. A. Houze, “The gate squall line of 9-10 august 1974,” *Advances in atmospheric sciences*, vol. 4, no. 1, pp. 85–92, 1987.

[212] G. Torri, “Isotopic equilibration in convective downdrafts,” *Geophysical Research Letters*, vol. 49, no. 15, e2022GL098743, 2022.

[213] G. Torri, “On the isotopic composition of cold pools in radiative-convective equilibrium,” *Journal of Geophysical Research: Atmospheres*, vol. 126, no. 10, e2020JD033139, 2021.

[214] G. Torri, D. Ma, and Z. Kuang, “Stable water isotopes and large-scale vertical motions in the tropics,” *Journal of Geophysical Research: Atmospheres*, vol. 122, no. 7, pp. 3703–3717, 2017.

[215] L. Touzé-Peiffer, R. Vogel, and N. Rochetin, “Detecting cold pools from soundings during eurec4a,” *arXiv preprint arXiv:2104.09146*, 2021.

[216] G. Tremoy *et al.*, “Clustering mesoscale convective systems with laser-based water vapor δ18o monitoring in niamey (niger),” *Journal of Geophysical Research: Atmospheres*, vol. 119, no. 9, pp. 5079–5103, 2014.

[217] K. E. Trenberth, “Changes in precipitation with climate change,” *Clim. Res.*, vol. 47, no. 1, p. 123, 2011.

[218] K. E. Trenberth, “Conceptual framework for changes of extremes of the hydrological cycle with climate change,” *Climatic Change*, vol. 42, pp. 327–339, 1999.

[219] J. M. Wallace and P. V. Hobbs, *Atmospheric science: an introductory survey*. Elsevier, 2006, vol. 92.

[220] Y.-J. Wang *et al.*, "A high-resolution absolute-dated late pleistocene monsoon record from hulu cave, china," *Science*, vol. 294, no. 5550, pp. 2345–2348, 2001.

[221] M. L. Weisman and R. Rotunno, ""a theory for strong long-lived squall lines" revisited," *J. Atmos. Sci.*, vol. 61, no. 4, pp. 361–382, 2004.

[222] K. Welsh and R. Sánchez-Murillo, "Rainfall, groundwater, and surface water isotope data from extreme tropical cyclones (2016-2019) within the caribbean sea and atlantic ocean basins," *Data in Brief*, vol. 30, p. 105 633, 2020.

[223] S Westra *et al.*, "Future changes to the intensity and frequency of short-duration extreme rainfall," *Rev. Geophys.*, vol. 52, no. 3, pp. 522–555, 2014.

[224] J. Windmiller and B. Stevens, "The inner life of the atlantic itcz," Copernicus Meetings, Tech. Rep., 2023.

[225] J. Worden, D. Noone, and K. Bowman, "Importance of rain evaporation and continental convection in the tropical water cycle," *Nature*, vol. 445, no. 7127, pp. 528–532, 2007.

[226] J. C. Wyngaard, "Toward numerical modeling in the "terra incognita"," *Journal of the atmospheric sciences*, vol. 61, no. 14, pp. 1816–1826, 2004.

[227] T. Xu *et al.*, "Stable isotope ratios of typhoon rains in fuzhou, southeast china, during 2013–2017," *Journal of Hydrology*, vol. 570, pp. 445–453, 2019.

[228] D. Yang, "A shallow-water model for convective self-aggregation," *Journal of the Atmospheric Sciences*, vol. 78, no. 2, pp. 571–582, 2021.

[229] M.-H. Yang and R. A. Houze Jr, "Sensitivity of squall-line rear inflow to ice microphysics and environmental humidity," *Monthly weather review*, vol. 123, no. 11, pp. 3175–3193, 1995.

[230] C.-K. Yu, C.-Y. Lin, L.-W. Cheng, J.-S. Luo, C.-C. Wu, and Y. Chen, "The degree of prevalence of similarity between outer tropical cyclone rainbands and squall lines," *Scientific Reports*, vol. 8, no. 1, p. 8247, 2018.

[231] J. Yuan and R. A. Houze, "Global variability of mesoscale convective system anvil structure from a-train satellite data," *Journal of Climate*, vol. 23, no. 21, pp. 5864–5888, 2010.

[232] A. Zeng, M. Chen, L. Zhang, and Q. Xu, "Are transformers effective for time series forecasting?" In *Proceedings of the AAAI conference on artificial intelligence*, vol. 37, 2023, pp. 11 121–11 128.

[233] Q. Zhang, Y. Han, V. O. Li, and J. C. Lam, “Deep-air: A hybrid cnn-lstm framework for fine-grained air pollution estimation and forecast in metropolitan cities,” *IEEE Access*, vol. 10, pp. 55 818–55 841, 2022.

[234] R. Zhang and T. L. Delworth, “Impact of Atlantic multidecadal oscillations on India/Sahel rainfall and Atlantic hurricanes,” *Geophys. Res. Lett.*, vol. 33, p. L17712, 2006.

[235] X. Zhang *et al.*, “Indices for monitoring changes in extremes based on daily temperature and precipitation data,” *Wiley Interdisciplinary Reviews: Climate Change*, vol. 2, no. 6, pp. 851–870, 2011.

[236] E. Zipser, “Mesoscale and convective–scale downdrafts as distinct components of squall-line structure,” *Monthly Weather Review*, vol. 105, no. 12, pp. 1568–1589, 1977.

[237] P. Zuidema, G. Torri, C. Muller, and A. Chandra, “Precipitation-induced atmospheric cold pools over oceans and their interactions with the larger-scale environment,” *Surv. Geophys.*, vol. 38, 2017.

[238] P. Zuidema, G. Torri, C. Muller, and A. Chandra, “A survey of precipitation-induced atmospheric cold pools over oceans and their interactions with the larger-scale environment,” *Surveys in Geophysics*, vol. 38, no. 6, pp. 1283–1305, 2017.

Appendix A

Appendix

A.1 List of Publication

Article in Preparation

1. Abramian S., Muller C. and Risi C., **XAI for Predicting Mesoscale Convective System Size in Global Cloud Resolving Model** *Journal of Advances in Modeling Earth Systems, exp. 2024.*

Accepted Article

1. Abramian S., Muller C. and Risi C., **Extreme Precipitation in Tropical Squall Lines** *Journal of Advances in Modeling Earth Systems, 2023.*

Published Articles

1. Risi, C., Muller, C., Vimeux, F., Blosse,P., Védeau G., Dufaux, C., Abramian, S., **What controls the mesoscale variations in water isotopic composition within tropical cyclones and squall lines? Cloud resolving model simulations.** *Journal of Advances in Modeling Earth Systems, 2023.*
2. Abramian, S., Muller, C., and Risi, C., **Shear-Convection Interaction and Orientation of Tropical Squall Lines.** *Geophysical Research Letters, vol. 49-1, p.e2021GL095184, 2021.*
3. Abramian, S., Desmorat, B., Desmorat, R. et al. **Recovering the Normal Form and Symmetry Class of an Elasticity Tensor.** *Journal of Elasticity, Springer Verlag, vol. 142, p.1–33. 2020.*

Outreach Article

1. Muller, C., Abramian S., **The cloud dynamics of convective-storm.** *Physics Today, May 2023.*

A.2 List of Scientific Communications at Conferences

1. Abramian, S., Muller, C., Risi, C., Roca R., and Fiolleau, T Has the life cycle of MCSs been written from the start ? (Présentation), *3rd Workshop on Convective Organization, Triest, Italy, 2023.*
2. Abramian, S., Muller, C., Risi, C., Roca R., Fiolleau, T Investigating Mesoscale Convective Life Cycle with Machine Learning (Présentation), *CFMIP-Gass Meeting, Paris, France 2023.*
3. Abramian, S., Muller, C., and Risi, C. Extreme Precipitation in Tropical Squall Lines (Présentation), *European Geophysical Union, Vienna, Austria, 2023.*

4. Abramian, S., Muller, C., and Risi, C. Squall Lines Orientation and its Impact on Precipitation Extremes (Présentation), *In 3rd Pan-Gass Gewex Meeting, Monterey, CA, 2022.*
5. Abramian, S., Muller, C., and Risi, C. Shear Convection Interaction in Cloud Resolving Model (Présentation), *23rd Meeting in Atmospheric and Oceanic Fluid Dynamics, Breckenridge, CO, 2022.*
6. Abramian, S., Muller, C., and Risi, C. Investigating Extremes Precipitation in Tropicales Squall Lines (Présentation), *European Geophysical Union, Vienna, Austria, 2022.*
7. Abramian, S., Muller, C., and Risi, C. Investigating Extremes Precipitation in Tropicales Squall Line, (Poster), *2nd Workshop On Convective Organization, Utrecht, Netherlands, 2022.*
8. Abramian, S., Muller, C., and Risi, C. L'orientation des lignes de grains tropicales et ses conséquences sur les extrêmes de précipitations (Présentation), *Journée de la Convection Profonde, Bordeaux, France, 2022.*
9. Abramian, S., Muller, C., and Risi, C. Investigating tropical squall lines with a cloud resolving model (Short Presentation), *EGU General Assembly 2021, online, 19–30 Apr 2021.*
10. Abramian, S., Muller, C., and Risi, C. What sets tropical squall lines orientation, and why ? (Poster) *Cloud FeedBack Model Intercomparison Project Virtual Meeting 2021.*

What controls the mesoscale variations in water isotopic composition within tropical cyclones and squall lines? Cloud resolving model simulations in radiative-convective equilibrium

Camille Risi [1], Caroline Muller [1], Françoise Vimeux [2,3], Peter Blossey [4], Grégoire Védeau [1,3], Clarisse Dufaux [1], Sophie Abramian [1]

[1]Laboratoire de Météorologie Dynamique, IPSL, CNRS, École Normale Supérieure, Sorbonne Université, PSL Research University, Paris, France
[2] HydroSciences Montpellier, Université de Montpellier, CNRS, IMT, IRD, Montpellier, France
[3]Laboratoire des Sciences du Climat et de l'Environnement (CEA, CNRS, UVSQ), IPSL, Université Paris Saclay, Gif-sur-Yvette, France
[4]Department of Atmospheric Sciences, University of Washington, Seattle, USA

Key Points:

- Cloud resolving model simulations capture robust aspects of mesoscale isotopic variations observed in tropical cyclones and squall lines
- Rain evaporation and rain-vapor diffusive exchanges are the main drivers of isotopic depletion within tropical cyclones and squall lines
- Horizontal advection spreads isotopic anomalies, thus reshaping the stable isotope patterns at the mesoscale.

Corresponding author: Camille RISI, `Camille.Risi@lmd.ipsl.fr`

Abstract

Water isotopes are tracers of convective processes and are often used as proxies for past precipitation. These applications require a better understanding of the impact of convective processes on the isotopic composition of water vapor and precipitation. One way to advance this understanding is to analyze the isotopic mesoscale variations during organized convective systems such as tropical cyclones or squall lines. The goal of this study is to understand these isotopic mesoscale variations with particular attention to isotopic signals in near-surface vapor and precipitation that may be present in observations and in paleoclimate proxies. With this aim, we run cloud resolving model simulations in radiative-convective equilibrium in which rotation or wind shear is added, allowing us to simulate tropical cyclones or squall lines. The simulations capture the robust aspects of mesoscale isotopic variations in observed tropical cyclones and squall lines. We interpret these variations using a simple water budget model for the sub-cloud layer of different parts of the domain. We find that rain evaporation and rain-vapor diffusive exchanges are the main drivers of isotopic depletion within tropical cyclones and squall lines. Horizontal advection spreads isotopic anomalies, thus reshaping the mesoscale isotopic pattern. Variations in near-surface relative humidity and wind speed have a significant impact on d-excess variations within tropical cyclones. This study contributes to our understanding of mesoscale isotopic variability and provides physical arguments supporting the interpretation of paleoclimate isotopic archives in tropical regions in terms of past cyclonic activity.

Plain Language Summary

Naturally-available, stable water molecules can be light (one oxygen atom and two hydrogen atoms) or heavy (one hydrogen atom is replaced by a deuterium atom). These different molecules are called water isotopes. In large, long-lived, severe storms such as tropical cyclones or squall lines (thunderstorms that organize into lines), the rain is observed to be more depleted in heavy isotopes. Several studies have exploited this property to reconstruct the past variations in the frequency of occurrence of tropical cyclones or severe thunderstorms based on isotope variations observed in speleothems. The aim of this study is to understand what controls the depletion in heavy isotopes of the rain in tropical cyclones and squall lines. With this aim, for the first time we use high-resolution simulations (2-4 km in horizontal) to simulate the internal dynamics of tropical cyclones and squall lines and their isotope composition. We design a simple model to interpret the results. We show that the rain evaporation and rain-vapor exchanges deplete the water vapor, and the subsequent rainfall, in heavy isotopes.

1 Introduction

The isotopic composition of water vapor (HDO or $H_2^{18}O$) evolves along the water cycle as phase changes are associated with isotopic fractionation. The isotopic composition of precipitation recorded in paleoclimate archives has significantly contributed to the reconstruction of past hydrological changes across the tropics (Wang et al., 2001; Cruz et al., 2009). Indeed, over tropical oceans, the precipitation is usually more depleted in heavy isotopes as precipitation rate increases, an observation called the amount effect (Dansgaard, 1964). In concert with the precipitation, the water vapor over tropical oceans is also more depleted as precipitation rate increases according to satellite and in-situ observations (Worden et al., 2007; Kurita, 2013). Over tropical land, both the precipitation and water vapor are generally observed to be more depleted as the precipitation rate increases on average over the previous days before the observation of isotopic depletion and on average over some large-scale domain upstream of the region of depletion, for example in Western Africa (Risi et al., 2008; Tremoy et al., 2012), Southeast Tibetan Plateau (Gao et al., 2013), Southern India (Lekshmy et al., 2014; Sinha & Chakraborty, 2020), Southern tropical America (Vimeux et al., 2005; Vimeux et al., 2011) or the Maritime Continent (Moerman et al., 2013; Conroy et al., 2016). In the tropics, the importance of precipitation rate, either at the local or at the regional scale, in controlling the water isotopic composition of water vapor and precipitation is thus well established. However, the relationship between the water isotopic composition and precipitation rate can vary temporally and spatially. For example, it may depend on the proportion of stratiform versus convective rain (Aggarwal et al., 2016), on the organization of convection (Lawrence et al., 2004; Risi et al., 2008; Chakraborty et al., 2016) or on the shape of vertical velocity profiles (Moore et al., 2014; Torri et al., 2017; Lacour et al., 2017). For a more robust and quantitative interpretation of water isotopic archives in terms of past hydrological changes or cyclonic activity, a better understanding of how the precipitation rate impacts the isotopic composition of water vapor and precipitation is thus necessary.

In the tropics, most of the precipitation falls under deep convective systems (Houze, 2004). It is associated with processes which deplete the water vapor in heavy isotopes. In particular, observational studies have highlighted the role of rain evaporation (Worden et al., 2007), diffusive liquid-vapor exchanges (Lawrence et al., 2004), mesoscale downdrafts (Risi et al., 2010; Kurita, 2013) and microphysical processes in stratiform regions of convective systems (Aggarwal et al., 2016). Modeling studies with high resolution simulations have confirmed the key role of rain evaporation and diffusive liquid-vapor (Torri, 2021, 2022), and of microphysical processes in stratiform regions of convective systems, especially melting of depleted snow that subsequently evaporates (Risi et al., 2021).

One way to test the importance of these processes is to investigate the observed evolution of the isotopic composition of precipitation or near-surface water vapor within “organized” convective systems (Risi et al., 2010). By organized, we mean that the convective system has different parts, characterized by different convective or microphysical processes, and connected through some mesoscale circulation. For example, tropical cyclones are a spectacular manifestation of convective organization, usually with an eye at the center, surrounded by convective walls with intense rainfall and spiral rain bands reaching several hundreds of kilometers (Houze, 2010) (Figure 1a). The precipitation and near-surface water vapor collected in the vicinity of tropical cyclones often show stronger depletion towards the cyclone center, more depleted water vapor in spiral bands than in between bands (Gedzelman et al., 2003; Xu et al., 2019; Bhattacharya et al., 2022), and more enriched water vapor in the eye (Fudeyasu et al., 2008). The depletion has been interpreted in terms of progressive rain out towards the center and rain-vapor diffusive exchanges (Lawrence et al., 2002). The enrichment in the eye has been interpreted in terms of sea spray evaporation (Fudeyasu et al., 2008). As another example, squall lines are elongated, propagative convective systems with a gust front, followed by a convective region of intense rainfall, a transition region with a paused rainfall, and a trailing stratiform region of light rainfall (Houze, 2004) (Figure 1b). The precipitation collected during squall lines often features a W shape with more depleted rain in convective and stratiform regions (Taupin & Gallaire, 1998; Risi et al., 2010). In the near-surface water vapor, many squall lines show isotopic depletion in the convective and stratiform regions (Tremoy et al., 2014). This pattern has been interpreted in terms of rain evaporation and mesoscale downdrafts.

Better understanding the evolution of the isotopic composition of precipitation or near-surface water vapor within “organized” convective systems is also useful to better understand how convective organization is recorded in paleoclimate archives. In particular, more organized convective systems, such as squall lines (Risi et al., 2008; Tremoy et al., 2014; Maupin et al., 2021) or tropical cyclones (Lawrence & Gedzelman, 1996; Lawrence et al., 2004; Price et al., 2008; Chakraborty et al., 2016; Jackisch et al., 2022), have been observed to be associated with water vapor and precipitation that are more depleted in heavy isotopes than unorganized systems. In particular, the depleted rain of tropical cyclones leaves a depleted imprint in surface waters (Welsh & Sánchez-Murillo, 2020) and can significantly affect long-term averages of the isotopic composition of precipitation or surface waters (Lawrence, 1998; Baldini et al., 2016). This suggests that the annual-mean or multi-annual-mean isotopic composition of precipitation recorded in speleothems could be used to reconstruct past cyclonic activity (Lawrence & Gedzelman, 2003; Miller et al., 2006; Frappier et al., 2007; Chen et al., 2021), though this can be challenging (Jackisch et al., 2022). In the past few years, several studies have interpreted speleothems in terms of cyclonic frequency (Nott et al., 2007; Medina-Elizalde & Rohling, 2012; Baldini et al., 2016). Similarly, the depletion observed in Texan speleothems has been interpreted as enhanced activity of large, long-lived, organized convective systems (Maupin et al., 2021). In addition to paleoclimate applications, better understanding how convective processes impact the water isotopic composition is also relevant to assess the added value of water isotopic measurements to better quantify convective processes and better evaluate their representation in models (Bony et al., 2008; Field et al., 2014; Diekmann et al., 2021; Ramos et al., 2022).

The goal of this paper is to investigate the processes controlling the evolution of near-surface water vapor and precipitation within squall lines and tropical cyclones. So far, this question has often been addressed using observational studies or simple box models (Gedzelman et al., 2003; Lawrence et al., 2002; Fudeyasu et al., 2008; Tremoy et al., 2014; Xu et al., 2019; Bhattacharya et al., 2022). Here for the first time, we used three-dimensional high-resolution simulations, in which convective motions are explicitly represented, to simulate the isotopic composition of water vapor and precipitation in tropical cyclones and squall lines. Using these simulations and a simple box model of the sub-cloud layer, we quantified the relative importance of the different processes that have been suggested by previous studies, e.g. progressive rain out, rain-vapor exchange, downdrafts (Lawrence et al., 2002; Risi et al., 2010; Tremoy et al., 2014; Xu et al., 2019; Bhattacharya et al., 2022). Our simulations are run in a radiative-convective equilibrium configuration. Because of this idealized configuration, no one-to-one comparison can be made with real observed system. Therefore, we focus on robust features that have been observed in most squall lines and tropical cyclones in previous studies.

2 Methods

2.1 Isotopic variables

The water content in heavy isotopes (HDO or $H_2^{18}O$) is expressed in ‰ as $\delta D = (R_D/R_{D,SMOW} - 1) \times 1000$ and $\delta^{18}O = \left(R_{^{18}O}/R_{^{18}O,SMOW} - 1\right) \times 1000$, where R_D and $R_{^{18}O}$ respectively are the ratio of Deuterium over Hydrogen atoms and of ^{18}O over ^{16}O atoms in the water, and SMOW is the Standard Mean Ocean Water reference. Hereafter, when there is a relatively large ratio of heavy over light atoms in some water, we will refer to this water as relatively enriched in heavy atoms, or simply relatively enriched. Conversely, when there is a relatively small ratio of heavy over light atoms in some water, we will refer to this water as relatively depleted in heavy atoms, or simply relatively depleted.

To first order, δD variations are 8 times those in $\delta^{18}O$ (Craig, 1961), so we will focus on δD here. However, slight deviations in the δD–$\delta^{18}O$ relationship can be quantified by the second-order parameter d-excess: $d = \delta D - 8 \cdot \delta^{18}O$. It reflects kinetic effects associated with diffusivity differences between the different water isotopologues. We will also show some results for d-excess as it can reflect kinetic effects in rain evaporation or surface evaporation.

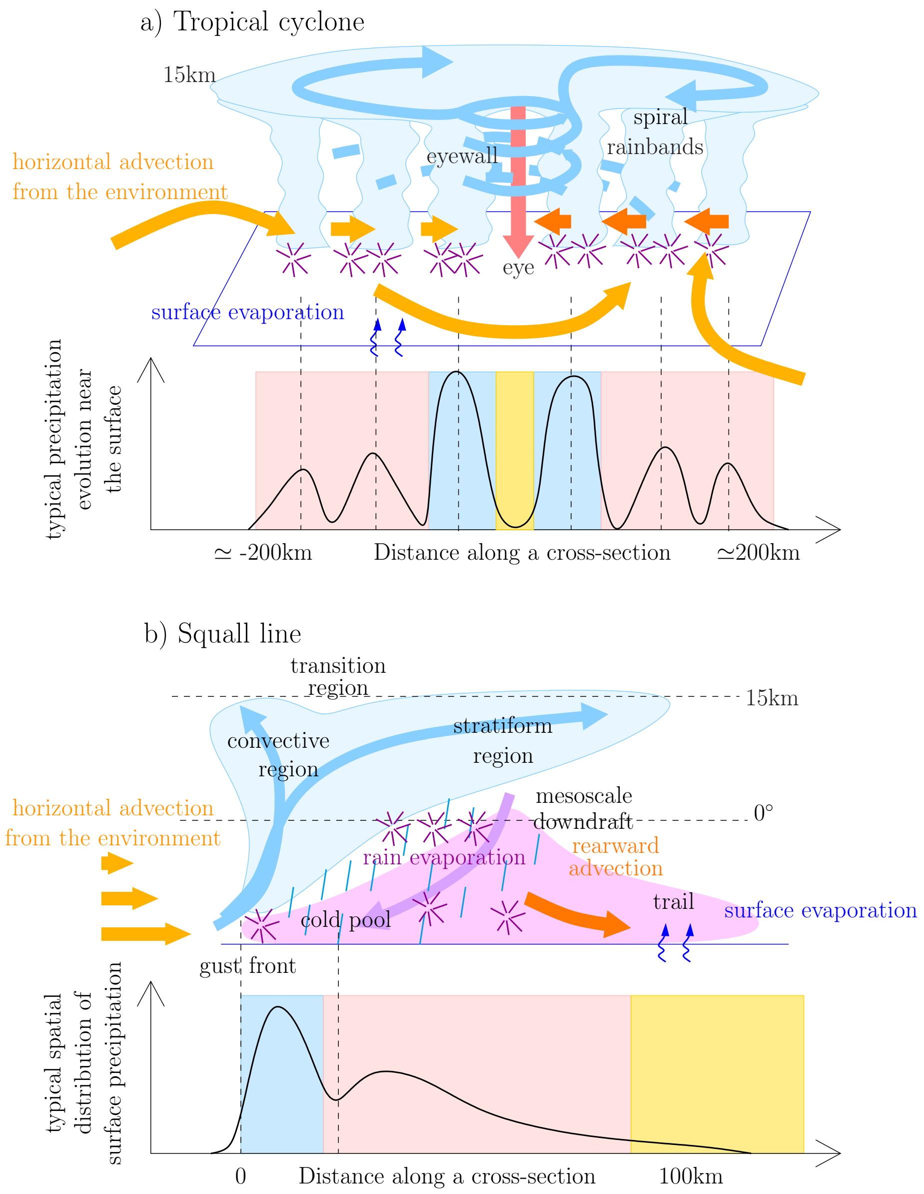

Figure 1. A schematic of the main structural elements of tropical cyclones (a) and squall lines (b). The observed typical spatial distribution of the surface precipitation is also indicated. The vertical and horizontal scales are approximate and may vary depending on events. The yellow, blue and pink rectangles in (a) respectively represent the eye, eyewall and rain band regions of the cyclone, as will be defined later in the article; the blue, pink and yellow rectangles in (b) respectively represent the convective, stratiform and trail regions of the squall line, as will also be defined later in the article.

2.2 Model and simulations

2.2.1 Cloud Resolving Model

We used the same Cloud Resolving Model (CRM) as that used in Risi et al. (2020), namely the System for Atmospheric Modeling (SAM) non-hydrostatic model (Khairoutdinov & Randall, 2003), version 6.10.9, which is enabled with water isotopes (Blossey et al., 2010). This model solves anelastic conservation equations for momentum, mass, energy and water, which is present in the model under six phases: water vapor, cloud liquid, cloud ice, precipitating liquid, precipitating snow, and precipitating graupel. We used the bulk, mixed-phase microphysical parameterization from (Thompson et al., 2008) in which water isotopes were implemented (Moore et al., 2016). At the ocean surface, there is no representation of sea spray. Therefore, we did not simulate the possible impact of sea spray on the isotopic composition in the eye (Fudeyasu et al., 2008).

2.2.2 Radiative-convective equilibrium with large-scale forcing

Simulations are three-dimensional, with a doubly-periodic domain. They are run in radiative-convective equilibrium over an ocean surface. The sea surface temperature (SST) was set at 30°C. We did not prescribe any diurnal cycle.

Organized convection is typically observed in regions of large-scale ascent (Tan et al., 2013; Jakob et al., 2019). Therefore, we impose a large-scale vertical ascent with a cubic shape, reaching -40 hPa/d at 5 km and 0 hPa/d at the surface and above 100 hPa (Risi et al., 2020). Simulations were also run without vertical ascent, and gave similar results except that the convective systems were smaller and with a less well-defined internal structure. For example, the tropical cyclone without ascent does not show any eye at the center. We thus focus on the simulations with large-scale ascent in the following.

The simulations were run for 50 days. The last 10 days of simulation are analyzed with one three-dimensional output file every day. In radiative-convective equilibrium, all snapshots exhibit similar behavior (videos in SI).

2.2.3 Set-up for the cyclone simulation

We used a domain of 1024 km×1024 km with a horizontal resolution of 4 km and 96 vertical levels. This horizontal resolution is sufficient to properly simulate the internal structure of a cyclone (Gentry & Lackmann, 2010). Cyclones spontaneously develop in radiative-convective equilibrium simulations when some rotation is added (Khairoutdinov & Emanuel, 2013; Muller & Romps, 2018). Here the effect of rotation is added through a Coriolis parameter that corresponds to a latitude of 40°. Although no tropical cyclones are expected to form at such latitudes, a strong rotation allows us to simulate a small cyclone (Chavas & Emanuel, 2014) that can fit our small domain. This allows the simulation to remain computationally reasonable.

The initial conditions are spatially homogeneous and an unique cyclone develops spontaneously through self-aggregation mechanisms after a few days. This is consistent with the time scale for cyclogenesis in other self-aggregation studies (Muller & Romps, 2018).

2.2.4 Set-up for the squall line simulation

We used a domain of 256 km×256 km with a horizontal resolution of 2 km and 96 vertical levels. Squall lines spontaneously develop in radiative-convective equilibrium simulations when horizontal wind shear is added (Robe & Emanuel, 2001; Muller, 2013; Abramian et al., 2022). We added a horizontally uniform wind in the x direction that reaches 10 m/s at the surface and linearly decrease to 0 m/s at 1 km. According to Rotunno et al. (1988), the shear with our settings leads to the formation of a strong and long-lived squall line, perpendicular to the background wind. The uniform surface wind is subtracted when calculating surface fluxes, to avoid this simulation from having significantly higher surface fluxes. The radiative fluxes are imposed, because interactive radiation leads to some radiative feedbacks that disfavors the organization into squall lines. The convection quickly organizes into a line, after about one day of simulation.

2.3 Simple box model of the sub-cloud layer

To quantify the relative importance of processes in determining the isotopic composition in the different parts of the domain, we design a simple box model for the subcloud layer (SCL) (Figure 2a). The model is the same as that in Risi et al. (2020), except that here we account for horizontal advection and non-stationary effects. Accounting for these effects is necessary because the simple model will be applied in the different sub-domains highlighted in Figure 1. Whereas the SCL is in quasi-equilibrium in the domain-mean, the SCL is not in quasi-equilibrium in sub-domains. For example, the eye of the cyclone wanders across the domain and is thus never in quasi-equilibrium.

Previous studies have used model tendencies along backward trajectories to quantify the relative importance of processes on local conditions (Dütsch et al., 2018; Attinger et al., 2019). This approach is most relevant when large-scale horizontal transport plays a key role. In radiative-convective equilibrium however, local processes and vertical transport dominate. A simple box model was thus judged more relevant.

2.3.1 Water vapor budget

The SCL is defined as the atmospheric levels from the surface to the SCL top, where the SCL top is the level just below the lowest level where the domain-mean massic cloud water content exceeds 10% of its maximum value. With this definition, we find that the SCL is approximately well-mixed in our simulations. Therefore, in the box model, we can assume that the specific humidity is vertically uniform throughout the SCL, consistent with previous mixed-layer models (Stevens, 2006; Neggers et al., 2006; Albright et al., 2022). We define W as the water mass in the SCL per area unit (in $kg.m^{-2}$):

$$W = \int_{z=0}^{z_t} \rho \cdot q \cdot dz \tag{1}$$

where q is the specific humidity near the surface, ρ is the air density, z is the altitude above sea level and z_t is the altitude of the SCL top. The water budget of the SCL in a given sub-domain writes (Figure 2a):

$$\frac{dW}{dt} = E_{sfc} + F_d \cdot q \cdot (r_d - 1) - F_u \cdot q \cdot (r_u - 1) + E_{horiz} + E_{ev} - E_c \tag{2}$$

where E_{sfc} is surface evaporation, F_d and F_u are the downward and upward mass fluxes at SCL top, E_{horiz} is the flux of water through horizontal advection, E_{ev} is the rain evaporation, E_c is some condensation that may occur if the SCL top is not horizontally uniform, $r_u = q_u/q$, $r_d = q_d/q$, q_u and q_d are the specific humidity in updrafts and downdrafts. All these variables are directly diagnosed from the simulations for each sub-domains as detailed in (Risi et al., 2021).

2.3.2 Isotopic budget

As for the water vapor budget, the budget for heavy water vapor isotopes in the SCL is:

$$\frac{d(R \cdot W)}{dt} = R_{sfc} \cdot E_{sfc} + F_d(R_d \cdot q_d - R \cdot q) - F_u(R_u \cdot q_u - R \cdot q) + R_{horiz} \cdot E_{horiz} + R_{ev} \cdot E_{ev} - R_c \cdot E_c \tag{3}$$

where R is the isotopic ratio of the near-surface vapor, R_u and R_d are the isotopic ratios in updrafts and downdrafts, R_{sfc}, R_{horiz}, R_{ev} and R_c are the isotopic compositions of the surface evaporation, horizontal advection, rain evaporation and condensation fluxes.

We define:

$$E_{res} = E_{horiz} - \frac{dW}{dt} \tag{4}$$

E_{res} is the flux of water through both horizontal advection and non-stationary effects, and is calculated as a residual. For example, in the cyclone's eyewall where the air is very moist (the relative humidity is greater than 95%), we expect that horizontal advection will have a drying effect, i.e. $E_{horiz} < 0$. In addition, since the cyclone wanders across the domain, the eyewall often arrives in dry parts of the domain, i.e. $\frac{dW}{dt} > 0$. Therefore, both horizontal advection and non-stationary effects contribute to drying the eyewall, i.e. $E_{res} < 0$.

Similarly, we define the isotopic ratio of the flux R_{res}:

$$R_{res} = \frac{R_{horiz} \cdot E_{horiz} - \frac{d(R \cdot W)}{dt}}{E_{horiz} - \frac{dW}{dt}} \tag{5}$$

To solve the isotopic budget equation for R, the isotopic ratios R_{sfc}, R_d, R_u, R_{res}, R_{ev} and R_c are all expressed as a function of R. The isotopic ratio of surface evaporation is given by (Craig & Gordon, 1965):

$$R_{sfc} = \frac{R_{oce}/\alpha_{eq}(SST) - h \cdot R}{\alpha_K \cdot (1 - h)} \tag{6}$$

where R_{oce} is the isotopic ratio at the ocean surface, $\alpha_{eq}(SST)$ is the equilibrium fractionation coefficient at the sea surface temperature, α_K is kinetic fractionation coefficient (Merlivat & Jouzel, 1979) and h is the relative humidity normalized at the SST and accounting for ocean salinity calculated as follows:

$$h = q/q_{sat}^{surf}(SST) \tag{7}$$

where $q_{sat}^{surf}(SST) = 0.98 \cdot q_{sat}(SST)$ and q_{sat} is the humidity saturation as a function of temperature at the sea level pressure. Variables h and the kinetic fractionation as a function of surface wind speed are diagnosed from the CRM. We assume that $\delta D_{oce} = 0‰$.

The isotopic ratios in updrafts and downdrafts are assumed to follow logarithmic functions: $R_u = R \cdot (r_u)^{\alpha_u - 1}$ and $R_d = R \cdot (r_d)^{\alpha_d - 1}$ where R_u and R_d are isotopic ratios in updrafts and downdrafts, and α_u and α_d are the $q - \delta D_v$ steepness coefficients for updrafts and downdrafts (Risi et al., 2020). We set $R_{res} = \phi_{res} \cdot R$, $R_{ev} = \phi_{ev} \cdot R$ and $R_c = \phi_c \cdot R$. All parameters α_u, α_d, ϕ_{res}, ϕ_{ev} and ϕ_c can be diagnosed from the simulation for each sub-domain.

$$R = \frac{R_{oce}/\alpha_{eq}(SST)}{h + \alpha_K \cdot (1 - h) \cdot A} \tag{8}$$

where

$$A = \frac{((r_u)^{\alpha_u} - 1) + \frac{F_d}{F_u} \cdot (1 - (r_d)^{\alpha_d}) - \frac{E_{ev}}{qF_u} \cdot \phi_{ev} + \frac{E_c}{qF_u} \cdot \phi_c - \frac{E_{res}}{qF_u} \cdot \phi_{res}}{(r_u - 1) + \frac{F_d}{F_u} \cdot (1 - r_d) - \frac{E_{ev}}{qF_u} + \frac{E_c}{qF_u} - \frac{E_{res}}{qF_u}} \tag{9}$$

In absence of vertical mixing ($r_u = r_d = 1$), rain evaporation, condensation, horizontal advection and non-stationary effects ($E_{ev} = E_c = E_{res} = 0$), then $A = 1$ and equation 8 reduced to the classical closure (Merlivat & Jouzel, 1979) (hereafter MJ79 closure).

Note that the diagnostic of E_{res} and ϕ_{res} as residuals guarantees that the water and isotopic budgets of the SCL are closed. However, it does not guarantee that equation 8 with input parameters diagnosed from the CRM simulations yields exactly the same isotopic ratios as those directly simulated by the CRM. This is because many simplifying assumptions underlie the simple model. In particular, we neglect spatial and temporal co-variations between all the different parameters within each sub-domain. In addition, we diagnose the parameters related to vertical mixing (q_u, q_d, α_u, α_d) assuming a simple upstream advection scheme (Godunov, 1959), whereas the advection scheme in the SAM model is more sophisticated (Smolarkiewicz & Grabowski, 1990). As will be illustrated in sections 4.3 and 4.4, the simple box model of this study systematically overestimates the δD_v simulated by the CRM by a few ‰, and systematically underestimates d_v by a few ‰. While we keep in mind these mismatches, we will show that the simple box model is nevertheless able to simulate the isotopic variations between different subdomains of the cyclone and the squall line, justifying its relevance.

2.3.3 Method to decompose anomalies in isotopic ratios

To decompose the anomaly in the isotopic ratio in each sub-domain relative to that in the environment, we categorize the parameters controlling R in our simple box model into 6 processes:

1. Parameter h: near-surface relative humidity, which impacts the kinetic processes during ocean surface evaporation (Merlivat & Jouzel, 1979) (Figure 2b, red).
2. Parameter α_K: kinetic fractionation coefficient, which depends on the surface wind speed (Merlivat & Jouzel, 1979) (Figure 2b, orange).
3. Parameters F_d/F_u, r_u, r_d, α_u and α_d: vertical mixing through the SCL top (green in Figure 2b). This includes the effect of the horizontal humidity contrasts (r_u and r_d). When horizontal humidity contrasts between dry and moist zones of a subdomain are larger, dry subsiding regions import drier air and more depleted water vapor into the SCL, while ascending regions export moister air and more enriched water vapor from the SCL. This has thus a depleting effect. This also includes the effect of variations in the steepness of the relationship between q and δD_v for updrafts and downdrafts (α_u and α_d). When the $q - \delta D_v$ steepness is larger, downdrafts import more depleted vapor into the SCL and updrafts export more enriched vapor out of the SCL (Risi et al., 2021). The $q - \delta D_v$ steepness depends on the enriching or depleting processes that occur above the SCL. Typically, the dominant effect is rain evaporation above the SCL, which depletes the water vapor, especially near the melting level (Risi et al., 2021). While the effects of horizontal humidity contrasts and q-δD_v steepness were separated in (Risi et al., 2021), here we combine these two effects to reduce non-linear effects during the decomposition.
4. Parameters $E_{ev}/(qF_u)$ and ϕ_{ev}: rain evaporation in the SCL (purple in Figure 2b).
5. Parameters $E_c/(qF_u)$ and ϕ_c: condensation in the SCL (cyan in Figure 2b).
6. Parameters $E_{res}/(qF_u)$ and ϕ_{res}: horizontal advection and non-stationary effects (dark green in Figure 2b).

We can thus write the isotopic ratio predicted by the simple box model in each sub-domain s as

$R_s = R\left(p_{s,1}, p_{s,2}, p_{s,3}, p_{s,4}, p_{s,5}, p_{s,6}\right) = R\left(\left(p_{s,i}\right)_{i=1,6}\right)$, where $p_{s,i}$ is the vector of parameters corresponding to the process i and the sub-domain s, and R is the function defined in equation 8. The difference between the isotopic ratio in the sub-domain and that in the environment thus writes:

$$\Delta R_s = R\left(\left(p_{s,i}\right)_{i=1,6}\right) - R\left(\left(p_{e,i}\right)_{i=1,6}\right) \tag{10}$$

where $p_{e,i}$ is the vector of parameters corresponding to the process i and the environment. For each sub-domain s and each process j, we estimate the contribution of process j to ΔR_s as:

$$c_{s,j} = R\left(\left(\frac{p_{s,i}+p_{e,i}}{2}\right)_{i=1,6,i\neq j}, p_{s,j}\right) - R\left(\left(\frac{p_{s,i}+p_{e,i}}{2}\right)_{i=1,6,i\neq j}, p_{e,j}\right) \tag{11}$$

Because R is a non-linear function of its parameters, $\sum_{j=1}^{6} c_{s,j}$ does not necessarily equal ΔR_s. We estimate the impact of non-linear effects as a residual:

$$c_{s,non\,linear} = \Delta R_s - \sum_{j=1}^{6} c_{s,j} \tag{12}$$

3 Simulated patterns and qualitative comparison with observations

3.1 Tropical cyclone

3.1.1 mesoscale structure

To visualize the mesoscale structure of the tropical cyclone, in Figure 3 we plot maps of the precipitation rate, near-surface air temperature, surface pressure anomaly, near-surface relative humidity, near-surface water vapor δD and surface rain δD for an arbitrary snapshot. The simulated cyclone exhibits features that are typical of observed cyclones (Houze, 2010). It exhibits a small eye with weak precipitation (Figure 3a) and warm air (Figure 3b), consistent with the subsidence in the eye. The eye is surrounded by an eyewall and spiraling rain bands with intense precipitation and strong cyclonic winds. Around the cyclone, strong compensating subsidence develops, leading to a dry environment and some scattered, isolated cumulus and cumulonimbus clouds and their cold pools (Figure 3a-b,d).

To better document the different parts of the tropical cyclone, we plot composites of meteorological and isotopic variables as a function of the distance r to the storm center (Figure 4 and 5). All 10 snapshots were used to compute the composites. The storm center is defined as the minimum surface pressure over the domain for each snapshot. The typical structure of a tropical cyclone is well captured:

- The eye is associated with minimum pressure (around 50hPa lower than in the environment, typical of category 4 cyclones), a local minimum in precipitation, maximum near-surface air temperature and relative humidity and weak winds (Figure 4a-c). The eye is, however, too small to see the expected subsidence in Fig 4.
- The eyewall is associated with maximum precipitation and horizontal winds. The air is strongly ascending, almost saturated throughout the full troposphere (Figure 5a), and condensation is intense except in the shallow sub-cloud layer (Figure 5c).

(a) SCL water budget

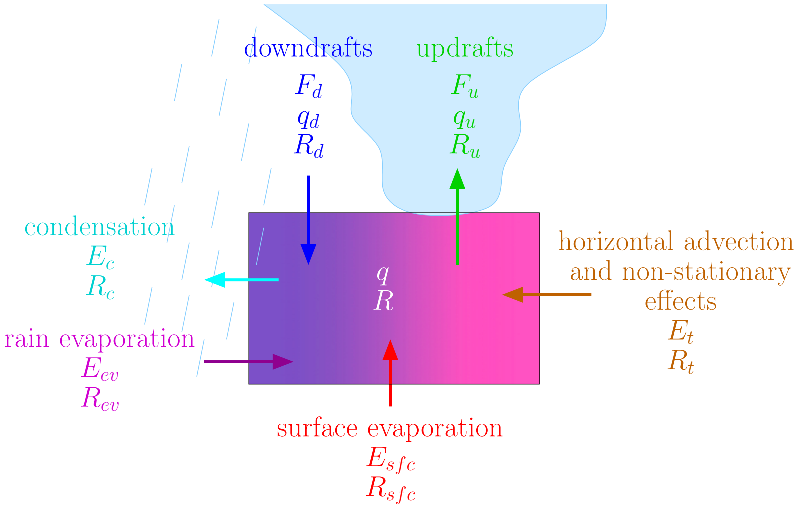

(b) SCL isotope ratio decomposition

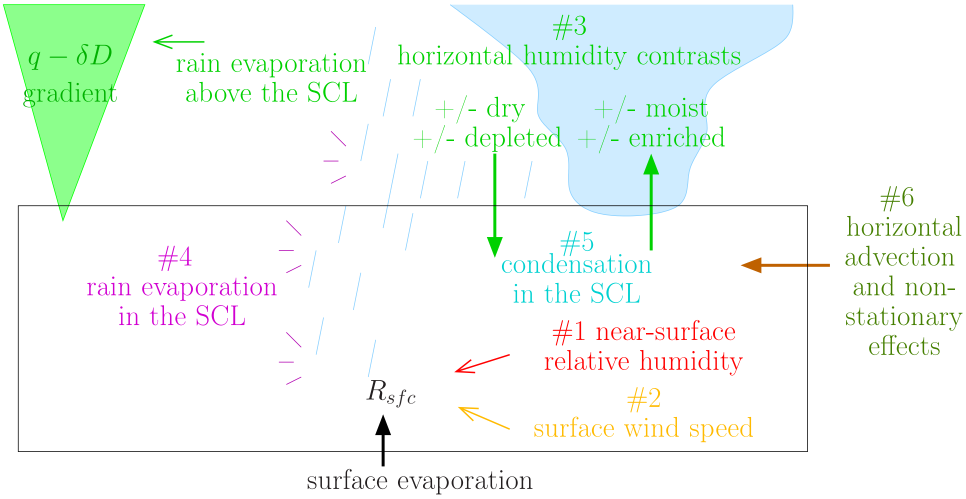

Figure 2. A description of the simple box model and of the decomposition of the SCL water vapor isotopic ratio into different contributions. (a) Simple model to predict the SCL water vapor composition. It accounts for surface evaporation, rain evaporation, cloud condensation, updrafts and downdrafts at the SCL top, and horizontal advection and non-stationary effects quantified as a water budget residual. (b) The 6 contributions in the decomposition of the isotopic ratio: near-surface relative humidity (#1, red) and surface wind speed (#2, orange), which both contribute to control the isotope composition of the surface evaporation; horizontal humidity contrasts and rain evaporation above the SCL (#3, green), which both contribute to the SCL depletion by vertical mixing; rain evaporation (#4, purple); condensation (#5, cyan) within the SCL; and horizontal and non-stationary effects (#6, dark green).

- Rainbands beyond the eyewall are associated with significant but weaker precipitation and winds. In rain band clouds, the condensation rate is large (orange shades in Figure 5c). Below the rain band clouds, the air is dry (Figure 5a), allowing large rates of snow sublimation and rain evaporation (blue shades in Figure 5c).

3.1.2 Definition of sub-domains

Based on the previous description of mesoscale structure, we divide all grid points into 5 sub-domains. These sub-domains are defined automatically based on some arbitrary thresholds, to which results are not crucially sensitive. We define:

- the “eye” as grid points with $r \leq r_{wall}$, where r_{wall} is the first r value for which the precipitation exceeds 20 times the domain-average precipitation (yellow rectangles in Figure 4).
- the “eyewall” as grid points with $r_{wall} < r \leq r_{band}$, where r_{band} is the first r value greater than r_{wall} and with the precipitation lower than 20 times the domain-average precipitation (blue rectangles in Figure 4).
- the “environment” as grid points with $r > r_{env}$, where r_{env} is the first r value greater than r_{band} and with the precipitation lower than 0.8 times the domain-average precipitation (white in Figure 4).

The precipitation thresholds have been adjusted so as to match the simulated cyclone structure to that described in previous studies (Houze, 2010). In between the eyewall and the environment (pink rectangles in Figure 4), rain bands are not radially symmetric. Therefore, we define “rain bands” as grid points with $r_{band} < r \leq r_{env}$ and precipitation greater than 4 times the domain-average precipitation, and “in between rain bands” as the other points.

3.1.3 Simulated isotopic evolution

The water vapor is most enriched in the eye and in the dry environment (Figure 3e-f, Figure 4e), and most depleted in heavy isotopes in the eyewall and spiraling rain bands. The water vapor d-excess is lower in the eye, and higher in the eyewall and rain bands (4e-f). The water vapor is more depleted and has a higher d-excess within the rain bands than between the rain bands (Figure 4d-e, dashed black).

The precipitation δD (δD_p) varies in concert with the water vapor δD (δD_v) where the precipitation is highest (Figure 4e, dashed black). The precipitation is slightly more depleted than if in equilibrium with the vapor. This suggests that the rain originates from condensation at a higher altitude and undergoes little evaporative enrichment as it falls, consistent with the high relative humidity. In addition, the rain quickly falls to the ground, leaving less time for the rain to isotopically equilibrate with the vapor.

3.1.4 Comparison with isotopic observations

Observed isotopic patterns in tropical cyclones can be diverse (Guilpart, 2018). However, some robust features emerge from the literature.

- There is a local maximum in δD_v and δD_p in the eye (Gedzelman et al., 2003; Fudeyasu et al., 2008). This is what the CRM simulates, with δD_v and δD_p slightly greater in the eye than in the environment (Figure 4e)
- Outside the eye, many studies have observed that the water vapor and precipitation are more depleted towards the storm center (Gedzelman et al., 2003; Fudeyasu et al., 2008; Munksgaard et al., 2015; Skrzypek et al., 2019; Xu et al., 2019; Sanchez-

(a) precipitation rate (mm/d) (b) surface air temperature (°C)

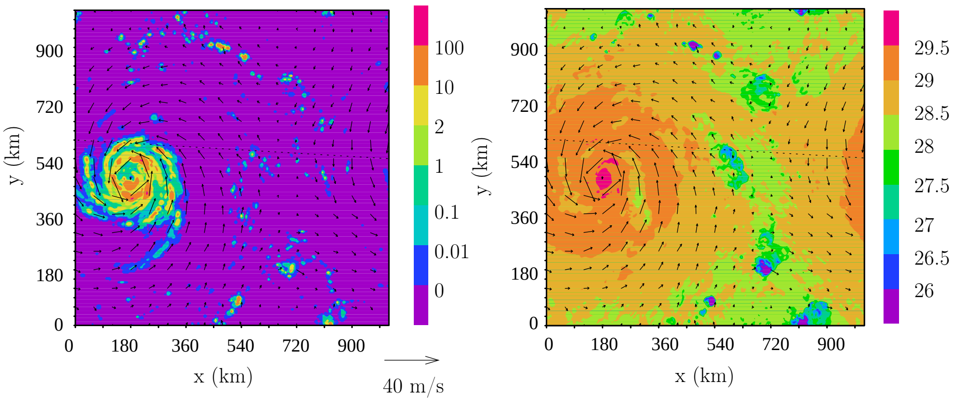

(c) pressure anomaly (Pa) (d) surface air relative humidity (%)

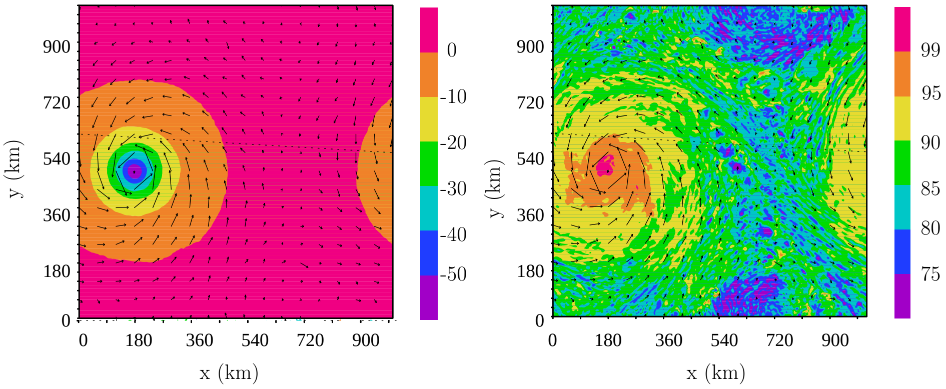

(e) near-surface δD_v (‰) (f) surface δD_p (‰)

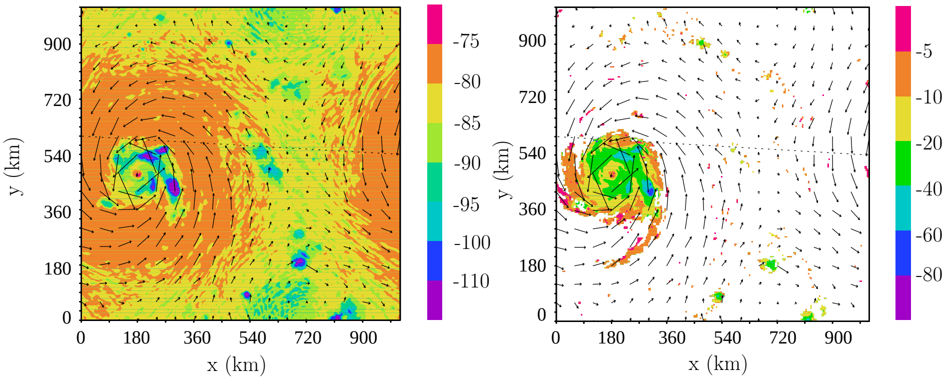

Figure 3. Snapshots of the cyclone simulation: (a) precipitation rate, (b) near-surface air temperature, (c) surface pressure anomaly relative to the domain-mean, (d) near-surface relative humidity, (e) near-surface δD_v and (f) δD_p. The near surface winds are shown as arrows. Note that due to the doubly-periodic domain, the missing part of the cyclone on the left edge of the domain appears on the right edge of the domain. The snapshot was chosen as the one where the cyclone is the closest to the center of the domain, for easier visualization.

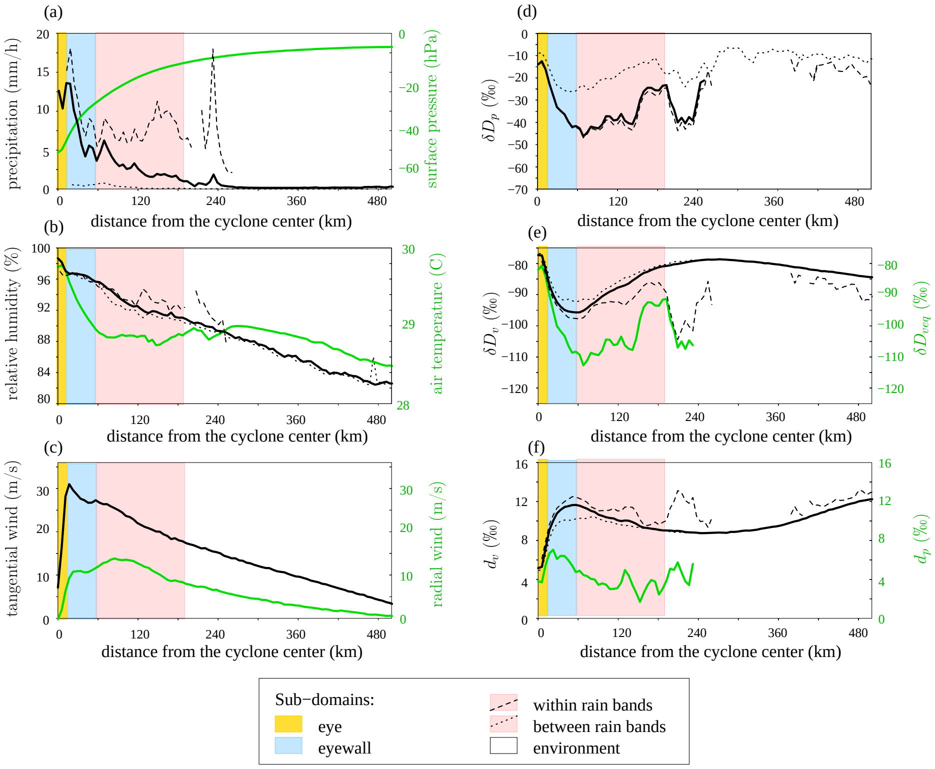

Figure 4. Evolution of surface variables as a function of distance to the cyclone center: precipitation rate (a, black), surface pressure (a, green), near-surface air temperature (b, black), near-surface relative humidity (b, green), tangential (c, black) and radial (c, green) wind, surface precipitation δD (d), near-surface water vapor δD (e, black), water vapor δD that would be in equilibrium with the precipitation (e, green), near-surface water vapor d-excess (f, black) and precipitation d-excess (f, green). The colored rectangles indicate the different sub-domains: the eye (yellow), the eyewall (blue), within and between rain bands (pink). The environment is in white. To distinguish between within rain bands and between rain bands, dashed and dotted black lines indicate the same as black lines but for grid points where the precipitation rate is respectively higher and lower than 4 times the domain-mean precipitation, representing respectively within rain bands and between rain bands.

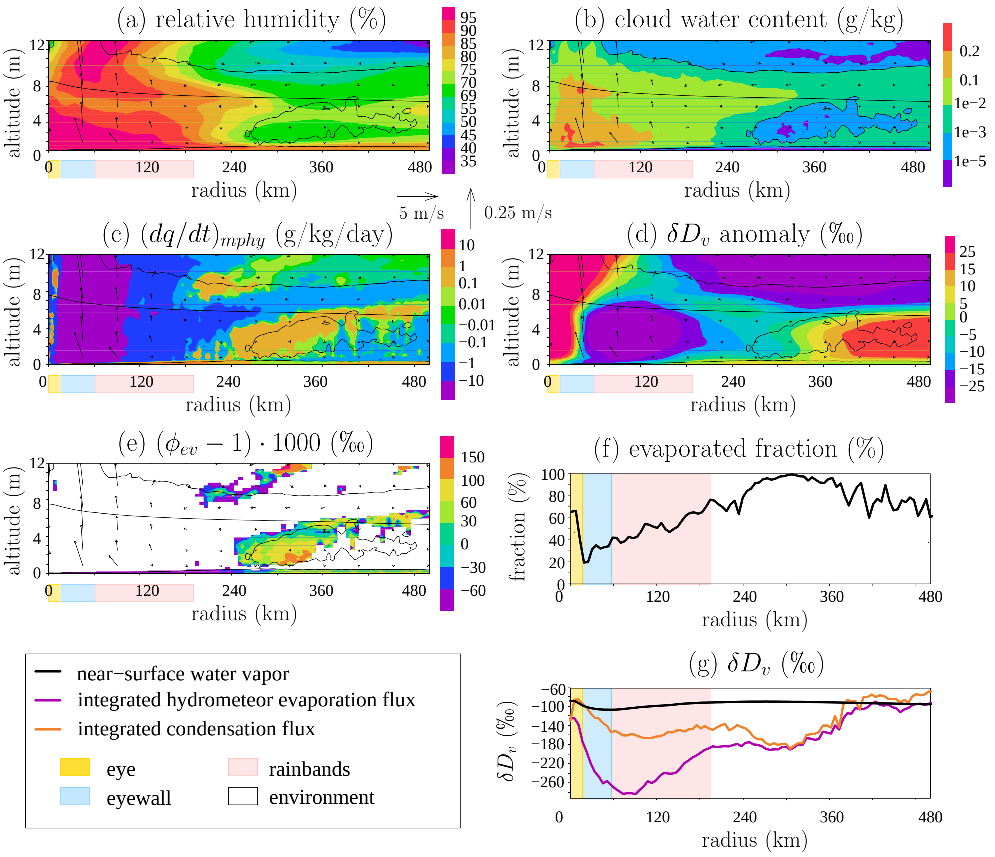

Figure 5. Variables as a function of altitude and of the distance r to the cyclone center: (a) Relative humidity; (b) cloud water content (cloud condensate and cloud ice); (c) specific humidity tendency due to phase changes (negative and positive values represent condensation/deposition and evaporation/sublimation respectively); (d) water vapor δD anomaly relative to the domain-mean δD_v at each level; (e) $(\phi_{ev} - 1) \cdot 1000$, where $\phi_{ev} = R_{ev}/R_v$ is the relative enrichment of the isotopic ratio of the hydrometeor evaporation/sublimation relative to the water vapor isotopic ratio. ϕ_{ev} is shown only when significant hydrometeor evaporation/sublimation occurs; (f) fraction of the vertically-integrated condensation flux that evaporates before reaching the ground; (g) δD in the near-surface vapor (black), in the vertically-integrated condensation flux (orange) and in the vertically-integrated evaporation flux (purple). The vertically-integrated condensation and evaporation fluxes are calculated as the volumetric-mass weighted integrals of the specific humidity tendency due to phase changes (c) where the tendency is respectively negative and positive. In (a-e), the vectors show the radial and vertical components of the wind, with the vertical wind multiplied by 20 for better readability. The nearly-horizontal black line shows the 0°C isotherm. The black contours highlights the 10^{-3} g/kg contour for cloud water content. The yellow, blue and pink boxes indicate the eye, eyewall and rainbands defined in section 3.2.2.

Murillo et al., 2019; Jackisch et al., 2022). This is what the CRM simulates (black line in the pink rectangle in Figure 4e).

- At a given distance from the storm center, the water vapor or precipitation is often more depleted within rain bands than in between (Munksgaard et al., 2015; Guilpart, 2018; Sun et al., 2022). This is also what the CRM simulates (Figure 4e, dashed black line relative to dotted black line).
- The observed d-excess in water vapor or precipitation is lower in the eye (Fudeyasu et al., 2008), higher in the environment and higher in the rain bands than in between (Munksgaard et al., 2015). These observations are consistent with our simulation (Figure 4f).

3.2 Squall line

3.2.1 mesoscale structure

In presence of wind shear, the convection organizes into lines of intense precipitation perpendicular to the imposed surface winds (Figure 6a). The environment is dry, with only a few isolated cumulonimbi. Under the squall line, a cold pool is driven by mesoscale downdrafts (Zipser, 1977; Gamache & Houze, 1981). The cold pool has a sharp edge at the front of the line, corresponding to the gust front, and a long trail due to the imposed rearward horizontal winds near the surface (Figure 6b).

To better document the different parts of the squall line, we plot composites of meteorological and isotopic variables as a function of the along-x distance to the gust front (Figures 7 and 8). For each snapshot and each value of y in the x-y domain, we select the value of x where the along-x gradient in surface pressure is at maximum. If the x-mean precipitation rate exceeds the x-y-mean value and if the gradient in surface pressure exceeds 1.7 Pa/km, we assume that it is a gust front. This procedure was visually defined to optimally detect gust fronts. We define a new x-axis and translate all rows so that all gust fronts of the different rows are aligned at x_{gust}=30 km. We arbitrary set x_{gust}=30 km so that the squall lines stand in the middle of the composite plots. Rows of the domain where the precipitation is lower than the domain mean, or where a gust front could not be identified, are considered “environment” and are not taken into account in the composite.

The precipitation rate is maximum just after the gust front (Figure 7a), consistent with observations (Chong, 2010). The precipitation maximum is located where the along-x near-surface surface wind becomes null (Figure 7c), favoring the maintenance of strong updrafts (Rotunno et al., 1988). Elsewhere, the surface wind blows rearward. Near the gust front, the temperature drops and the relative humidity rises (Figure 7b). The recovery to their environment value is slow due to the rearward advection.

Our simulated squall line shows only one precipitation peak. This is at odds with observations that often show two peaks, one for the convective region and one for the stratiform region, separated by a transition region (Biggerstaff & Houze Jr, 1991; Chong, 2010). In our simulation, the convective region transitions continuously to the stratiform region. Increasing the horizontal resolution to 1 km did not help to simulate a transition region.

In spite of this shortcoming, the convective and stratiform regions of the squall line can be identified from water vapor tendencies (Figure 8c).The convective region can be identified by its intense condensation throughout the entire troposphere (Figure 8c, around 50-60 km). The stratiform region can be identified by the condensation restricted to the upper troposphere (the anvil) and evaporation below (mesoscale downdraft) (Figure 8c, around 60-80 km). This pattern of condensation and evaporation is consistent with what we know from the squall line water budgets (Gamache & Houze, 1983; Chong & Hauser, 1990).

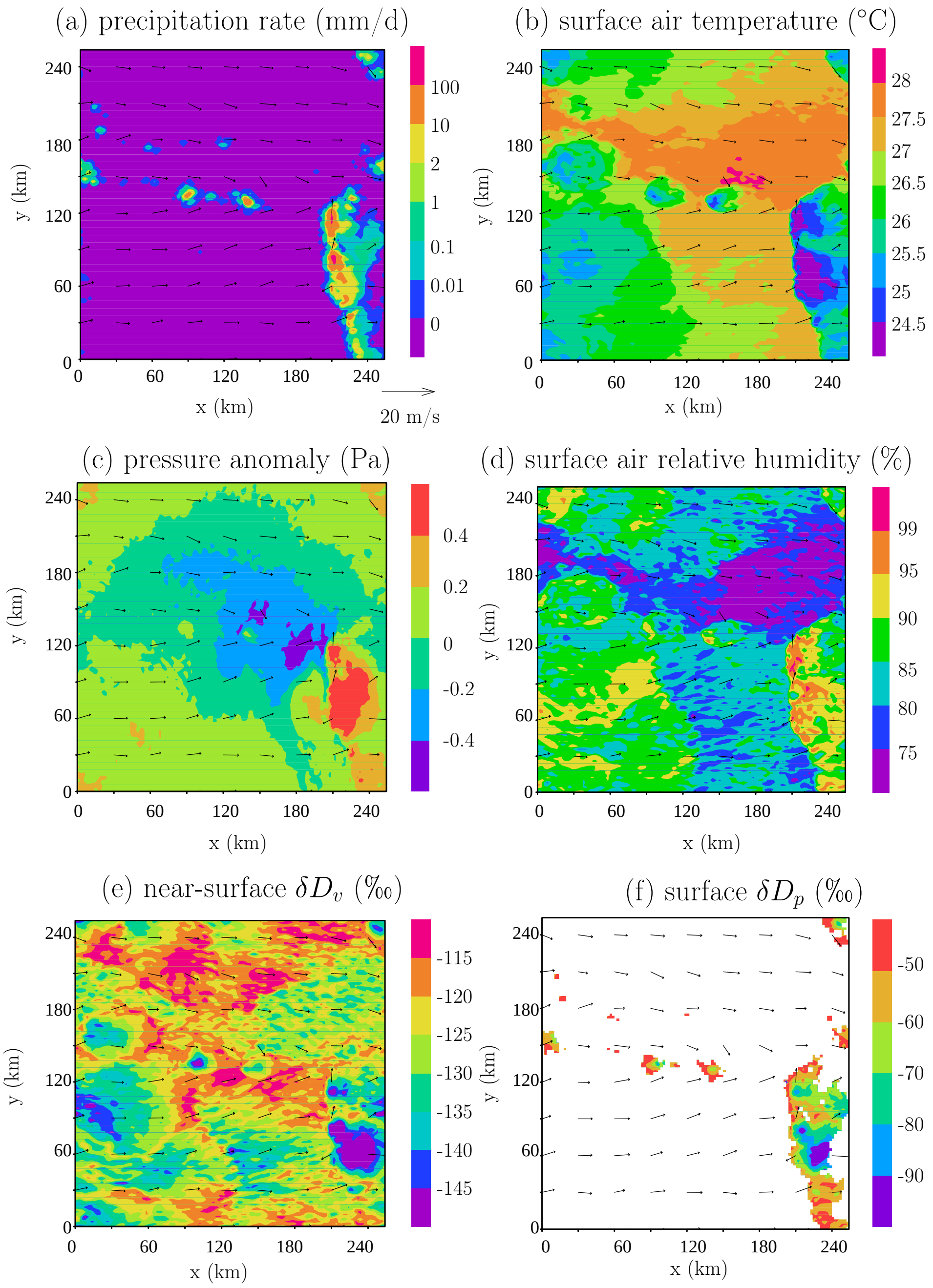

Figure 6. Same as Figure 3, except that a snapshot of the squall line simulation is shown. Note that due to the doubly-periodic domain, the trailing region on the right edge of the domain continues on the left edge.

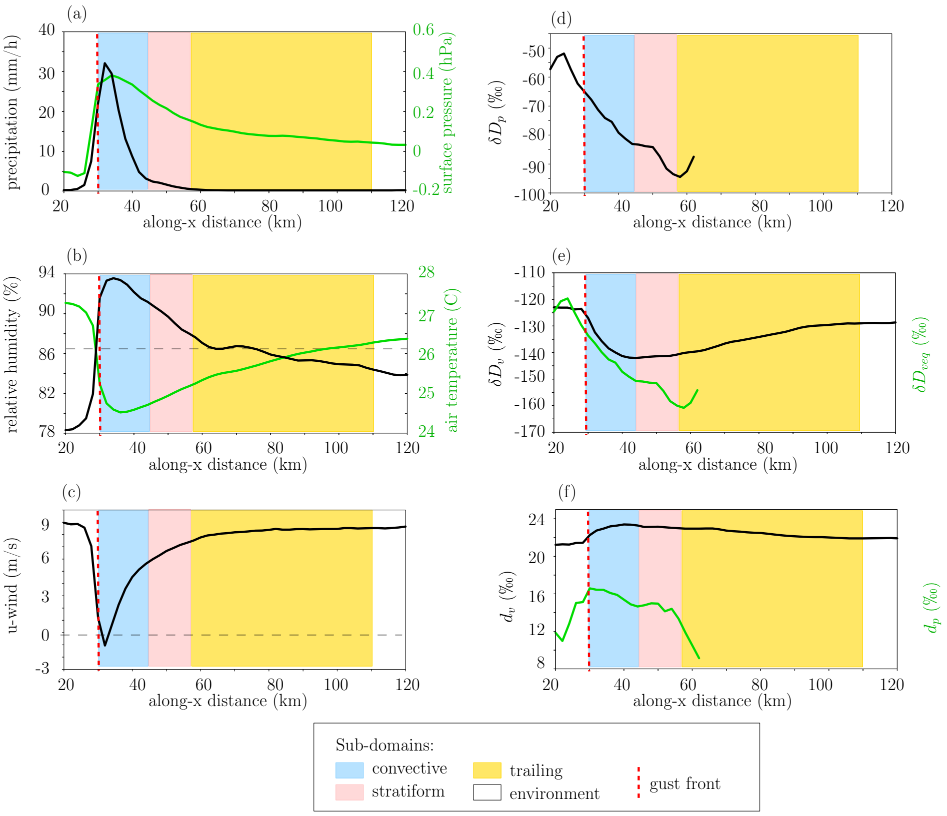

Figure 7. Same as Figure 4, except that variables for the squall line simulation are shown as a function of distance along the x-axis. The colored rectangles indicate the convective (blue), stratiform (pink) and trailing (yellow) sub-domains defined in section 3.2.2. The location of the gust front is indicated by the vertical red dashed line.

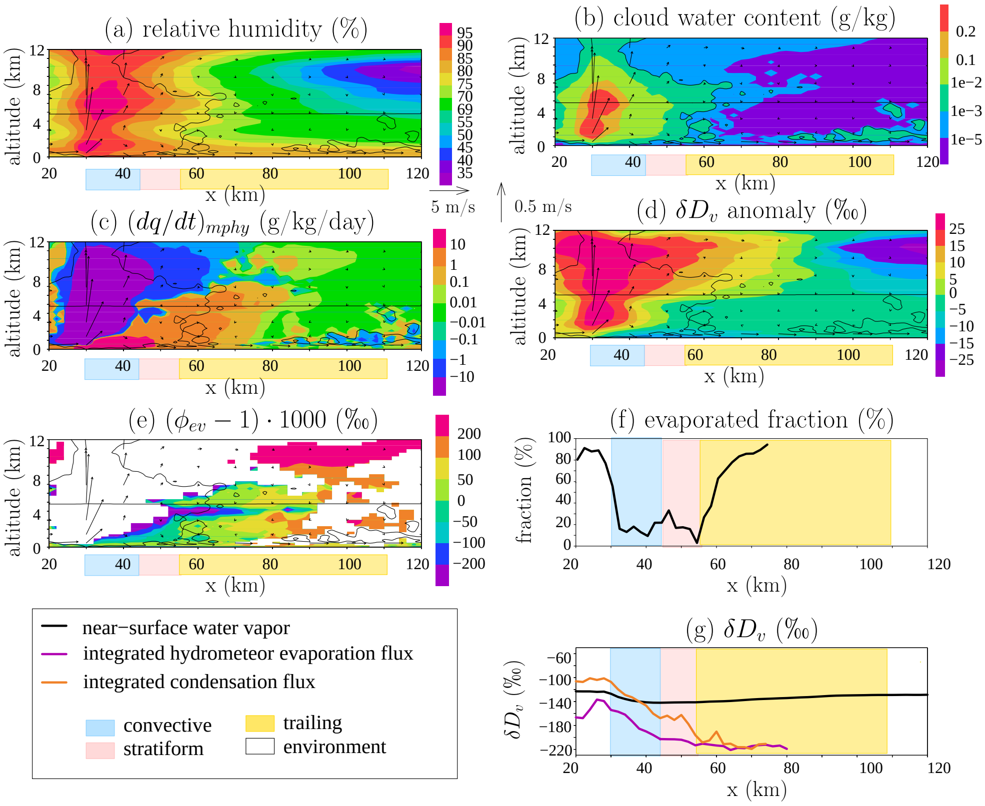

Figure 8. Same as Figure 5, except that variables for the squall line simulation are shown as a function of the distance along the x-axis. The blue, pink and yellow boxes indicate the convective, stratiform and trailing regions defined in section 3.2.2.

3.2.2 Definition of the sub-domains

Based on the above description of the mesoscale structure, we divide the grid points into 4 sub-domains: convective, stratiform, trailing and environment, as detailed below. Given the continuous transition in our simulations, we define the convective and stratiform sub-domains based on a precipitation threshold. For rows where x_{gust} is defined, we define:

- the convective region with x between x_{gust} and x_{xconv}, where x_{conv} is the lowest x value greater than x_{gust} and where the precipitation is lower than 8 times the domain-average precipitation (yellow rectangle in Figure 7). This precipitation threshold was adjusted to coincide with the transition from condensation through the entire troposphere to condensation above the melting level and rain evaporation below (Figure 8c), consistent with the transition from the convective to the stratiform region (Gamache & Houze, 1983; Chong & Hauser, 1990).
- the stratiform region with x between x_{conv} and x_{strati}, where x_{strati} is the lowest x value greater than x_{conv} and where the precipitation is below the domain-average precipitation (blue rectangle in Figure 7). This precipitation threshold was adjusted to coincide with the maximum extension of the anvil clouds, consistent with the typical structure of a squall line (Houze, 1977).

The horizontal winds near the surface spread the cold pool rearward beyond the precipitating region. Therefore, we also define a sub-domain called “trailing”, with x between x_{strati} and x_{trail}, where x_{trail} is the x value greater than x_{strati} and $T(x) < T(x_{gust}) - 1$, where T is the near-surface temperature in K (pink rectangle in Figure 7). All grid points that are not categorized as “convective”, “stratiform” or “trailing” are called “environment” (white in Figure 7).

3.2.3 Simulated isotopic evolution

Simulated squall lines show a progressive depletion of the vapor in the convective region, maximum depletion at the end of the convective region, and a long recovery in the stratiform and trailing regions (Figure 7e). The δD_v reaches its environment value about 100 km after the convective peak.

The δD_p varies in concert with δD_v (Figure 7d). In the convective and stratiform regions, δD_p is lower than in equilibrium with the vapor (green in Figure 7e), consistent with a quick fall and little evaporative enrichment. The weak precipitation that falls upwind of the convective region, where the air is dry, has a δD_p higher than that in equilibrium with vapor, indicating evaporative enrichment during rain evaporation.

The d-excess in the vapor is higher in the convective and stratiform regions, and to a lesser extent in the trailing region, than in the environment (Figure 7f). The low d-excess in the precipitation reflect the effect of evaporative enrichment, especially before the gust front and in the trailing region.

3.2.4 Comparison with isotopic observations

Isotopic observations during squall lines often show a “W” shape with minimum δD_p in the convective and stratiform regions and a local maximum in the transition region (Taupin & Gallaire, 1998; Risi et al., 2010). Our simulation is consistent with this observation, except that since our simulation does not exhibit any transition region, it shows a “V” shape instead of a “W” shape.

Investigation of the vapor isotopes of the squall lines in the Sahel showed that the isotopic evolution can be diverse, but some robust features emerge (Tremoy et al., 2014).

- In 80% of 74 observed squall lines (Tremoy et al., 2014), there is a depletion in the convective region compared to the environment before the squall line. This is consistent with our simulation.
- More than half of the observed squall lines show additional depletion in the stratiform region (Tremoy et al., 2014). This is also consistent with our simulation.
- For squall lines showing an isotopic depletion in the convective or stratiform region, the recovery from this depletion takes several hours after the end of the rain (Tremoy et al., 2014). Considering a propagation speed of about 20 m/s, this is consistent with the recovery distance of about 100 km in our simulation.
- In 78% of observed squall lines, the "W" shape often observed in the precipitation is not observed in the vapor (Tremoy et al., 2014). Our simulations are thus consistent with this majority of squall lines

Our simulated isotopic evolution during the squall line thus captures the features that are most commonly observed in squall lines. Some squall lines may feature different variations, and even enrichment in the convective and stratiform regions (Tremoy et al., 2014). To check whether our simulations could capture such a diversity of isotopic variations, we performed many sensitivity tests, including simulations without large-scale ascent, with large-scale ascent peaking in the upper troposphere to favor stratiform development (Su et al., 2000), increased horizontal resolution, interactive radiation, reduced sublimation or reduced rain evaporation to favor the maintenance of the stratiform region (Yang & Houze Jr, 1995; Bryan & Morrison, 2012), bowling alley domain, or prescribed horizontal wind in the upper troposphere to favor the development of the stratiform region (Caniaux et al., 1994). Depending on the simulations, the stratiform region is more or less extended and the squall lines are more or less organized, but the meteorological and isotopic evolution is always similar. We thus keep in mind that our simulations match the majority of squall lines, but not all of them. In addition, some observed feature in squall lines over land, such as the enrichment of the water vapor in some stratiform regions due to nearly total evaporation of the rain in dry air (Tremoy et al., 2014), cannot be captured by our simulations with an oceanic setting that favors a relatively moist environment.

4 Understanding mesoscale isotopic variations

Since δD in the precipitation varies in concert with δD in the SCL water vapor, we will focus most of this section on understanding mesoscale isotopic variations in the water vapor.

4.1 Impact of rain evaporation

Observational and modeling studies highlighted the key role of rain evaporation and rain-vapor exchanges in depleting the water vapor within organized systems (Lawrence et al., 2004; Tremoy et al., 2014; Xu et al., 2019). Around tropical cyclones and downwind of squall lines, dry air (Figures 5a 8a) favors thick layer of rain evaporation in the middle and lower troposphere (orange shade in Figures 5c, 8c). Maximum evaporation occurs in the cold pool under the convective and stratiform regions of the squall line (red shade in Figure 8c). The fraction of the formed condensate that evaporates before reaching the ground is in the range of 0-30% in the convective and stratiform regions of the squall line and 20-40% in the eyewall of the cyclone. It increases to 40-80% in the rain bands of the cyclone and reaches 100% in the trailing region of the squall line and in the environment of both systems (Figures 5f, 8f).

To analyze the isotopic effect of rain evaporation in more detail, we calculate $\phi_{ev} = R_{ev}/R_v$, where R_v and R_{ev} are the isotopic ratios in water vapor and in hydrometeor evaporation/sublimation. Hydrometeor evaporation/sublimation includes the evaporation of rain and cloud droplets (below the 0°C isotherm) and the sublimation of ice, snow or graupel (above the 0°C isotherm. ϕ_{ev} represents the isotope enrichment of hydrometeor evaporation relative to water vapor: if $(\phi_{ev}-1)\cdot 1000 > 0‰$, hydrometeor evaporation/sublimation enriches the water vapor; if $(\phi_{ev}-1)\cdot 1000 < 0‰$, hydrometeor evaporation/sublimation depletes the water vapor. R_{ev} is calculated as $(dq_{HDO}/dt)_{mphy}/(dq/dt)_{mphy}$, where q_{HDO} is the mixing ratio for HDO (i.e. the ratio of the mass of HDO molecules over the mass of dry air), q is the water vapor mixing ratio, and $(dq/dt)_{mphy}$ and $(dq_{HDO}/dt)_{mphy}$ are the water vapor and HDO tendencies associated with phase changes. If hydrometeor evaporation/sublimation occurs, then the $(dq/dt)_{mphy}$ tendency is positive. In contrast, if cloud condensation or deposition onto the snow, cloud ice or graupel occurs, then the $(dq/dt)_{mphy}$ tendency is negative. R_{ev} is calculated only where $(dq/dt)_{mphy} > 0$. We can see that near the rain bands of the cyclone and in the stratiform region of the squall line, there is a strongly depleting effect of rain evaporation just below the melting level (purple shade in Figures 5e and 8e, where the nearly horizontal black line indicates the 0°C isotherm). This is because just below the melting level, most of the rain originates from snow melt, which is more depleted than locally formed droplets because the snow has formed at higher altitudes (Risi et al., 2021). There is also a depleting effect in the sub-cloud layer of the cyclone. The depleting effect of rain evaporation is associated with negative anomalies in water vapor δD in the rain bands and under the eyewall of the cyclone, and under the stratiform region of the squall line (purple shade in Figures 5d and 8d).

Figures 5g and 8g compare the δD in the near-surface vapor, the vertically-integrated condensation flux and the vertically-integrated hydrometeor evaporation flux. The δD in the vertically-integrated condensation flux is most negative in the eyewall and rain bands of the cyclone and in the convective and stratiform regions of the squall line (orange in Figures 5f and 8f), consistent with the condensation occuring higher in altitude in anvil clouds (Figures 5b-c and 8b-c). Where the formed condensate evaporates totally, or nearly totally, as is the case in the environment, then the δD in the vertically-integrated hydrometeor evaporation flux equals that in the vertically-integrated condensation flux (orange and purple lines are almost identical in Figures 5f and 8f). There, the rain evaporation has an enriching effect (yellow and orange shades in Figures 5e and 8e), consistent with Tremoy et al. (2014). In contrast, where the evaporated fraction is smaller and the air is moister, the δD in the vertically-integrated hydrometeor evaporation flux is more depleted than in the vertically-integrated condensation flux (orange in Figures 5f and 8f). This contributes to the depleting effect of the rain evaporation in the eyewall and rain bands of the cyclone and in the convective and stratiform regions of the squall line (purple shade in Figures 5e and 8e), and thus to the depleted water vapor in these regions (purple shade in Figures 5d and 8d, black line in Figures 5f and 8f).

To summarize, rain evaporation and diffusive exchanges deplete the water vapor under the convective and stratiform regions of the cyclone and of the squall line. This depletion is due to the higher condensation altitude, the lower evaporated fraction of the rain and the moister air in which the evaporation occurs. The depleting effect of rain evaporation and diffusive exchanges in stratiform regions of convective systems has already been highlighted in previous studies (Kurita, 2013; Aggarwal et al., 2016), including in cyclones (Lawrence et al., 2004; Munksgaard et al., 2015).

4.2 Simulations with de-activated fractionation during rain evaporation

To quantify the effect of rain evaporation and rain-vapor diffusive exchanges, additional simulations in which these effects are de-activated were run, as in Field et al. (2010); Risi et al. (2021). The fractionation coefficients were set to unity during all post-condensational processes. This impacts the simulation of isotopic variables, but not the simulation of meteorological variables.

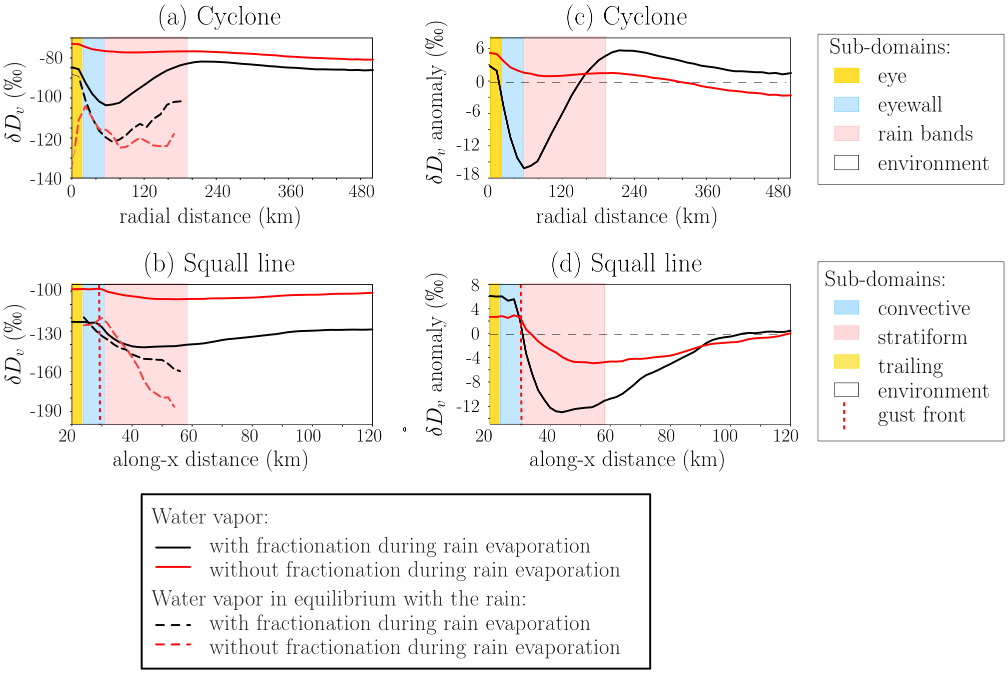

Figure 9. Results of the simulations with de-activated fractionation during rain evaporation. (a-b) Evolution of near-surface δD_v (solid) and of the water vapor δD in equilibrium with the near-surface precipitation (dashed) as a function of r for tropical cyclones (a) and as a function of x for squall lines (b), in simulations where rain evaporation and rain-vapor diffusive exchanges are activated (black) and de-activated (red). (c-d) Evolution of the near surface δD_v anomaly relative to the environment as a function of r for tropical cyclones (c) and as a function of x for squall lines (d).

Both in the cyclone and squall line simulations, δD_v would be higher without fractionation during rain evaporation than with fractionation (solid lines in Figure 9a-b), and the rain would be more depleted than if in equilibrium with the vapor (dashed lines in Figure 9a-b). The δD_p would be minimum under the rain bands in the cyclone simulation, and under the stratiform region in the squall line simulation, reflecting the higher condensation altitude in these regions (section 4.1). With fractionation during rain evaporation, the rain-vapor diffusive exchanges make the vapor more isotopically enriched and the rain more isotopically depleted, thus bringing the rain and the vapor close to isotopic equilibrium (black lines in Figure 9a-b). This explains why δD_v and δD_p vary in concert. The δD_v is most negative where the condensation forms high in altitude and where the rain rate is strong enough to isotopically impact the water vapor. This explains why the δD_v is most negative near the transition between the eyewall and rainbands for the cyclone, and between the convective and stratiform region for the squall line (black solid lines in Figure 9a-b).

Without fractionation during rain evaporation, the mesoscale δD_v variations would be strongly reduced (Figure 9c-d). Peak-to-peak variations are respectively about 22‰ and 8‰ with and without fractionation in the cyclone case, and respectively 18‰ and 8‰ in the squall line case. This confirms the key role of rain evaporation and rain-vapor diffusive exchanges to deplete the low-level water vapor at the mesoscale scale.

4.3 Insights of the simple box model for the tropical cyclone

To quantify the relative importance of different processes in different regions of the domain in the case of the cyclone, a simple box model of the SCL was designed (section 2.3). We quantify the different terms of the water vapor budget in the different regions (section 4.3.1), before evaluating the predictions by the simple box model and decomposing the isotopic differences for water vapor δD (section 4.3.2) and d-excess (section 4.3.3).

4.3.1 SCL water vapor budget

The cyclone in itself (sub-domains eye, eyewall, rain bands and between rain bands) covers less than 10% of the domain (Figure 10a). In all sub-domains, the main source of water vapor is surface evaporation (red in Figure 10b). Surface evaporation is more than twice larger in the eyewall, in rain bands and in-between rain bands than in the environment, consistent with the maximum winds. Surface evaporation is half smaller in the eye than in the environment, due to weak winds and moist near-surface air. Rain evaporation is also a significant moistening term in the eyewall and the rain bands (purple in Figure 10b). Condensation is insignificant (cyan in Figure 10b). Everywhere except in the eye, updrafts and downdrafts have a drying effect on the SCL (green and blue), because updrafts are preferentially moister and downdrafts are preferentially drier. In the eye, updrafts and downdrafts slightly moisten the SCL because the core of the eye is descending and almost saturated whereas air parcels near the eyewall may be drier and ascending. Horizontal advection and non-stationary effects dry the cyclone and slightly moisten the environment (dark green in Figure 10b). This is because dry air from the environment converge towards to cyclone center (horizontal advection effect). In addition, the cyclone wanders across the domain and thus mixes with air that was previously in the dry portions of the domain (non-stationary effect). In turn, in the wake of the cyclone, the environment is left moistened.

4.3.2 Evaluating and decomposing the water vapor δD_v in each sub-domain

In spite of its overestimate of the δD_v simulated by the CRM (green compared to red in Figure 11c), the simple box model is able to simulate the more depleted water vapor in all sub-domains relative to the δD_v simulated by the MJ79 closure (blue in Figure 10c) and to capture the main δD_v differences between the sub-domains: the slightly more enriched vapor in the eye relative to environment, the more depleted vapor in the eyewall, rain bands and between bands relative to the environment, and the more depleted vapor in the bands relative to in-between bands (Figure 10c).

The slightly more enriched vapor in the eye relative to the environment is mainly explained by the higher relative humidity (red in Figure 10d). When the relative humidity is close to 1, the vapor is nearly in equilibrium with the ocean. In this case, the influence of A in equation 8 becomes small. As a consequence, the prediction by the simple box model is close to that of the MJ79 closure in the eye (blue in in Figure 10c). In addition, in the eye, the rain evaporation is weak because there is little rain, and the horizontal advection into the eye is weak because the winds are mainly tangential, further limiting the influence of A in equation 8. We note that a relative enrichment inside the eye is simulated in spite of the neglect of sea spray in our simulations. This does not exclude the possibility for a role of sea spray in nature (Fudeyasu et al., 2008), but this role is not necessary to explain the enrichment in the eye.

Figure 10d shows the decomposition of the δD_v anomaly for the different sub-domains relative to the environment. The more depleted vapor in the eyewall relative to the environment is mainly due to the enhanced depletion by vertical mixing trough the SCL top (green in Figure 10d). The steeper isotopic gradient above the SCL, driven by the stronger rain evaporation above the SCL (section 4.1), likely contributes to this term. The rain evaporation in the SCL also contributes to the more depleted vapor in the eyewall (purple in Figure 10d).

The more depleted vapor in the rain bands relative to the environment (and relative to between rain bands) is mainly due to the enhanced depletion by rain evaporation within the SCL (purple in Figure 10d). Alone, rain evaporation in the SCL would deplete the vapor in the rain bands by nearly 50‰ relative to the environment. As in the eyewall, the enhanced depletion by vertical mixing trough the SCL top also contributes to the depletion (green in Figure 10d).

The more depleted vapor between rain bands relative to the environment is mainly due to the horizontal advection and non-stationary effects (dark green in Figure 10d). Horizontal winds bring depleted water vapor from the rain bands (Figure 10d). Consistently, horizontal advection has an enriching effect in rain bands, where the isotopic gradients are reversed: horizontal winds bring enriched water vapor from in-between rain bands.

The contributions of the kinetic fractionation during surface evaporation and of condensation in the SCL are marginal. The marginal impact of condensation is consistent with the absence of clouds in the SCL, and confirms that rain-out does not directly impact the SCL isotopic composition.

To summarize, the δD_v differences between the sub-domains are mainly explained by rain evaporation and rain-vapor diffusive exchanges inside the SCL, which deplete the eyewall and rain bands, consistent with previous studies (Gedzelman et al., 2003). Horizontal advection plays a key role to smooth the isotopic patterns, contributing to the progressive depletion as the air converges towards the center of cyclones suggested in previous studies (Gedzelman et al., 2003; Xu et al., 2019).

4.3.3 Evaluating and decomposing the water vapor d-excess in each sub-domain

In spite of its underestimate of the d_v simulated by the CRM (green compared to red in Figure 10e), the model is able to capture the higher d_v than predicted by MJ79 closure (blue in Figure 10c) and several features simulated by the CRM: (1) the minimum d_v in the eye, (2) the higher d_v in the rain bands relative to between bands (Figure 10e). We will thus focus on understanding these two features:

1. The minimum d_v in the eye is due to the moist conditions that reduce the kinetic effects during surface evaporation (red in Figure 10f).
2. The higher d_v in the rain bands relative to the environment or between bands is mainly due to the rain evaporation in the SCL (purple in Figure 10f), which yields water vapor with high d-excess because of the relatively larger diffusivity of HDO relative to that of $H_2^{18}O$. Alone, it would contribute to an increase in d-excess by more than 15‰ relative to the environment.

As for δD_v, horizontal advection acts to smooth the d_v patterns, decreasing d_v in the rain bands and increasing it between rain bands (dark green in Figure 10f). The stronger the winds, the larger the kinetic fractionation during surface evaporation (yellow in Figure 10f). The contribution of this effect is however relatively small: alone, it would increase the d-excess by less than 5‰ in the eyewall, bands and in-between bands, relative to the environment (yellow in Figure 10f).

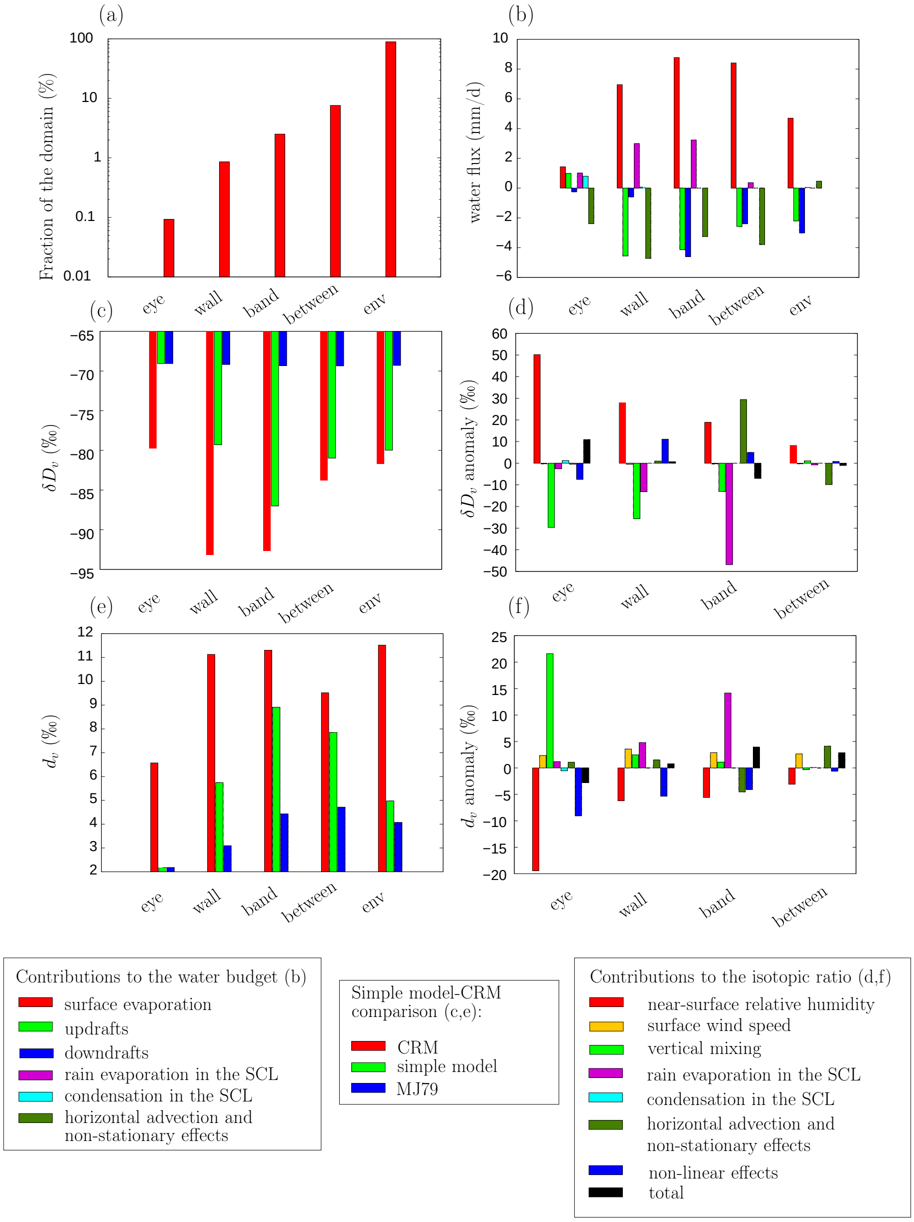

Figure 10. Results for the simple model of the SCL water vapor budget applied to the cyclone simulation. (a) Fraction of the domain, in log scale, covered by the five sub-domains of the cyclone: eye, eyewall ("wall"), rain bands ("bands"), in-between bands ("between") and the environment ("env"). (b) Water fluxes contributing to the water budgets of the different sub-domains of the cyclone: Surface evaporation (red), updrafts (green), downdrafts (blue), rain evaporation (pink), condensation (cyan) and residual term associated with horizontal advection and non-stationary effects (dark green). (c) δD_v simulated by SAM (red), by the simple model (green) and by the MJ79 closure (blue bars). (d) Decomposition of the δD_v anomaly in different sub-domains relative to the environment into 6 contributions: near-surface relative-humidity (red), surface wind speed (yellow), vertical mixing through the SCL top (green), rain evaporation within the SCL (purple), condensation within the SCL (cyan) and horizontal advection and non-stationary effects (dark green). The total is shown in black and non-linear effects are shown in blue. (e-f) Same as (c-d) but for d_v.

4.4 Insights of the simple box model for the squall line

4.4.1 SCL water vapor budget

The convective, stratiform and trailing regions of the squall line cover about 15% of the domain (Figure 11a). Surface evaporation is the main source of water in the SCL and is approximately uniform in all sub-domains (red in Figure 11b). The rain evaporation is a significant source in both the convective and stratiform parts (purple). In the convective part, the main sink of water is the export of moist air through updrafts (green in Figure 11b), consistent with the vigorous updrafts. Horizontal advection and non-stationary effects moisten the convective zone by advecting air from the stratiform region moistened by rain evaporation, and dries the trailing region by advecting drier air from the environment (dark green in Figure 11b).

4.4.2 Evaluating and decomposing the water vapor δD_v in each sub-domain

The box model performs better for the squall line than for the cyclone simulation. It captures well the relative variations across the sub-domains, in particular the maximum depletion in the stratiform region and the depletion in the convective and trailing regions relative to the environment (Figure 11c). We will thus focus on understanding these differences.

In both the convective and stratiform parts of the squall line, the depletion relative to the environment is mainly due to the rain evaporation and rain-vapor diffusive exchanges in the SCL that deplete the water vapor (purple in Figure 11d). Alone, it would deplete the convective and stratiform regions by about 30 and 45 ‰ respectively, far exceeding the total difference relative to the environment. In the stratiform region, vertical mixing, which likely includes the effect of rain evaporation above the SCL, also significantly contributes to the depletion (green in Figure 11d). This is consistent with the depleting effect of rain evaporation both in the SCL and near the melting level (Figure 8d), and with the major effect of fractionation during rain evaporation on the isotopic evolution in squall lines (section 4.2).

In the trailing region, where the precipitation is weak, the depletion in heavy isotopes of the vapor is explained by horizontal advection and non-stationary effects (dark green in Figure 11d). Alone, it would contribute to a 55‰ depletion relative to the environment. This reflects the effect of horizontal advection spreading the depleted water vapor from the stratiform region. In contrast, the horizontal advection explains why the convective region is less depleted than the stratiform region: horizontal advection brings enriched water vapor from the environment towards the squall line front.

To summarize, the δD_v differences between the sub-domains are mainly explained by rain evaporation and rain-vapor diffusive exchanges inside the SCL, and also probably above the SCL. This is consistent with previous studies (Risi et al., 2010; Tremoy et al., 2014). Horizontal advection then plays a key role in spreading the isotopic anomaly rearward.

4.4.3 Evaluating and decomposing the water vapor d-excess in each sub-domain

The simple box model is able to capture the fact that d_v is much larger than would be predicted by the MJ79 closure. It also captures the higher d_v in the stratiform region relative to the convective and trailing region.

The higher d_v in the stratiform region is mainly explained by the vertical mixing (green in Figure 11f). Vertical mixing probably brings water vapor with high d_v due to rain evaporation above the SCL. Rain evaporation in the SCL strongly increases d_v in the convective region (purple in Figure 11f), but this is compensated by the advection of vapor (dark green in Figure 11d). Since the environment has a lower d_v than the convective region (red in Figure 11c), the advection of air from the environment to the convective region acts to deplete the convective region. Variations in near-surface relative humidity and winds are smaller than in the cyclone simulations, so the contributions of these effects are marginal.

4.5 Discussion

We find many common aspects for the mesoscale isotopic variability between cyclone and squall line simulations.

- In both convective systems, rain evaporation and rain-vapor diffusive exchanges both within and above the SCL (especially near the melting level) are the main drivers of the depletion in heavy isotopes of the vapor in the eyewall and rain bands for the cyclone, and in the convective and stratiform parts of the squall line. This is consistent with previous studies (Gedzelman et al., 2003; Tremoy et al., 2014; Xu et al., 2019). These processes have also a crucial impact on d-excess.
- In both cases, horizontal advection and non-stationary effects act to smooth the isotopic patterns. It leads to the gradual depletion towards the eyewall observed in tropical cyclones, and it spreads the isotopic anomalies rearward in the case of the squall line. This is consistent with previous studies (Xu et al., 2019).
- In both cases, the effect of condensation on the SCL water vapor is indirect. Condensation in the free troposphere maintains the vertical gradient in δD_v that allows the rain evaporation to have a depleting effect on the SCL water vapor. Through this indirect effect, condensation and precipitation are necessary for the depletion of the water vapor SCL (Yoshimura et al., 2003).

The main difference between the two convective systems is in the effect of kinetic effects during surface evaporation. Strong winds and moist conditions in tropical cyclones significantly impact the d-excess, whereas they have a marginal effect in squall lines.

Some similarities can also be found between processes controlling the isotopic composition in tropical cyclones and those in extra-tropical cyclones and cold fronts, as documented by previous studies (Pfahl et al., 2012; Aemisegger et al., 2015; Thurnherr & Aemisegger, 2022). Isotopically depleted water vapor and rain were observed in extratropical cyclones. This was explained by the interplay between air mass advection and depletion by rain-vapor interaction, consistent with our study, although in extratropical cyclones the large-scale advection and large-scale gradients in temperature also contributed to depleting the vapor (Pfahl et al., 2012; Aemisegger et al., 2015). Low d_v was also observed in the warm sector of extratropical cyclones. As in tropical cyclones, this was explained by ocean evaporation in a moist environment, although in extratropical cyclones dew formation also contributes to lowering d_v (Thurnherr & Aemisegger, 2022).

5 Conclusion

Using cloud resolving model simulations of cyclones and squall lines, and a simple model for the SCL water vapor budget, we investigate how convective processes impact the isotopic composition of water vapor and precipitation at the mesoscale. We show that the main factors depleting heavy isotopes of the water vapor at the mesoscale is rain evaporation, especially in the sub-cloud layer of rain bands and of the eyewall in tropical cyclones, and in the mesoscale downdraft of the stratiform region in squall lines (purple in Figure 12). The mesoscale δD_v patterns are subsequently reshaped by horizontal advection (orange in Figure 12). These mechanisms are overall consistent with those suggested in previous studies (Gedzelman et al., 2003; Tremoy et al., 2014; Xu et al., 2019).

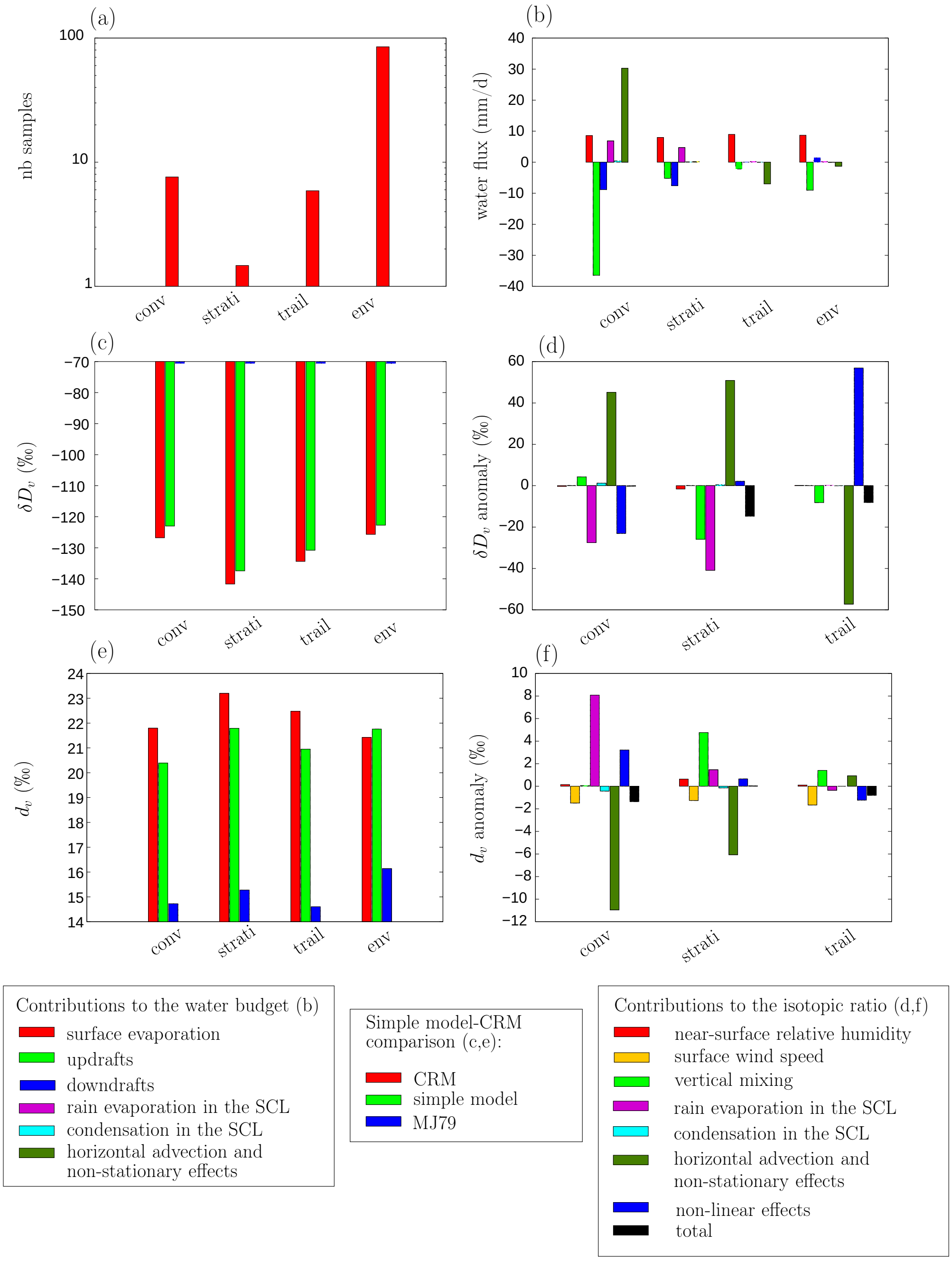

Figure 11. Results for the simple model of the SCL of the SCL water vapor budget applied to the squall line simulation. Same as Figure 10 but for the four sub-domains of the squall line: convective (“conv”), stratiform (“strati”) and trailing (“trail”) regions, and the environment (“env”). Note that in (c), the prediction by the MJ79 closure (blue) is nearly -70‰ in all sub-domains, so it is hard to see.

a) Tropical cyclone

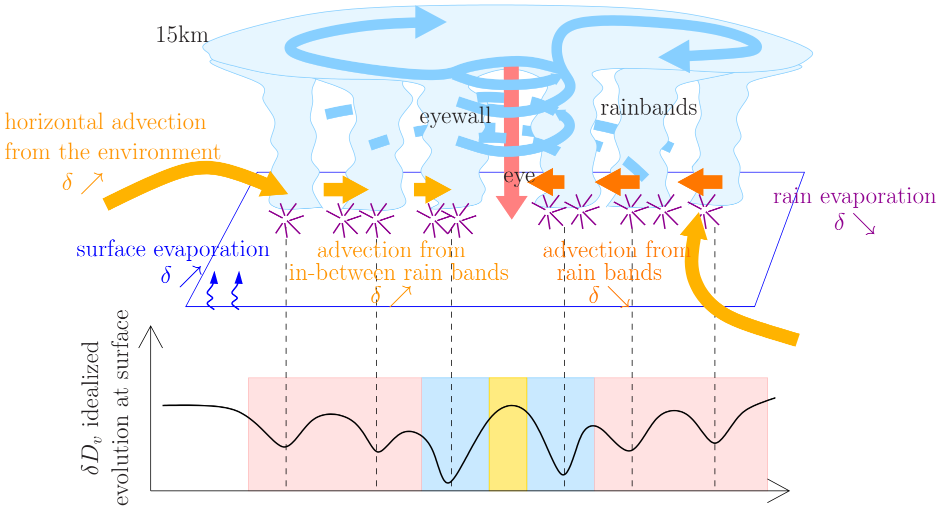

b) Squall line

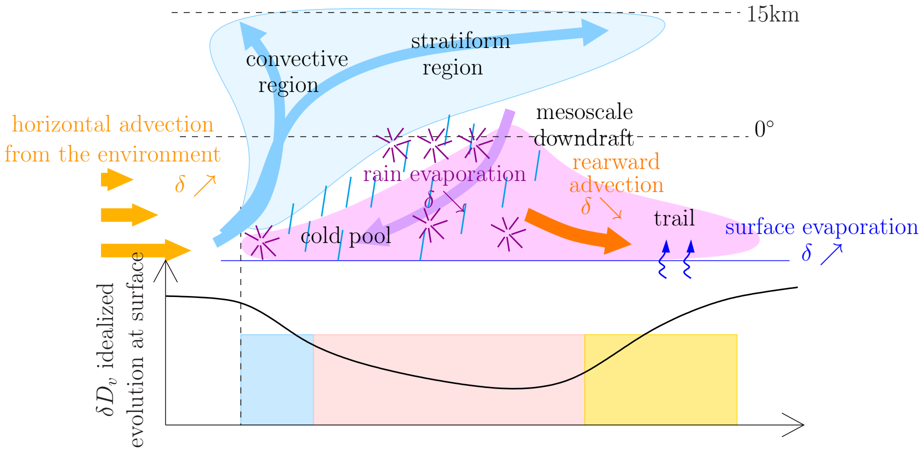

Figure 12. A schematic of the processes controlling the water vapor composition inside tropical cyclones (a) and squall lines (b). The key driver is rain evaporation, indicated by purple stars. Rain evaporation depletes water vapor in the rain bands and eyewall of tropical cyclones and in the convective and stratiform regions of squall lines. Horizontal advection then reshapes this pattern. Dark orange arrows indicate horizontal advection from depleted regions to less depleted regions, contributing to the spread of the depleted anomalies inward in cyclones and rearward in squall lines. Light orange arrows indicate horizontal advection from less depleted regions to more isotope depleted regions, partially compensating the depletion in most depleted regions.

In contrast to these previous studies however, we highlight that condensation has no direct impact and that the evaporation of sea spray is not necessary to explain the relative enrichment in the cyclone eye.

This study contributes to our understanding of mesoscale isotopic variability. It provides physical arguments for the more depleted rain observed in tropical cyclones and squall lines relative to the rain in small-scale convection. Therefore, this study supports the interpretation of paleoclimate isotopic archives in tropical regions in terms of past cyclonic activity (Nott et al., 2007; Medina-Elizalde & Rohling, 2012; Baldini et al., 2016) or past frequency of large, long-lived, organized convective systems such as squall lines (Maupin et al., 2021).

However, when considering paleoclimate records at the annual scale or larger, the isotopic composition reflects an average over many convective systems of different organization types. In our simulations, this is equivalent to the domain-mean δD in simulations of tropical cyclones or squall lines relative to the domain-mean δD in simulations of isolated cumulonimbi, rather than the δD in tropical cyclone or squall lines relative to their environment in a given simulation. This paper focuses on mesoscale isotopic variations and does not discusses domain-mean values, because the realism of simulated mesoscale variations could be more easily assessed than the realism of domain-mean values. In particular, we realized that the domain-mean δD in the precipitation or water vapor of our tropical cyclone simulation was more enriched in heavy isotopes than that in simulations of squall lines or even of isolated cumulonimbi (Risi et al., 2020). This is at odds with observations of depleted cyclonic rains in the tropics (Lawrence et al., 2004). This discrepancy may be due to limitations in the radiative-convective equilibrium configuration. In radiative-convective equilibrium, the cyclone maintains a strong subsidence in its environment, which favors unrealistically dry conditions that allows enriched water vapor in the SCL to accumulate. In reality, tropical cyclones propagate and are thus not in equilibrium with their environment. In addition, tropical cyclones may occur in specific large-scale conditions. To account for the propagation of tropical cyclones and for the interplay with the large-scale circulation, more realistic simulations are necessary, e.g. using regional cloud-resolving models (de Vries et al., 2022). In parallel, the interplay between large-scale circulation and convective organization deserves to be better documented in observations. It is possible that part of the observed depletion associated with tropical cyclones is mediated by large-scale conditions and domain-mean precipitation. To rigorously assess the role of convective organization, we would need to compare isotopic observations for different kinds of convective organization but for the same precipitation rate and large-scale context, as is now done for humidity (Tobin et al., 2012). This will allow us to rigorously assess the realism of the domain-mean isotopic composition in our simulations and will be the subject of a future study.

Finally, many other processes need to be investigated before drawing any paleoclimate conclusions from this study, including large-scale horizontal advection (Chen et al., 2021), land-atmosphere interactions along the air mass trajectories, infiltration processes, processes in the karstic systems and during calcite formation (Lases-Hernández et al., 2020). Our study is a first step towards a more comprehensive understanding of water isotopic variations.

Open Research Section

Information on SAM can be found on this web page:
`http://rossby.msrc.sunysb.edu/~marat/SAM.html`. All simulation outputs used in this article are archived in the PANGEA data repository: `https://doi.pangaea.de/10.1594/PANGAEA.937534`.

Acknowledgments

This work was granted access to the HPC resources of TGCC under the allocation 2092 made by GENCI. CR. CM. and FV. acknowledge the national french program INSU-LEFE for the funding of the SAM-iso proposal at the AO LEFE 2021. C.M. gratefully acknowledges funding from the European Research Council (ERC) under the European Union's Horizon 2020 research and innovation programme (Project CLUSTER, grant agreement No 805041). P.B. was supported by the National Science Foundation under Grant No. AGS-1938108. G.V. contributed as part of his internship as a Master student at Sorbonne Université, with a funding from Paris Sciences & Lettres "ANR-10-IDEX-0001-02". C. D. contributed as part of her internship as a Bachelor student at Sorbonne Université. S.A. contributed as part of her PhD, with a funding from Ecole Normale Supérieure de Paris-Saclay. We thank all reviewers for their constructive comments.

References

Abramian, S., Muller, C., & Risi, C. (2022). Shear-convection interactions and orientation of tropical squall lines. *Geophys. Res. Lett.*, *49*(1), e2021GL095184, DOI: doi.org/10.1029/2021GL095184.

Aemisegger, F., Spiegel, J., Pfahl, S., Sodemann, H., Eugster, W., & Wernli, H. (2015). Isotope meteorology of cold front passages: A case study combining observations and modeling. *Geophys. Res. Lett.*, *42*(13), 5652–5660.

Aggarwal, P. K., Romatschke, U., Araguas-Araguas, L., Belachew, D., Longstaffe, F. J., Berg, P., … Funk, A. (2016). Proportions of convective and stratiform precipitation revealed in water isotope ratios. *Nat. Geosci.*, *9*(8), 624-629, https://doi.org/10.1038/ngeo2739.

Albright, A. L., Bony, S., Stevens, B., & Vogel, R. (2022). Observed subcloud layer moisture and heat budgets in the trades. *J. Atmos. Sci.*.

Attinger, R., Spreitzer, E., Boettcher, M., Forbes, R., Wernli, H., & Joos, H. (2019). Quantifying the role of individual diabatic processes for the formation of pv anomalies in a north pacific cyclone. *Quart. J. R. Meteor. soc.*, *145*(723), 2454–2476.

Baldini, L. M., Baldini, J. U., McElwaine, J. N., Frappier, A. B., Asmerom, Y., Liu, K.-b., … Breitenbach, S. F. M. (2016). Persistent northward north atlantic tropical cyclone track migration over the past five centuries. *Sci. Rep.*, *6*, 37522, https://doi.org/10.1038/srep37522.

Bhattacharya, S. K., Sarkar, A., & Liang, M.-C. (2022). Vapor isotope probing of typhoons invading the taiwan region in 2016. *J. Geophy. Res.*, e2022JD036578.

Biggerstaff, M. I., & Houze Jr, R. (1991). Kinematic and precipitation structure of the 10–11 june 1985 squall line. *Mon. Wea. Rev.*, *119*(12), 3034–3065, https://doi.org/10.1175/1520-0493.

Blossey, P. N., Kuang, Z., & Romps, D. M. (2010). Isotopic composition of water in the tropical tropopause layer in cloud-resolving simulations of an idealized tropical circulation. *J. Geophys. Res.*, *115*, D24309, doi:10.1029/2010JD014554.

Bony, S., Risi, C., & Vimeux, F. (2008). Influence of convective processes on the isotopic composition (deltaO18 and deltaD) of precipitation and water vapor in the Tropics. Part 1: Radiative-convective equilibrium and TOGA-COARE simulations. *J. Geophys. Res.*, *113*, D19305, doi:10.1029/2008JD009942.

Bryan, G. H., & Morrison, H. (2012). Sensitivity of a simulated squall line to horizontal resolution and parameterization of microphysics. *Mon. Weather Rev.*, *140*(1), 202–225, https://doi.org/10.1175/MWR-D-11-00046.1.

Caniaux, G., Redelsperger, J.-L., & Lafore, J.-P. (1994). A numerical study of the stratiform region of a fast mooving squall line. part 1: general description and water and heat budgets. *J. Atm. Sci*, *51*, 2046-2074, https://doi.org/10.1175/1520-0469.

Chakraborty, S., Sinha, N., Chattopadhyay, R., Sengupta, S., Mohan, P., & Datye, A. (2016). Atmospheric controls on the precipitation isotopes over the Andaman Islands, Bay of Bengal. *Sci. Rep.*, *6*(1), 1–11, https://doi.org/10.1038/srep19555.

Chavas, D. R., & Emanuel, K. (2014). Equilibrium tropical cyclone size in an idealized state of axisymmetric radiative–convective equilibrium. *J. Atmos. Sci.*, *71*(5), 1663–1680, https://doi.org/10.1175/JAS-D-13-0155.1.

Chen, F., Huang, C., Lao, Q., Zhang, S., Chen, C., Zhou, X., … Zhu, Q. (2021). Typhoon control of precipitation dual isotopes in southern china and its palaeoenvironmental implications. *J. Geophys. Res.: Atmospheres*, *126(14)*, 2020JD034336, https://doi.org/10.1029/2020JD034336.

Chong, M. (2010). The 11 August 2006 squall line system as observed from MIT Doppler radar during the AMMA SOP. *Quart. J. R. Meteor. soc.*, *136(S1)*, https://doi.org/10.1002/qj.466.

Chong, M., & Hauser, D. (1990). A tropical squall line observed during the COPT81 experiment in West Africa: Part III: heat and moisture budgets. *Mon. Wea. Rev.*, *118*, 1696-1706, https://doi.org/10.1175/1520-0493.

Conroy, J. L., Noone, D., Cobb, K. M., Moerman, J. W., & Konecky, B. L. (2016). Paired stable isotopologues in precipitation and vapor: A case study of the amount effect within western tropical pacific storms. *J. Geophy. Res.*, *121*(7), 3290–3303, https://doi.org/10.1002/2015JD023844.

Craig, H. (1961). Isotopic variations in meteoric waters. *Science*, *133*, 1702-1703, DOI: 10.1126/science.133.3465.170.

Craig, H., & Gordon, L. I. (1965). Deuterium and oxygen-18 variations in the ocean and marine atmosphere. *Stable Isotope in Oceanographic Studies and Paleotemperatures*, *Laboratorio di Geologia Nucleate, Pisa, Italy*, 9-130.

Cruz, F. W., Vuille, M., Burns, S. J., Wang, X., Cheng, H., Werner, M., … Nguyen, H. (2009). Orbitally driven east-west antiphasing of South American precipitation. *Nat. Geosci.*, *2*, 210-214, https://doi.org/10.1038/ngeo444.

Dansgaard. (1964). Stable isotopes in precipitation. *Tellus*, *16*, 436-468, https://doi.org/10.3402/tellusa.v16i4.8993.

de Vries, A. J., Aemisegger, F., Pfahl, S., & Wernli, H. (2022). Stable water isotope signals in tropical ice clouds in the west african monsoon simulated with a regional convection-permitting model. *Atm. Chem. Phys.*, *22*, 8863?8895, DOI: https://doi.org/10.5194/acp-22-8863-2022.

Diekmann, C. J., Schneider, M., Knippertz, P., de Vries, A. J., Pfahl, S., Aemisegger, F., … others (2021). A lagrangian perspective on stable water isotopes during the west african monsoon. *J. Geophys. Res.: Atmospheres*, *126*(19), e2021JD034895.

Dütsch, M., Pfahl, S., Meyer, M., & Wernli, H. (2018). Lagrangian process attribution of isotopic variations in near-surface water vapour in a 30-year regional climate simulation over europe. *Atm. Chem. Phys.*, *18*(3), 1653–1669.

Field, R. D., Jones, D. B. A., & Brown, D. P. (2010). The effects of post-condensation exchange on the isotopic composition of water in the atmosphere. *J. Geophy. Res.*, *115, D24305*, doi:10.1029/2010JD014334.

Field, R. D., Kim, D., LeGrande, A. N., Worden, J., Kelley, M., & Schmidt, G. A. (2014). Evaluating climate model performance in the tropics with retrievals of water isotopic composition from Aura TES. *Geophy. Res. Lett.*, DOI: 10.1002/2014GL060572.

Frappier, A. B., Sahagian, D., Carpenter, S. J., González, L. A., & Frappier, B. R. (2007). Stalagmite stable isotope record of recent tropical cyclone events. *Geology*, *35*(2), 111–114, https://doi.org/10.1130/G23145A.1.

Fudeyasu, H., Ichiyanagi, K., Sugimoto, A., Yoshimura, K., Ueta, A., Yamanaka,

M. D., … Ozawa, K. (2008). Isotope ratios of precipitation and water vapor observed in Typhoon Shanshan. *J. Geophys. Res.*, *113*, D12113, doi:10.1029/2007JD009313.

Gamache, J. F., & Houze, R. A. (1981). Mesoscale air motions associated with a tropical squall line. *Mon. Weather Rev.*, *110*, 118-135, https://doi.org/10.1175/1520-0493.

Gamache, J. F., & Houze, R. A. (1983). Water budget of a mesoscale convective system in the tropics. *J. Atmos. Sci.*, *40*, 1835-1850, oi: http://dx.doi.org/10.1175/1520-0469(1983)040.

Gao, J., Masson-Delmotte, V., Risi, C., He, Y., & Yao, T. (2013). What controls southern Tibetan Plateau precipitation deltaO18 at seasonal and intra-seasonal scales? A case study at Lhasa and Nyalam. *Tellus*, *65(1)*, https://doi.org/10.3402/tellusb.v65i0.21043.

Gedzelman, S., Lawrence, J., Gamache, J., Black, M., Hindman, E., Black, R., … Zhang, X. (2003). Probing hurricanes with stable isotopes of rain and water vapor. *Mon. Wea. Rev.*, *131*, 112-1127, DOI: https://doi.org/10.1175/1520-0493.

Gentry, M. S., & Lackmann, G. M. (2010). Sensitivity of simulated tropical cyclone structure and intensity to horizontal resolution. *Mon. Wea. Rev.*, *138*(3), 688–704, DOI: https://doi.org/10.1175/2009MWR2976.1.

Godunov, S. K. (1959). Finite-difference methods for the numerical computations of equations of gas dynamics. *Math. Sb.*, *7*, 271-290.

Guilpart, E. (2018). *Etude de la composition isotopique (deutérium et oxygène 18) de la vapeur d'eau dans l'atmosphère sur l'île de la réunion: apport à la compréhension des processus humides atmosphériques en région tropicale.* Unpublished doctoral dissertation, Université Paris-Saclay (ComUE).

Houze, R. A. (1977). Structure and dynamics of a tropical squall line system. *Mon. Wea. Rev.*, *105*, 1540-1567.

Houze, R. A. (2004). Mesoscale convective systems. *Rev. Geophys.*, *42 (4)*, DOI: 10.1029/2004RG000150.

Houze, R. A. (2010). Clouds in tropical cyclones. *Mon. Wea. Rev.*, *138*(2), 293–344, DOI: https://doi.org/10.1175/2009MWR2989.1.

Jackisch, D., Yeo, B. X., Switzer, A. D., He, S., Cantarero, D. L. M., Siringan, F. P., & Goodkin, N. F. (2022). Precipitation stable isotopic signatures of tropical cyclones in metropolitan manila, philippines, show significant negative isotopic excursions. *Nat. Hazards Earth Syst. Sci.*, *22*(1), 213–226, DOI: https://doi.org/10.5194/nhess-22-213-2022.

Jakob, C., Singh, M., & Jungandreas, L. (2019). Radiative convective equilibrium and organized convection: An observational perspective. *J. Geophy. Res.*, *124*(10), 5418–5430, DOI: https://doi.org/10.1029/2018JD030092.

Khairoutdinov, M., & Emanuel, K. (2013). Rotating radiative-convective equilibrium simulated by a cloud-resolving model. *J. Adv. Model. Earth Sci.*, *5*(4), 816–825, DOI: https://doi.org/10.1002/2013MS000253.

Khairoutdinov, M., & Randall, D. A. (2003). Cloud resolving modeling of the ARM summer 1997 IOP: Model formulation, results, uncertainties, and sensitivities. *J. Atm. Sci.*, *60*(4), 607–625, DOI: https://doi.org/10.1175/1520-0469.

Kurita, N. (2013). Water isotopic variability in response to mesoscale convective system over the tropical ocean. *J. Geophy. Res.*, *118(18)*, 10-376, DOI: https://doi.org/10.1002/jgrd.50754.

Lacour, J.-L., Risi, C., Worden, J., Clerbaux, C., & Coheur, P.-F. (2017). Isotopic signature of convection's depth in water vapor as seen from iasi and tes d observations. *Earth Planet. Sci. Lett.*, *7*, 9645-9663, doi.org/10.5194/acp-17-9645-2017.

Lases-Hernández, F., Medina-Elizalde, M., & Frappier, A. B. (2020). Drip water δ18o variability in the northeastern Yucatán Peninsula, Mexico:

Implications for tropical cyclone detection and rainfall reconstruction from speleothems. *Geochim. Cosmochim. Acta*, *285*, 237–256, DOI: https://doi.org/10.1016/j.gca.2020.07.008.

Lawrence, J. R. (1998). Isotopic spikes from tropical cyclones in surface waters: Opportunities in hydrology and paleoclimatology. *Chem. Geol.*, *144*(1-2), 153–160.

Lawrence, J. R., & Gedzelman, S. D. (1996). Low stable isotope ratios of tropical cyclone rains. *Geophys. Res. Lett.*, *23*, 527-530, DOI: https://doi.org/10.1029/96GL00425. doi: 10.1029/96GL00425

Lawrence, J. R., & Gedzelman, S. D. (2003). Tropical ice core isotopes: Do they reflect changes in storm activity? *Geophys. Res. Lett.*, *30(2)*, 44-1, DOI: https://doi.org/10.1029/2002GL015906.

Lawrence, J. R., Gedzelman, S. D., Dexheimer, D., Cho, H.-K., Carrie, G. D., Gasparini, R., … Biggerstaff, M. I. (2004, March). Stable isotopic composition of water vapor in the tropics. *J. Geophys. Res.*, *109*, D06115, doi:10.1029/2003JD004046. doi: 10.1029/2003JD004046

Lawrence, J. R., Gedzelman, S. D., Gamache, J., & Black, M. (2002). Stable isotope ratios: Hurricane Olivia. *J. Atmos. Chem*, *41*, 67-82, DOI: https://doi.org/10.1023/A:1013808530364.

Lekshmy, P., Midhun, M., Ramesh, R., & Jani, R. (2014). 18 o depletion in monsoon rain relates to large scale organized convection rather than the amount of rainfall. *Scientific reports*, *4*, 5661, DOI: https://doi.org/10.1038/srep05661.

Maupin, C. R., Roark, E. B., Thirumalai, K., Shen, C.-C., Schumacher, C., Van Kampen-Lewis, S., … others (2021). Abrupt southern great plains thunderstorm shifts linked to glacial climate variability. *Nat. Geosci.*, *14*(6), 396–401, DOI: https://doi.org/10.1038/s41561-021-00729-w.

Medina-Elizalde, M., & Rohling, E. J. (2012). Collapse of classic maya civilization related to modest reduction in precipitation. *Science*, *335*(6071), 956–959, DOI: 10.1126/science.1216629.

Merlivat, L., & Jouzel, J. (1979). Global climatic interpretation of the Deuterium-Oxygen 18 relationship for precipitation. *J. Geophys. Res.*, *84*, 5029-5332, DOI: https://doi.org/10.1029/JC084iC08p05029.

Miller, D. L., Mora, C. I., Grissino-Mayer, H. D., Mock, C. J., Uhle, M. E., & Sharp, Z. (2006). Tree-ring isotope records of tropical cyclone activity. *Proc. Natl. Acad. Sci. USA*, *103*(39), 14294–14297.

Moerman, J. W., Cobb, K. M., Adkins, J. F., Sodemann, H., Clark, B., & Tuen, A. A. (2013). Diurnal to interannual rainfall δ18o variations in northern Borneo driven by regional hydrology. *Earth Planet. Sci. Lett.*, *369*, 108–119, DOI: https://doi.org/10.1016/j.epsl.2013.03.014.

Moore, M., Blossey, P., Muhlbauer, A., & Kuang, Z. (2016). Microphysical controls on the isotopic composition of wintertime orographic precipitation. *J. Geophys.l Res.*, *121*(12), 7235–7253, DOI: https://doi.org/10.1002/2015JD023763.

Moore, M., Kuang, Z., & Blossey, P. N. (2014). A moisture budget perspective of the amount effect. *Geophys. Res. Lett.*, *41*, 1329-1335, doi:10.1002/2013GL058302.

Muller, C. (2013). Impact of convective organization on the response of tropical precipitation extremes to warming. *J. Clim.*, *26*(14), 5028–5043, DOI: https://doi.org/10.1175/JCLI-D-12-00655.1.

Muller, C., & Romps, D. M. (2018). Acceleration of tropical cyclogenesis by self-aggregation feedbacks. *Proc. Natl. Acad. Sci.*, *115 (12)*, 2930-2935, DOI: https://doi.org/10.1073/pnas.1719967115.

Munksgaard, N. C., Zwart, C., Kurita, N., Bass, A., Nott, J., & Bird, M. I. (2015). Stable isotope anatomy of tropical cyclone ita, north-eastern Australia, april 2014. *PloS one*, *10*(3), e0119728, https://doi.org/10.1371/journal.pone.0119728.

Neggers, R., Stevens, B., & Neelin, J. D. (2006). A simple equilibrium model for shallow-cumulus-topped mixed layers. *Theor. Comput. Fluid Dyn.*, *20*(5-6), 305–322.

Nott, J., Haig, J., Neil, H., & Gillieson, D. (2007). Greater frequency variability of landfalling tropical cyclones at centennial compared to seasonal and decadal scales. *Earth Planet. Sci. Lett.*, *255*(3-4), 367–372, DOI: https://doi.org/10.1016/j.epsl.2006.12.023.

Pfahl, S., Wernli, H., Yoshimura, K., & Dubey, M. (2012). The isotopic composition of precipitation from a winter storm–a case study with the limited-area model cosmo iso. *Atmos. Chem. Phys.*, *12*(3).

Price, R. M., Swart, P. K., & Willoughby, H. E. (2008). Seasonal and spatial variation in the stable isotopic composition (δ18o and δD) of precipitation in south Florida. *J. Hydrol.*, *358*(3-4), 193–205, DOI: https://doi.org/10.1016/j.jhydrol.2008.06.003.

Ramos, R., LeGrande, A., Griffiths, M., Elsaesser, G., Litchmore, D., Tierney, J., … Nusbaumer, J. (2022). Constraining clouds and convective parameterizations in a climate model using paleoclimate data. *J. Adv. Model. Earth Syst.*, *14*(8), e2021MS002893.

Risi, C., Bony, S., Vimeux, F., Chong, M., & Descroix, L. (2010). Evolution of the water stable isotopic composition of the rain sampled along Sahelian squall lines. *Quart. J. Roy. Meteor. Soc.*, *136 (S1)*, 227 - 242, DOI: https://doi.org/10.1002/qj.485.

Risi, C., Bony, S., Vimeux, F., Descroix, L., Ibrahim, B., Lebreton, E., … Sultan, B. (2008). What controls the isotopic composition of the African monsoon precipitation? Insights from event-based precipitation collected during the 2006 AMMA campaign. *Geophys. Res. Lett.*, *35*, doi:10.1029/2008GL035920. doi: 10.1029/2008GL035920

Risi, C., Muller, C., & Blossey, P. (2021). Rain evaporation, snow melt, and entrainment at the heart of water vapor isotopic variations in the tropical troposphere, according to large-eddy simulations and a two-column model. *J. Adv. Model. Earth Sci.*, *13*(4), e2020MS002381, DOI: https://doi.org/10.1029/2020MS002381.

Risi, C., Muller, C., & N, B. P. (2020). What controls the water vapor isotopic composition near the surface of tropical oceans? Results from an analytical model constrained by large-eddy simulations. *J. Adv. Model. Earth Sci.*, *12(8)*, DOI: https://doi.org/10.1029/2020MS002106.

Robe, F. R., & Emanuel, K. A. (2001). The effect of vertical wind shear on radiative–convective equilibrium states. *J. Atm. Sci.*, *58*(11), 1427–1445, DOI: https://doi.org/10.1175/1520-0469.

Rotunno, R., Klemp, J. B., & Weisman, M. L. (1988). A theory for strong, long-lived squall lines. *J. Atm. Sci.*, *45*(3), 463–485, DOI: https://doi.org/10.1175/1520-0469.

Sanchez-Murillo, R., Durán-Quesada, A. M., Esquivel-Hernández, G., Rojas-Cantillano, D., Birkel, C., Welsh, K., … others (2019). Deciphering key processes controlling rainfall isotopic variability during extreme tropical cyclones. *Nat. Commun.*, *10*(1), 1–10, DOI: https://doi.org/10.1038/s41467-019-12062-3.

Sinha, N., & Chakraborty, S. (2020). Isotopic interaction and source moisture control on the isotopic composition of rainfall over the Bay of Bengal. *Atmos. Res.*, *235*, 104760, DOI: https://doi.org/10.1016/j.atmosres.2019.104760.

Skrzypek, G., Dogramaci, S., Page, G. F., Rouillard, A., & Grierson, P. F. (2019). Unique stable isotope signatures of large cyclonic events as a tracer of soil moisture dynamics in the semiarid subtropics. *J. Hydrol.*, *578*, 124124, DOI: https://doi.org/10.1016/j.jhydrol.2019.124124.

Smolarkiewicz, P. K., & Grabowski, W. W. (1990). The multi-dimensional positive definite advection transport algorithm: Non-oscillatory option. *J. Comput. Phys*, *86*, 355-375, DOI: https://doi.org/10.1016/0021-9991(90)90105-A.

Stevens, B. (2006). Bulk boundary-layer concepts for simplified models of tropical dynamics. *Theor. Comput. Fluid Dyn.*, *20*(5-6), 279–304.

Su, H., Bretherton, C. S., & Chen, S. S. (2000). Self-aggregation and large-scale control of tropical deep convection: A modeling study. *J. Atm. Sci.*, *57*(11), 1797–1816, DOI: https://doi.org/10.1175/1520-0469.

Sun, C., Tian, L., Shanahan, T. M., Partin, J. W., Gao, Y., Piatrunia, N., & Banner, J. (2022). Isotopic variability in tropical cyclone precipitation is controlled by Rayleigh distillation and cloud microphysics. *Commun. Earth Environ.*, *3*(1), 1–10, DOI: https://doi.org/10.1038/s43247-022-00381-1.

Tan, J., Jakob, C., & Lane, T. P. (2013). On the identification of the large-scale properties of tropical convection using cloud regimes. *J. Clim.*, *26*(17), 6618–6632, DOI: https://doi.org/10.1175/JCLI-D-12-00624.1.

Taupin, J.-D., & Gallaire, R. (1998). Variabilité isotopique à l'échelle infra-événement de quelques épisodes pluvieux dans la région de Niamey, Niger. *Comptes Rendus de l'Académie des Sciences-Series IIA-Earth and Planetary Science*, *326*(7), 493–498.

Thompson, G., Field, P. R., Rasmussen, R. M., & Hall, W. D. (2008). Explicit forecasts of winter precipitation using an improved bulk microphysics scheme. Part II: Implementation of a new snow parameterization. *Mon. Weather Rev.*, *136*(12), 5095–5115, DOI: https://doi.org/10.1175/2008MWR2387.1.

Thurnherr, I., & Aemisegger, F. (2022). Disentangling the impact of air-sea interaction and boundary layer cloud formation on stable water isotope signals in the warm sector of a southern ocean cyclone. *Atmos. Chem. Phys.*, *22*(15), 10353-10373.

Tobin, I., Bony, S., & Roca, R. (2012). Observational evidence for relationships between the degree of aggregation of deep convection, water vapor, surface fluxes and radiation. *J. Clim.*, *25(20)*, 6885-6904 , DOI: https://doi.org/10.1175/JCLI-D-11-00258.1.

Torri, G. (2021). On the isotopic composition of cold pools in radiative-convective equilibrium. *J. Geophy. Res.*, *126*(10), e2020JD033139.

Torri, G. (2022). Isotopic equilibration in convective downdrafts. *Geophys. Res. Lett.*, *49*(15), e2022GL098743.

Torri, G., Ma, D., & Kuang, Z. (2017). Stable water isotopes and large-scale vertical motions in the tropics. *J. Geophys. Res*, *122(7)*, 3703-3717, DOI: https://doi.org/10.1002/2016JD026154.

Tremoy, G., Vimeux, F., Mayaki, S., Souley, I., Cattani, O., Favreau, G., & Oi, M. (2012). A 1-year long delta18O record of water vapor in Niamey (Niger) reveals insightful atmospheric processes at different timescales. *Geophys. Res. Let.*, *39(8)*, DOI: https://doi.org/10.1029/2012GL051298.

Tremoy, G., Vimeux, F., Soumana, S., Souley, I., Risi, C., Cattani, O., … Oi, M. (2014). Clustering mesoscale convective systems with laser-based water vapor delta18O monitoring in Niamey (Niger). *J. Geophys. Res.*, *119(9)*, 5079-5103, DOI: 10.1002/2013JD020968.

Vimeux, F., Gallaire, R., Bony, S., Hoffmann, G., & Chiang, J. C. H. (2005, December). What are the climate controls on deltaD in precipitation in the Zongo Valley (Bolivia)? Implications for the Illimani ice core interpretation. *Earth Planet. Sci. Lett.*, *240*, 205-220: DOI: https://doi.org/10.1016/j.epsl.2005.09.031. doi: 10.1016/j.epsl.2005.09.031

Vimeux, F., Tremoy, G., Risi, C., & Gallaire, R. (2011). A strong control of the South American SeeSaw on the intraseasonal variability of the isotopic composition of precipitation in the Bolivian Andes. *Earth. Planet. Sci. Lett.*, *307 (1-2)*, 47-58, DOI: https://doi.org/10.1016/j.epsl.2011.04.031.

Wang, Y. J., Cheng, H., Edwards, R. L., An, Z. S., Wu, J. Y., Shen, C. C., & Dorale, J. A. (2001). A high-resolution absolute-dated late Pleistocene Monsoon record from Hulu Cave, China. *Science*, *294(5550)*, 2345-8, DOI: 10.1126/science.106461.

Welsh, K., & Sánchez-Murillo, R. (2020). Rainfall, groundwater, and surface water isotope data from extreme tropical cyclones (2016-2019) within the caribbean sea and atlantic ocean basins. *Data in Brief*, *30*, 105633, DOI: https://doi.org/10.1016/j.dib.2020.105633.

Worden, J., Noone, D., & Bowman, K. (2007). Importance of rain evaporation and continental convection in the tropical water cycle. *Nature*, *445*, 528-532, DOI; https://doi.org/10.1038/nature05508.

Xu, T., Sun, X., Hong, H., Wang, X., Cui, M., Lei, G., … Jiang, X. (2019). Stable isotope ratios of typhoon rains in Fuzhou, Southeast China, during 2013–2017. *J. Hydrol.*, *570*, 445–453, DOI: https://doi.org/10.1016/j.jhydrol.2019.01.017.

Yang, M.-H., & Houze Jr, R. A. (1995). Sensitivity of squall-line rear inflow to ice microphysics and environmental humidity. *Mon. Wea. Rev.*, *123*(11), 3175–3193, DOI: https://doi.org/10.1175/1520-0493.

Yoshimura, K., Oki, T., Ohte, N., & Kanae, S. (2003). A quantitative analysis of short-term O18 variability with a Rayleigh-type isotope circulation model. *J. Geophys. Res.*, *108*, D20, 4647, doi:10.1029/2003JD003477.

Zipser, E. (1977). Mesoscale and convective scale downdrafts as distinct components of squall-line structure. *Mon. Wea. Rev.*, *105*, 1568-1589, DOI: https://doi.org/10.1175/1520-0493.

RÉSUMÉ

La convection atmosphérique fait référence aux mouvements d'air verticaux dans lesquels les nuages se forment, et on parle de convection profonde lorsque ces mouvements couvrent toute la hauteur de la troposphère. Quand la convection profonde s'organise, elle peut prendre diverses formes, dont celle de systèmes convectifs méso-échelle (MCSs) qui désignent des ensembles nuageux caractérisés par une échelle horizontale de l'ordre de la centaine de kilomètres, et d'une durée de vie de plusieurs heures. L'exemple le plus spectaculaire est sans doute le cyclone tropical, dont les vents en rotation sont parmi les plus forts de notre planète. Il en existe d'autres types, comme les lignes de grains qui décrivent un alignement d'orages sur plusieurs centaines de kilomètres. Ces systèmes convectifs méso-échelles sont à l'origine de la plupart des événements extrêmes tels que les fortes pluies et les crues soudaines. Pourtant, leur organisation reste peu comprise et donc peu prise en compte dans les estimations climatiques. Plus précisément, l'échelle caractéristique de la centaines de kilomètres des MCSs est inférieure à la résolution spatiale des modèles climatiques globaux, qui traitent donc les systèmes convectifs profonds comme des phénomènes sous-maille. Leur dynamique est alors calculée à l'aide de paramétrisation, c'est à dire d'un modèle réduit des équations des fluides. Cependant, du fait du manque de connaissances théoriques sur le développement de la convection, les modèles de paramétrisation actuels ne parviennent pas à anticiper la formation de phénomènes extrêmes et peinent à prédire leur évolution avec le réchauffement climatique. Cette barrière scientifique fait partie des grands défis énoncés par le Word Climate Research Program1 (WCRP) : Nuages, circulation et sensibilité climatique. Ce projet de thèse cherche 1) à clarifier les mécanismes physiques à l'origine de la formation des système convectifs méso-échelle tropicaux sur océans, 2) à comprendre les précipitations extrêmes qui leur sont associées. Ce travail porte en particulier sur les lignes de grains, et s'appuie sur des simulations numériques, l'élaboration de modèles théoriques et la confrontations à des données d'observations satellitaires. A terme, l'objectif de cette thèse sera de contribuer à l'amélioration des modèles de paramétrisation de l'organisation de la convection dans les tropiques, et cherchera à déterminer si les lignes de grains vont devenir plus fréquentes et plus intenses avec le réchauffement climatique, et si oui pourquoi.

MOTS CLÉS

Convection Profonde. Précipitations Extrêmes. Ligne de grains. Orages. Cloud Resolving model. Machine Learning. Isotopes.

ABSTRACT

Atmospheric convection refers to the vertical air motions in which clouds form, and deep convection occurs when these motions cover the entire height of the troposphere. When deep convection is organized, it can take various forms, including mesoscale convective systems (MCSs), which are cloud clusters characterized by a horizontal scale of the order of a hundred kilometres, and a lifetime of several hours to days. The most spectacular example is probably the tropical cyclone, whose rotating winds are among the strongest on our planet. There are other types, such as squall lines, which describe a line of thunderstorms several hundred kilometres long. These mesoscale convective systems are responsible for most extreme events such as heavy rainfall and flash floods. However, their organization remains poorly understood and therefore little taken into account in climate estimates. More precisely, the characteristic scale of hundreds of kilometres of MCSs is lower than the spatial resolution of global climate models, which therefore treat deep convective systems as submesh phenomena. Their dynamics are then calculated using parametrisation, i.e. a reduced model of the fluid equations. However, due to the lack of theoretical knowledge on the development of convection, current parameterisation models are unable to anticipate the formation of extreme phenomena and have difficulty predicting their evolution with global warming. This scientific barrier is part of the major challenges set out by the Word Climate Research Program1 (WCRP): Clouds, circulation and climate sensitivity. This thesis project seeks 1) to clarify the physical mechanisms behind the formation of tropical oceanic mesoscale convective systems, 2) to understand the extreme precipitation associated with them. This work focuses in particular on squall lines, and is based on numerical simulations, the development of theoretical models and confrontation with satellite observations. In the long term, the objective of this thesis will be to contribute to the improvement of parameterization models of the organization of convection in the tropics, and will seek to determine if squall lines will become more frequent and intense with global warming, and if so why.

KEYWORDS

Deep Convection. Extreme Precipitation. Squall Line. Storms. Cloud Resolving Model. Machine Learning. Isotopes.